WEAR AND CORROSION BEHAVIOR OF DUPLEX TREATED MECHANICAL PARTS

Teză destinată obţinerii
titlului ştiinţific de doctor inginer
la
Universitatea Politehnica Timişoara
în domeniul ȘTIINȚA ȘI INGINERIA MATERIALELOR
de către

Ing. Ramona Monica Dobra

Conducători ştiinţifici:	prof.univ.dr.ing Ion Mitelea prof.univ.dr.ing Viorel-Aurel Șerban
Referenţi ştiinţifici:	prof.univ.dr.ing. Valeriu Deac cer.pr.I,dr. Nicolae Farbaș conf.univ.dr.ing. Corneliu Crăciunescu

Ziua susţinerii tezei: 06.02.2013

Seriile Teze de doctorat ale UPT sunt:

1. Automatică
2. Chimie
3. Energetică
4. Ingineria Chimică
5. Inginerie Civilă
6. Inginerie Electrică
7. Inginerie Electronică şi Telecomunicaţii
8. Inginerie Industrială
9. Inginerie Mecanică
10. Ştiinţa Calculatoarelor
11. Ştiinţa şi Ingineria Materialelor

Universitatea „Politehnica” din Timişoara a iniţiat seriile de mai sus în scopul diseminării expertizei, cunoştinţelor şi rezultatelor cercetărilor întreprinse în cadrul şcolii doctorale a universităţii. Seriile conţin, potrivit H.B.Ex.S Nr. 14 / 14.07.2006, tezele de doctorat susţinute în universitate începând cu 1 octombrie 2006.

România, 300159 Timişoara, Bd. Republicii 9,
tel. 0256 403823, fax. 0256 403221
e-mail: editura@edipol.upt.ro

Familiei mele,

DOBRA, Ramona Monica

Wear and corrosion behavior of Duplex treated mechanical parts

Teze de doctorat ale UPT, Seria 11, Nr. 33, Editura Politehnica, 2013, 191 pagini, 207 figuri, 41 tabele.

ISSN: 1842-7855

ISSN-L: 1842-7855

ISBN: 978-606-554-626-4

Cuvinte cheie: Ingineria Suprafetelor, tratamente Duplex, nitrurare, carburare, calire CIF, uzare, coroziune

Rezumat, Principalele cauze care conduc la scoaterea din uz a echipamentelor şi pieselor mecanice se datorează în primul rând uzurii ”morale” (înlocuirea echipamentelor şi pieselor mecanice vechi cu cele noi), accidentelor şi altor forme de erori umane şi într-o proporţie majoritară din cauza degradării suprafeţei, fie prin uzare, coroziune (degradare chimică) sau oboseală. De-a lungul timpului, cercetătorii au încercat să investigheze sau cel puţin să reducă degradarea suprafeţei prin utilizarea tratamentelor de suprafaţă şi a tehnicilor de lubrifiere, lucru ce a condus la dezvoltarea unei noi discipline, numită Inginerie de Suprafață. În ultimii 20 de ani s-au înregistrat progrese semnificative în domeniul Ingineriei de Suprafaţă: optimizarea proceselor tradiționale (galvanizare, pulverizare termică și tratamente termochimice), comercializarea unor tehnici moderne (CVD, PVD/PAPVD, pulverizare în plasmă și implantare de ioni), dezvoltarea tehnologiilor inovative și depunerea de materiale noi (straturi amorfe).
Cu toate acestea, echipamentele şi piesele mecanice vor funcționa în condiții tot mai severe, (sarcini intensive și medii agresive), cu scopul atingerii unei productivităţi şi eficiențe energetice ridicate, cu un consum redus de energie. Prin urmare, existămulte situații în care combinația mai multor proprietăți, cum ar fi rezistenţa la uzare suprapusăpeste capacitatea portantă, oboseală şi coroziune, este absolut necesară. Aceste noi provocări pot fi îndeplinite cu succes printr-o tehnologie nouă, inovativă -Tratamente Duplex-, cunoscută în literatura de specialitate şi ca Inginerie de Suprafaţă Duplex. În acest context, cercetările întreprinse au avut ca scop generarea de straturi de suprafață Duplex, cu rezistenţă ridicată la uzare, coroziune şi oboseală.

Foreword

I am using this opportunity to express my gratitude to everyone who supported me throughout the course of my PhD thesis. I am thankful for their aspiring guidance, invaluably constructive criticism and friendly advice and I am sincerely grateful to them for sharing their truthful and illuminating views on a number of issues related to the thesis.

Foremost, I would like to express my sincere gratitude to Prof. Rui Villar and the collective from IST and LNEG Lisbon for accepting me in a research stage and for their continuous support, for their patience, motivation, enthusiasm, and immense knowledge. Their guidance helped me in all the time of research and writing of this thesis. Also, I would like to thank my thesis coordinators, Prof. Mitelea and Prof. Serban for their encouragement, and insightful comments.

I thank my fellow labmates from Materials and Manufacturing Engineering Department of Timisoara: dr. Dragos Buzdugan, dr. Cioana Cristian, dr. Vlad Tut, dr. Iancu Serban, dr. Florin Cornea, dr. Iosif Hulka, and Dr. Cosmin Codrean for the stimulating discussions, for the sleepless nights we were working together before deadlines, and for all the fun we have had in the last four years. Also I thank my friends from IST Lisbon: PhD students Liliana Cangueiro, Bruno Nunes, and Tomi Liu for their support during my PhD stage.

Last but not the least, I would like to thank to my parents and brother for their support throughout this period.

Timişoara, 02.2013 Ramona Monica Dobra

CONTENTS

I – STATE OF THE ART
1. INTRODUCTION TO SURFACE ENGINEERING

1.1 Introduction

Nowadays there is a growing need to reduce or control wear, corrosion and fatigue in order to extend the lifetime of equipments, to make engines and devices more efficient, to develop new advanced products, to conserve material resources, to save energy and to improve safety [1]. According to Rabinowicz, the major things that cause equipments and mechanical parts to lose their usefulness are: obsolescence, accidents and surface degradation, Figure 1.1 [2].

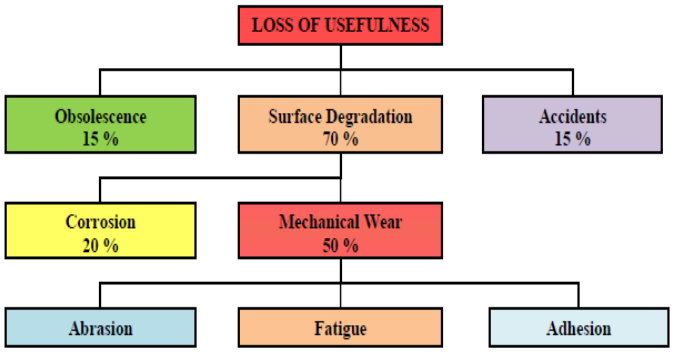

Figure 1.1: Major factors that cause equipments and parts failure (adapted from [2])

Obsolescence is fundamental to engineering and technology evolution; the old must be replaced by the new. There are some inventions that have long life cycles, for example grease fitting. Its design has changed little since Oscar Zerk invented it in the early 1920's, and is still widely used today. On the other hand, the automobiles are dynamic and in constant flux. Most of them face practical obsolescence long before they are functionally inoperable. Accidents and other forms of human errors can lead also to equipments failure. The third major reason refers to surface degradation, which can be divided into chemical degradation (corrosion) and mechanical damage, as presented in Figure 1.1 [2]. Mechanical surface degradation is divided into wear and fatigue [2, 3].

The economical impact of friction, wear and corrosion on society is huge. It has been estimated that the economic cost of wear and friction in USA exceeds US$100 billion per annum [4]. Experts estimate that tribological damages cause a loss of approx. 1% of the German National Product (GNP). The economic effect of corrosion damage is even higher, approaching approx. 3.5–4.2% of the GNP [5].

The control of surface degradation has been realized by design changes, surface treatments, by selecting new, improved materials or by utilizing lubrication techniques, which has led to the development of a new discipline, called Surface Engineering [1]. Surface Engineering has had a very significant technological,

economical and environmental impact on modern science and technology by reducing the capital investment, increasing profitability, design changes and technical innovation [6, 7, 8]. This development has been encouraged by two important reasons. The first one is the development of new coatings and treatment methods, which provide characteristics and properties that were previously unachievable. The second reason has been the admission of engineers and materials scientists that the surface is the most important part in engineering components. Most failures occur at the surface, either by wear, corrosion or fatigue [1].

According to Haefer, the surface is responsible for all mechanical, thermal, chemical, and electrochemical interactions with the environment. Therefore, the main requests that need to be fulfilled by technical surfaces are:

- High corrosion, wear and fatigue resistance;
- optical and decorative characteristics [9];

The surface has also other important characteristics, such as thermal, electronic and magnetic that influences the material selection [1]. For example, the components used in micro-technology can require special electromagnetic properties of surfaces. The requirements of part surfaces are also determined by the load conditions under which the final product operates. Figure 1.2 presents the main types of load conditions, divided into volume and surface loads [5].

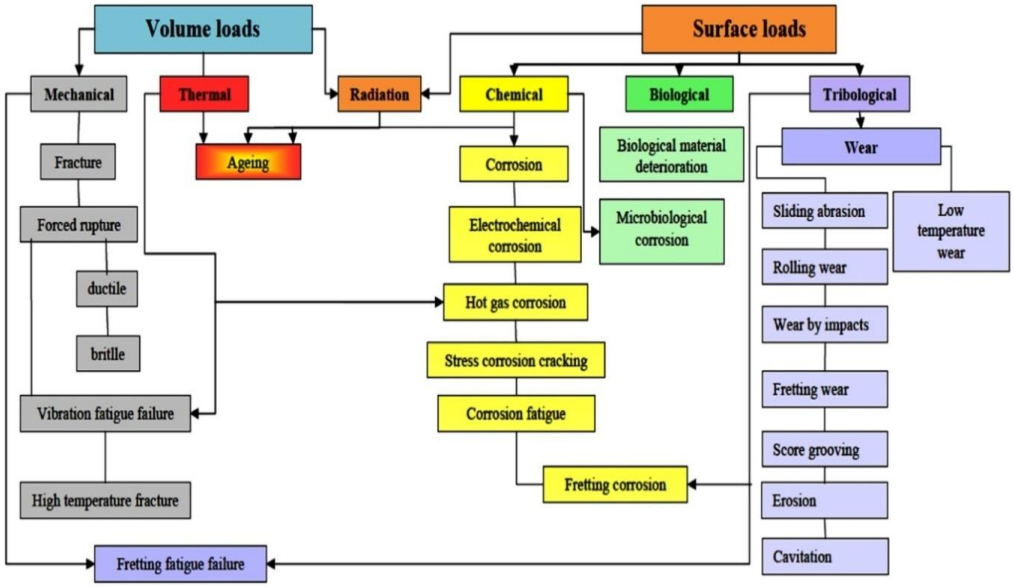

Figure 1.2: Volume and surface loads of mechanical parts (adapted from [5])

1.2 Surface characteristics

The shape of a surface is characterized by the surface topography (Figure 1.3 a) and by the surface profile, (Figure 1.3 b). A typical metallic surface has a profile with "hills and valleys". The height difference from the bottom of the valley to the top of a hill is typically 0.1 up to 3 μm [1].

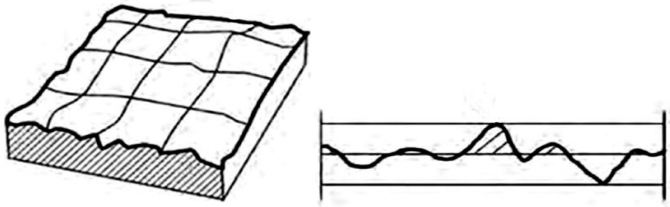

a b

Figure 1.3: Typical metallic surface: a–surface topography;
b – surface profile (adapted from [1])

When one surface is placed upon another, the first contact between the surfaces will take place at the top points of the highest peaks of the surfaces [10]. Experiments suggest that there are huge numbers of these contacts. However, the true area of contact, Figure 1.4, is considerably smaller than the nominal area of contact [1].

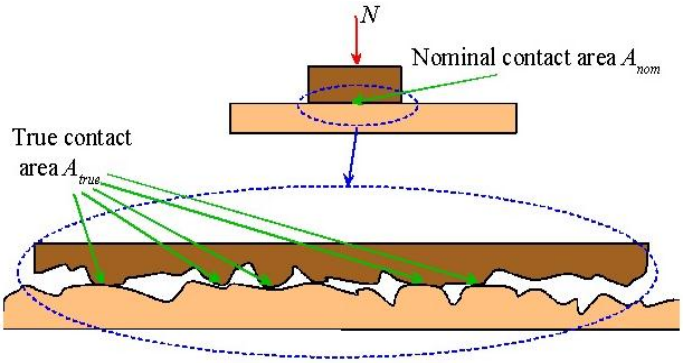

Figure 1.4: The real contact aria between two surfaces (adapted from [1])

The chemical and physical nature of a surface depends on the material's composition and the surrounding environment. A schematic representation of a solid surface is presented in Figure 1.5 [11]. Depending on the machining process, mechanical parts have a surface layer with different properties, compared to the core. During machining, the energy that is formed in the surface can be transformed in deformation, strain hardening, recrystallization and texturing. During polishing, grinding and machining, the surface layers are plastically deformed with or without a temperature gradient. They become highly strained and residual stresses may appear. Usually, the thickness of the worked layer (deformed layer) ranges between 1–100 μm. The Beilby layer in metals is produced by melting and surface flow during machining. Typically, this layer has an amorphous or micro-crystalline structure and a thickness up to 1–100 nm [1].

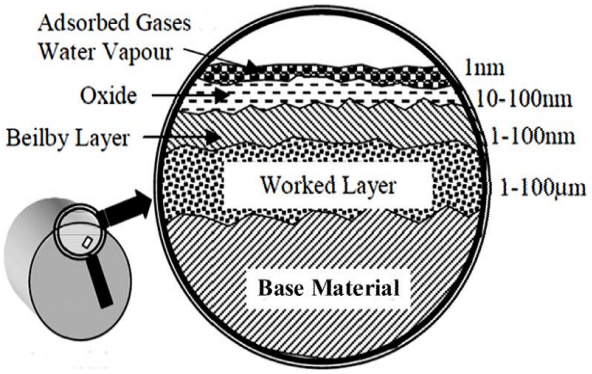

Figure 1.5: Schematic representation of a solid surface (adapted from [11])

Metals react with oxygen and form oxide layers. In other environments they may form nitrides, sulphides and chlorides. The thickness of the oxide layer is about 10–100 nm and depends on the material reactivity to the environment, temperature reaction and time. The physical and chemical nature of surfaces has been described by many researchers [11-14]. Adsorbed contaminant layers can be formed from the environment by chemical or physical adsorption. The most common constituents of physical adsorbed layers are water vapour molecules, oxygen or hydrocarbons that may be condensed and physically adsorbed on the surface. The layer can be monomolecular (about 1 nm thick) or poly-molecular (5 nm thick) [1].

1.3 Surface degradation caused by wear, corrosion and fatigue

1.3.1 Friction and wear of materials

Friction and wear are two phenomena which appear when two bodies are in contact and slide over each other. They are not material properties, but system properties and depend on the materials in contact and the operational conditions. Friction is needed for traction and braking systems but must be minimized in order to reduce the energy dissipation. Wear is needed for cutting processes but should be minimized in sliding and rolling contact applications in order to increase lifetime [15].

1.3.1.1 Friction

Friction represents the resisting force to relative motion of solid surfaces, fluid layers, and material elements sliding over each other [16]. There are several types of friction:

- Dry friction, which appears at the contact between two solid surfaces; it can be static (the surfaces in contact do not move relative to each other) and dynamic (the surfaces are moving relative to each other) [17];
- Lubricated friction, which appears at the contact between two solid surfaces separated by a fluid [18, 19];

- Fluid friction, which describes the friction between layers within a viscous fluid that are moving relative to each other [20, 21];
- aerodynamic friction, which occurs at the contact between a gas and a solid surface;
- liquid friction, which occurs at the contact between a liquid and a solid surface [16];

The friction process was studied by many researchers. An excellent overview of the history of friction investigations has been presented by Dowson [22]. Two basic laws of friction were formulated in 1699 by Amontons. He stated that (1) the friction force is directly proportional to the normal load and (2) the friction force is independent of the apparent contact area. In 1785, Coulomb stated that the friction force is independent of sliding velocity, which is now known as the third law of friction [15]. In unlubricated sliding conditions, the first law of friction is respected for many material combinations, for example steel on polished aluminium [23], alumina sliding against zirconia [15], etc. Yet, there are some materials combinations that not obey the first law, such as diamonds and certain very soft materials. For these special materials, friction is proportional to a reduced value of the load [24]. The second law is observed when a wood surface slides against a steel surface [24]. The third law can be observed in dry sliding contact of alumina doped with 1 % wt CuO against alumina [15]. But at very high and low speeds, the third law of friction is not respected [24].

Some researchers have concentrated their studies on the effect of plastic deformation and surface roughness on friction. They showed that friction arises from plastically deformed asperities as they slide over each other. Heilmann and Rigney suggested an energy-based friction model where metallurgical effects were included [1]. However, their results have been disputed by Tangena et al. They concluded that if surface asperities are plastically deformed, the influence of surface roughness on the contact parameters will be small, due to the fact that the asperities will deform in such way that a continuous surface is obtained [25]. It was confirmed by Rabinowicz, who found a minor influence of surface roughness on friction in static experiments with noble metals [26]. Bowden and Tabor [27] observed that the frictional force arises from the adhesion force (F_{adh}) and the deforming force (F_d), as shown schematically in Figure 1.6. The deformation force is called 'ploughing friction' when occurs on a macro-scale and 'asperity deformation' when occurs on micro-scale.

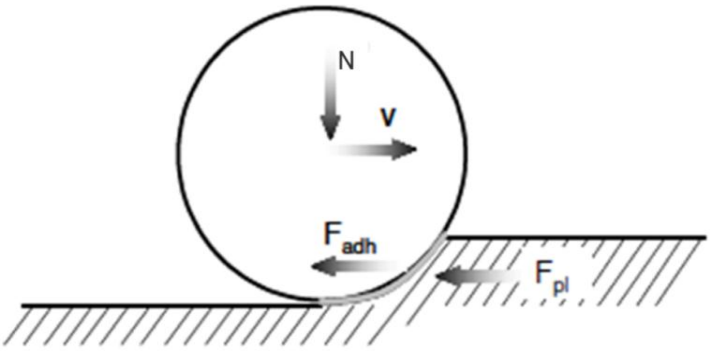

Figure 1.6: Friction according to Tabor (adapted from [27])

The friction process is often quantified by the friction coefficient, which can be written, based on the first law of friction, as:

$$\mu = \frac{F}{N} \tag{1.1}$$

where F is the friction force and N the normal load [1]. In Table 1.1 are presented some values of friction coefficients for various material pairs [28].

Table 1.1: Friction coefficient values [28]

Materials	Friction coefficient
Steel on soft surface (lead, bronze, etc.)	0.1-0.5
Steel on ceramics	0.1-0.5
Ceramics on ceramics	0.05-0.5
Polymers on polymers	0.05-1.0
Metals and ceramics on polymers	0.04-0.5
High temperature lubricants	0.05-0.2
Clean metals in air	0.8-2.0

Figure 1.7 presents the values of friction coefficients for steel on steel catalogued by Lim and Ashby based on experimental measurements [29].

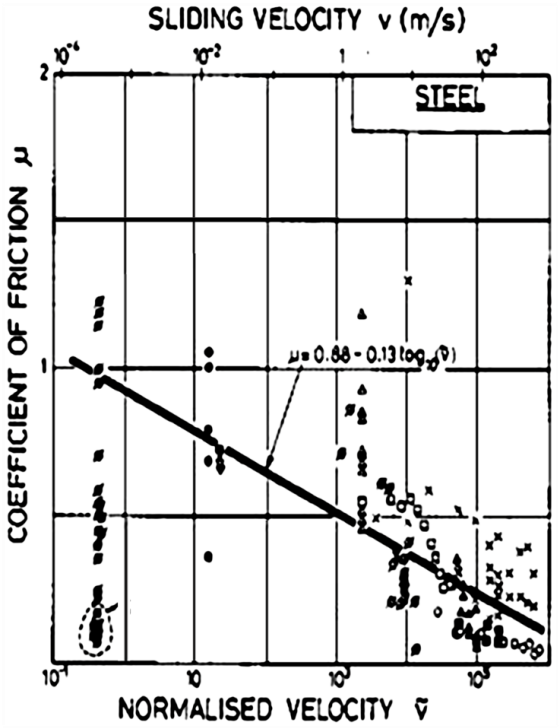

Figure 1.7: Steel on steel friction coefficient (adapted from [29])

1.3.1.2 Wear

Wear is commonly defined as the progressive loss of material due to the contact between two moving surfaces. It can appear from the contact and relative motion of two solids, but also at the contact between a liquid or gas (water jet, air bubble implosions) with a solid [30]. Still, any definition of the wear process is still a "light sentence" because of its complexity [31]. Halling said that "wear is familiar to everyone and probably we all feel that we understand what is meant by wear. However, the formulation of a precise definition of wear is difficult [32] ".

From an engineering point of view, wear is often classified as either mild or severe. Mild wear refers to processes that produce smooth surfaces, with minimal plastic deformation. Severe wear is often associated with seizure, a situation usually unacceptable. But, this classification does not say much about the active wear mechanism. In many situations, there are several mechanisms operating simultaneously [33]. Therefore, researchers often tend to classify wear based on the dominant active mechanism. The basic mechanisms of wear are abrasive [33, 34], adhesive [35-37], fatigue [38-40] and chemical wear [41-42]. Combinations of these mechanisms lead to characteristic damage modes, such as: delamination, fretting, pitting, scuffing and galling, cutting, ploughing, electrical, as presented in Figure 1.8 [1].

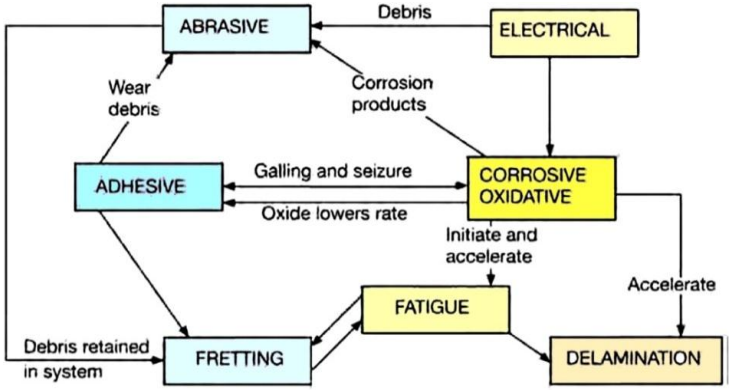

Figure 1.8: Mechanisms and modes of wear (adapted from [1])

The transition from one dominant wear mechanism to another can be studied by constructing diagrams, known as wear maps, showing the rate and dominance regime of a number of wear mechanisms [33]. An example of such map is presented in Figure 1.9 and describes the unlubricated pin-on-disc wear behaviour of steels over a wide range of sliding conditions [43].

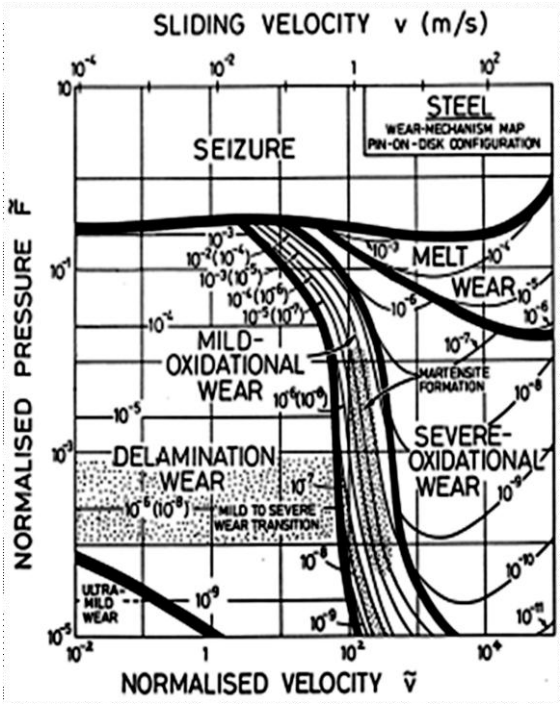

Figure 1.9: Wear map for steels (adapted from [43])

From the technological point of view, abrasive and contact fatigue wear are the most important. It was estimated that the total wear of machine elements can be identified in 80-90% as abrasion and 8% fatigue wear [1].

Abrasive wear occurs in contacts where one of the surfaces is considerably harder than the other (two bodies wear, Figure 1.10 [44]) or when hard particles are introduced between the surfaces (three bodies wear, Figure 1.11 [45]) [1].

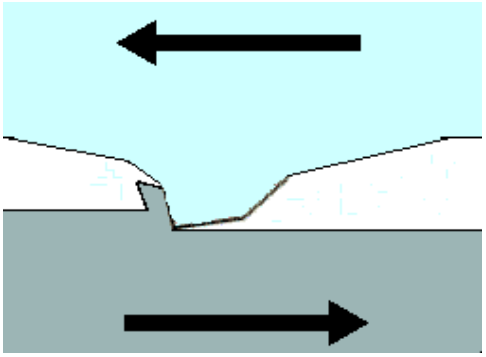

Figure 1.10: Two bodies wear (adapted from [44])

Particles enter the clearance space between the two moving surfaces, bury themselves in one of the surface, act like cutting tools and remove the material from the opposing surface. The greatest damage is produced by the particles with equal sizes or slightly larger than the clearance space [46].

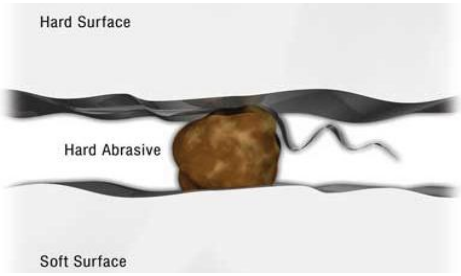

Figure 1.11: Three bodies wear (adapted from [45])

Depending on the geometry of the harder surface and the degree of penetration, the removal of material can take different forms, such as ploughing or cutting, as shown by Hokkirigawa and Kato [47]. Typical components subjected to abrasion are hydraulic pumps (gear, piston pumps, vane, etc), cylinders (piston seals, bearings, etc.), journal bearings and hydraulic motors [46].

Adhesive wear appears when asperities of one surface come into contact with asperities of the counter surface. They may adhere strongly to each other and form asperity junctions [1], as shown in Figure 1.12. The mechanical parts subjected to adhesive wear are ball bearings, journal bearings, etc [46].

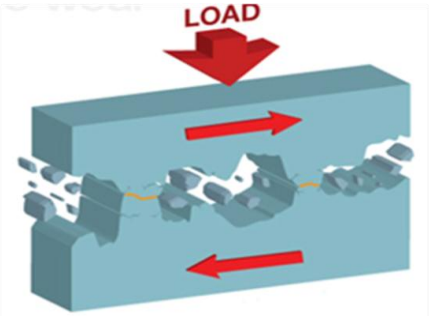

Figure 1.12: Adhesive wear process (adapted from [46])

Fatigue wear, also called rolling contact fatigue, predominantly occurs in roller bearings and gear contacts [1]. The failure occurs as a result of repeated stress caused by particles trapped between two moving surfaces, Figure 1.13 [46].

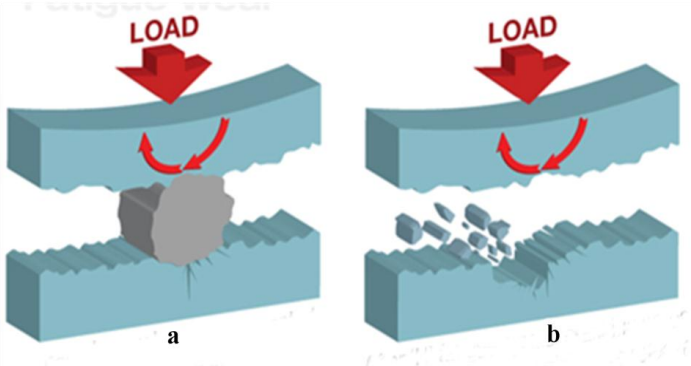

Figure 1.13: Fatigue wear processes (adapted from [46])

At first, the surfaces are dented and the cracking begins (Figure 1.13 a). These cracks spread after repeated stress, even without additional damage, but eventually the surface fails, producing a spall (Figure 1.13 b) [45, 46].

In chemical wear, the process is dominated by the chemical reactions that occur in the contact of two surfaces. These reactions are influenced by the environment in combination with mechanical contact mechanisms, as shown in Figure 1.14. The most common chemical wear process is represented by oxidation wear. On the top of metal surfaces a thin layer of oxides is formed. This is an important protecting layer because without it both the friction and wear in metal contacts would be extremely high [1].

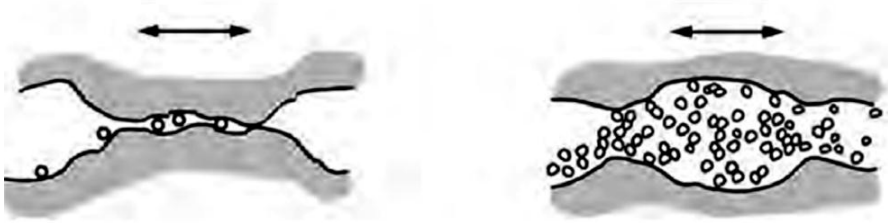

Figure 1.14: Chemical wear process (adapted from [1])

Besides the wear mechanism, engineers are also interested in quantifying the amount of material that is removed from the surface. Archard proposed an equation to calculate the volume of worn material as:

$$V = \frac{K \times N}{H} \tag{1.2}$$

Where V is the volume of the removed material, K is a constant (wear coefficient), N the normal load and H the hardness of the softer surface. The ratio K/H is called the specific wear rate and by modifying equation (1.2), the specific wear rate can be calculated as [48]:

$$Q = \frac{V}{N} \left[\frac{mm^3}{N}\right] \tag{1.3}$$

The volume of worn material increase linearly (constant specific wear rate) as a function of sliding distance. But, sometimes it can be observed a sudden change in the wear volume (changing specific wear rate) depending on the wear mechanism involved [15].

1.3.2 Corrosion

Metals appear in nature most commonly as oxide or sulphide ores, in which they are in a higher oxidation state than that of the free metal. Extraction of the metal from its ore involves the reduction of the oxidized form, resulting in an increase of internal free energy. Consequently, the metal will try to lose its excess energy by becoming oxidized again, through loss of electrons [49], Figure 1.15 [50].

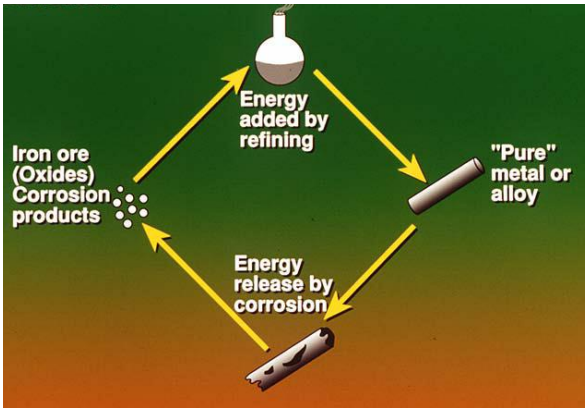

Figure 1.15: Corrosion process (adapted from [50])

This oxidizing tendency of metals is the driving force for corrosion and it is found virtually in all metals, except the very noble metals, such as gold or platinum [49]. All corrosive attacks begin at the metal surface, as presented in Figure 1.16 [51].

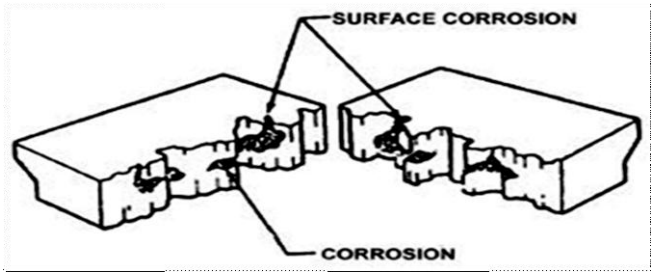

Figure 1.16: Corrosion attack (adapted from [51])

Corrosion only rarely produces a uniform loss of engineering components. More often, the corrosion process manifests through localized attacks, producing pits, blisters, cracks and crevices, which can lead to a catastrophic failure, especially if mechanical stresses are present. Figure 1.17 presents schematically some of the more common corrosion morphologies encountered in practice, such as uniform, pitting, intergranular, crevice, fatigue, stress corrosion, etc. [52].

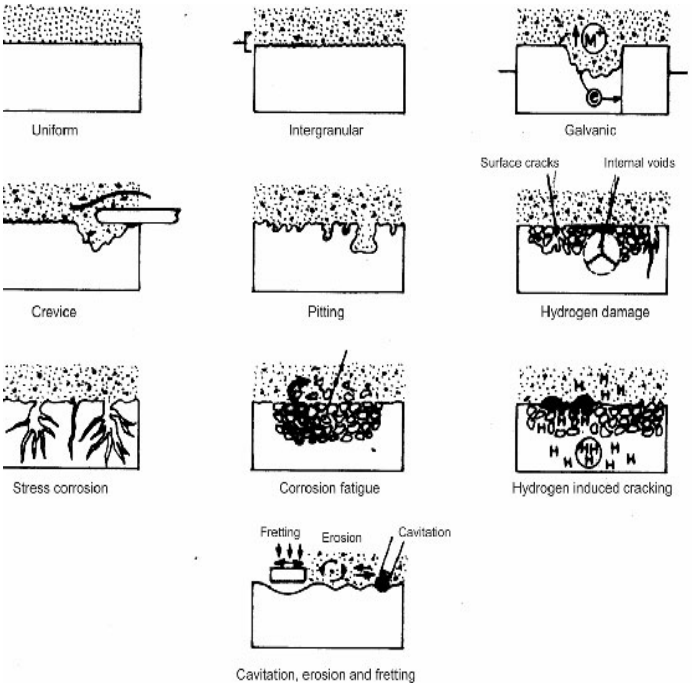

Figure 1.17: Schematic illustration of different types of corrosion (adapted from [52])

1.3.3 Fatigue

Fatigue of metals is a very complex phenomenon, which is still not fully understood and it is also the main topic of many researchers. In materials science, fatigue is defined as the progressive and localized structural damage that occurs when a material is subjected to cyclic loading. The nominal maximum stress values are lower than the ultimate tensile stress limit, and may be below the yield stress limit of the material [53-58].

In Figure 1.18 is presented the major surface features that appear on almost every fatigue process [54].

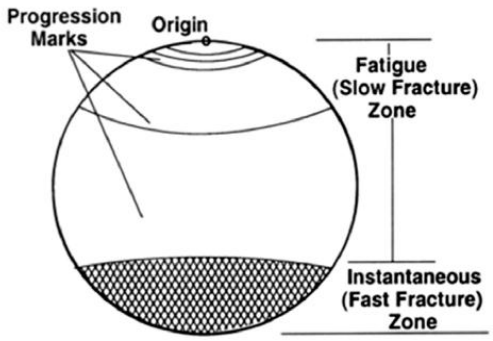

Figure 1.18: Fatigue major surface features (adapted from [54])

The origin is where the crack actually starts and grows slowly across the fatigue zone. A single origin usually indicates a failure with low overstress, while the presence of multiple origins may be the result of either high stress or high stress concentrations. During this slow crack growth, the load variations determine variations of the crack growth rate, which appears as progression marks. The progression marks show how the crack has grown and are only present in fractures where there have been substantial stress variations. When the cracks reached the point where the remaining material was overstressed the overload zone resulted. The overload zone, or fast fracture zone, is the portion of the piece where the final catastrophic failure occurs [54-56]. In Figures 1.19-1.20 are presented some failure caused by surface fatigue [54].

Figure 1.19: A basic fatigue failure complicated by several holes (adapted from [54])

From figure 1.19, it can be observed two origins crack (1). The progression marks work across the fracture zone. The growth of the fracture zone is essentially straight across the zone (2) [54].

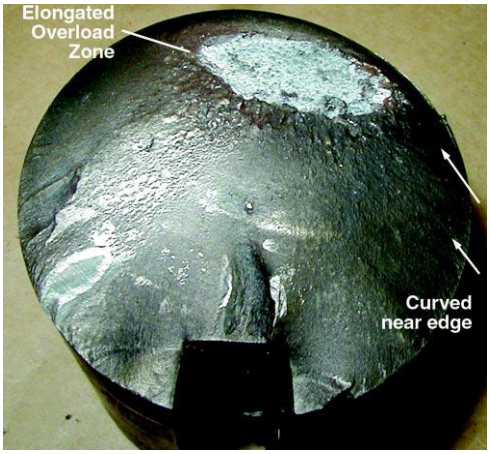

Figure 1.20: A cross-sectional view of classic fatigue failure (adapted from [54])

Figure 1.20 presents a cross-sectional view of a classic fatigue failure. It can be observed that the piece is arched with the smallest radius near the outer edge. This small radius confirms a high stress concentration that, when multiplied by the stress concentration caused the failure. The elongated shape of the overload zone indicates that some plane bending loads were present [54].

1.4 Surface treatments

As mentioned before, selecting an appropriate surface treatment can prevent or at least delay the surface degradation caused by wear, corrosion or fatigue [5]. A great variety of surface treatments have been developed over the years to improve wear, corrosion and fatigue resistance [59] and new surface treatment techniques are becoming available also [60]. Surface treatments can be divided in two major groups:

- heat treatments;
- surface coatings [61].

James and co-workers attempted to classify a very wide range of the processes by the method in which the surface layer was formed. The three basic divisions are material added to a surface (welding, thermal spraying and electro-deposition processes), chemical changed surface (thermochemical treatments) and the modification of the surface microstructure [62]. Bell has proposed an alternate classification of surface treatments, such as thermal treatments, thermo-chemical treatments, plating and coating and implantation. Plating and coating in Bell's classification correspond to those treatments involving addition of material to the surface, and thermal treatment and thermochemical treatment correspond to those treatments that change the surface microstructure and those treatments that change the surface chemistry, respectively [63].

Selecting an appropriate technology to produce a certain combination of surface characteristics is a very complex process. It involves systematic correlation of specifications with attainable surface properties. Usually, the selection process also includes economic and ecological evaluations [5].

1.4.1 Heat treatments

According to Eckstein, the term heat treatment is referred to as: "a collective term for a single process, or a combination of production processes, used to optimize or obtain specific processing characteristics or usability by changing materials properties". It is used for solid metallic materials and includes thermal, thermo-chemical or thermo-mechanical operations [64]." Heat treatments improve processing characteristic, such as machining or forming properties, or pieces properties, including hardness, toughness, strength, or wear, corrosion and fatigue resistance. Heat treatment processes can be divided in thermal processes, thermo-chemical processes and thermo-mechanical processes [5], Figure 1.21 [65].

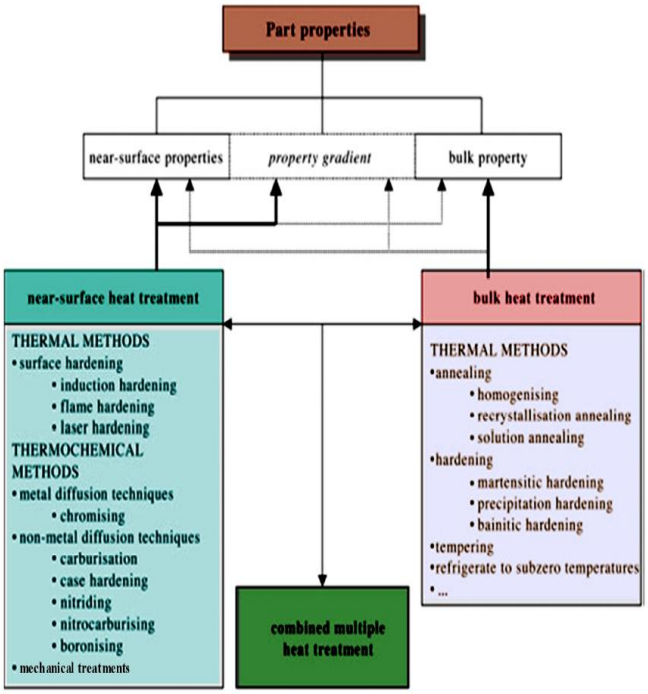

Figure 1.21: Schematic classification of heat-treatment techniques (adapted from [65])

1.4.2 Surface coatings

According to Rickerby and Matthews, the coating processes can conveniently be divided into four generic groups: gaseous state, solution state, molten/semi-molten state and solid-state processes, depending on the state of the depositing phase [66], Figure 1.22 [1].

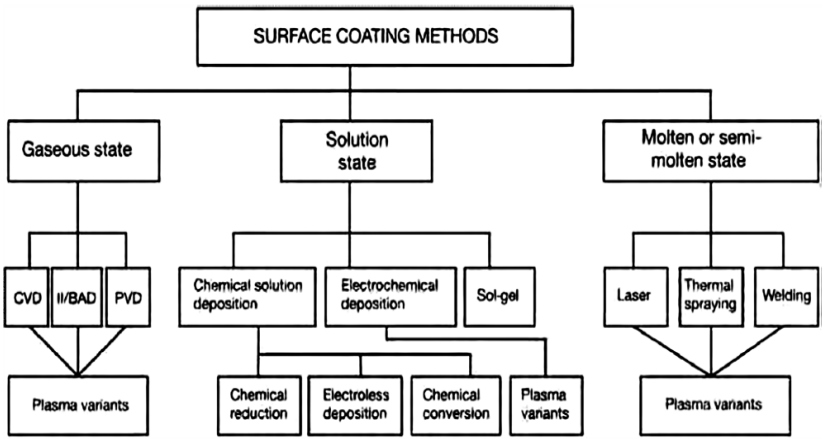

Figure 1.22: A general classification of coatings techniques (adapted from [1])

The coated surface must possess a suitable combination of properties, for example in terms of hardness, elasticity, shear strength, fracture toughness, thermal expansion and adhesion. From Figure 1.23, it can be observed four different zones, each with different properties which must be considered [67].

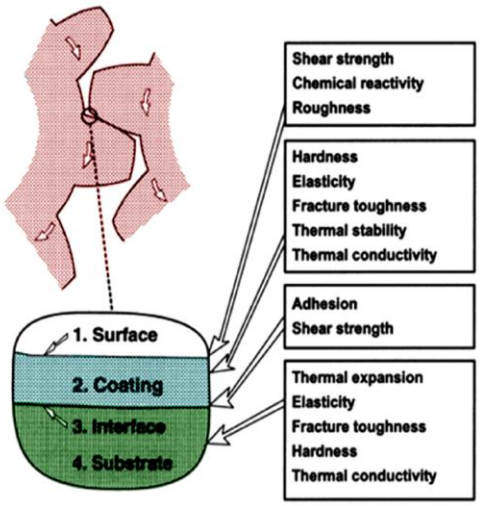

Figure 1.23: Important properties in different zones of the coated surface (adapted from [67])

A major problem of surface coatings is that many desired properties, such as good adhesion at the coating/substrate interface or high hardness and toughness of the coating cannot easily be obtained simultaneously. Increased hardness and strength is often concomitant with decreasing toughness and adherence. Therefore, the final coating design is always a compromise between different technical requirements on the coating properties and economical requirements of the coatings [1].

The factors that determine the coating material properties are the constitution of the material system and the fabrication parameters, such as the coating process and thickness, as shown in Figure 1.24 [68]. Both of these determine the microstructure of the coating, including its density, grain size, grain boundaries and grain orientation [1].

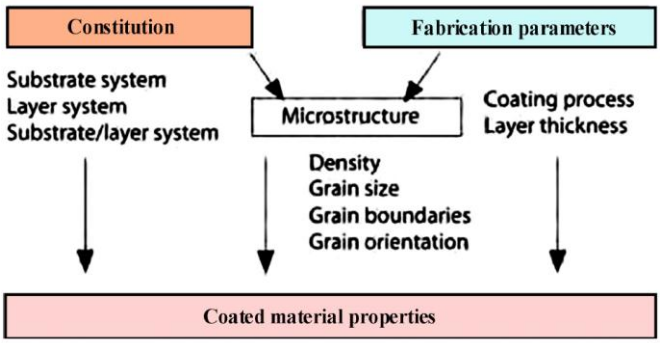

Figure 1.24: Factors that influence the properties of coated surfaces (adapted from [68])

According to Rickerby and Matthews, the whole coated surface system, with its properties and functional parameters can be considered as a compound system that needs to be optimized in order to gain maximum benefit [66].

1.4.3 Innovative surface treatments

The past 20 years have seen many advances in the field of Surface Engineering: optimisation of traditional processes (for example electroplating, weld surfacing, thermal spraying and thermochemical treatments), commercialisation of modern techniques (CVD, PVD, plasma thermo-chemical processes, plasma spraying and ion implantation), developments of innovative hybrid technologies (plasma immersion ion implantation and plasma source ion implantation) and deposition of new materials (diamond coatings) [1].

But, despite of these great achievements, many mechanical systems will operate under ever more severe conditions, such as intensive loads, high speeds and harsh environments, in order to achieve high productivity, high power efficiency and low energy consumption. Therefore, there are many situations where the combination of several properties, such as wear resistance, load bearing capacity and fatigue performance are absolutely necessary.

These new challenges can be successfully achieved through a new, innovative surface technology, Duplex surface engineering [69]. The term has been used for the first time in 1990, but the concept was introduced in 1979 by Brainard and Weeler. Duplex Surface Technology will be fully discussed in Chapter 2.

2. DUPLEX TREATMENTS: PRINCIPLES, CLASSIFICATION AND APPLICATIONS

2.1 Definition

Duplex Treatments, also known in literature as Duplex Surface Engineering or Duplex technology, as the name implies, involves the application of two surface treatments, in order to produce a surface layer with properties unobtainable through any individual surface technology [69-74]. Treatments combined in this way, sometimes called hybrid processes, have a high potential for the future treatment of metals. The principle of Duplex treatments is presented in Figure 2.1 [72].

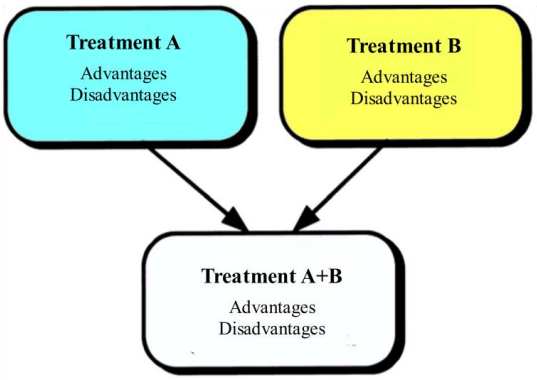

Figure 2.1: Principle of Duplex treatments (adapted from [72])

Two single treatments, with their advantages and disadvantages, are combined into one treatment, so that their advantages are added and their disadvantages are preferably annihilated [69-72]. Combined processes can be realized in different sequences, one after the other in two plants, Figure 2.2 a, one after the other in one plant, Figure 2.2 b or simultaneously, in one plant, Figure 2.2c.

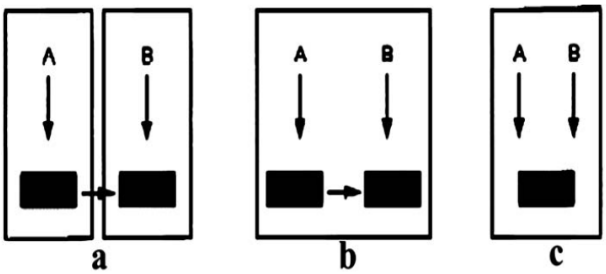

Figure 2.2: Sequence of combined processes (adapted from [72])

The treatments combined in one plant, either one after the other or simultaneously, avoid the transport of mechanical parts between plants and may improve quality by eliminating surface contaminations during transport [72].

A very important aspect is that Duplex treatments are not simply mixing two surface treatments which may individually produce desirable properties. A Duplex treated component is typical a multi-layer system and the resultant performance depends more on the combined effects from the two individual treatments, rather than the effect provided by individual ones. For instance, inappropriate combinations and/or incorrect control will lead to worse rather than improved combined effects [71]. Therefore, it is essential to identify correctly the metallurgical reactions, so that the effects resulting from the first treatment are not deteriorated by the second one [69].

2.2 Types of Duplex treatments

The number of possible combined processes is very large. An important task is the substantial choice of technical and economical promising combinations. According to Kessler and co-workers, Duplex treatments can be combined as presented in Table 2.1 [72].

Table 2.1: System of combined processes [72]

		Treatment B			
		B1	B2	……	Bn
Treatment A	A1	combined treatments A1 + B1	combined treatments A1 + B2	……	combined treatments A1 + Bn
	A2	combined treatments A2 + B1	combined treatments A2 + B2	…….	combined treatments A2 + Bn
	⋮	⋮	⋮	⋮	⋮
	An	combined treatments An + B1	combined treatments An + B2	……..	combined treatments An + Bn

They set up a matrix with single treatments, A in lines, B in columns. In the intersections of matrix lines and columns, different combined processes can be found. They have also divided the surface treatments into five groups: thermal, mechanical, thermo-chemical, ion implantation and coating processes.

This kind of matrix was set up for steels from the above mentioned five process groups. The matrix contains a large number of combined processes, Table 2.2. The foreseeable potential of the combined processes is added, which will have to be adapted for future developments. Besides the technical potentials, the costs of the combined processes have to be considered too. The benefit of this classification is its clear frame for a large number of combined processes. It allows a systematic choice of combined processes for practical applications and estimation of their potentials [72].

Table 2.2: System of combined processes for steels [72]

	Changing properties				
	Rearranging particles		Introduction particles		
Treatment B / **Treatment A**	Thermal heat treatments	Mechanical treatments	Termochemical treatments	Ion Implantation	Coating processes
Thermal heat treatments	-	+	+	-	+
Mechanical treatments	-	-	+	-	+
Termochemical treatments	++	+	++	+	+++
Ion Implantation	-	-	+	-	-
Coating processes	+++	+	++	+	+

*Note: +++ very high potential, ++ high potential, + potential existing, - to be analyzed

According to Bell, Duplex treatments can be divided into two general types: in the first type, two individual processes complement each other and the combined effects result from both processes (for example PVD treatment of nitrided steel). In the second type, one process supplements and reinforces the other, thus serving as pre or post-treatment. Therefore, the resultant properties are mainly related to one process, for example electron beam surface melting of a sprayed overlay. Some examples of Duplex Surface Engineering technologies are presented in Table 2.3 [69]

Table 2.3: Duplex treatments classification [69]

TYPE I Complementary technology	**TYPE II Supplementary technology**
Nitriding + PVD coating	Energy beam melting of overlay coatings
Energy beam processes + Plasma nitriding	Laser treatment + Nitriding
Diffusion treatment + PVD coating	Laser hardening + Nitriding
Carburizing + Nitriding	Sprayed MoS_2 on Ni coatings
Electroplated deposits + PVD coatings	SiC intermediate layer for DLC coatings

2.2.1 Thermochemical treatments followed by coating technologies

This type of Duplex technology consists in applying a thermochemical treatment prior to the coating deposition, in order to enhance the surface performance, usually by increasing the load support or load-bearing capacity of the coating [69-71]. The classification of this type of Duplex technology is presented in Table 2.4 [72].

Table 2.4: Duplex treatments types [72]

Treatment B / Treatment A	CVD	PVD	PACVD	Thermal spraying	Electrochem./ chemical deposition
Carburizing	++	-	-	-	-
Nitriding	+	+++	++	-	-
Boriding	-	-	-	-	-

*Note: +++ very high potential, ++ high potential, + potential existing, - to be analyzed

A prior diffusion treatment combined with a coating can provide a composite effect, which improves the tribological behavior of treated parts, as illustrated in Figure 2.3 [1].

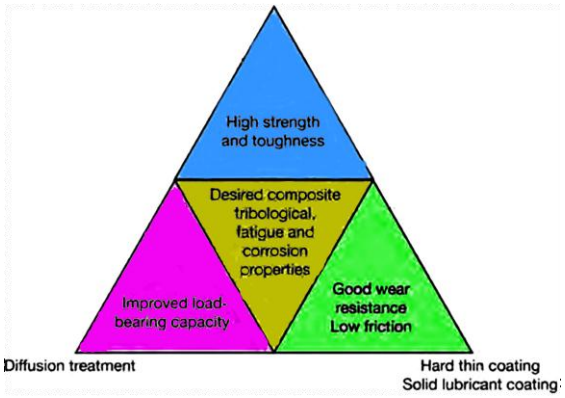

Figure 2.3: Benefits of Duplex treatments (adapted from [1])

PVD treatment of nitrided steel is the most widely researched and well documented [71-76]. Depending on the nitriding and coating process conditions, as well as the surface preparation prior to coating, a variety of combinations can be produced, including ceramic coating/dense compound layers, ceramic coating/diffusion layers and ceramic coating/decomposed compound layers (black layer) [71]. Parts treated this way exhibit low friction and wear (characteristic of ceramic coatings), and high load bearing capacity and fatigue strength (characteristics of the nitrided surface). In addition, improved coating-subsurface adhesion strength can be also achieved if these two processes are properly combined and carefully controlled [69].

Leyland and co-workers successfully combined plasma nitriding with ion-plated hard TiN. They have demonstrated, in scratch tests, that the load carrying capacity of a high-speed steel is improved with more than 25% by applying a plasma-nitriding treatment prior to TiN coating, as shown in Figure 2.4 [77].

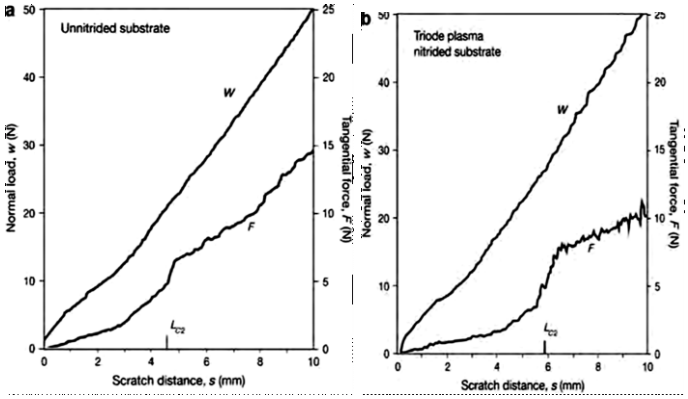

Figure 2.4: Load carrying capacity: a – untreated; b – Duplex treated [77]

Experimental work has also demonstrated that the combined plasma nitriding and PVD TiN coating treatment can significantly improve the corrosion resistance of mechanical parts. As can be seen in Figure 2.5, the corrosion current density of Duplex treated En40B steel is several orders of magnitude lower, compared to plasma nitrided or TiN coated. The dense, compound layer formed during plasma nitriding plays an important role in the corrosion resistance of parts treated this way [78].

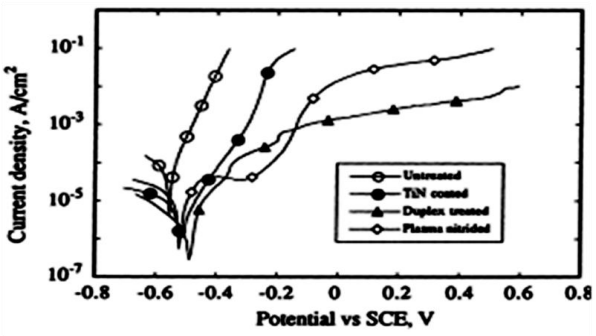

Figure 2.5: Polarization curves [78]

A wider range of materials, including low alloyed and austenitic steel, Ti alloys and Co-based alloys, were investigated by Rie and co-workers in a study that presents the benefit of Duplex treatments. They used plasma nitriding or nitrocarburizing as a precursor to subsequent coating by PVD/PACVD techniques [79-81]. Those Duplex treatments are now finding successful application on press tools [82]. There was practical success for plasma nitrided steel followed by PACVD (Ti(BN), TiB_2) coatings on die casting and forging tools [82, 83]. Pfohl and Rie demonstrated friction and wear improvements for TiBN and TiB_2 coatings on plasma nitrided steels in dry sliding wear tests [84].

Batista and co-workers examined the impact resistance of Duplex and non-Duplex treated hardened AISI HI3 steel coated with (Ti,Al)N and CrN. The Duplex samples exhibited at least a doubling in the scratch test upper critical load, and the number of impacts before adhesive failure occurred was increased about 50 times for the (Ti,Al)N coatings and around 5 for the CrN coatings [85].

Duplex treatment consisting in plasma nitriding followed by PVD deposition of TiN, TiAlN, DLC and CrN enhances the surface properties, including the tribological properties (wear, friction) and fatigue strenght of the treated parts. Figure 2.6 shows both the hardness profile for Duplex treatment, plasma nitriding and PVD coating [86].

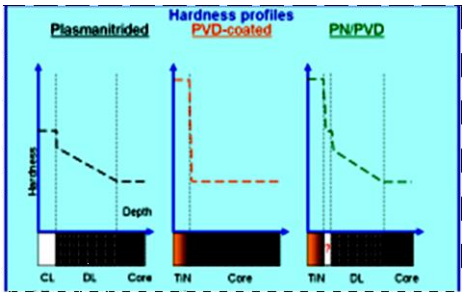

Figure 2.6: Hardness profiles [86]

Another important aspect is the fact that nitriding and PVD treatments can be realized in the same plant, because the treatment parameters (temperature, atmosphere, pressure) are similar. The possibility to realize nitriding and coating in one process was demonstrated by Michler, who deposited CHSi on work tool steel, which was plasma nitrided in the same chamber, under similar conditions. This provided enhanced film adhesion and high wear resistance [87].

Another example that shows the benefits of Duplex treatments is the combination of nitrocarburizing and thermo-reactive deposition of chrome at a low temperature, realized by Alsaran and co-workers. The purpose of this Duplex treatment is to form a hard chromium carbonitride surface layer for applications which need high wear resistance. Nitrocarburizing ensures a solid bond between the layer and the sublayer and creates transition properties in the separation zone. The low temperature of the process keeps the basic material properties. The efficiency of this combination has been demonstrated by comparing the wear resistance of untreated, nitro-carburized and Duplex treated pieces. The results are presented in Table 2.5. It can be noticed the fact that the wear rate obtained for Duplex treated state is decreased 4 - 5 times compared with tempering and hardening state [88].

Table 2.5: Wear rate [88]

Structural state	Wear rate [mm^3/m]
hardened + tempered	0.000715
nitro-carburized	0.000250
Duplex treated	0.000146

Another combined process with a high potential is represented by the combination between carburizing and chemical vapour deposition (CVD). Kessler and co-workers deposited TiN onto a carburized constructional steel AISI 4140 [72].

2.2.2 Coatings followed by thermal treatments

Coatings and thermal treatments of steels allow several different combined processes. The classification of these types of Duplex treatments is presented in Table 2.6 [72].

Table 2.6: Coatings and thermal treatments of steels [72]

Treatment A \ Treatment B	Full hardening	Surface hardening	Annealing
CVD	+++	++	-
PVD	+	+	-
PACVD	+	+	-
Thermal spraying	-	-	+
Electrochemical/ chemical deposition	-	-	+

*Note: +++ very high potential, ++ high potential, + potential existing, - to be analyzed

The combination of CVD and quench hardening of steels is of particular importance, because the high coating temperature and the slow cooling often result in soft steel substrates. Once again, the advantage of combined processes is illustrated by the addition of the high hardness of the thin CVD-coatings. A possible disadvantage of this is represented by the deformation compared to the coating thickness [72]. Deformation can be reduced by gas quenching instead of oil quenching, according to Keßler [89].

A good example of this combination is represented by the Duplex treatment consisting in HT- CVD TiN-coating and vacuum hardening. After CVD-coating, the substrate has pearlitic structure and hardness of 350 HV1. Figure 2.7 shows the surface microstructure obtained after the Duplex treatment. It can be observed that the TiN layer has 6 mm thickness and is homogeneous without microscopic defects. The structure near the interface consists of fine martensite, retained austenite and carbides [72].

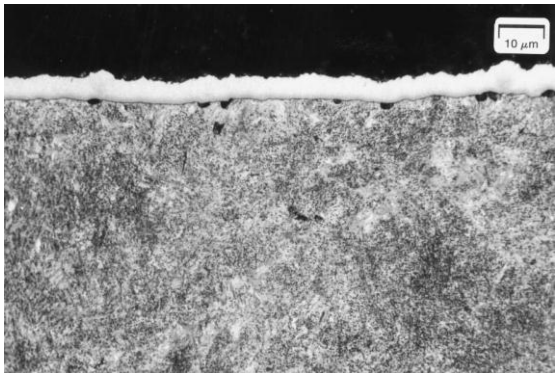

Figure 2.7: Microstructure of Duplex treated AISI 52100 [72]

2.2.3 Thermo-chemical treatments followed by thermal treatments

Another example of Duplex Surface Technology is given by the combination of thermo-chemical and thermal treatments [72]. Qiang and co-workers showed that the combination of nitrocarburizing and quenching is very effective to improve the sliding wear behavior of AISI 1045 steel. The experimental results for lubricated and unlubricated wear tests are presented in Figures 2.8 a, 2.8 b respectively.

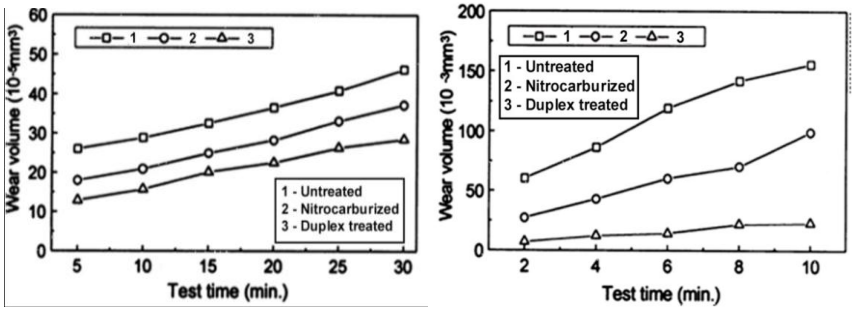

Figure 2.8: Wear volumes under lubricated a) and b) unlubricated conditions [90]

As it can be observed from Figure 2.8 this type of Duplex treatment improves the wear-resistance significantly under lubricated and unlubricated conditions due to the intermetallic structure, higher hardness and the lower friction coefficient of the compound layer [90]. Other examples of these types of Duplex treatments are presented in [91, 92].

2.2.4 Thermo-chemical treatments followed by mechanical treatments

The fatigue resistance of mechanical parts can be improved by means of Duplex treatments consisting in thermochemical treatments followed by mechanical treatments. Of this type, carburizing followed by shot peening was widely studied [93-95]. This type of Duplex surface engineering has found its application in automotive industry, especially for gears. Oshawa and co-workers have proven that the fatigue strength of Duplex treated gears is higher than the resistance of carburized gears, as presented in Figure 2.9 [96].

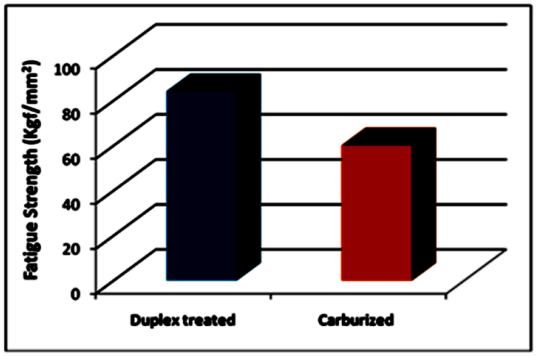

Figure 2.9: Fatigue strength of Duplex treated gears [adapted from 96]

Even if many reports indicate that Duplex treatments consisting in carburizing followed by shot peening are a valid method to improve the fatigue strength of gear teeth, there are only a limited number of papers that presents the effect on pitting fatigue strength. Kobayashi and co-workers investigated the effects of shot peening on the pitting fatigue strength of carburized gears. The results of roller pitting fatigue tests showed that the Duplex treated pieces have about 1.15 times higher

fatigue limit at 2 x 10^7 cycles and about 10 times longer life under 3200 MPa Hertz's contact pressure, compared to carburized ones [97].

However, carburizing requires high process temperature and induces geometrical distortion, and requires further working processes. Therefore, gear manufacturers are considering nitriding as a possible substitute of carburizing. In fact, nitriding requires lower temperature (~530°C) and does not deform the gear teeth [98].

Guanhua and co-workres have studied the effect on fatigue resistance of nitriding and shot peening. They have also analyzed the effect of residual stress induced by shot peening [99]. Jingpu has studied the effect of shot peening of contact fatigue behavior of 40Cr steel after nitriding. He has also analyzed different failure modes under different pressure values. From ths S-N curves included in that paper it is evident that shot peening has a positive effect on the fatigue behavior of nitrided pieces [98].

Oshawa et al. [96] studied the improvement of shot peening on gas-nitrided elements. They were able to prove that shot peening increases the rotating bending fatigue limit with more than 20%. Also the influence of the peening media and parameters on surface roughness was investigated.

Pariente and Guagliano investigated the effect of shot-peening on the rotational bending fatigue of gas nitrided 42CrMo4 grade steel. They achieved, after 3 million cycles, a fatigue limit of 850 MPa [101]. In the work of Guagliano and Vergani, notched specimens made from 39NiCrMo3 grade steel were subjected to gas nitriding and subsequently to shot-peening. The nitrided specimens exhibited a bending fatigue strength level of 379 MPa. After shot-peening, a significant rise in bending fatigue strength was noted (674-724 MPa), depending on the intensity of the shot-peening and depth of the notch [98].

Nakonieczny et al. have studied the effect of Duplex treatment consisting in nitriding and shot-peening on the mechanical properties of 40HM (AISI4140) grade steel. The results are presented in Table 2.7 [102].

Table 2.7: Mechanical properties [102]

State	HV 0.5	HV1	HV5	Residual stresses [MPa]	Bending fatigue strength [MPa]	Contact fatigue strength [MPa]
Nitrided	761	780	748	-641± 45	872±12.6	3937
Duplex treated	841	840	846	-1556±48	889±15.6	4130

2.2.5 Coatings followed by thermo-chemical treatments

This kind of Duplex surface technology has a high industrial impact associated with increased chemical and mechanical properties of treated parts. The most studied combination is represented by electrolytic hard chromium coatings and thermochemical treatments consisting in nitriding, nitro-carburizing and carburizing [103, 104].

Such Duplex treatments start with the deposition of an electrolytic hard chrome coating on the metal substrate. The characteristics of the coating are selected according to hardness, wear resistance and the piece's required thickness, shape and size, substrate and dimensional specifications. The selected

thermochemical treatments are carried out in a gaseous phase or by interaction with plasma [105].

The combination of electrolytic hard chromium coatings and plasma/gas nitriding has been studied by many researchers [106-109]. They have studied the microstructure of the obtained layers, the effect of production parameters (time and temperature) on corrosion and wear resistance, and their potential application, for example to fuel cells. Usually, by applying this type of Duplex treatment is obtained a multi-layer structure, Figure 2.10 [105].

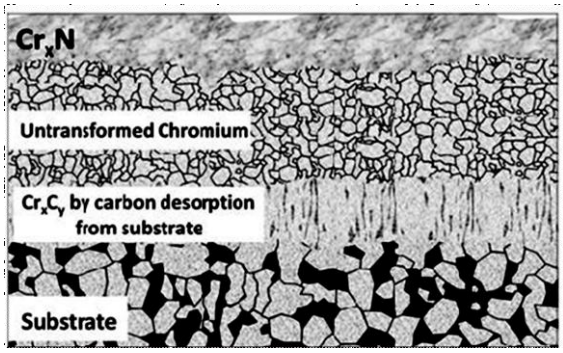

Figure 2.10: Microstructure of pieces Duplex treated by chromium deposition and nitriding [105]

Another possible combination is represented by electrolytic hard chromium deposition followed by nitro-carburizing. By applying this type of combined process, it can be obtained high hardness values, such as 1450 HV [109] and 2200 HK [106], higher than those obtained with nitriding. Regarding the combination between chromium deposition and carburizing, there has only been one report since now, which can be found in [110].

2.2.6 Thermo-chemical treatments followed by post-oxidation

Automotive and hydraulic parts often require a combination of good corrosion resistance, low friction properties and high wear resistance in addition to high hardness. To achieve these requirements, several Duplex treatments consisting in salt bath nitriding and post oxidation, gas nitrocarburising and post oxidation, plasma nitriding and post oxidation have been developed [111].

Mahboubi realized a Duplex treatment consisting in plasma nitriding followed by post oxidation on AISI 1045 steel. Nitriding was realized at 550 °C for 5 h and post oxidation treatment was performed at 500 °C, for 1 h, using different oxidizing gas mixtures of O_2/H_2, under 4 mbar pressures. Duplex and non-Duplex samples were subjected to corrosion tests. The results are presented in Figure 2.11. As it can be observed, corrosion density of Duplex treated samples decreases, compared with untreated and plasma nitrided samples, which indicates improved corrosion behavior [112].

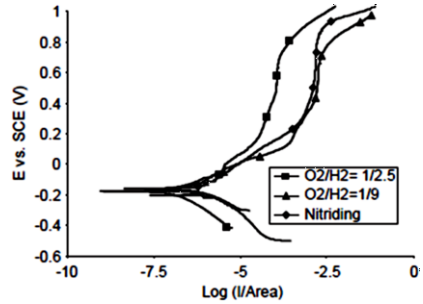

Figure 2.11: Polarization curves [112]

Marušić and co-workers studied the effect of Duplex treatment consisting in post-oxidation and nitrocarburizing on corrosion resistance of AISI 1045. Corrosion resistance of treated and untreated samples was studied in 5% sodium chloride solution, at 25 °C. The results of the polarization measurements are presented in Figure 2.12 [113].

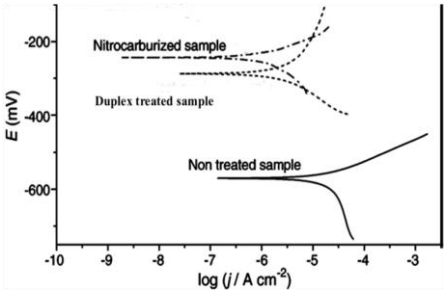

Figure 2.12: Polarization curves [113]

It can be seen that the corrosion potential of nitrocarburized and Duplex treated samples are shifted towards more positive values, compared to untreated ones.

Zhang et al. have investigated the effect of nitrocarburizing and post-oxidation on fatigue behavior of 34CrMo4 alloy steel. Fatigue tests of treated and untreated specimens were performed in an open environment, at room temperature, by four-axle cantilever-type rotary bending fatigue machine. The S–N curves obtained are shown in Figure 2.13 [114].

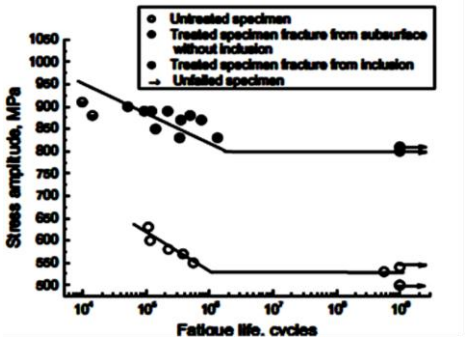

Figure 2.13: S-N curves of treated and untreated samples [114]

The fatigue limit of untreated specimen is 530 MPa and of the Duplex treated specimen increases to 800 MPa, which means an increase of about 51%.

The examples presented confirm the fact that this type of Duplex treatment improves the corrosion, wear and fatigue resistance of mechanical pieces.

2.2.7 Other types

Besides the examples presented above, there are other types of Duplex treatments that are in research stages. A good example is represented by the combination of two thermo-chemical treatments.

For instance, Krumes and co-workers have studied the possible combination of boronizing and nitriding of construction steels, such as: low-carbon type (C15E and C45E) and low alloying ones (20MnCr5 and 42CrMo4). The boronizing process was carried out in conventional furnace at a temperature of 900 °C for 4 h, cooled slowly to room temperature. In the second step, carried out subsequently after boronizing, the same specimens were plasma nitrided at 520 °C, for 40 minutes. The treated samples were investigated by means of optical microscopy and micro-hardness tests [115].

Another possible combination is represented by carburizing followed by amorphous carbon deposition. The samples treated this way were subjected to pitting tests. Investigations have shown that pitting resistance is doubled and friction has been reduced by almost 5 times [116].

2.3 Applications of Duplex treatments

Duplex surface engineering highly improves properties such as bending fatigue, thermal fatigue, friction, wear and corrosion, etc. Examples of successful industrial applications of this new technology can be found in engineering components, tools for cutting and forming, electronic equipments.

In engineering components, such as sliding bearings, rolling bearings, gears, pistons, cylinders, valves, injectors, plungers, rotors, pumps and transmissions, these treatments are used to reduce wear, increase component lifetimes and reduce friction. Industrial sectors in which such improvements are utilized include the automotive, aircraft and other transportation industries, metals manufacturing industries, etc.

In very severe surface conditions prevailing at the surface of metal cutting and forming tools, Duplex treatments are successfully used to protect the substrate from wear and to increase the tool lifetime by several orders of magnitude [1]. Some applications of Duplex treatments will be reviewed bellow.

2.3.1 Rolling Contact Bearings

Rolling bearings are one of the most commonly-encountered machine components [1], Figure 2.14. In general, a rolling bearing is a bearing which carries a load by placing round elements between two surfaces. Rolling contact bearings are designed to carry pure radial loads, pure axial loads or a combination of the two [117]. Materials commonly used for rolling contact bearings are carburized or case-hardened steels, high-carbon chromium steel (SAE52100), high-speed steels for use at temperatures up to 430°C and stainless steel for corrosive environments [1].

Figure 2.14: Rolling contact bearings [117]

Considerable improvements in lifetime of rolling contact bearings have been achieved by the use of Duplex hard TiC/CrC or soft MoS2/TiN and MoS2/Cr2O3 surface coatings on treated steel substrates [1].

2.3.2 Gears

Gears are the most commonly used elements for torque transmission due to their accurate transmission rate, high torque and high-speed capability [1], Figure 2.15 [118]. One limitation in their use may be noise. The lifetime of a gear transmission is generally limited by tooth fracture, rolling contact fatigue failure and also scuffing or scoring failure, especially at low speeds. In modern machines, high performance gears are required to operate at ever-increasing torque and speed for power transmission. This high performance can be obtained through Duplex surface engineering [1].

Figure 2.15: Gears [118]

The potential advantages of using Duplex surface engineering on gears are:

- prevention of scuffing or scoring with wear-resistant low-friction coatings;
- increasing rolling contact fatigue life by surface stress level reduction;
- decreasing the noise level using a soft coating;
- strengthening [1];

Mao et al. demonstrated in dry running gear test, that duplex treated gears (PVD deposition of TiN followed by plasma-nitriding) reduced the weight loss 50 times, while TiN coated gears reduced it to less than half, compared with uncoated gears. For nitrided gears, the weight loss was reduced 10 times [120]. The Duplex treatment of gears is expensive, but can considerably improve the wear performance in dry running conditions [1]. Bell and co-workers proved that Duplex treated En40B gears not only show significantly improved wear resistance, but also exhibit enhanced load bearing capacity, Table 2.8 [69].

Table 2.8: Gear test results [69]

Structural state	Weight loss (mg)	Load carrying capacity (Nm)
Non-treated	550	12.5
Coated with TiN	250	38
Plasma nitrided	50	72
Duplex treated	10	86

2.3.3 Wood cutting tools

The cutting conditions in wood and pulp are abrasive due to hard debris in the work material. In wood machining, even if the application of coatings as wear or corrosion protection of cutting knives is not common, some previous works showed their efficiency in peeling and routing [1].

Figure 2.16: Wood cutting tool [120]

Even if the coatings increased the service life of the cutting tools, their adhesion is not sufficient. This could be a limit to their employment and marketing. Nevertheless, the solution to increase the adhesion of the coatings on steel tools was to realise a previous nitriding before the coating (Duplex treatment). Previous works showed the efficiency of Duplex treatments consisting in nitriding followed by PVD deposition of TiN, Cr_2N and TiN/TiAlN. Other experiments showed that chromium nitride (Cr_xN) coating on nitrided low alloy steel knife surfaces increased the lifetime more than 2.5 times in accelerated wear tests [1].

2.3.4 Forging dies

The wear encountered by forging dies not only reduces the tools lifetime, it can also result in intolerable surface conditions of the product. In recent years, increasing demands for lower costs, increased productivity and better product quality are the main driving forces in the development of hard coatings for cutting and forming applications. However, the advantages of hard coatings are not fully explored for forging dies.

During the forging process, dies are heavily loaded and exposed to complex loading conditions. The coating without proper substrate support is not capable of sustaining the loading conditions that takes place during the hot forging. One of the possible ways to achieve this is by combining thermochemical treatments with hard coating depositions by PVD, CVD, or PACVD [120, 122].

Leskovsek and co-workers investigated the possible improvements of hot forging of automotive parts by applying a Duplex treatment consisting in nitriding followed by PACVD TiCN and TiN-TiB_2 deposition. Due to the high mechanical and thermal loading, the TiCN coated and plasma-nitrided forging-die inserts made were used for an industrial test. After the industrial test, the TiCN duplex coated was examined and compared with a standard forging-die insert, which was only nitrided. As shown in Figure 2.17, the height of the duplex treated insert after 13.500 forged pieces did not change, while the height of the nitrided forging-die insert was reduced by 1/5 of the initial height [123].

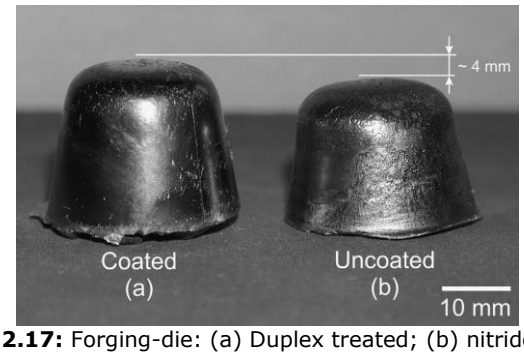

Figure 2.17: Forging-die: (a) Duplex treated; (b) nitrided [123]

2.4 Economical impact of Duplex Treatments

The last years have seen the evolution of many new surface engineering technologies and many improvements in traditional techniques for surface treatment [1]. This evolution has stimulated the growth of new multi disciplinary subject of Surface Engineering. The integration of the concepts of materials engineering, contact mechanics and tribology, with the basic sciences of chemistry and physics, has demonstrated significant potential for the enhanced performance of engineering components for use in all sectors. Therefore, designers are now more than before in a position to change the properties of surfaces and to produce the desired friction, wear and corrosion properties precisely where they are needed [69].

These changes can be realized by exploring the potential of Duplex surface engineering. The use of this new technology to control tribology and corrosion in a variety of applications is of special interest because of the huge effects of friction, wear and corrosion in relation to energy use, environment and economy. The lubricants were the first significant solution for friction and wear control, but there is a trend to limit their use due to both pollution and cost.

Today, Duplex surface engineering offers a major solution for friction, wear and corrosion control in our society [1].

II. EXPERIMENTAL PROCEDURE
3. OBJECTIVES, MATERIALS AND CHARACTERIZATION TECHNIQUES

3.1 Thesis objectives

As discussed before, the main cause of mechanical parts failure is represented by the surface degradation through wear, corrosion and fatigue. At present, there are many opportunities to improve the surface properties of mechanical parts. One of modern technology used to combat the surface degradation is represented by Duplex treatments. The properties obtained from implementing this new technology have proved to be superior compared to those obtained from any conventional surface technology [69].

Given these considerations, the main purpose of this research is represented by the generation of Duplex surface layers, with high wear, corrosion and fatigue resistance.

The present research was focused on the following main objectives:

- The selection of Duplex surface treatments by analyzing the advantages and disadvantages of possible combinations. As a result, the Duplex treatments selected for this research consisted in the combination of thermochemical treatments (carburizing, nitriding respectively) followed by thermal (surface induction quenching) and mechanical treatments (work hardening through shot peening), respectively.
- The materials selection, considering their application and cost;
- The optimization of the treatments parameters, so that the properties obtained from the first treatment are not damaged by the application of the second one;
- Structural characterization of Duplex treated materials (optical microscopy, scanning electronic microscopy, glancing incidence, internal stresses);
- Mechanical characterization by means of microhardness and microindentation tests;
- Electrochemical corrosion behaviour of Duplex treated materials in different environments;
- Friction and wear behaviour (sliding dry and abrasive) of treated materials by means of Duplex surface technology;
- Rotating bending fatigue behaviour and finite element simulation of Duplex treated materials;

3.2 Materials

Steels are the most used engineering materials because of their high mechanical properties, machining, forging capability and lower cost, compared with other materials. They are widely used in automotive industry, construction industry

and other engineering areas. Also, given the fact that the treatments selected for this research are carburizing and nitriding, the materials selected for these experiments were EN 16MnCr5 and EN 34CrNiMo6.

EN 16MnCr5 (EN 10084-1998; EMC5; AISI 5115/5117; EC80) steels have high mechanical and hardenability properties and lower cost compared to other carburizing steels. These types of steels are widely used for antifriction bearings and gears, shafts, axles, cam, etc [124]. The effective chemical composition along with the prescribed one is presented in Table 3.1. The effective chemical composition was determined by means of Innov- XRD Analyzer from the endowment of National R&D Institute for Welding and Mechanical Testing from Timisoara.

Table 3.1: Chemical composition of EN16MnCr5

Component	C	Cr	Mo	Si	Mn	P	S	Cu	Fe
Prescribed values [wt.%]	0,16	0.21	0.02	0,25	1.15	0	0.28	0.21	95,399
Effective values [wt.%]	0,162	0.22	0,015	0,139	0,63	0,01	0,004	1,48	96,14

These types of steels have the following characteristics:

- Increased uniformity of grain size in improved condition;
- Optimum hardness in both primary treatment and final treatment stage;
- enhanced structural and dimensional stability when appropriate quenching media is used;
- increased hardening [124];

The time-temperature-time (TTT) diagram of EN16MnCr5 is presented in Figure 3.1 [125]

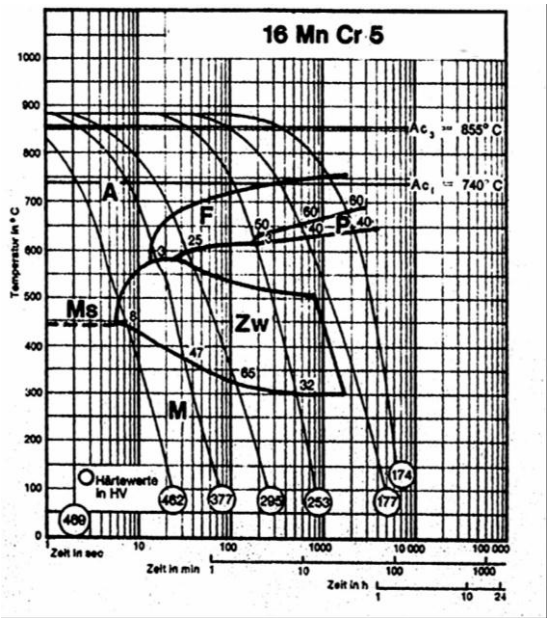

Figure 3.1: TTT diagram of 16MnCr5 [125]

According to the diagram, the thermal parameters of EN 16MnC5 are:

- quenching temperature of 860 - 900°C in oil or water;
- annealing temperature of 650 - 700°C;
- normalizing temperature of 860 - 900°C [125]

EN 34CrNiMo6 (DIN 34CrNiMo6, AISI 4337/4340) is a heat treatable, low alloy steel containing nickel, chromium and molybdenum. It is known for its toughness and capability of developing high strength in the heat treated condition while retaining good fatigue strength. It can be heat-treated to produce a wide range of tensile strength in moderate sections [126]. The effective chemical composition along with and the prescribed one is presented in Table 3.2.

Table 3.2: Chemical composition of EN 34CrNiMo6

Component	C	Cr	Mo	Si	Mn	P	S	Ni	Fe
Prescribed values [wt.%]	0,367	1,582	0,204	0,148	0,678	0,012	0,009	1,601	95,399
Real values [wt.%]	0,34	1,51	0,21	0,139	0,63	0,01	0,004	1,48	96,14

Typical applications of this type of steels are for structural use, such as aircraft landing gear, power transmission gears and shafts and other structural parts, general engineering parts, gears, connecting rods and bolts, etc. The time-temperature-time (TTT) diagram of EN 34 CrNiMo6 is presented in Figure 3.2 [126]

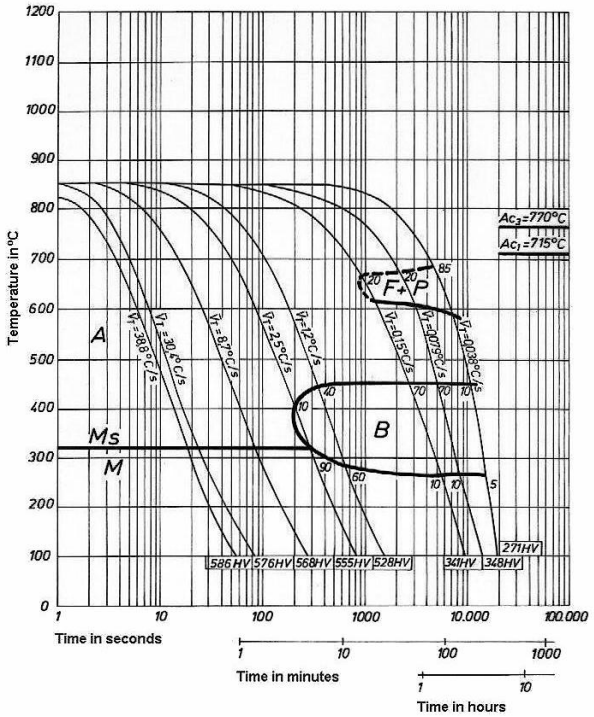

Figure 3.2: TTT diagram of EN 34CrNiMo6 [126]

According to the diagram, the thermal parameters of En 34CrNiMo6 are:

- Normalizing temperature of 850-880 °C;
- Hardening at a temperature of 830-860°C followed by oil quenching;
- Tempering temperature of 540-660°C [126].

3.3 Characterization techniques

In order to characterize the Duplex treatments selected for this study, several techniques were used. The basic mechanisms and equipment of each technique are briefly presented in the following.

3.3.1 Optical microscopy

The optical microscope, often referred to as the "light microscope", is a type of microscope which uses visible light and a system of lenses to magnify images of small samples [127].

In this work an Olympus PMG3 optical microscope (Figure 3.3) from endowment of Superior Technical Institute of Lisbon, is used to examine and acquire images of the micro-structural and morphological characteristics of metallographically prepared sections of Duplex treated samples.

Figure 3.3: Olympus PMG 3 optical microscope

The main characteristics of this type of microscope are:

- Adjustable Binocular Head;
- Pair of 10xM Eyepieces;
- Main Microscope Body with 1-2x Zoom System;
- 5x, 10x, 20x, 50x and 100x Neo S Plan B/D/DIC Objective Lenses;
- Rotating Polarizer & Analyzer;
- Mechanical X-Y Stage with Insert;

3.3.2 Scanning electron microscopy (SEM)

In scanning electron microscopy (SEM) the image of the sample surface is created by scanning it with a high-energy beam of electrons in a raster scan pattern. The electrons interact with the sample electrons, producing various signals that can be detected and that contain information about the sample's surface topography and composition. SEM can achieve resolution better than 1 nanometer. The specimens can be observed in high vacuum, low vacuum and wet condition [128].

In this work, Hitachi S-2400 (Figure 3.4) and JSM-7001F (Figure 3.5) scanning electron microscopes, from endowment of Superior Technical Institute of Lisbon, were used.

Figure 3.4: Hitachi S-2400 SEM

The equipment specifications are:

- Resolution: 4.0 nm.
- Magnification: 20x (WD = 35 mm) - 300,000x
- Accelerating voltage: 0.3-3 (0.1 kV steps), 4-8 (1 kV steps), 10, 12, 15, 18, 20, 22, 25 kV.
- Electronic FOV movement: ±20 microns (WD = 30 mm).
- Specimen Stage Specifications:
- Range of Movement X: 0 - 80mm
- Range of Movement Y: 0 - 40mm
- Range of Movement T: -20 - 90 degrees
- Range of Movement R: 360 degrees continuous
- Range of Movement Z: 5 - 35mm
- Maximum specimen size: 150mm

Figure 3.5: JSM-7001F SEM

The equipment specifications are:

- Magnification: 10x – 3.000.000x
- Accelerating voltage: 0.5-30 kV.
- Maximum probe current 200 nA:
- Range of Movement X: 0- 50 mm
- Range of Movement Y: 0 – 70 mm
- Range of Movement T: -5 - 70 degrees
- Range of Movement R: 360°
- Range of Movement Z: 0 – 38 mm
- Multi live image display up to 4 images in simultaneous display
- high speed cascade evacuation

3.3.3 X-Ray diffractions

The constituent phases of Duplex and non - Duplex samples were determined by means of X-ray diffraction, using a PW 3020 Diffractometer equipped with a PW 1835 Goniometer (Figure 3.6) from endowment of Superior Technical Institute of Lisbon. The technique is based on the diffraction of X-rays by crystals where the inter-planar distances are of the same order of magnitude of the wavelength of X-ray radiation [129].

Figure 3.6: PW 3020 Diffractometer

Equipment specifications:

- Accelerating voltage: 0.5-30 kV.
- Maximum probe current 200 nA:
- Range of Movement X: 0- 50 mm

3.3.4 Glancing incidence

In glancing incidence, the X-rays pass through a suitable slit system and are fall on the sample at a glancing angle α, while the detector on the 2θ axis scans the XRD pattern. This method has been found to be an effective and valuable technique in characterizing a variety of multicomponent and multiphase materials in thin film form [130]. Duplex and non- Duplex samples were analyzed using a Siemens D5000 diffractometer (Figure 3.7) from endowment of Faculty of Science, University of Lisbon.

Figure 3.7: Glancing incidence equipment

Equipment specifications:

- Accelerating voltage: 0.5-30 kV.
- Maximum probe current 200 nA:
- Range of Movement X: 0- 50 mm

3.3.5 Micro-indentation

Depth sensing indentation equipment allows the determination of two of the most commonly measured mechanical properties of materials, namely the hardness and the Young's modulus and also internal stresses [1].

The Duplex treated specimens were examined using a Dynamic Ultra Micro Hardness (DUH) equipped with a Vickers square base pyramidal indenter (Figure 3.8) from endowment of Superior Technical Institute of Lisbon.

Figure 3.8: Dynamic Ultra Micro Hardness equipment

- Evaluation of hardness and material parameters in accordance with standards (ISO 14577-1 Annex A)
- Highly precise evaluation of elastic modulus
- Low test force with measurement resolution of 0.196 μN
- Ultra wide test force range of 0.1 to 1,961 mN
- High precision measurement of indentation depth

3.3.6 Electrochemical corrosion

The corrosion behavior of Duplex treated materials was investigated in different environments by means of liniar polarization, using a electrolytic cell and a potentiostat (Figure 3.9) from endowment of National Laboratory of Energy and Geology of Lisbon.

Figure 3.9: Corrosion testing equipment

- Power requirements (Hz): 47.5 – 63
- Measure potential ranges: ±8 V
- Measure current range: 1μA- 1A
- Scanning speed: 10mV/s

3.3.7 Ball cratering method

The wear behavior of Duplex and non - Duplex samples was determined by ball cratering micro scale wear test. The samples were tested using the equipment developed by Vilar et al. (Figure 3.10).

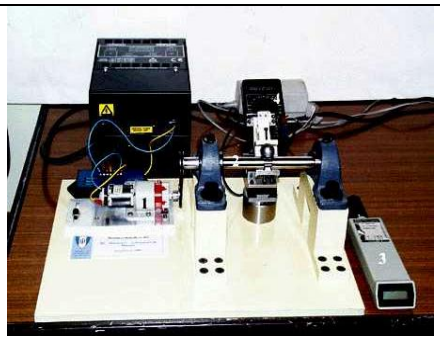

Figure 3.10: Ball cratering wear equipment

- Ball: steel balls, WC-Co balls 15 mm and 25 mm diameter.
- Abrasive Agent: SiC

3.3.8 Pin-on-disk

The sliding wear rate and coefficient of friction of the investigated samples were determined using a CSM pin-on-disc tribometer (Figure 3.11) from endowment of Fachhochschule Gelsenkirchen, University of Applied Sciences, Germany.

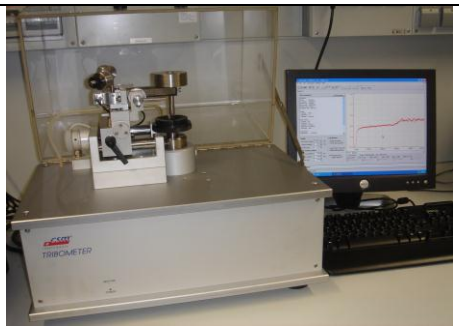

Figure 3.11: CSM Tribometer

- Loads up to 10 N;
- Adjustable radius (up to 30 mm);
- Radial speeds between 0.3-500 rpm

3.3.9 Rotating bending fatigue

The fatigue limit was determined by means of rotating bending fatigue, using the equipment from endowment of Department Strength of Materials, Mechanical Faculty of "Politehnica" University of Timisoara (Figure 3.12).

Figure 3.12: Rotating bending fatigue equipment

- Torque: 270 Nm
- Frequency: 100–200 Hz

4. INVESTIGATIONS OF DUPLEX TREATMENT BASED ON GAS CARBURIZING FOLLOWED BY SURFACE INDUCTION QUENCHING

4.1 Introduction

One of the Duplex treatments selected for this study is represented by the combination of gas carburizing and surface induction quenching.

Carburizing is an important thermochemical treatment used for automotive and aerospace components. The carburizing process involves the production of a relatively high level of carbon in the surface layer of mechanical parts composed of low carbon steel. The carburizing performance depends on the effective control of three principal parameters: temperature, time and carburizing atmosphere [131]. Tempered martensite is the dominant microstructure constituent of properly carburized steel. However, the martensite changes in morphology, amount, and properties as a function of distance from the surface. Other microstructural constituents, such as retained austenite, grain boundaries carbides, and surface oxides may also be present and significantly affect the performance of carburized parts. The carburizing treatment does not ensure a radical change of the treated layer properties. Therefore, it is necessary to realize a hardening and tempering treatment in order to obtain the desired properties of both the core and the surface layer [131-133].

Surface induction hardening, compared to other conventional hardening treatments, allows the selective hardening of a part, in order to achieve desired hardness over a specific area and depth. Because the part is selectively heated, the heat-affected zone can be adjusted to minimize distortion and other problems. Surface hardening with induction creates parts that have excellent resistance to fatigue. A hard outer case is created over a ductile core, with high compressive stresses at the surface. These compressive stresses at the surface improve fatigue properties by delaying crack initiation and propagation during service [132].

4.2 Duplex treatment technology

The material used in realizing the Duplex treatment was EN16MnCr5 carburizing steel, with the chemical composition presented in Chapter 3, Table 3.1. The material was supplied in annealed state, in bar form, with a length of 3 m and a diameter of 20 mm. The Duplex treatment was performed on cylindrical samples, with a diameter of 10 mm and length of 30 mm. The samples were cut using a STREAM LINE SLV OEM 30 machine, from endowment of National R&D Institute for Welding and Material Testing of Timisoara, Figure 4.1.

Figure 4.1: STREAM LINE SLV OEM 30

4.2.1 Gas Carburising

The first step in realizing the Duplex treatment consisted in gas carburizing. Gas carburizing in batch furnaces is a widely adapted procedure used for surface hardening, yet it faces some challenges in performance reliability and process control. The quality of the carburized parts is determined based on the hardness and case depth required for a particular application and on compliance with specifications and tolerances. Therefore, to ensure reliable service life of the carburized parts it is imperative to select the right carburizing parameters.

Endothermic atmospheres produced by mixing endogas and enriching hydrocarbon gas have been successfully used in industrial gas carburizing for over 50 years. Compared to previous carburizing methods, such as salt or pack carburizing, it offers an advantage of carbon potential control. Endothermic gas is most commonly produced by mixing air and natural gas and consists of CO, CO_2, CH_4, H_2, H_2O and N_2 [133].

The transfer mechanism of the carbon in gas carburizing is presented in Figure 4.2 [134].

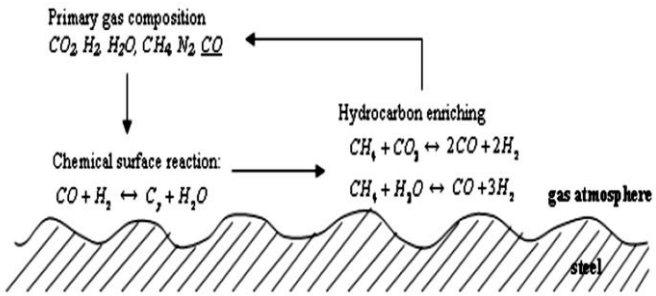

Figure 4.2: Schematic of the carbon transfer mechanism in gas carburizig [134]

The carburizing process was carried out in a box furnace in the heat treatment laboratory of DUROTERM Bucharest. The atmosphere was formed of endogas and CH_4 with a debit of 2.5L per hour. The equipment used for this process is presented in Figure 4.3.

Figure 4.3: Gas carburizing equipment

4.2.1.1. The determination of gas carburizing parameters

The determination of gas carburizing parameters was made by criterial method. This method is used for a rapid and accurate determination of the parameters involved in carburizing process like: total carburization time, concentration in any moment and at any distance in the carburized layer, the distance at which, after a certain time a certain concentration is achieved. The carburizing temperature is determined by the nature of the material. The nature of the material takes into account the chemical composition and the critical points at heating [133].

The carburizing temperature is selected in the austenitic domain because allows an easy diffusion of carbon into the surface and usually is determined by [135]:

$$T_C = A_{C3} + 30....50\ °C \qquad (4.1)$$

The superior limit is used for the alloyed steels. Knowing that the value of A_{C3} for EN 16MnCr5 is 850° C results thus a carburizing temperature of 900°C. Due to the chemical composition, the carbon concentration of the sample core is C_0 = 0.16 % C. The carburizing process is regarded as completed when the foreseen layer thickness has been attained, which is considered as being the distance from the surface (on perpendicular direction) to the point where the carbon concentration reaches 0.4%. So, another known parameter is the concentration in useful depth $C(x,\tau)$ = 0.4%C. The carbon concentration of the surface is C_S = 1 % C and the desired thickness of the carburized layer is x = 0.8 mm.

The diffusion coefficient (D) is established knowing the carburizing temperature and the ΔC, which represents the difference between the carbon concentration of the surface C_S and the initial carbon concentration C_0. In literature are given tables with the values of the diffusion coefficient function of temperature and concentration difference [135].

$$D = f(T_C = 900°C, \Delta C = C_S - C_0 = 0.84\ \%C) = 1.2 \times 10^{-7}\ cm^2/s \qquad (4.2)$$

The mass transfer coefficient (k) is given by the atmosphere used for carburizing. Similar to diffusion coefficient, its values are given in literature function of temperature and the specific reactions in the carburizing environment. Using endogas and CH_4 as carburizing atmosphere k = 1 x 10^{-5} cm/s.

In order to reduce the number of parameters, non-dimensional criteria will be employed, obtained by adequate combination of the quantities mentioned above, as follows:

- the "Biot" criterion [135], which establishes the correlation between the coordinate of the considered parameter, x [cm], the mass transfer coefficient, k [cm/s] and the diffusion coefficient, D [cm^2/s]:

$$\mathrm{Bi} = \frac{k \cdot x}{D} = \frac{10^{-5} \cdot 0.08}{1.2 \cdot 10^{-7}} = 5.33 \tag{4.3}$$

- the "Tihonov" criterion [157], is obtained with the relation:

$$\mathrm{Ti} = k\sqrt{\frac{\tau}{D}} \tag{4.4}$$

- the concentration criterion, θ_c, which express the relation between the concentration C(x,τ) in a current point located at a distance x from the part surface at a random moment of reference τ, carbon concentration of the gas atmosphere (C_{ech}=1.1C_S=1.1·1=1.1 %C) and the initial carbon concentration (C_0) [135]:

$$\theta_C = \frac{C(x,\, t) - C_0}{C_{ech} - C_0} = \frac{0.4 - 0.16}{1.1 - 0.16} = 0.25 \tag{4.5}$$

In these conditions, for a certain moment and a certain coordinate, the concentration criterion can be expressed only in function of the non-dimensional criteria previously presented, in the form: θc=f (Bi, Ti). This dependence is also represented graphically, in the nomogram presented in Figure 4.4 [135].

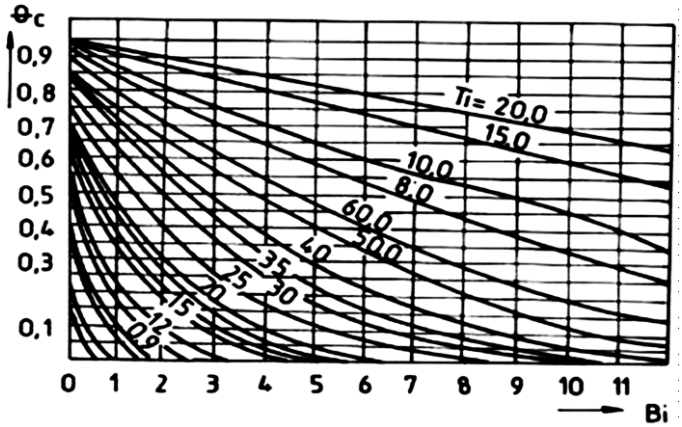

Figure 4.4: Correlation curves of the criterion θc=f(Bi,Ti) [132]

Using the values of Bi and Θ_C in the nomogram a value of 4 for Ti was obtained. The total carburizing time is determined using the relation of Tihonov criterion:

$$\tau = \frac{Ti^2 \cdot D}{k^2} = \frac{4^2 \cdot 1.2 \cdot 10^{-7}}{(1 \cdot 10^{-5})^2} = 24000s \cong 6\ h\ 40\ min \tag{4.6}$$

4.2.2 Surface induction quenching

The second step in realizing the Duplex treatment consisted in high frequency surface induction quenching. This type of treatment is realized by heating the piece through high-frequency alternating current provided by a copper inductor, Figure 4.5. This produces a changing magnetic flux that produces an electromotive voltage which induces a surface current. So, due to the effect Joule – Lenz, it occurs a superficial heating of the piece [132].

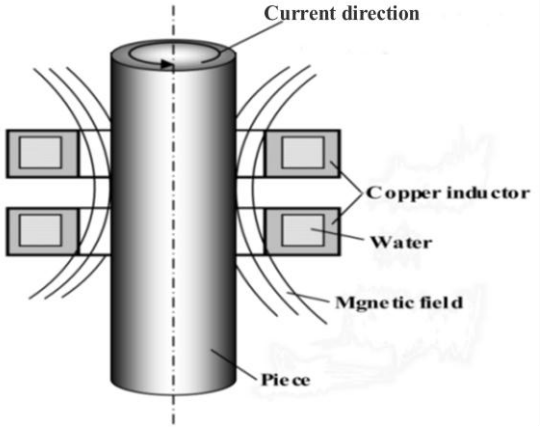

Figure 4.5: Schematic diagram of high frequency surface induction treatment [132]

The equipment used to realize this surface treatment is presented in Figure 4.6, and consists in a medium frequency generator, a transformer and a copper inductor.

Figure 4.6: The heating/melting 12 Kw equipment

To obtain optimal results, the induction coil has to be adjusted to the samples geometry. Therefore, a special induction coil has been made. The distance between the samples and the induction coil was around 10 mm. The parameters of the treatment are presented in Table 4.1.

Table 4.1: High frequency surface induction parameters

Tension [V]	390
Current intensity [A]	3
Frequency [kHz]	72
Process duration [s]	4

Using these parameters, a layer thickness of 0.8 mm was obtained. The cooling was realized in water.

4.2.2.1 Low tempering

Upon surface induction quenching, the parts are in a highly stressed condition. To avoid cracking, the parts should be tempered immediately after quenching. Like any other heat treatment, tempering is dependent on temperature and time. The temperature must be closely controlled, to develop the desired hardness range. For tempering time, a rule of thumb is one hour per 25mm of thickness [135]. According to these, the samples were subjected to low tempering treatment, at 180 °C for 30 minutes. The design of Duplex treatment consisting in gas carburizing and surface induction quenching and low tempering, following the determination of the optimal parameters of each treatment, is presented in Figure 4.7.

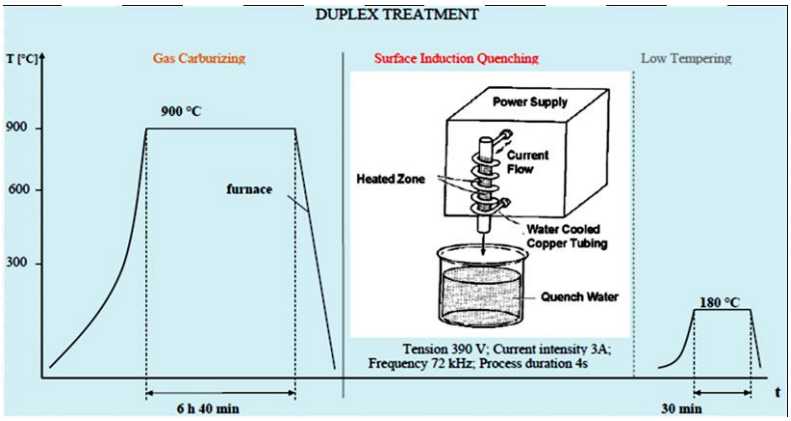

Figure 4.7: Duplex treatment design

4.3 Structural characterization

4.3.1 Optical microscopy

Duplex and non-Duplex samples were examined by optical microscopy following a series of distinct steps. Firstly, the samples were cross-sectioned to reveal the region of interest and subsequently mounted using Duracryl resin. Mounting a specimen provides a safe and ergonomic way to hold the samples during grinding and polishing operations.

The deformed layer that appears after sectioning and mounting the samples was removed by the application of finer abrasives. Initially, the surface was ground

using increasingly finer silicon carbide grit papers, from a coarse particle size of roughly 33 μm to a finest, in the region of 10 μm [127].

The surface of the samples was polished with diamond suspensions of 0.25% μm using a Phoenix 4000 polishing machine from endowment of Materials and Manufacturing Department, Mechanical Faculty of Politehnica University of Timisoara, Figure 4.8. In order to reveal the microstructure of the specimens, the surfaces were etched with 3% nital.

Figure 4.8: Phoenix 4000 polishing machine

The resulting micrographs of Duplex and non-Duplex samples are presented in Figure 4.9

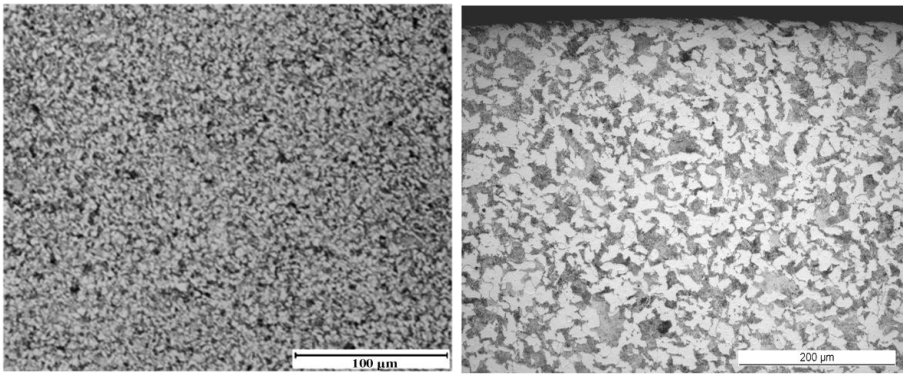

a – annealed state

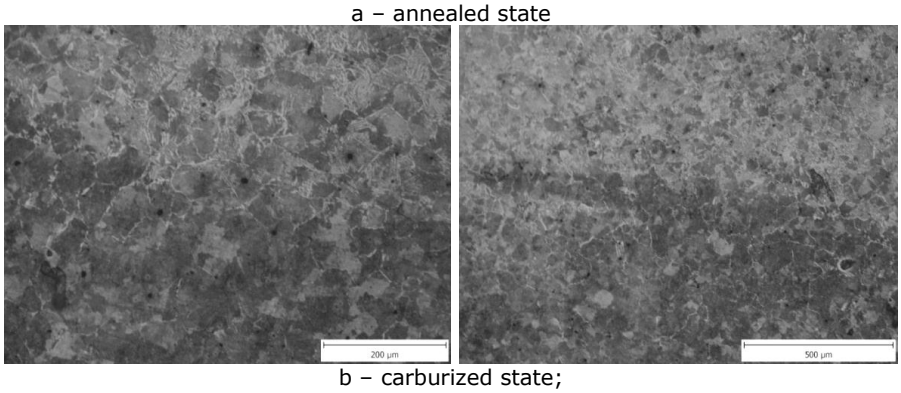

b – carburized state;

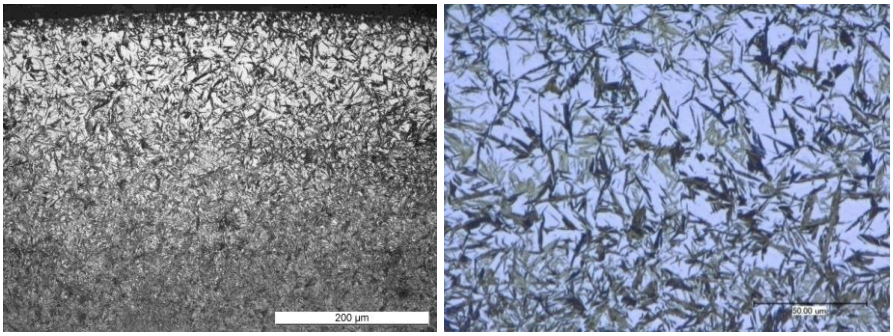

c – Duplex treated state;

Figure 4.9: Micrographs of Duplex and non-Duplex samples: a – annealed state; b – carburized state; c – Duplex treated state.

In annealed state, Figure 4.9 a, the structure is composed of ferrite (Feα) and pearlite (P), with a higher proportion of ferrite specific to a low alloyed carburizing steel. After carburizing, figure 4.9 b, the superficial layer is formed of perlite grains surrounded by a fine network of secondary cementite (Ce_{II}). As we move away from marginal layer, the structure is formed only of perlite, which marks a decrease in carbon content. In Duplex treated state, figure 4.9 c, the structure is formed of tempered martensite and residual austenite. A fine structure of martensite correlated with secondary cementite leads to a superficial layer structure that provide a significant increase of hardness, wear and fatigue resistance. The structural changes highlighted ensure a gradient of properties in the pieces section.

4.3.2 X-ray diffractions

In order to identify the constituent phases, X-ray analyze was performed on Duplex and non-Duplex samples. The tests were realized using Cu Kα monochromatic radiation of wavelength 1.541840 Å. The parameters are presented in Table 4.2

Table 4.2: XRD parameters

Intensity [mA]	Tension [KV]	Step size	Time per step [s]	Scan speed [s]	Scan angle [°]
30	40	0.04	0.5	0.08	20-90

Figure 4.10 a, b, c shows the X-ray diffraction patterns for untreated, carburized and Duplex treated samples.

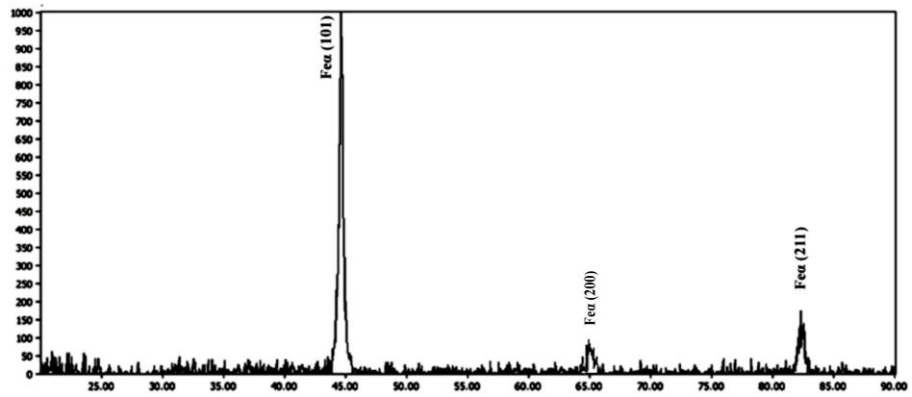

a- annealed state;

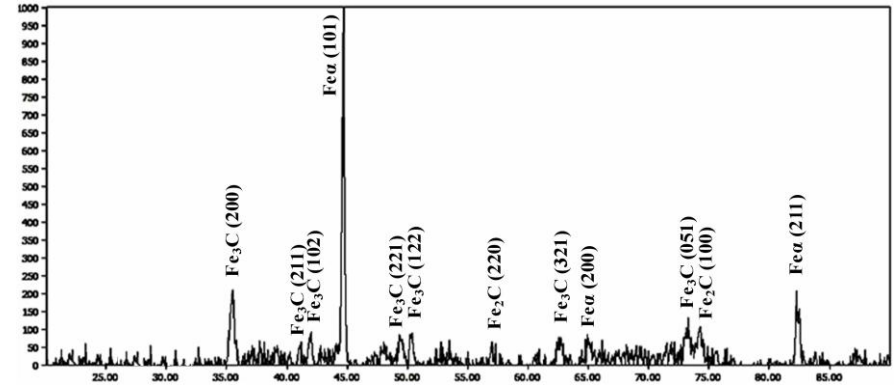

b – carburized state;

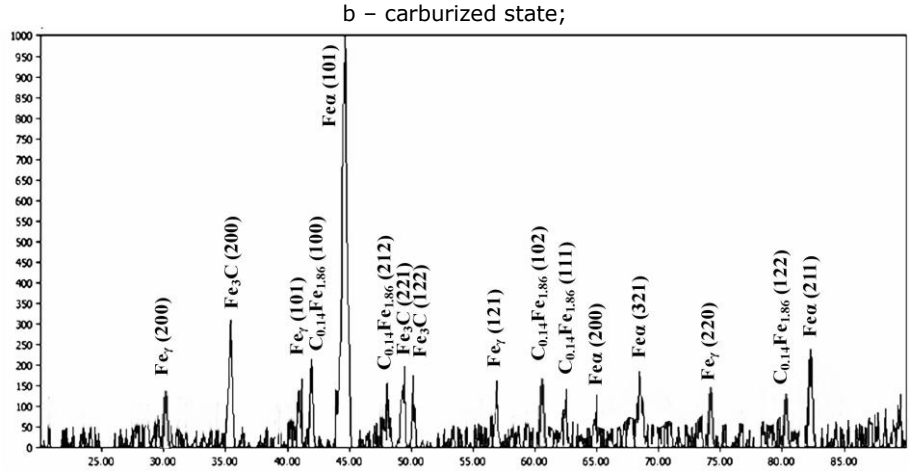

c- Duplex treated state;

Figure 4.10: X-ray diffraction patterns: a – annealed state; b – carburized state; c – Duplex treated state

The result of X-ray analysis showed only the presence of iron phases on the annealed samples. The reflections from the cubic iron phases produce 3 peaks, that can be indexed as (101), (200) and (211), which occur at 2θ values of approximately 44.674º, 65.023° and 82.335 respectively (Figure 4.10 a).

For the carburized samples, X-ray diffraction analyzes reveals the presence of iron phases and iron carbides. Reflections of orthorhombic Fe_3C (cementite) phase produce 7 peaks, that can be indexed as (200), (211), (102), (221), (122), (321) and (051), which occur at 2θ values of approximately 35.234°, 42.867°, 43.743°, 49.116°, 51.800°, 64.121° and 73.149°. Orthorhombic iron carbide Fe_2C reflection produce 2 peaks, that can be indexed as (220) and (100), which occur at 2θ values of approximately 57.955° and 74.255°. The reflections from the cubic iron phases produce 3 peaks, that can be indexed as (101), (200), and (211), which occur at 2θ values of approximately 44.674º, 65.023° and 82.335° (Figure 4.10 b).

Martensite phases ($C_{0.14}Fe_{1.86}$) were determined on the Duplex treated samples, as expected. The reflections of this phase produce 5 peaks, that can be indexed as (100), (212), (102), (111) and (122), and which occur at 2θ values of approximately 42.720°, 48.632°, 61.012, 63.132° and 81.415°. Determination of martensite phases proved that the cementation process was effectively carried out. In addition to the martensite phase, austenite (retained austenite, Fe_γ), iron and iron carbide phases were determined on Duplex treated specimens.

Reflections of retained austenite (Feγ) produce 4 peaks that can be indexed as (200), (101), (121) and (220), and occur at 2θ values of approximately 30.120°, 41.430°, 57.123° and 74.220°. The reflections from the cubic iron phases produce 3 peaks, that can be indexed as (101), (200), and (211), which occur at 2θ values of approximately 44.674º, 65.023° and 82.335°.

Reflections of orthorhombic Fe_3C (cementite) phase produce 3 peaks that can be indexed as (200), (221), and (122) which occur at 2θ values of 35.234°, 49.116° and 51.800°, Figure 4.10 c.

4.3.3 Glancing incidence X-ray diffraction

Glancing incidence diffraction techniques are used when the information needed lies within a thin top layer of the material. Conventional X-ray diffraction reveals information about a top layer of a thickness in the order of 5-10 μm. In contrast, by employing a glancing angle technique this thickness may be an order of magnitude smaller [130]. The test parameters are presented in Table 4.3.

Table 4.3: Glancing incidence X-ray diffraction parameters

Intensity [mA]	Tension [KV]	Step size	Increment	Scan speed [°/min]	Scan angle [°]	Div.slit	
						Actual	Requested
30	40	0.04	0.04	5	20-90	0.100	0.100

The glancing incidence patterns are presented in Figure 4.11.

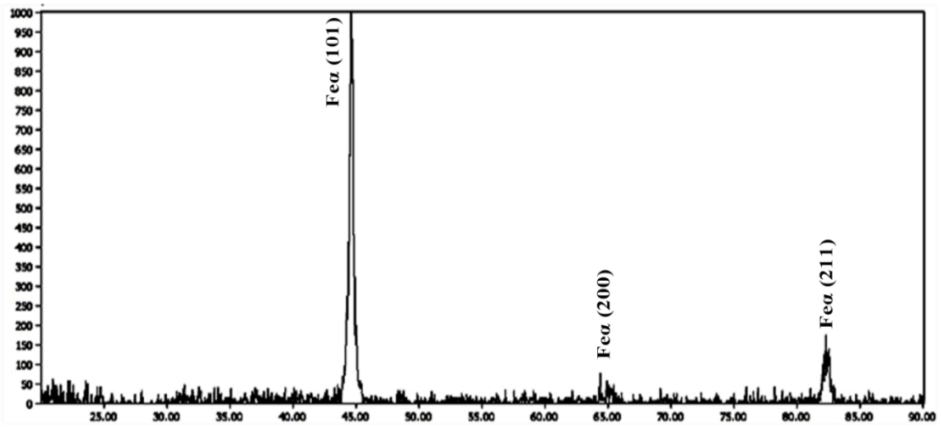

a - annealed state;

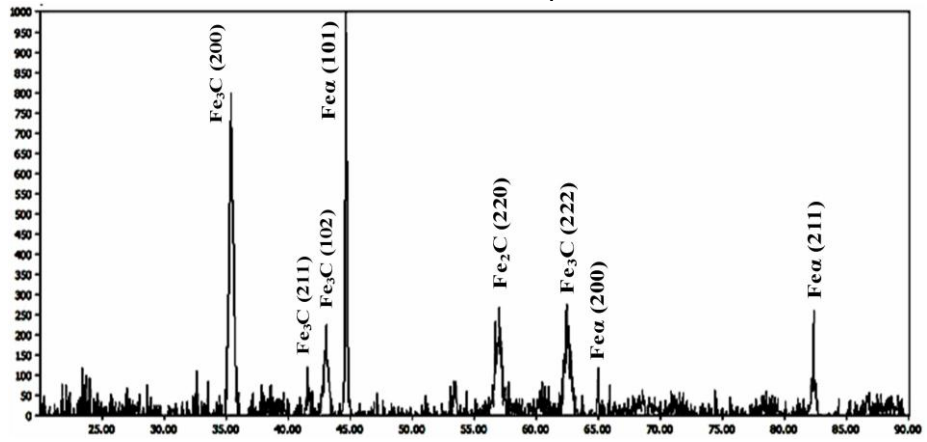

b- carburized state;

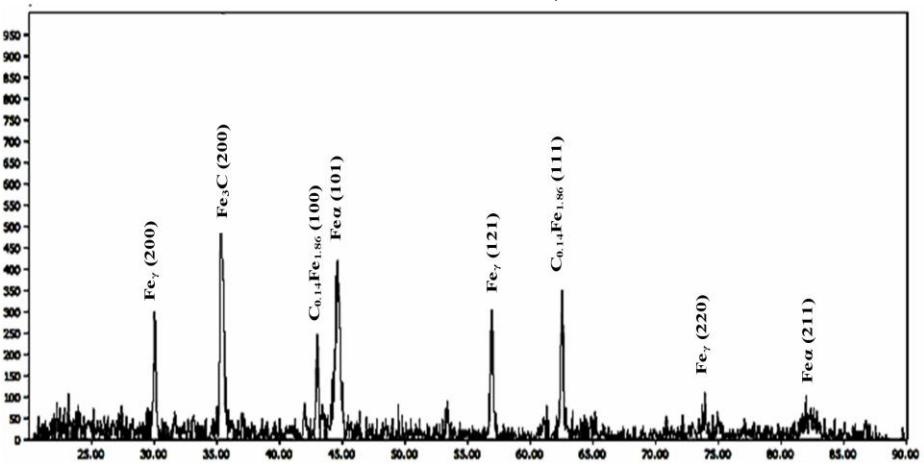

c – Duplex treated state;

Figure 4.11: Glancing incidence patterns: a – annealed; b – carburized; c – Duplex treated

As it can be observed from Figure 4.11 a, only iron phases (Fe-α) are presented in the annealed samples structure. The reflection of Fe-α produce 3 peaks indexed as (101), (200) and (211), at 2θ values of approximately 44.674º, 65.023° and 82.335°.

Figure 4.11 b reveals the presence of iron and iron carbides phases in the structure of carburized samples. Reflections of orthorhombic Fe_3C (cementite) phase produce 4 peaks, that can be indexed as, (200), (211), (102) and (222) at 2θ values of approximately 35.208°, 42.880°, 43.743° and 63.262°. Orthorhombic iron carbide Fe_2C reflection produce 1 peak, indexed as (220), which occur at 2θ values of approximately 57.955°. The reflections from the cubic iron phases produce 3 peaks, that can be indexed as (101), (200), and (211), which occur at 2θ values of approximately 44.674º, 65.023° and 82.335°. As mentioned before, glancing incidence reveals information about top layers of small thickness. Therefore, at the marginal layer, the structure of the carburized samples is formed of cementite (Fe_3C) and iron carbide (Fe_2C).

As expected, martensite ($C_{0.14}Fe_{1.86}$) and austenite (residual) phases were determined on the Duplex treated samples, Figure 4.11 c. It can be observed a higher proportion of residual austenite. The reflections of martensite phase produce 2 peaks that can be indexed as (100) and (111), which occur at 2θ values of approximately 42.720° and 63.132°. Reflections of retained austenite (Feγ) produce 3 peaks that can be indexed as (200), (121) and (220), and occur at 2θ values of approximately 30.120°, 57.123° and 74.220°. It can also be observed the presence of iron phases and cementite. Iron phase reflections from produce 2 peaks, that can be indexed as (101) and (211) and occur at 2θ values of approximately 44.674º and 82.335°. Reflections of orthorhombic Fe_3C (cementite) phase produce 1 peak, that can be indexed as (200) and occur at 2θ of 35.234°.

4.4 Micro-hardness tests

Vickers micro hardness was evaluated at the cross-section of the specimens for treated and non-treated samples. The specimens were mounted and polished and the hardness measurements were realized using Volpert Micro-Vickers Hardness Tester Digital, with a load of 200g and a loading time of 10 seconds. About twenty readings were taken on each sample and the average value is reported as the data point and plotted in Figure 4.12 against the distance from the surface.

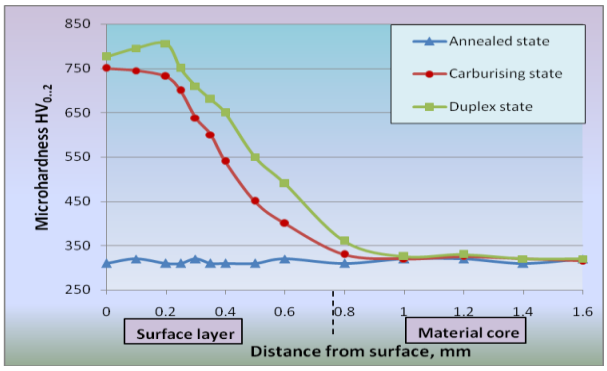

Figure 4.12: Hardness profile of Duplex and non- Duplex samples

The hardness tests showed that the hardness values of Duplex treated specimens decreased from the surface to the core depending on the carbon profile, which reaches maximum content at surface and decreases in the core, as it can be observed in Figure 4.12. At the surface, the hardness values ranged from 806 HV0.2 to 370 HV0.2, while in the core, the values are constant, ranging from 310 to 320 HV0.2. The maximum value of 806 $HV_{0.2}$ was obtained at a distance of 0.2 mm from surface, due to the presence of a higher proportion of residual austenite at surface, as illustrated by glancing incidence X-ray diffraction.

Regarding the carburized state, the hardness also decreases from surface to core, obtaining in the surface a maximum value of 750 HV0.2. In the core, the values are constant, ranging from 310 to 320 HV0.2. As it can be observed from figure 4.66, the hardness values obtained for the annealed state are constant, ranging from 310 to 320 HV0.2.

The hardness prints for each structural state are presented in Figure 4.13. SEM imagines were taken from surface to the core for each hardness values. After that, each SEM photos was combined and Figure 4.13 was obtained.

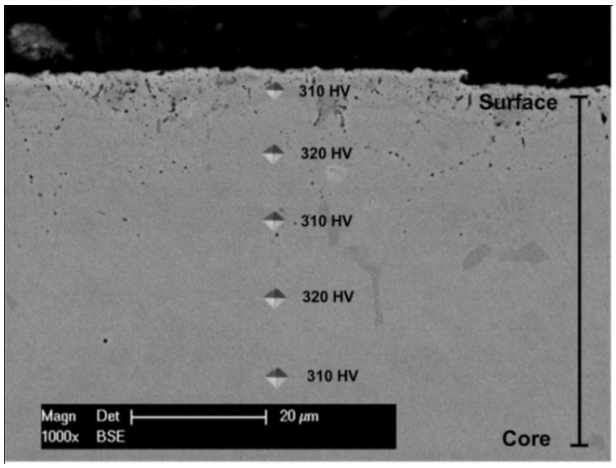

a – annealed state;

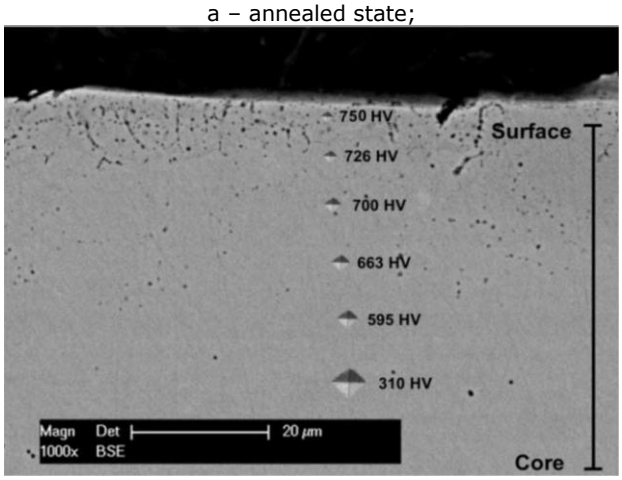

b – carburized state;

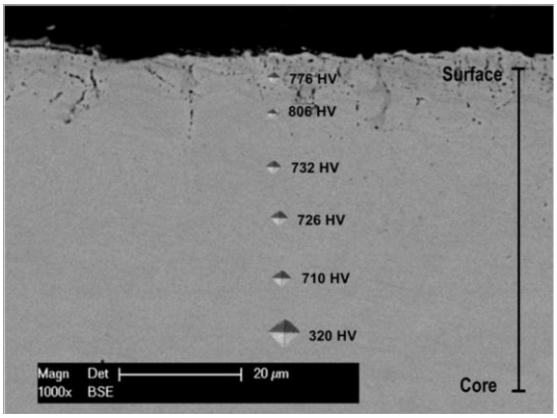

c – Duplex treated state;

Figure 4.13: Hardness prints: annealed; b – carburized; c – Duplex treated;

4.5 Instrumented indentation tests

Mechanical properties of materials, such as hardness, bulk modulus, tensile properties and toughness can be determined by indentation tests. From a general point of view, the indentation test consists of performing a print at the material surface by the penetration of a hard indenter, at a given indentation load. The indenter can have different geometrical shapes such as spherical, conical or pyramidal. Generally, pyramidal indenters are used to determine hardness, bulk modulus and cracking resistance of the material, whereas spherical indenters are mainly used to determine the tensile properties and bulk modulus [136-139].

The indentation load can be chosen in nano-, micro- or macro-indentation ranges which allow the study of local or global mechanical properties. The mechanical properties are determined by analyzing the geometrical dimensions of the residual indent (usual indentation) or from the analysis of load-depth curves (instrumented indentation tests). A schematic representation of a typical load-unload curve is presented in Figure 4.14, where F represents the load, *h* is the penetration depth, h_c is the contact depth, h_r is the permanent depth of penetration after the indenter is fully unloaded and S represents the contact stiffness [136].

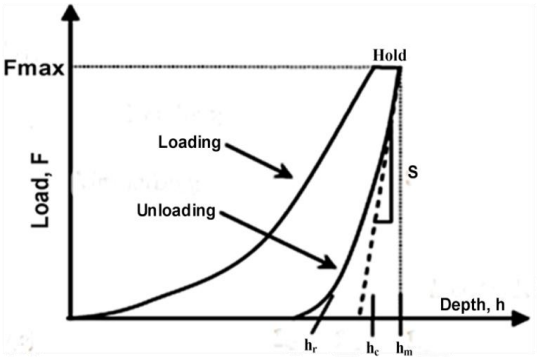

Figure 4.14: Load-depth curve [136]

The deformation during loading is both elastic and plastic, while during unloading only the elastic displacements are recovered. There are three important parameters that must be measured from the *F–h* curves: the maximum load (F_{max}), the maximum depth, (h_{max}), and the contact stiffness (S). The accuracy of hardness and modulus measurement depends on how well these parameters can be measured experimentally [138].

4.5.1 Bulk modulus determination

In this study, bulk modulus of Duplex and non – Duplex samples was determined from the analysis of the load-depth curves. The indentation prints are presented in Figure 4.15.

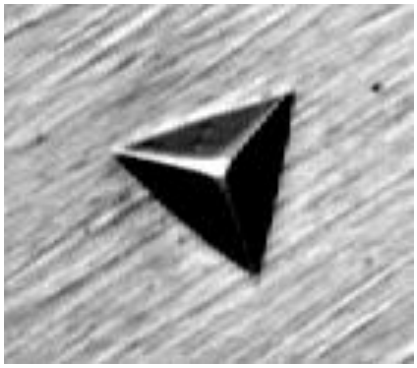

Figure 4.15: Indentation print

Each specimen was subjected to load-unload cycle under the same amount of maximum load and the loads vs. penetration depth curves were plotted, Figure 4.16. The holding time at loading was 15 s. To get more accurate values, twelve measurements, with the applied load ranging from 100 to 1000 mN, were performed. Before micro indentation testing can be performed, it is necessary to create a high-quality surface in order to ensure both accuracy and repeatability of the tests [138]. Therefore, the samples have been metallographically mounted, grinded and polished. The results obtained are presented in Table 4.4.

Tabelul 4.4: Values obtained by means of micro-indentation tests

Measurements	Annealed state			Carburized state			Duplex treated state		
	F [mN]	h_{max} [µm]	h_r [µm]	F [mN]	h_{max} [µm]	h_r [µm]	F [mN]	h_{max} [µm]	h_r [µm]
1	102.19	1.2276	1.1388	101.95	1.1023	0.984	101.32	0.8426	0.7085
2	101.87	1.4164	1.3386	101.94	1.1165	1.0571	101.22	0.8922	0.7637
3	207.47	1.9455	1.8056	207.69	1.6513	1.4597	207.73	1.0811	0.8554
4	207.87	2.0398	1.8996	207.69	1.7509	1.5725	209.99	1.1457	0.9273
5	407.31	3.1578	2.9536	406.95	2.4518	2.1557	410.07	1.8932	1.5916
6	407.95	3.1431	2.9403	406.73	2.6158	2.3318	406.37	1.8131	1.4914
7	609.86	3.9095	3.630	609.7	3.2166	2.8235	609.78	1.9897	1.543
8	611.52	3.8177	3.5161	609.49	3.3330	2.9445	609.77	2.2263	1.8106
9	809.14	4.3551	3.9967	808.14	3.9898	3.5017	809.06	2.4532	1.9224
10	810.41	3.8826	3.4646	808.15	3.8159	3.3122	808.65	2.4824	1.9637
11	1010.9	4.6774	4.2464	1008.45	4.4121	3.793	1007.33	2.6597	2.0278
12	1008.4	5.0388	4.6148	1007.39	4.7802	3.7934	1007.53	2.6562	1.9564

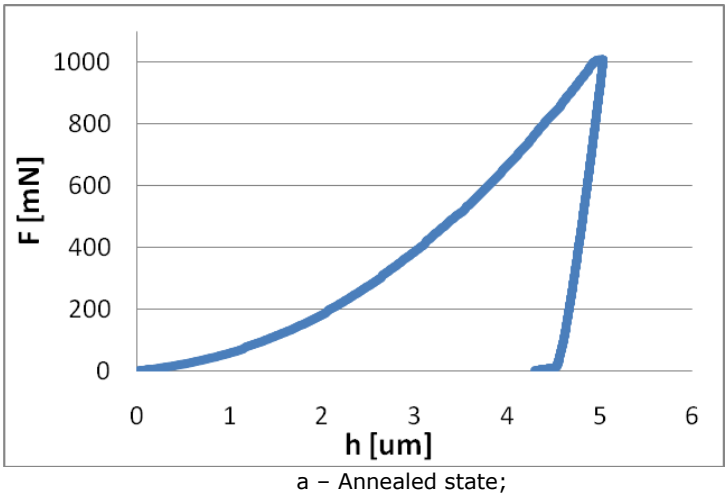

a – Annealed state;

b – Carburized state;

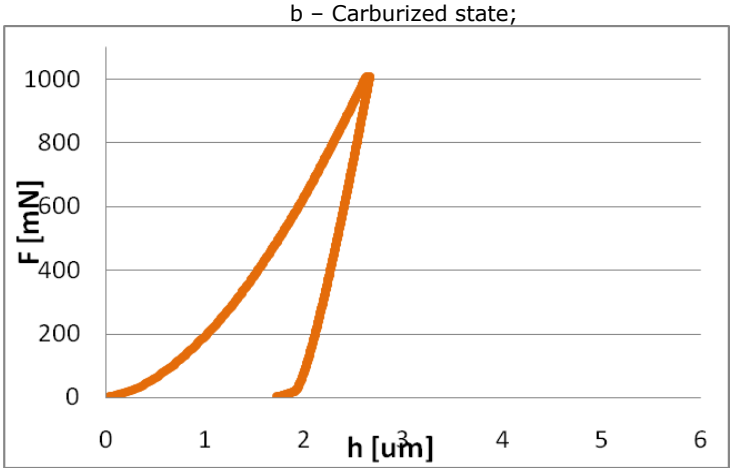

c – Duplex treated state;

Figure 4.16: Load – penetration depth curve: a - annealed state; b – carburized state; c – Duplex treated state.

As it can be observed from Figure 4.15 and Table 4.4, the penetration depths of Duplex treated samples are much lower compared with the penetration depths of annealed and carburized ones, due to the higher hardness of these specimens. The bulk modulus can be calculated from the total compliance of the sample and of the instrument, using the formula proposed by Oliver and Pharr [136].

$$Ct = \frac{1}{S(h_{\max})} = C_f + \sqrt{\frac{\pi}{24{,}5}} \cdot \frac{1}{2 \cdot \beta \cdot \gamma \cdot E_R} \cdot \frac{1}{h_c} \qquad (4.7)$$

Where:

- C_t - total compliance;
- S – material stiffness
- C_f - instrument compliance;
- β - correction factor which depends on the shape of the indenter (for Bergovich β=1.034);
- γ - correction factor which depends on the shape of the indenter (for Bergovich γ = 1,068)

- h_c – contact depth
- E_R- reduced elastic modulus.

The contact stiffness is the slope of the upper portion of the unloading curve during the initial stages of unloading. The contact depth is determined using the following formula [138]:

$$h_c = h_{max} - \left(0.75 \times \frac{F_{max}}{S}\right) \quad (4.8)$$

The instrument compliance C_f for Duplex and non - Duplex samples is determined by plotting the inverse of the contact stiffness (1/S) as function of the inverse contact depth $1/h_c$, as presented in Figure 4.17. The representation is linear, so the slope is directly linked to the bulk modulus of the material according to equation 4.7.

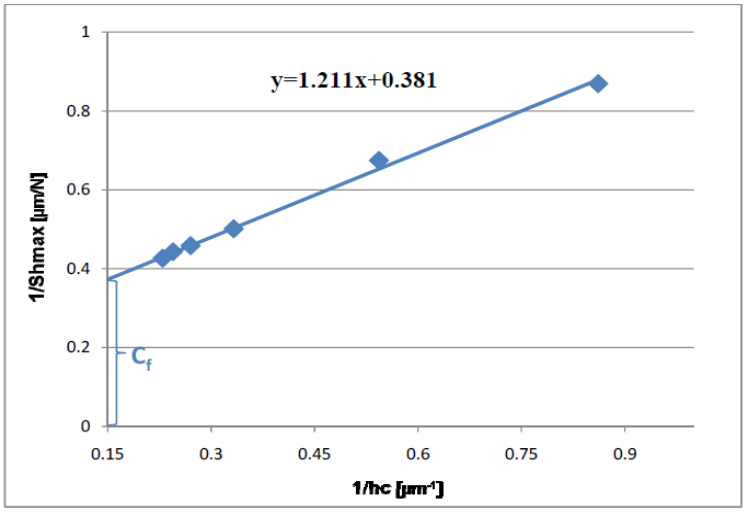

a – annealed state;

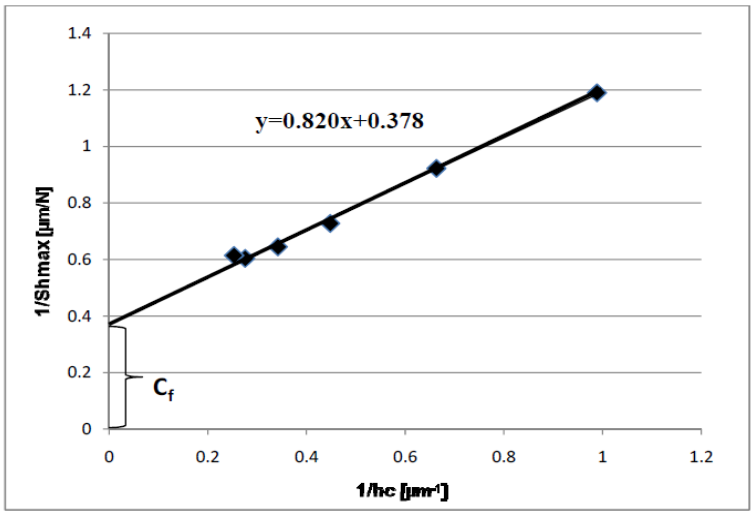

b – carburized state;

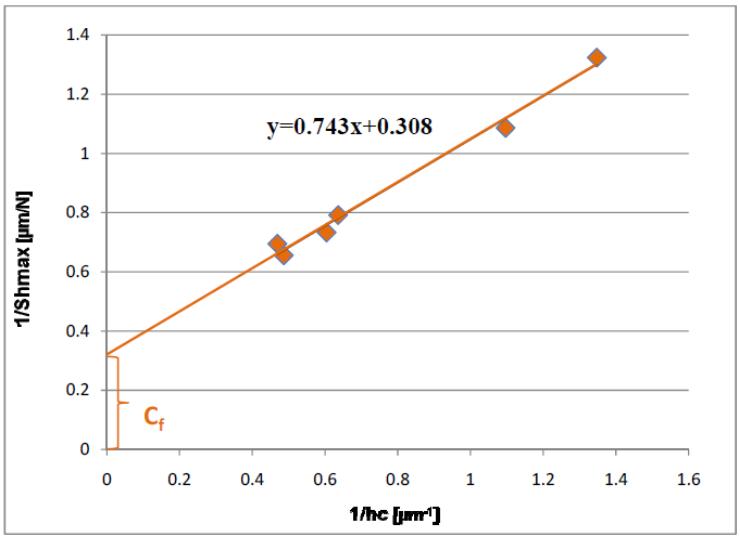

c – Duplex treated state;

Figure 4.17: Instrument compliance: a - annealed state; b - carburized state; c - Duplex treated state

The reduced bulk modulus reflects the elastic contact interaction between the indenter and sample. In order to determine the bulk modulus of each sample, the following relationship was used [136]:

$$\frac{1}{E_R} = \frac{1-\nu_m^2}{E_m} + \frac{1-\nu_i^2}{E_i} \tag{4.9}$$

Where:

- E_R – reduced elastic modulus;
- E_m – bulk modulus of the sample;
- Y_m – Poisson's ratio of the sample;
- E_i – elastic modulus of the indenter;
- Y_i – Poisson's ratio of the indenter;

Taking into consideration the elastic properties of the indenter, namely 1140 GPa for the bulk modulus and 0.07 for the Poisson's ratio and by taking 0.3 for the Poisson's ratio of the material, we obtain the values for the reduced modulus presented in Table 4.5.

Table 4.5: Values of bulk and reduced modulus

Structural state	Reduced modulus, E_R [GPa]	Bulk modulus, E_m [GPa]
Annealed	131	135
Carburised	197	217
Duplex treated	218	245

As it can be observed from Table 3.11, the values of bulk modulus increased from 135 GPa (annealed state) to 245 GPa (Duplex state), which represents an increase of about 80%.

4.5.2 Hardness determination

The hardness of a material is defined as its resistance to plastic deformation usually by indentation. The general relation to calculate a hardness number is given by [138]:

$$H = \frac{F}{A} \tag{4.10}$$

Where H is the hardness, F the applied load and A the area of the residual indent. For instrumented indentation tests, which allow the plot of a load-depth curve, the calculation of the hardness is realized using the maximum indentation depth reached by the indenter during the indentation test, the residual depth or the contact depth. Consequently, the hardness calculation can have different forms, as presented in Table 4.6, according to the indentation depth which is considered [138].

Table 4.6: Hardness numbers considering true or projected contact areas and different indentation depth [138]

Indentation depth	Maximum	Residual	Contact
True contact area	$HM = \frac{F}{26.43h_m^2}$	$H = \frac{F}{26.43h_r^2}$	$H = \frac{F}{26.43h_c^2}$
Projected contact area	$H = \frac{F}{24.5h_m^2}$	$H = \frac{F}{24.5h_r^2}$	$HIT = \frac{F}{24.5h_c^2}$

The Martens hardness, HM, and the contact hardness, HIT, are mainly used in micro and nano-indentation, respectively. The Martens hardness values for Duplex and non Duplex samples are presented in Table 4.7.

Table 4.7: Martens hardness values for Duplex and non – Duplex samples

No.	Annealed				Carburized				Duplex			
	F [mN]	h_{max} [mm]	HM [GPa]	HM ave	F [mN]	h_{max} [mm]	HM [GPa]	HM Ave	F [mN]	h_{max} [mm]	HM [GPa]	HM ave
1	102.19	1.22	**2.65**		101.95	1.10	**3.29**		101.32	0.84	**5.56**	
2	101.87	1.41	**1.98**		101.94	1.11	**3.21**		101.22	0.89	**4.95**	
3	207.47	1.94	**2.21**	**1.98**	207.69	1.65	**3.10**	**2.63**	207.73	1.08	**7.32**	**6.06**
4	207.87	2.03	**2.01**		207.69	1.75	**2.75**		209.99	1.14	**6.57**	
5	407.31	3.15	**1.69**		406.95	2.45	**2.87**		410.07	1.89	**4.86**	
6	407.95	3.14	**1.70**		406.73	2.61	**2.50**		406.37	1.81	**5.28**	
7	609.86	3.90	**1.69**		609.7	3.2166	**2.55**		609.78	1.98	**6.96**	
8	611.52	3.81	**1.78**		609.49	3.3330	**2.37**		609.77	2.22	**5.45**	
9	809.14	4.35	**1.85**		808.14	3.9898	**2.23**		809.06	2.45	**6.19**	
10	810.41	3.88	**2.38**		808.15	3.8159	**2.45**		808.65	2.48	**6.03**	
11	1010.9	4.67	**2.06**		1008.45	4.4121	**2.33**		1007.33	2.65	**6.79**	
12	1008.4	5.03	**1.75**		1007.39	4.7802	**1.95**		1007.53	2.65	**6.81**	

As it can observed from Table 4.7, the average values of Martens hardness corresponding to annealed state is 1.98 GPa, 2.63 GPa corresponding to the carburized state and 6.06 GPa for Duplex treated state. Martens hardness for Duplex state (Figure 4.18) increased 5 times compared to annealed state, and 2 times compared to carburized state respectively.

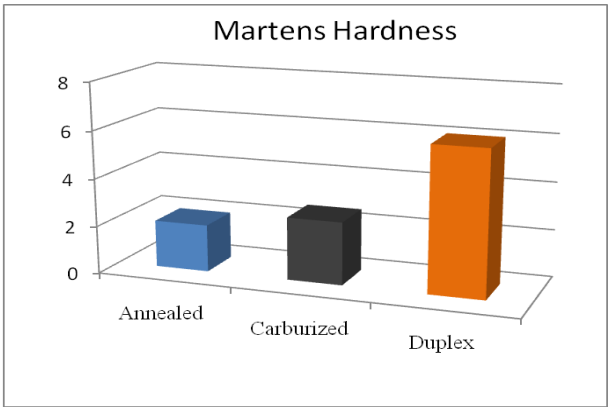

Figure 4.18: Martens hardness

4.5.3 Internal stresses

Residual stresses are stresses caused by external stimuli, and persist within the material after external stimuli have been removed. The magnitude of residual stresses has an important effect on the mechanical behaviour (fatigue, fracture, corrosion, etc.) of mechanical parts performance. These stresses may act in a positive way to enhance a material's performance (for example, surface compressive stresses improve fatigue resistance) or in a negative way to reduce service life (for example, surface tensile stresses that increase crack propagation). Residual stresses are present in most materials and arise during each processing step (mechanical forming, heat treatment, joining, fitting, etc.). They also appear under routine operation (ex. aerodynamic or hydrostatic pressure) and during maintenance and repair (cold-working, welding, straightening procedures) [131-137]. A variety of techniques is available for residual stress analysis. The methods can be classified as either destructive or non-destructive. Destructive techniques are those that destroy the state of equilibrium within a material [137].

Destructive techniques include hole-drilling (HD), bending deflection and sectioning method. These techniques are not only destructive to the structure under investigation, but sectioning the material will modify the stresses and strains will change. Non-destructive techniques determine stress based on the relationship between intrinsic material properties and residual stress. Techniques that measure intrinsic properties include ultrasonic (measures variation in speed of ultrasonic wave propagation), magnetic measurements (ex., magnetic induction, Barkhausen noise amplitude), neutron diffraction and X-ray diffraction (which measure change in atomic inter-planar spacing's of the crystal structure) [137-139].

A new method for estimating residual stresses, namely instrumented indentation, was first introduced by Suresh and Giannakopoulos. They have measured residual stress based on the calculation of the difference between the indentation contact areas of with and without stressed surfaces by analyzing load–depth curves. Compared with traditional techniques, the depth-sensing indentation technique provides a quick and effective method for measuring the residual stress [137].

Suresh and Giannakopoulos assumed that the indented surface has been subjected to prior mechanical and/or thermal treatments. Therefore, such prior history is assumed to result in an equal-biaxial state of residual stress (tensile or compressive) whose magnitude at the surface is $\sigma^R_{x,0} = \sigma^R_{y,0}$ uniformly over a depth of at least d^R, Figure 4.19 [137] .

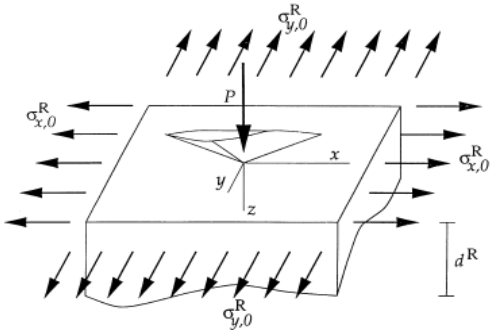

Figure 4.19: Schematic of sharp indentation with the associated nomenclature [137]

If the indented surface contains an equal-biaxial compressive residual stress, it would be equivalent to a compressive hydrostatic stress, plus a uni-axial tensile stress component.

$$-\sigma^{R}_{x,0} = -\sigma^{R}_{y,0} = -\sigma_{H} = -\sigma^{R}_{z,0} \quad (4.11)$$

Suresh and Giannakopoulos determined the effects of a compressive residual stress on the contact areas and indentation penetration depths. Figure 4.20 schematically shows the load-depth curve for the indentation of the virgin material, and that for the substrate with compressive residual stress [137].

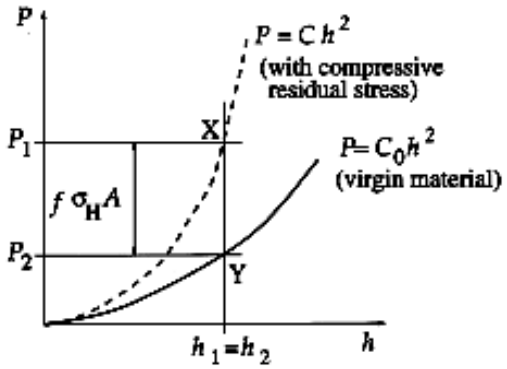

Figure 4.20: The indentation load-depth (P-h) curves for the surfaces with and without residual stresses [137]

The material with the residual stress is first indented with a load F1, which causes the indenter to penetrate it by a depth h_1 (noted X, Figure 4.20). Keeping the indentation depth h_1 constant, the indented material completely relaxes, from $\sigma^{R}_{x,0} = \sigma^{R}_{y,0}$ to zero, at a fixed penetration depth, $h_1=h_2$.

In order for the average contact pressure to remain constant, the equivalent plastic strain beneath the indenter should be preserved.

In this method, the measurement of residual stresses is based on the calculation of the difference between the indentation contact areas of with and without stressed surfaces by analyzing ‘‘indentation load–depth’’ data according to the below equation [137]:

$$\frac{A_c}{A_o} = \left(1 + \left(\frac{\sigma_r \times \sin\alpha}{\rho_{ave}}\right)\right)^{-1} \quad (4.12)$$

where A_c and A_o are the indentation contact areas with and without residual stress respectively. α is a geometric factor, related to the indentation angle of the indenter (for Bergovich α = 24.7) and ρ_{ave} is the average contact pressure:

$$\rho_{ave} = \frac{P_{max}}{A_{max}} \quad (4.13)$$

According to the upper-bound solution of the compressive residual stress, the magnitude of the force acting normal to the inclined faces of the indenter during indentation is $\sigma_r fA$, as shown in Figure 4.21 a [137, 141].

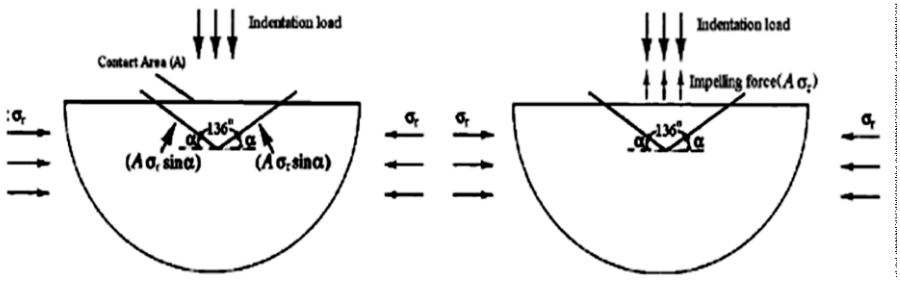

a) b)

Figure 4.21: Schematic representation of residual stress while indenter is under contact position with material a) for Suresh and Giannakopoulos b) for Atar et al. [137, 141]

Later, Atar et al (Figure 4.21 b) indicate that an impelling force having a value of $\sigma_r A$ is acting against the applied indentation load in the direction of indentation, rather than the component of the residual stress acting normal to the inclined faces of the indenter, as shown in Figure 4.21 b. Therefore, for the calculation of the residual compressive stress in materials, Eq. (4.12) should be modified as [141]:

$$\frac{A_C}{A_0} = \left(1 - \left(\frac{\sigma_r \times \sin\alpha}{\rho_{ave}}\right)\right)^{-1} \quad (4.14)$$

In this case, the internal stresses induced by surface induction quenching were determined by comparing the load-unload curves of annealed samples, which were considered the virgin material, with the load-unload curves of Duplex treated samples, considered the stressed material

After comparing the load-unload curves corresponding to the structural states, the residual stresses were calculated by the two different approaches presented. The residual stress values are presented in Table 4.8, and illustrated in Figure 4.22.

Table 4.8: Values of the residual stress

Fm [mN]	hc [µm]	Fm [mN]	hc [µm]	A_0 [mm^2]	A_C [mm^2]	ρ_{ave} [N/mm^2]	Residual stress [MPa] By Suresh et al	Residual stress [MPa] by Atar et al
102.19	1.16	101.32	0.74	3.56E-05	1.46E-05	2868.45	**-990**	**-415**
207.47	1.84	207.73	0.91	8.95E-05	2.20E-05	2317.13	**-1700**	**-712**
407.31	3.00	406.37	1.57	2.39E-04	6.53E-05	1707.03	**-1080**	**-453**
609.86	3.70	609.78	1.65	3.62E-04	7.24E-05	1685.62	**-1608**	**-674**
809.14	4.09	809.06	2.06	4.41E-04	1.12E-04	1833.44	**-1291**	**-542**
1010.90	4.35	1007.53	2.13	5.01E-04	1.20E-04	2017.46	**-1527**	**-640**

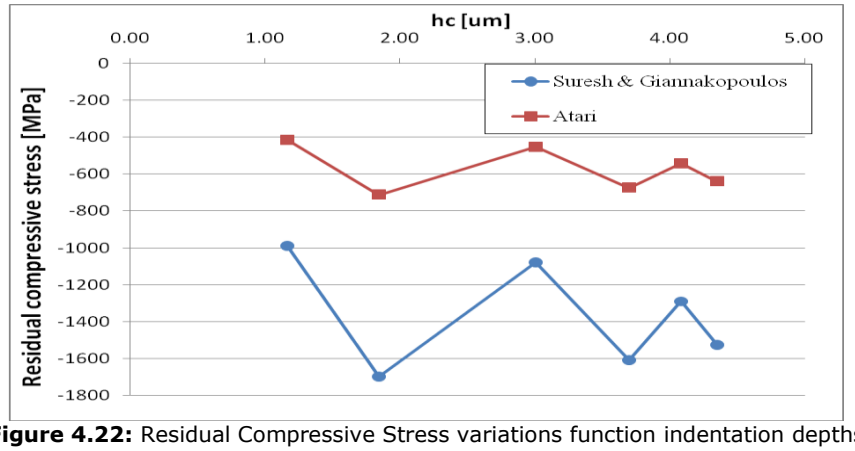

Figure 4.22: Residual Compressive Stress variations function indentation depths

The stress measurement revealed high compressive stresses, ranging between -415 MPa and -712 MPa (Atari et al.) and -990 MPa to -1700 MPa (Suresh et al.).

4.6 Corrosion behaviour

The corrosion behavior of Duplex and non - Duplex samples was electrochemical investigated in different environments by means of linear polarization. The linear polarization resistance measurement, which was first introduced by Stern and Geary, is a non-destructive technique that can be used in both lab and field measurements. In this method, over potential in the range of 25 mV about the open circuit potential of the sample is applied and the induced current is recorded. Since the applied voltage is small, the current response will be linear [52].

In order to conduct the linear polarization resistance test, three electrodes (the working electrode, the counter (auxiliary) electrode and the reference electrode) have to be attached to a potentiostat. Figure 4.23 shows a schematic representation of linear polarization resistance test.

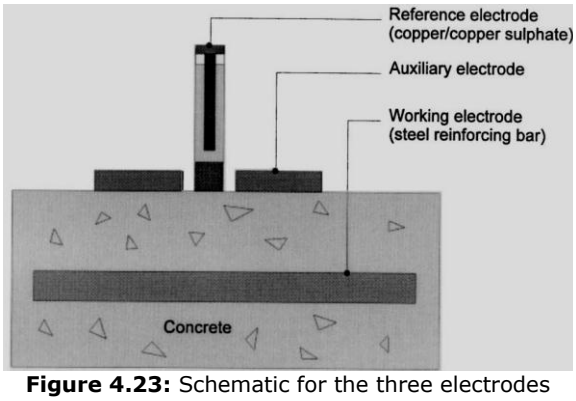

Figure 4.23: Schematic for the three electrodes linear polarization measurements [142]

For the tests, 10 mm diameter discs were cut from the treated and non – treated samples, and cleaned in ultrasonically followed by hot air drying. The tested samples were painted with a non-conductive paint, as presented in Figure 4.24, so that only the treated part would be exposed in the solutions.

Figure 4.24: Sample preparation

In order to achieve a high reliability of the results, all electrochemical measurements were repeated at two times.

The sample preparation and experiments were performed at the National Laboratory of Energy and Geology of Lisbon. The electrochemical experiments were carried out at room temperature, by a three electrode cell assembly of 250 mL and a potentiostat/galvanostat EG&G (model 273) connected to a computer by a GPIB card and controlled by the software Corrview. The samples were placed as working electrode; a graphite bar was used as counter-electrode, and a silver-silver chloride electrode (Ag/AgCl) as a reference. The parameters related to the corrosion resistance, specifically, the polarization resistance (R_p), the corrosion current density (i_{corr}) and the potential of corrosion (E(I=0)), were obtained using the software Corrview. The solutions used for these tests are presented in Table 4.9.

Table 4.9: Solutions used for the electrochemical tests

PH	Solution
7	3 % NaCl
0.3	0.5 M H_2SO_4
0.3	0.1 M H_2SO_4

The solution 3% NaCl was prepared by mixing 60 g of NaCl with 2L distilled water. 0.5 M H_2SO_4 was prepared by mixing 30 ml H_2SO_4 with 1 L distilled water. 0.1 M of H_2SO_4 was prepared by mixing 100 ml of 0.5 M H_2SO_4 with 1L distilled water.

4.6.1 Corrosion resistance in 3 % NaCl

The linear polarization curves obtained for Duplex and non- Duplex samples are shown in Figure 4.25. The curves were obtained by plotting the current density change depending on the applied potential in time. The corrosion potential was selected depending to the equilibrium potential, and ranged from -0.7 to -0.2 V.

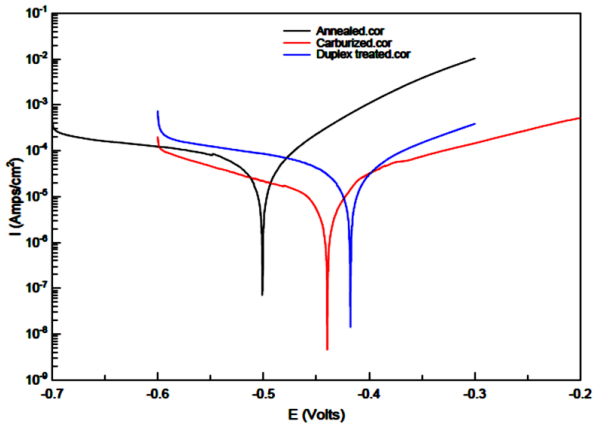

Figure 4.25: Polarization curves of Duplex and non- Duplex samples

As it can be observed from Figure 4.25, the corrosion potential of Duplex treated state is swept to more positive values, compared to the corrosion potential of carburized and annealed samples, which indicates that the Duplex treated samples are more nobler.The parameters obtained are presented in Table 4.10.

Tabelul 4.10: Parameter values of corrosion test in 3% NaCl [143]

Structural state	Annodic slope ba [mV]	Cathodic slope bc [mV]	Corrosion potential $-E_{corr}$ [V]	Current density i_{corr} [A/cm^2]
Annealed	84.79	318.46	0,500	$4.5952 *10^{-5}$
Carburized	186.01	407.70	0,439	$2.6608*10^{-5}$
Duplex state	146.6	414.15	0,417	$2.2642*10^{-5}$

Comparing the values of the current density, it can be observed a decrease from $4.5952 *10^{-5}$A/cm^2 (annealed state) to $2.264*10^{-5}$A/cm^2 (Duplex treated state). The shift of current density from higher to smaller values indicates improved corrosion behaviour. Hence, the Duplex treated sample has a higher corrosion resistance.

The amount of steel dissolving to form oxide can be calculated directly from measurements of the electric current generated by the anodic reaction:

$$Fe \rightarrow Fe^{2+} + 2e^-$$

and consumed by the cathodic reaction:

$$H_2O + ½\ O_2 + 2e^- \rightarrow 2OH^-$$

The corrosion rate can then be calculated using Faraday equation according to ASTM G 59 and G 102):

$$CR(\mu m/yr) = k \times \frac{icorr}{d} \times EW \quad (4.15)$$

- CR- corrosion rate in μm/year;
- k is a conversion factor (3.27×10^6 μm·g·A^{-1}·cm^{-1}·yr^{-1});
- i_{corr} is the corrosion current density in μA/cm;

- EW is the equivalent weight; The equivalent weight of an element or radical is equal to its atomic weight or formula weight divided by the valence it assumes in compounds;
- d is the density of EN 16MnCr5(7.85 g/cm³);

The equivalent weight of Iron can be calculated as follows

$$EW(Fe) = \frac{\text{Gram Atomic weight}}{\text{No. of electrons transferred}} = \frac{55.85}{2(Fe \rightarrow Fe^{2+} + 2e^{-})} = 27.9$$

According to equation 4.15, it was obtained o corrosion rate of 0.534 mm year^{-1} for annealed state, 0.309 mm year^{-1} for carburized state, and 0.262 mm year^{-1} for Duplex treated state. Figure 4.26 presents the corrosion rate for the three structural states. It can be observed a decrease of the corrosion rate of about 45 % for the Duplex treated sample compared to annealed state.

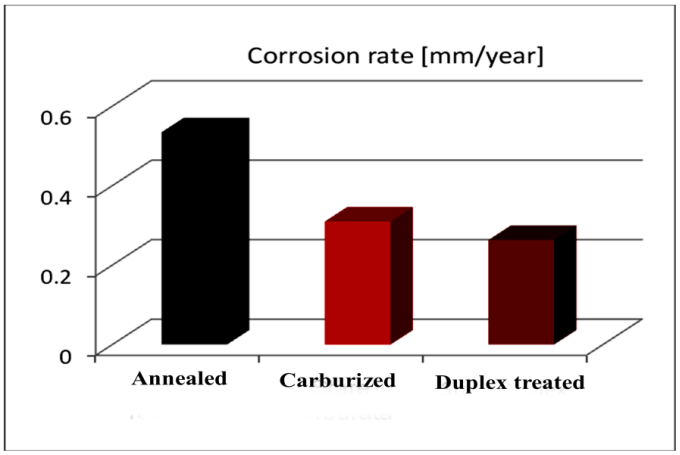

Figure 4.26: Corrosion rates

In order to identify the corrosion products, glancing incidence X-ray diffractions tests were performed. The tests parameters are presented in Table 4.11.

Table 4.11: Glancing incidence X-ray diffraction parameters

Intensity [mA]	Tension [KV]	Step size	Increment	Scan speed [°/min]	Scan angle [°]	Div.slit	
						Actual	Requested
30	40	0.04	0.04	5	20-90	0.100	0.100

The patterns for each structural state are presented in Figure 4.27.

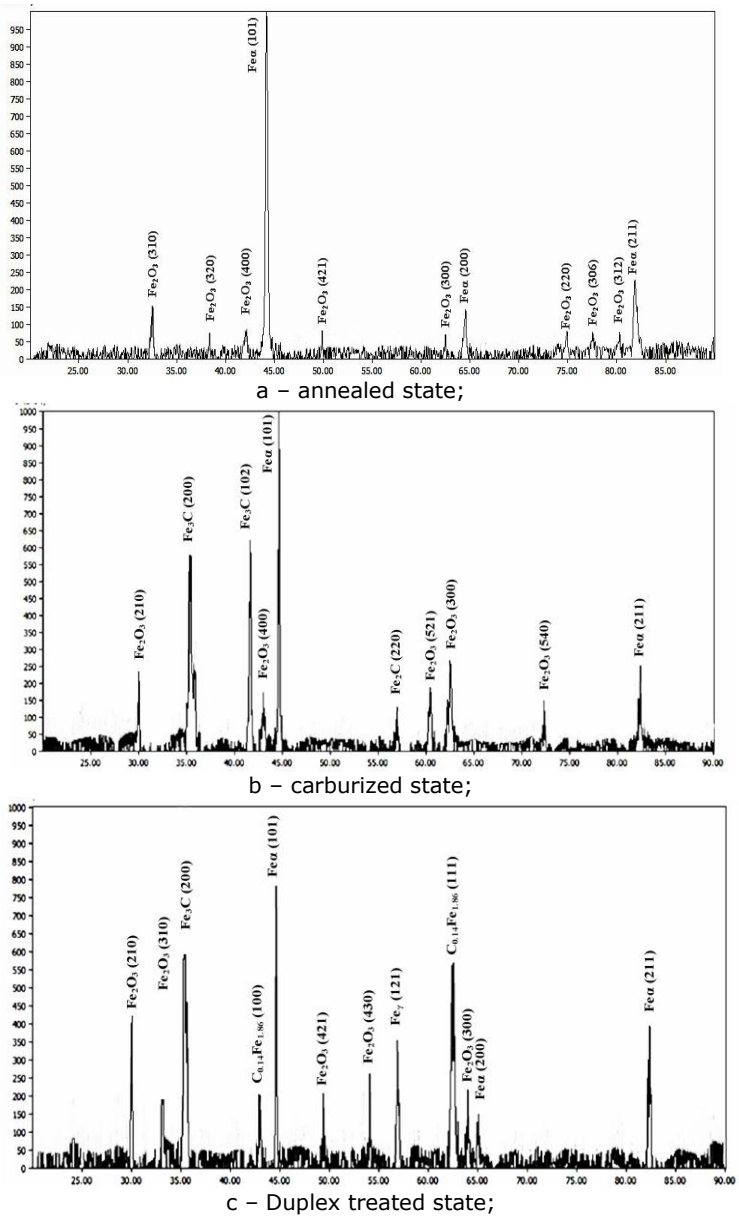

Figure 4.27: Glancing incidence X-ray diffractions patterns: a – annealed state; b – carburized state; c - Duplex treated state;

For the annealed state, the phase analysis reveals only two crystallographic phases: Fe-α and Fe_2O_3 (hematite). Reflection of Fe-α produce 3 peaks, that can be indexed as (101), (200) and (211), which occur at 2θ values of approximately 44.674º, 65.023° and 82.335° respectively. Hematite reflection produce 8 peaks, that can be indexed as (310), (320), (400), (421), (300), (220), (306) and (312) and occur at 2θ values of approximately 33.883°, 38.848, 43.285°, 50.008°, 63.966°, 75.409°, 77.662° and 80.613 (Figure 4.27 a).

For the carburized samples, glancing incidence X-ray diffraction analyzes reveals the presence of iron and iron carbide phases, cementite and hematite. Reflections of orthorhombic Fe_2C phase produce 1 peak that can be indexed as (220), and occurs at 2θ values of approximately 57.955. Hematite reflection produce 5 peaks, that can be indexed as (210), (400), (521), (300) and (540), which occur at 2θ values of approximately 30.010°, 43.285°, 60.687°, 63.966° and 72.403°. Fe-α reflections produce 2 peaks, indexed as (101), (211), which occur at 2θ values of approximately 44.674º and 82.335° respectively (Figure 4.27 b). Reflections of Fe_3C produce 2 peaks, that can be indexed as (200) and (102) and occurs at 2θ of 35.234° and 41.234°.

Glancing incidence analyze showed the presence of Fe-α, $C_{0.14}Fe_{1.86}$, Fe_2O_3, Fe_γ phases in Duplex treated samples. Reflection of Fe-α produce 3 peaks, that can be indexed as (101), (200) and (211), which occur at 2θ values of approximately 44.674º, 65.023° and 82.335° respectively. $C_{0.14}Fe_{1.86}$ reflections produce 2 peaks, indexed as (100) and (111), and occur at 42.720 and 63.132° respectively. Reflections of Fe_γ produce 1 peak indexed as (121) at 57.123°. Hematite reflection produce 5 peaks, that can be indexed as (210), (310), (421), (430) and (300), which occur at 2θ values of approximately 30.010°, 33.883°, 50.008°, 53.734°, and 54.926° and 63.966° (Figure 4.27 c).

The surfaces of the corroded samples were analyzed by image acquisition and by energy dispersive X-ray spectrometry (EDX). Figure 4.28 presents SEM images of corroded surfaces of Duplex and non- Duplex samples.

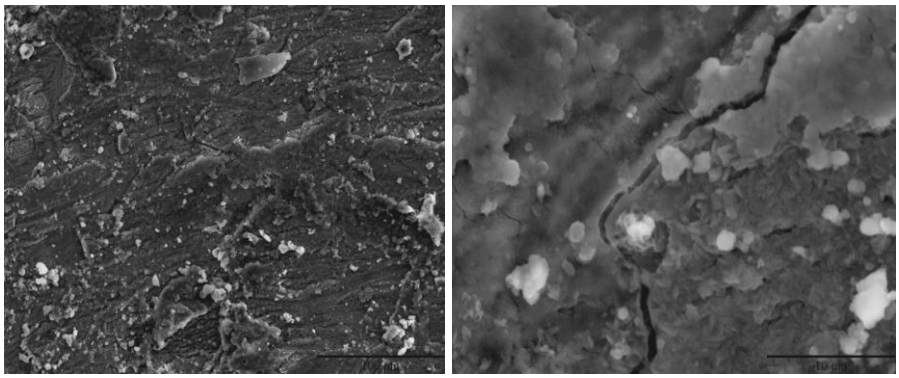

a – annealed state;

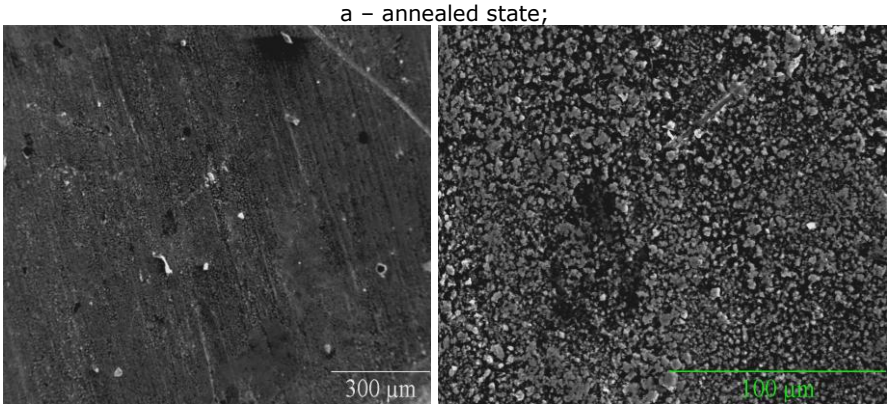

b – carburized state;

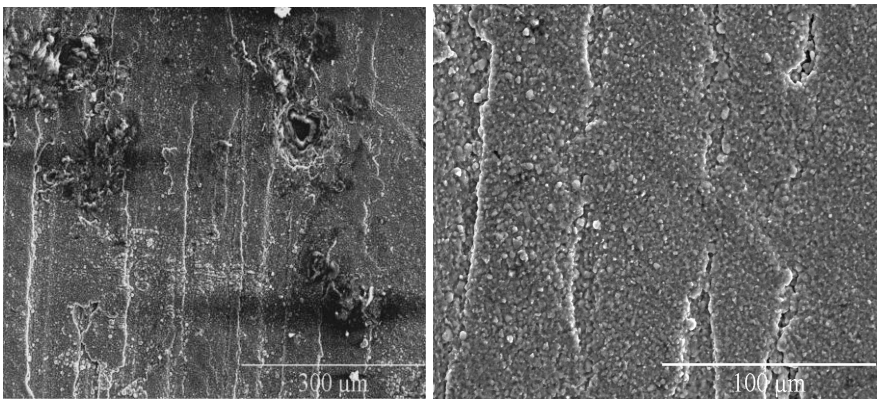

c – Duplex treated state;

Figure 4.28: SEM imagines of corroded surfaces:
a – annealed state; b - carburized state; c- Duplex treated state

Figure 4.28a shows corrosion pits of various sizes on the corroded surface of the untreated and carburized samples. In comparison, the corroded surface of the duplex treated specimens appears to be more likely as general form, although corrosion pits can be also observed, but the amount of the pits is much smaller. In this sense, it may be concluded that the Duplex treatment has improved the corrosion resistance of the EN 16MnCr5 in NaCl solution.

In order to determine the elemental composition of the corroded samples, EDX investigations were carried out, Figure 4.29.

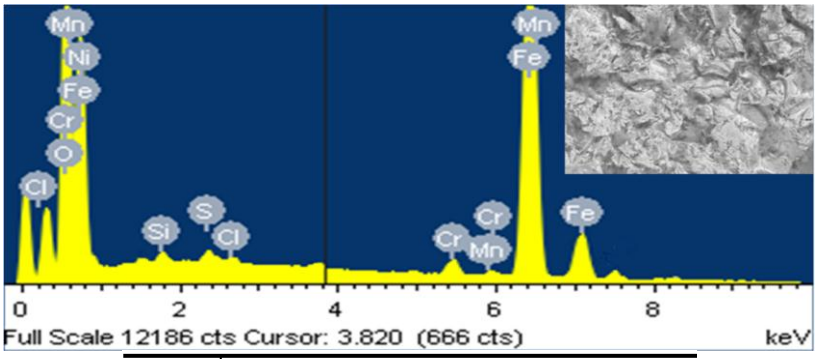

Element	App Conc.	Intensity Corrn.	Weight%	Weight% Sigma	Atomic%
C K	1.92	0.5928	9.59	0.23	24.99
O K	8.73	1.5183	17.06	0.21	33.37
Si K	0.10	0.8390	0.35	0.02	0.39
S K	0.08	0.9757	0.25	0.03	0.25
Cl K	0.09	0.8701	0.29	0.03	0.26
Cr K	0.57	1.0955	1.54	0.05	0.93
Mn K	0.17	0.9091	0.55	0.06	0.31
Fe K	20.41	0.9250	65.47	0.27	36.68
Totals			100.00		

a – annealed state;

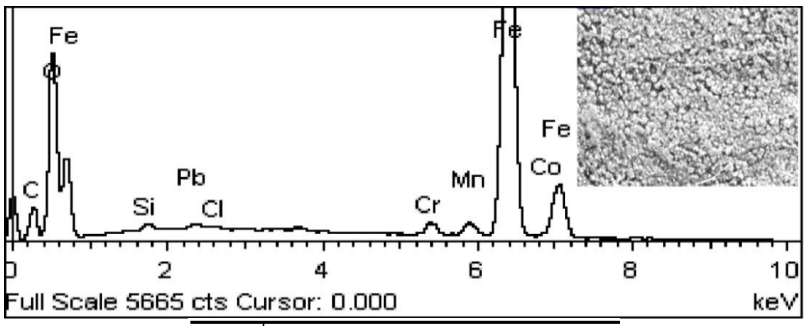

Element	App Conc.	Intensity Corrn.	Weight%	Weight% Sigma	Atomic%
C K	3.53	0.4729	7.66	0.50	20.52
O K	23.11	1.2979	18.24	0.35	36.70
Si K	0.31	0.6703	0.48	0.04	0.55
Cl K	0.12	0.8030	0.16	0.04	0.14
Cr K	1.36	1.1481	1.21	0.05	0.75
Mn K	1.58	0.9211	1.76	0.08	1.03
Fe K	63.23	0.9361	69.17	0.50	39.86
Co K	0.56	0.9156	0.62	0.12	0.34
Pb M	0.54	0.7875	0.70	0.12	0.11
Totals			100.00		

b – carburized state;

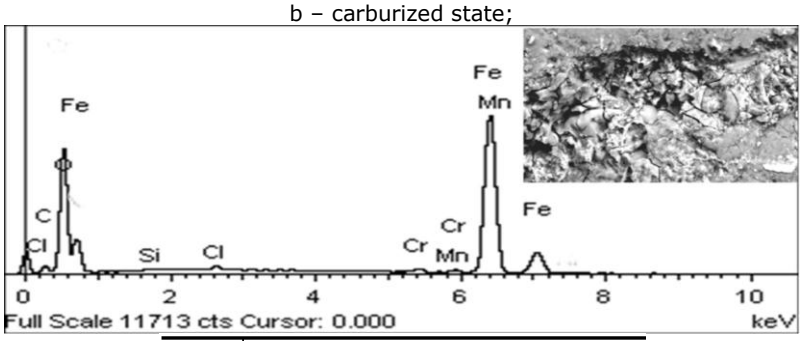

Element	App Conc.	Intensity Corrn.	Weight%	Weight% Sigma	Atomic%
C K	0.96	0.4623	2.71	0.54	7.15
O K	30.66	1.5123	26.36	0.39	52.28
Si K	0.09	0.6652	0.17	0.04	0.19
Cl K	0.35	0.8053	0.57	0.05	0.51
Cr K	0.61	1.1502	0.69	0.05	0.42
Mn K	0.48	0.9173	0.68	0.07	0.39
Fe K	48.47	0.9328	67.55	0.52	38.37
Totals			100.00		

c – Duplex treated state;

Figure 4.29: EDX analyze: a – annealed state; b – carburized state; c - Duplex treated state;

As it can be observed from Figure 4.29, the corroded surface of all the samples contains nearly all the elements of EN 16MnCr5 (Mn, Cr, Si, etc) and additionally O indicating that nearly all elements participate in the corrosion layer formation. Very clearly, the corroded surface is much richer in Fe while poorer in every metallic element. Another obvious aspect is that the surface contains O in a significant amount. Furthermore, clorium, Cl, which is present in the solution (NaCl), is also present in the corroded surface, which favors the formation of pits. Due to the paint used to protect the surface which was not tested, Pb and Co are other elements present in EDX spectrum (Figure 4.29 b). The elements distribution for each sample is presented in Figure 4.30.

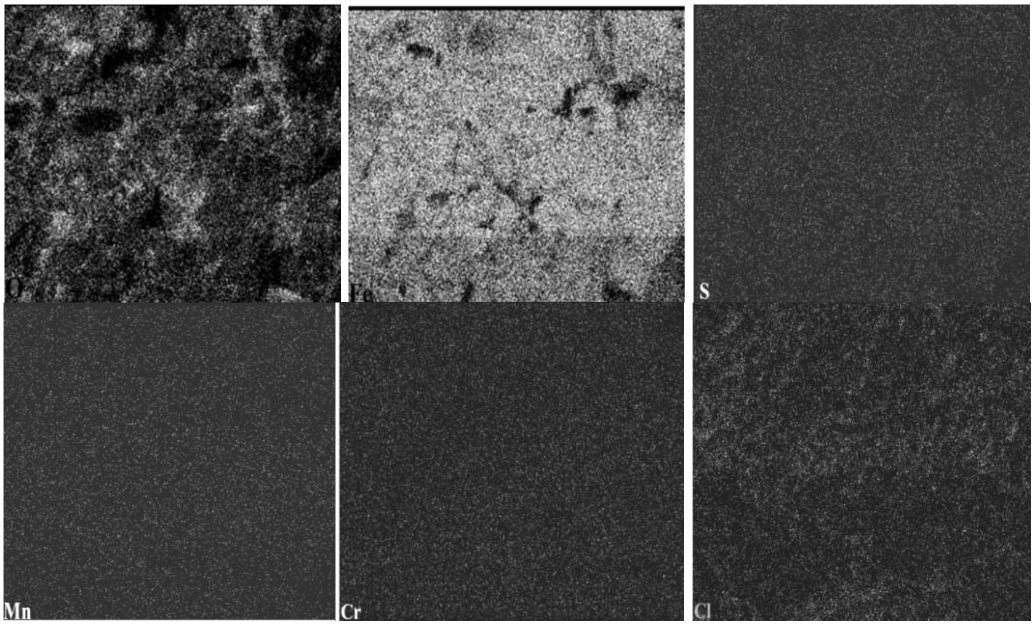

a – annealed state;

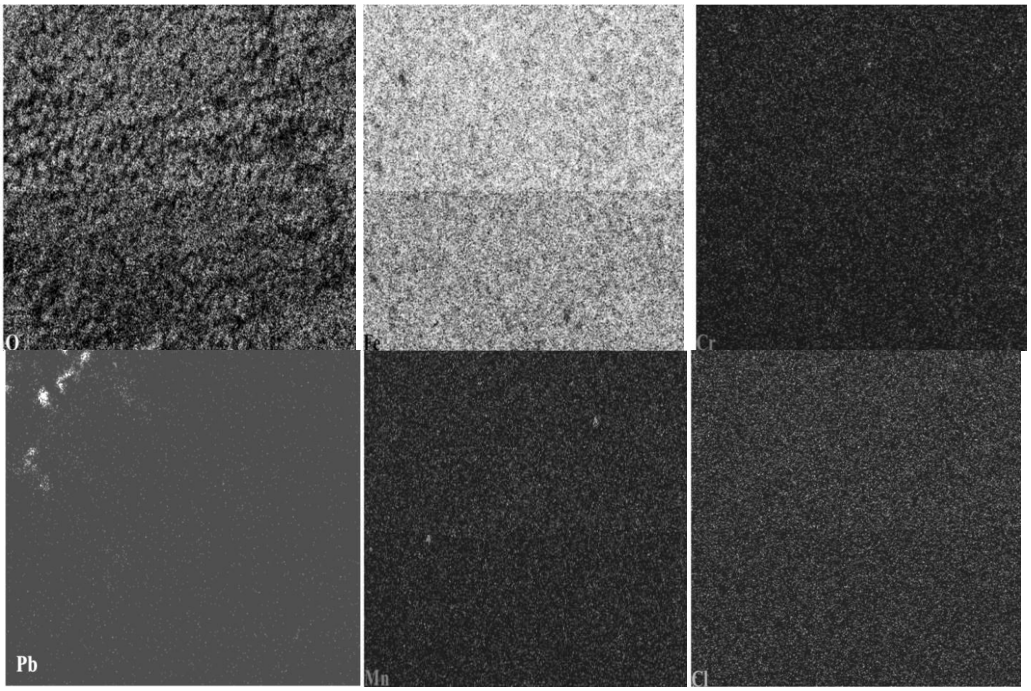

b – carburized state;

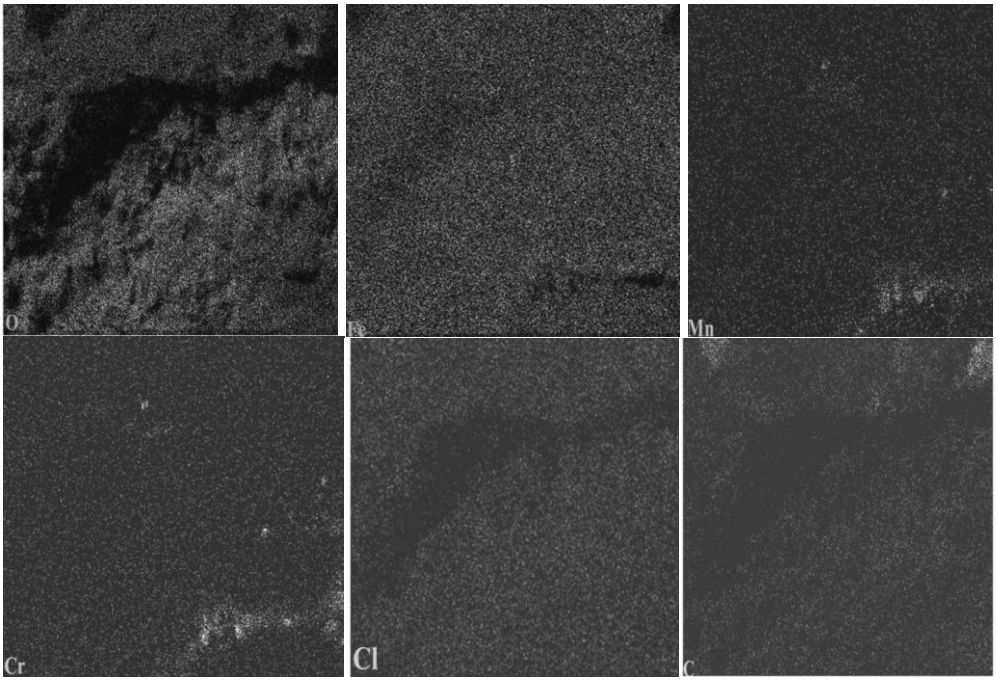

c – Duplex treated state;

Figure 4.30: EDX element distribution: a – annealed state; b – carburized state; c - Duplex treated state

From EDX map, it can be observed that O is uniformly distributed on the corroded surface of each structural state.

4.6.2. Corrosion behaviour in 0.5 M H_2SO_4

The influence of Duplex treatment on corrosion behaviour was also investigated in more agressive solution, namely 0.5 M H_2SO_4. In this case, the potential ranged from -0.7 to -0.3. The linear polarization curves obtained for Duplex and non- Duplex samples presented in Figure 4.31.

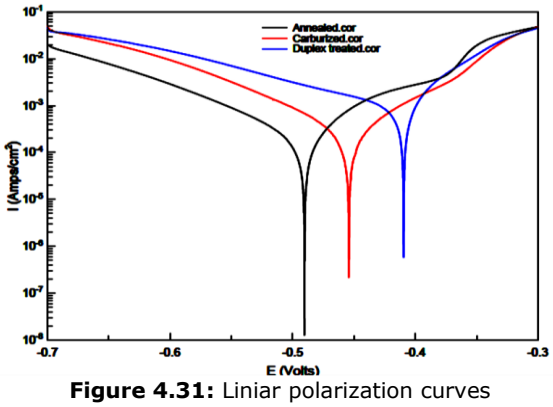

Figure 4.31: Liniar polarization curves

As it can be observed from figure 4.31, the corrosion potential of Duplex treated state is swept to more positive values, compared to the corrosion potential of carburized and annealed samples, which indicates that the Duplex treated samples are nobler. The corrosion parameters obtained are presented in Table 4.12.

Table 4.12: Parameter values of corrosion test in 0.5 M H_2SO_4

Structural state	Annodic slope, ba [mV]	Cathodic slope, bc [mV]	Corrosion potential, $-E_{corr}$ [V]	Polarization resistance [Ohm/cm^2]	Current density i_{corr} [A/cm^2]
Annealed	65.619	225.98	0,490	35.55	$4.7977*10^{-4}$
Carburized	68.453	68.607	0.452	67.25	$3.1232*10^{-4}$
Duplex state	85.342	113.01	0.409	84.91	$2.2823*10^{-4}$

From Table 4.12 it can be observed that the current density decreases from $4.7977*10^{-4}$A/cm^2 (annealed state) to $2.2823*10^{-4}$A/cm^2 (Duplex treated state). The shift of current density from higher to smaller values indicates improved corrosion behaviour. Hence, the Duplex treated sample has a higher corrosion resistance. Also, the polarization resistance increased from 35.55 Ohm/cm^2 (annealed state) to 84.91 Ohm/cm^2 (Duplex state), which indicates a better corrosion behaviour of Duplex treated samples.

According to equation 4.15, it was obtained o corrosion rate of 5.58 mm year^{-1} for annealed state), 3.98 mm year^{-1} for carburized state, and 3.24 mm year^{-1} for Duplex treated state. Figure 4.32 presents the corrosion rate of the three structural states. It can be observed a decrease of the corrosion rate of about 42 % for the Duplex treated state, compared to untreated state.

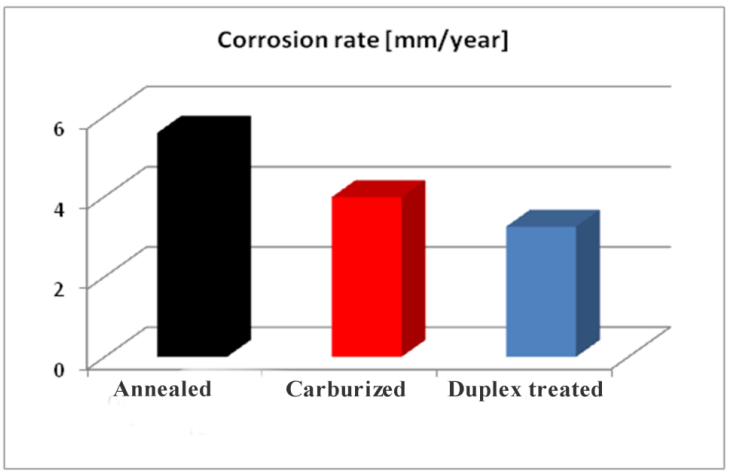

Figure 4.32: Corrosion rates of each structural state

In order to identify the corrosion products, glancing incidence X-ray diffractions tests were performed. The tests parameters are presented in Table 4.11. The patterns for each structural state are presented in Figure 4.33.

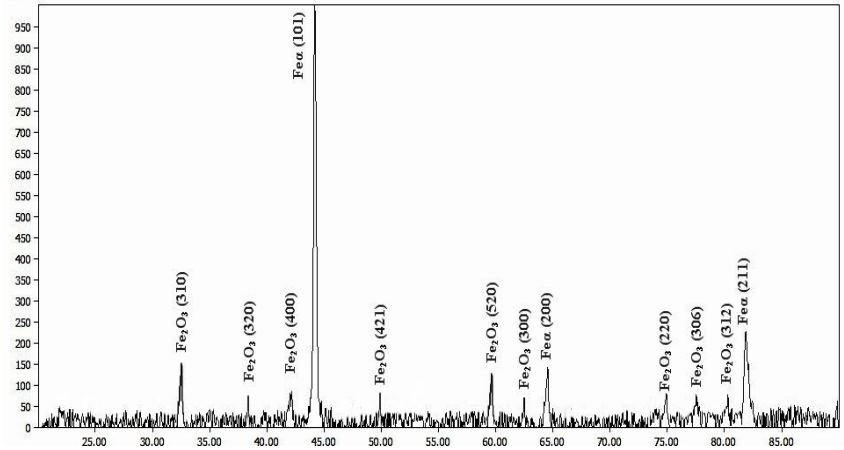

a – annealed state;

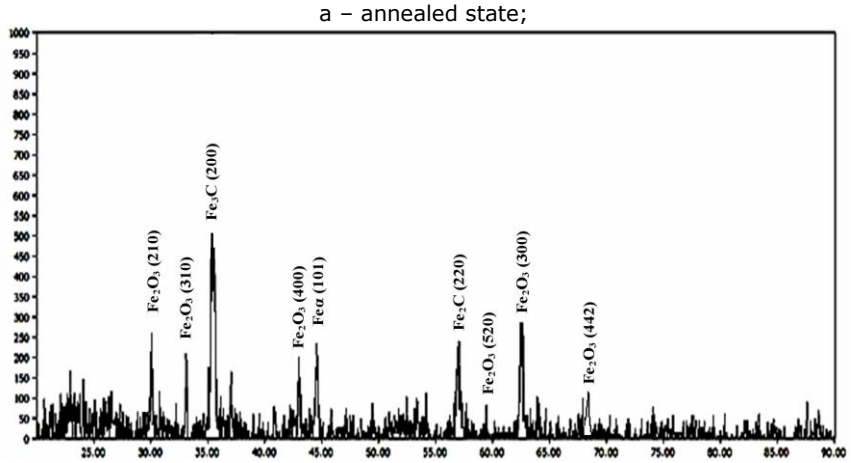

b – carburized state;

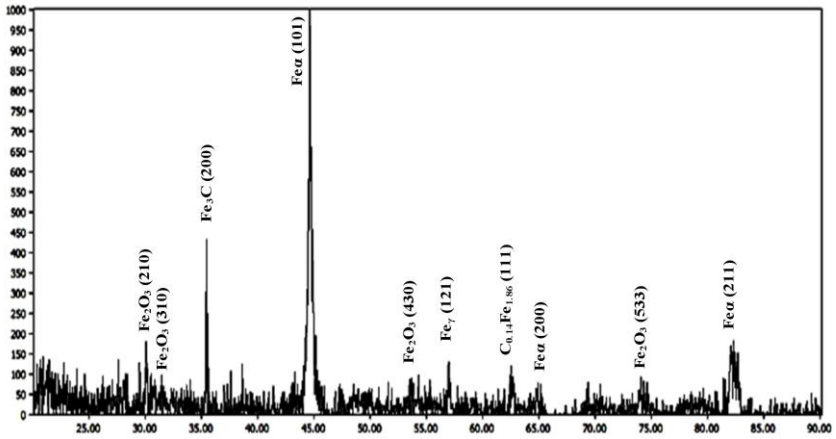

c – Duplex treated state;

Figure 4.33: Glancing incidence patterns: a – annealed state; b – carburized state; c - Duplex treated state;

For the annealed state, the phase analysis reveals only two crystallographic phases: Fe-α and Fe_2O_3 (hematite). Reflection of Fe-α produce 3 peaks, that can be indexed as (101), (200) and (211), which occur at 2θ values of approximately 44.674º, 65.023° and 82.335° respectively. Hematite reflection produce 9 peaks, that can be indexed as (310), (320), (400), (421), (520), (300), (220), (306) and (312) and occur at 2θ values of approximately 33.883°, 38.848, 43.285°, 50.008°, 59.570°, 63.966°, 75.409°, 77.662° and 80.613 (Figure 4.33 a).

For the carburized samples, glancing incidence X-ray diffraction analyzes reveals the presence of iron and iron carbide phases, cementite and hematite. Reflections of orthorhombic Fe_2C phase produce 1 peak that can be indexed as (220), and occurs at 2θ values of approximately 57.955. Hematite reflection produce 6 peaks, that can be indexed as (210), (310), (400), (520), (300) and (442), which occur at 2θ values of approximately 30.010°, 33.883°, 43.285°, 59.570°, 63.966° and 67.203°. Fe-α reflections produce 1 peak, indexed as (101), which occur at 2θ values of approximately 44.674º (Figure 4.33 b). Reflections of orthorhombic Fe_3C (cementite) phase produce 1 peak, that can be indexed as (200) and occurs at 2θ of 35.234°.

Glancing incidence analyze showed the presence of Fe-α, $C_{0.14}Fe_{1.86}$, Fe_2O_3, Fe_γ phases in Duplex treated samples. Reflection of Fe-α produce 3 peaks, that can be indexed as (101), (200) and (211), which occur at 2θ values of approximately 44.674º, 65.023° and 82.335° respectively. $C_{0.14}Fe_{1.86}$ reflection produce 1 peak indexed as (111) at 63.132°. Reflections of Fe_γ produce 1 peak indexed as (121) at 57.123°. Hematite reflection produce 4 peaks, that can be indexed as (210), (310), (430) and (533), which occur at 2θ values of approximately 30.010°, 33.883°, 54.926°, 53.734°, and 64.911° and 74.347.121° (Figure 4.33 c). Reflections of orthorhombic Fe_3C (cementite) phase produce 1 peak, that can be indexed as (200) and occurs at 2θ of 35.234°.

The surfaces of the corroded samples were analyzed by SEM and by energy dispersive X-ray spectrometry (EDX). Figure 4.34 presents SEM images of corroded surfaces of Duplex and non- Duplex samples.

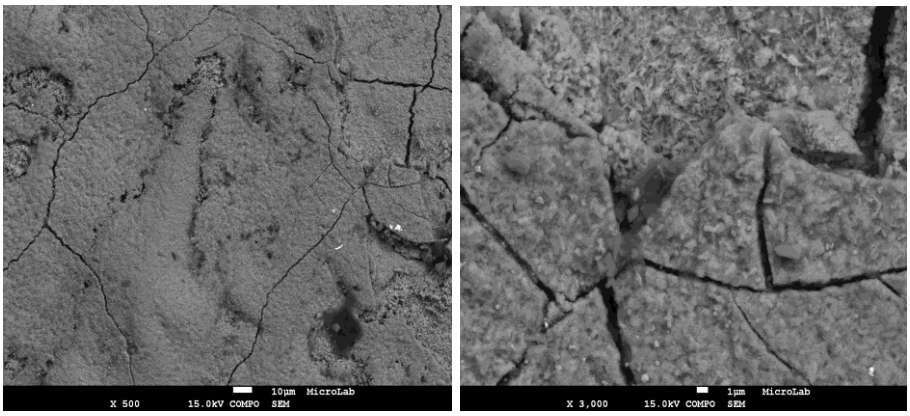

a – annealed state;

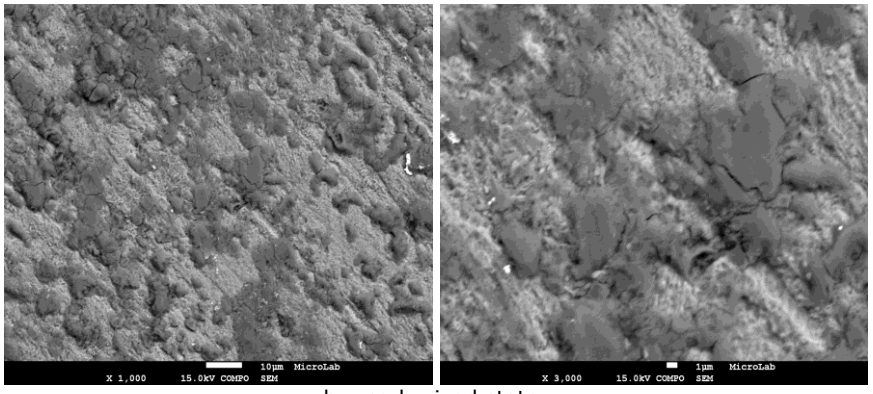

b – carburized state;

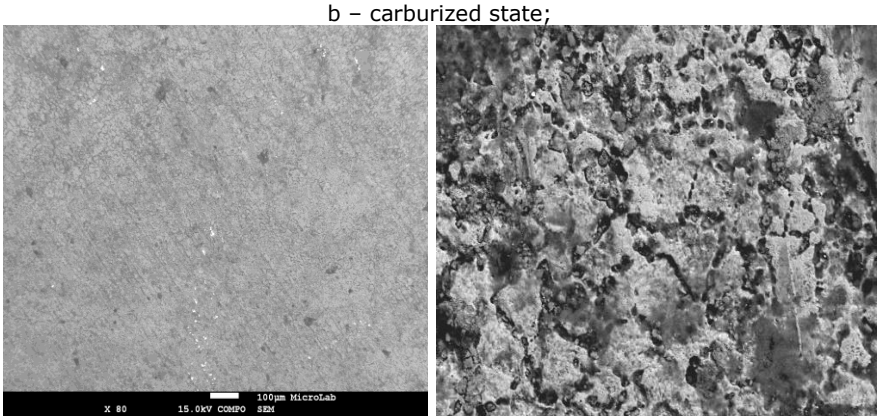

c – Duplex treated;

Figure 4.34: SEM images: a – annealed; b – carburized; c- Duplex treated

The tendency towards pitting corrosion can also be observed in 0.5 M H_2SO_4 polarization tests. But in this case, the surfaces of each structural state are more damaged, due to the solution's aggressivety. The micro-cracks can be observed all over the surface, especially for the annealed samples, which is damaged, the most.

EDX analysis for each structural state is shown in figure 4.35.

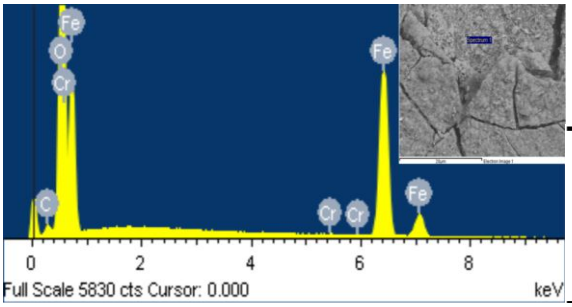

Element	App Conc.	Intensity Corrn.	Weight%	Weight% Sigma	Atomic%
C K	0.66	0.5977	3.56	0.12	9.55
O K	13.34	1.8087	26.93	0.15	48.19
Cr K	0.10	1.1303	0.28	0.03	0.17
Mn K	0.10	0.9118	0.37	0.05	0.22
Fe K	20.07	0.9253	70.36	0.19	40.61
Totals			100.00		

a – annealed state;

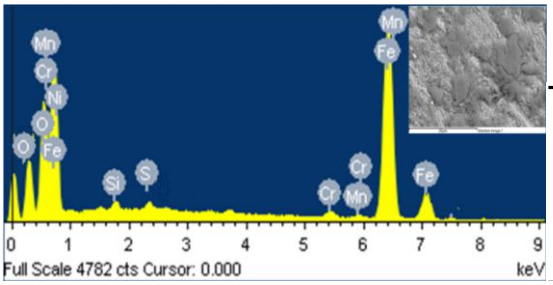

Element	App Conc.	Intensity Corrn.	Weight%	Weight% Sigma	Atomic%
O K	10.45	1.8727	17.61	0.17	42.35
Si K	0.07	0.8266	0.25	0.03	0.34
S K	0.34	0.9801	1.10	0.03	1.32
Cl K	0.07	0.8785	0.26	0.03	0.28
Cr K	0.40	1.1567	1.09	0.04	0.81
Mn K	0.34	0.9335	1.16	0.06	0.81
Fe K	23.63	0.9497	78.54	0.18	54.10
Totals			100.00		

b- carburized state;

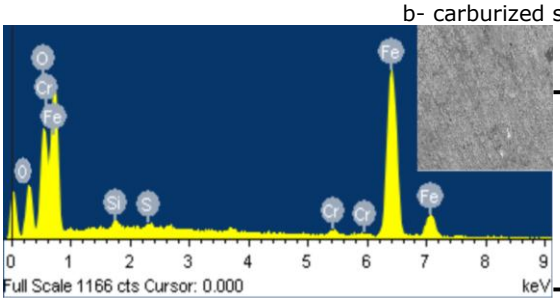

Element	App Conc.	Intensity Corrn.	Weight%	Weight% Sigma	Atomic%
O K	5.63	1.8461	12.05	0.63	31.97
Si K	0.19	0.8216	0.89	0.13	1.35
S K	0.17	0.9788	0.69	0.13	0.92
Cr K	0.53	1.1775	1.76	0.20	1.44
Fe K	20.62	0.9630	84.60	0.65	64.32
Totals			100.00		

c- Duplex treated state;

Figure 4.35: EDX analyze: a – annealed state; b- carburized state; c- Duplex treated state;

As aspected, EDX analyze reveales the presence of Fe and O and of other elements also, such as Mn, Cr, Si, and S, due to the chemical composition of EN 16MnCr5. The corroded surface is much richer in Fe compared to other elements. The surface contains O in a significant amount. The elements distribution for each sample is presented in Figure 4.36.

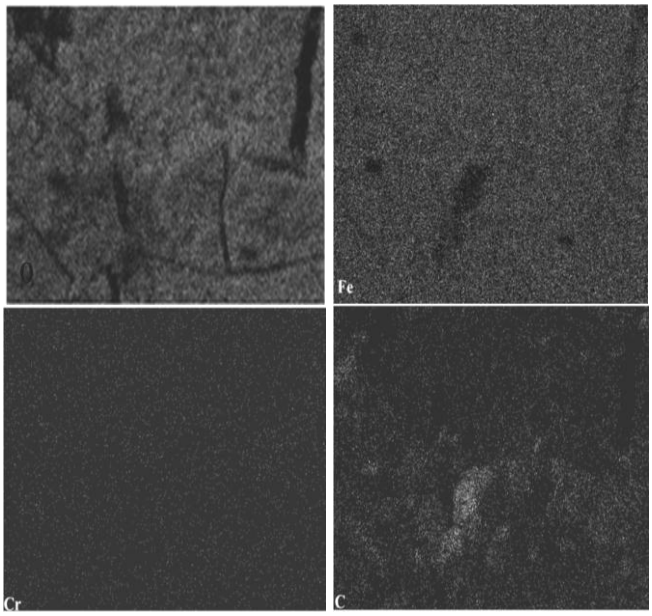

a- annealed state;

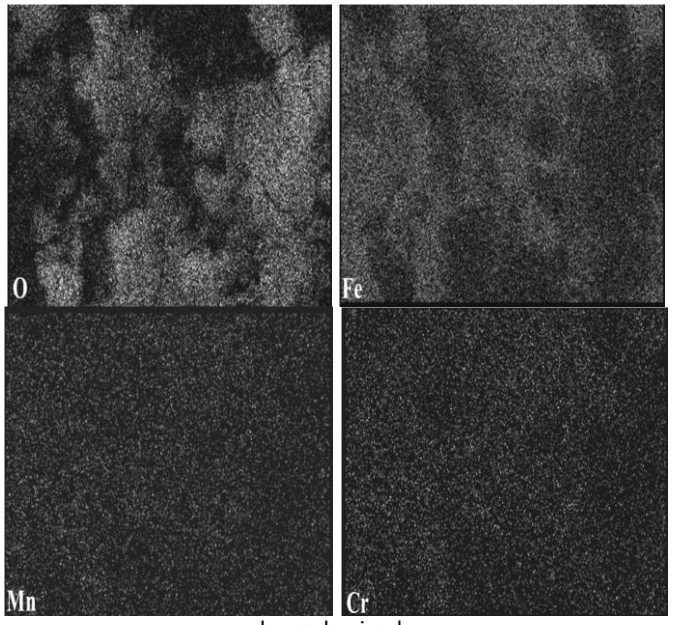

b- carburized;

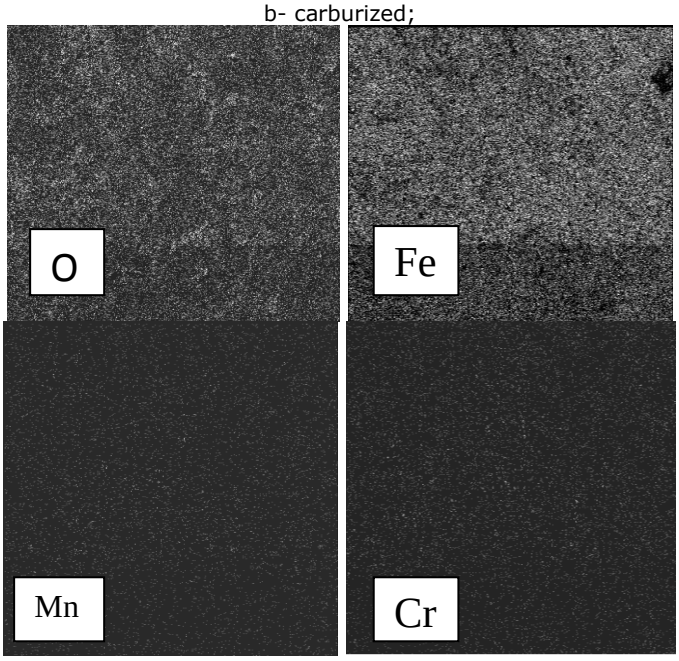

c – Duplex treated state;

Figure 4.36: EDX element distribution: a – annealed state; b – carburized state; c - Duplex treated state;

In can be clearly observed that O is uniformly distributed in the corroded surfaces.

4.6.3 Corrosion behaviour in 0.1 M H_2SO_4

Due to the fact that the H_2SO_4 concentration was to high, leading to a severe damage of the surfaces and high corrosion rates, the untreated and treated samples were tested in 0.1 M H_2SO_4. The corrosion potential renged from -0.7 to -0.3 V. The linear polarization curves obtained are presented in Figure 4.37.

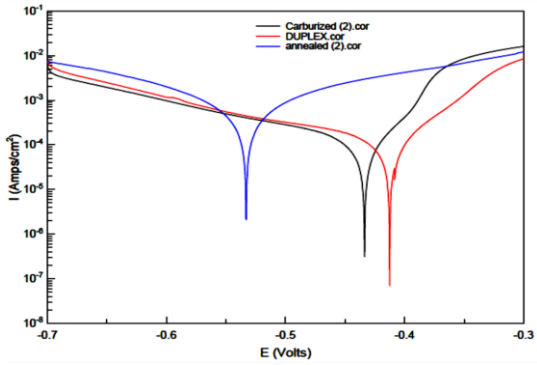

Figure 4.37: Linear polarization curves in 0.1 M H_2SO_4

As it can be observed from figure 4.37, the corrosion potential of Duplex treated state is swept to more positive values, compared to the corrosion potential of carburized and annealed samples, which indicates that the Duplex treated samples are nobler. The parameters obtained for corrosion tests in 0.1 M H_2SO_4 are presented in Table 4.13.

Tabelul 4.13: Parameter values of corrosion test in 0.1 M H_2SO_4

Structural state	Annodic slope, ba [mV]	Cathodic slope, bc [mV]	Corrosion potential, -E_{corr} [V]	Polarization resistance, R_p [Ohm/cm^2]	Current density i_{corr} [A/cm^2]
Annealed	246.79	219.81	0,53384	38.29	$3.782*10^{-4}$
Carburized	216.22	194.82	0,43359	136.66	$2.912*10^{-4}$
Duplex state	60.82	226.37	0,41261	141.48	$1.669*10^{-4}$

From Table 4.13, it can be observed that the current density decreases from $3.782*10^{-4}$A/cm^2 (annealed state) to $1.669*10^{-4}$A/cm^2 (Duplex treated state). The shift of current density from higher to smaller values indicates improved corrosion behaviour. Hence, the Duplex treated sample has a higher corrosion resistance. Also, the polarization resistance increased from 38.29 Ohm/cm^2 (annealed state) to 141.48 Ohm/cm^2 (Duplex state), which indicates a better corrosion behaviour of Duplex treated samples.

According to equation 4.11, it was obtained a corrosion rate of 4.39 mm year^{-1} for annealed state, 3.50 mm year^{-1} for carburized state, and 1.94 mm year^{-1} for Duplex treated state. Figure 4.38 presents the corrosion rate for the three structural states. It can be observed an increase of Duplex treated sample corrosion rate of about 75%, compared to annealed sample.

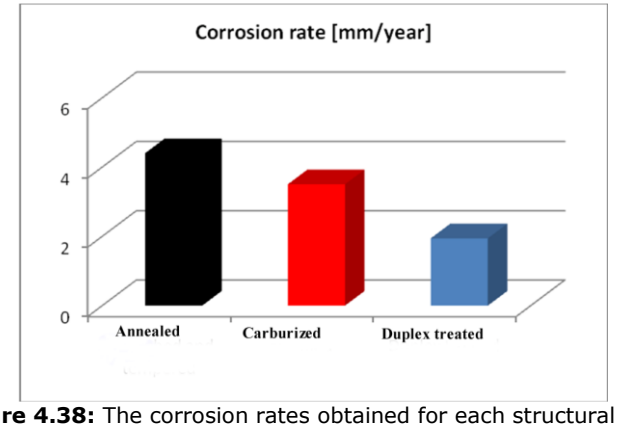

Figure 4.38: The corrosion rates obtained for each structural state

In order to identify the corrosion products, glancing incidence X-ray diffractions tests were performed. The patterns for each structural state are presented in Figure 4.39.

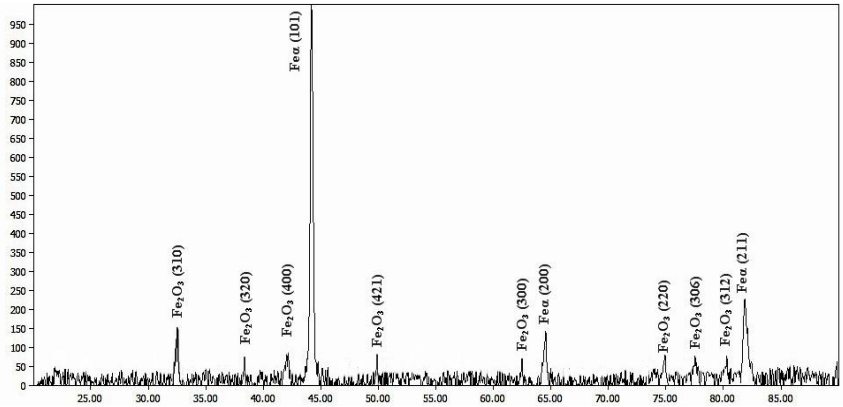

a- annealed state;

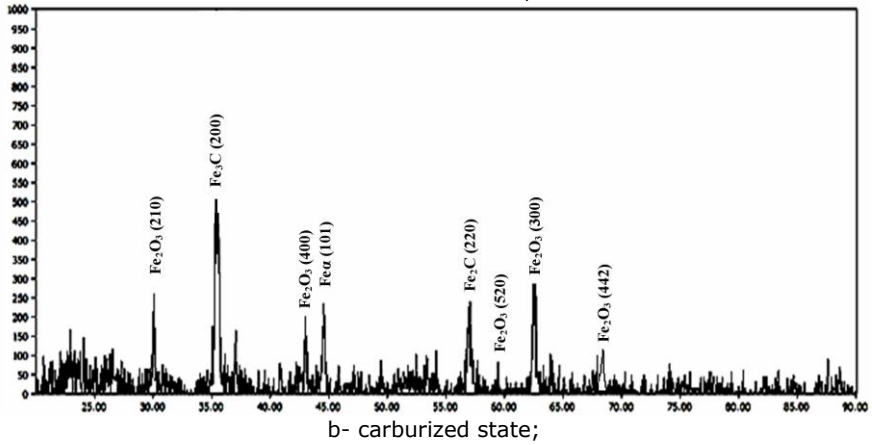

b- carburized state;

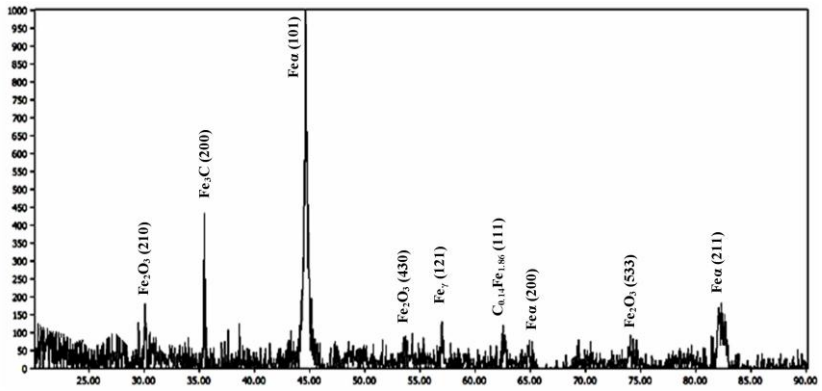

c- Duplex state;

Figure 4.39: Glancing incidence patterns: a – annealed state; b – carburized state; c - Duplex treated state;

For the annealed state, the phase analysis reveals only two crystallographic phases: Fe-α and Fe_2O_3 (hematite). Reflection of Fe-α produce 3 peaks, that can be indexed as (101), (200) and (211), which occur at 2θ values of approximately 44.674º, 65.023° and 82.335° respectively. Hematite reflection produce 8 peaks, that can be indexed as (310), (320), (400), (421), (300), (220), (306) and (312) and occur at 2θ values of approximately 33.883°, 38.848, 43.285°, 50.008°, 63.966°, 75.409°, 77.662° and 80.613 (Figure 4.39 a).

For the carburized samples, glancing incidence X-ray diffraction analyzes reveals the presence of iron phases, cementite and hematite. Reflections of orthorhombic Fe_2C phase produce 1 peak that can be indexed as (220), and occurs at 2θ values of approximately 57.955. Hematite reflection produce 5 peaks, that can be indexed as (210), (400), (520), (300) and (442), which occur at 2θ values of approximately 30.010°, 43.285°, 59.570°, 63.966°, and 67.203°. Fe-α reflections produce 1 peak, indexed as (101), which occur at 2θ values of approximately 44.674º (Figure 4.39 b). Reflections of orthorhombic Fe_3C (cementite) phase produce 1peak, that can be indexed as (200) and occur at 2θ of 35.234°.

Glancing incidence analyze showed the presence of Fe-α, $C_{0.14}Fe_{1.86}$, Fe_2O_3, Fe_γ phases in Duplex treated samples. Reflection of Fe-α produce 3 peaks, that can be indexed as (101), (200) and (211), which occur at 2θ values of approximately 44.674º, 65.023° and 82.335° respectively. $C_{0.14}Fe_{1.86}$ reflection produce 1 peak indexed as (111) at 63.132°. Reflections of Fe_γ produce 1 peak indexed as (121) at 57.123°. Hematite reflection produce 3 peaks, that can be indexed as (210), (430) and (533), which occur at 2θ values of approximately 30.010°, 54.926° and 74.234° (Figure 4.39 c).

The surfaces of the corroded samples were analyzed by SEM and by energy dispersive X-ray spectrometry (EDX). Figure 4.40 presents SEM images of corroded surfaces of Duplex and non- Duplex samples.

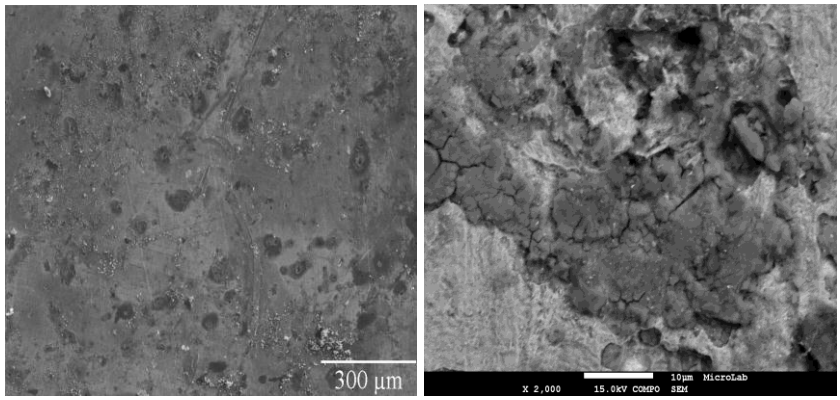

a- annealed state;

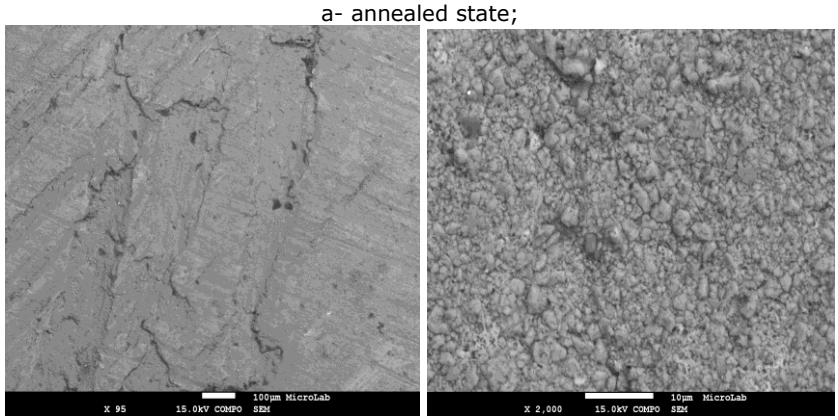

b- carburized state;

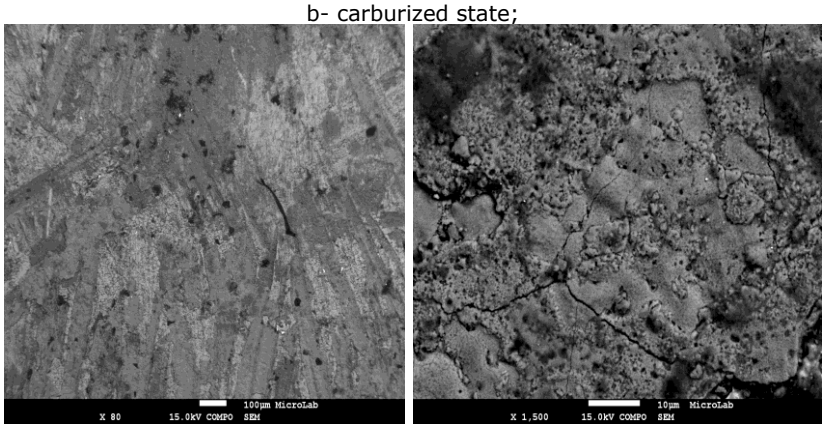

c- Duplex treated;

Figure 4.40: SEM images: a – annealed; b – carburized; c- Duplex treated

The tendency towards pitting corrosion can be observed on the samples surfaces. Typical pits are presented on the corroded samples surface and micro-cracks. It can be also observed that the pits present on the annealed surface are deeper and in a higher quantity compared with carburized and Duplex treated samples. Also, the micro-cracks can be observed on the surface of all structural states.

In order to determine the elemental composition of the corroded surface, EDX investigations were carried out. The spectrums corresponding to each structural state are presented in Figure 4.41.

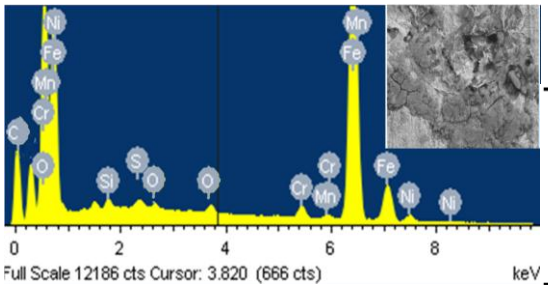

Element	App Conc.	Intensity Corrn.	Weight%	Weight% Sigma	Atomic%
C K	1.92	0.5928	9.59	0.23	24.99
O K	8.73	1.5183	22.06	0.21	33.37
Si K	0.10	0.8390	0.35	0.02	0.39
S K	0.08	0.9757	0.25	0.03	0.25
Cr K	0.57	1.0955	1.54	0.05	0.93
Mn K	0.17	0.9091	0.55	0.06	0.31
Fe K	20.41	0.9250	65.47	0.27	36.68
Ni K	0.79	0.8825	2.66	0.10	1.42
Cu K	0.14	0.8475	0.50	0.11	0.25
Totals			100.00		

a- annealed state;

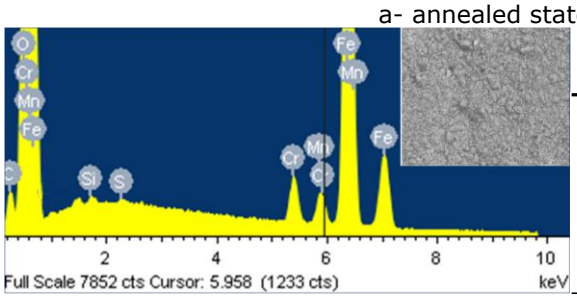

Element	App Conc.	Intensity Corrn.	Weight%	Weight% Sigma	Atomic%
C K	0.57	0.5817	2.85	0.11	8.70
O K	10.36	1.8130	18.67	0.16	38.16
Si K	0.05	0.8279	0.19	0.02	0.24
S K	0.03	0.9787	0.10	0.02	0.11
Cr K	1.24	1.1340	3.19	0.05	2.24
Mn K	0.89	0.9319	2.79	0.06	1.86
Fe K	23.54	0.9440	74.71	0.29	47.69
Totals			100.00		

b- carburized state;

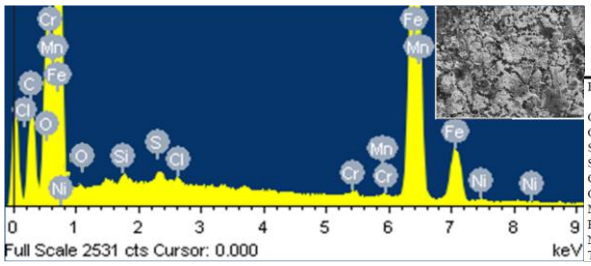

Element	App Conc.	Intensity Corrn.	Weight%	Weight% Sigma	Atomic%
C K	2.23	0.5774	11.30	0.75	31.16
O K	5.20	1.4663	10.36	0.20	21.45
Si K	0.13	0.8370	0.44	0.02	0.52
S K	0.14	0.9786	0.41	0.03	0.42
Cl K	0.10	0.8753	0.35	0.03	0.32
Cr K	0.31	1.1305	0.81	0.04	0.52
Mn K	0.15	0.9182	0.46	0.05	0.28
Fe K	23.47	0.9345	76.33	0.65	43.49
Ni K	0.23	0.8879	0.75	0.08	0.43
Totals			100.00		

c- Duplex treated state;

Figure 4.41: EDX spectrums: a- annealed; b- carburized; c- Duplex treated;

The corroded surface of all the samples contains nearly all the elements of EN 16MnCr5 (Fe, Mn, Cr, S, Si, etc) and additionally O. The surface is much richer in Fe, while poorer in every metallic element. Another obvious aspect is that the surface contains O in a significant amount. The elements distribution for each sample is presented in Figure 4.42.

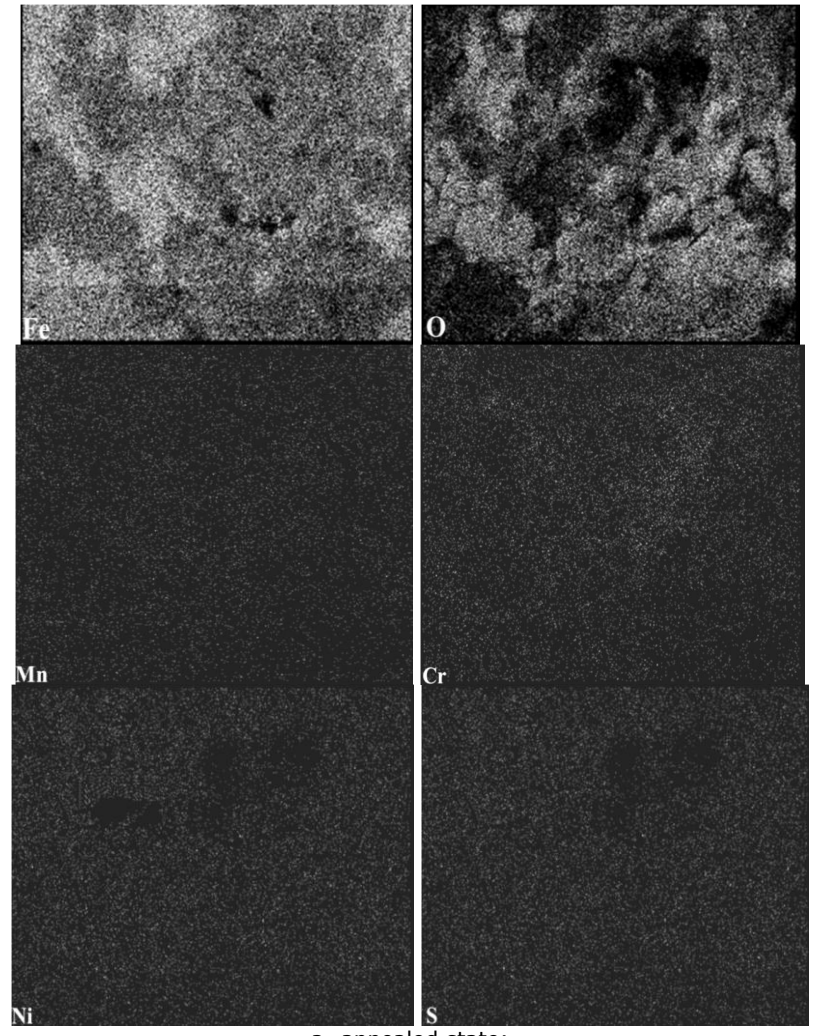

a- annealed state;

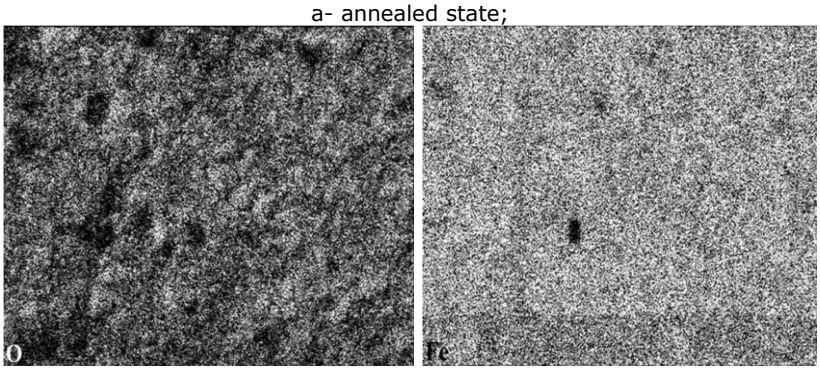

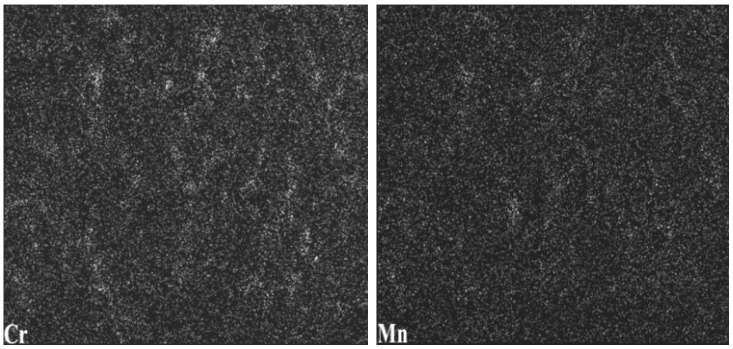

b - carburized;

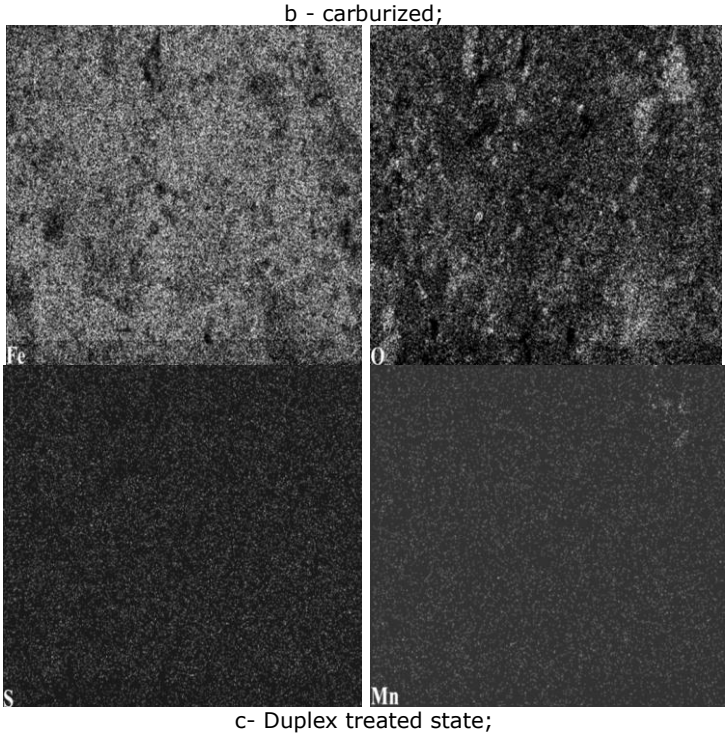

c- Duplex treated state;

Figure 4.42: EDX element distribution: a – annealed state; b – carburized state; c - Duplex treated state;

4.7 Wear behaviour

As mentioned in Chapter 1, unlubricated sliding and abrasive wear have a major impact in industry. Both occur when two bodies in contact slide over each other without the existence of a lubricant. Unlubricated sliding wear occurs when two tribological elements have similar hardness. In this case, when the contacting asperities are sufficiently strong, the interface separation is modified and material is transferred from one body to another. Abrasive wear occurs when a hard rough surface slides across a softer surface [1]. ASTM International defines it as the loss of

material due to hard particles or hard protuberances that are forced against and move along a solid surface.

The wear behaviour of Duplex and non-Duplex samples was investigated by means of ball cratering and pin-on-disk tests.

4.7.1 Ball cratering method

Traditional techniques, such as pin-on-disk, block–on–rings, disc-on–wheel or dry sand rubber wheel test have been used successfully [144, 145], but the samples require relatively large dimensions and sometimes standard geometry. A new promising method for wear testing of surface engineered materials is represented by ball cratering, otherwise known as micro-abrasion testing. It possesses many advantages compared to many conventional wear tests:

- the ability to test small volumes of material and thin coatings;
- easy to use;
- Low cost of the test equipment.

This method was developed from two earlier techniques, such as dimpling, which is used to prepare transmission electron microscope samples ready for ion-beam thinning and cap-grinding, which is used for the measurement of coating thickness [146]. Since this method allows obtaining reliable, reproducible and comparable results to those obtained in standard tests, it was used in order to determine the wear resistance of Duplex and non-Duplex samples.

In order to determine the wear behaviour of Duplex and non-Duplex samples, dry sliding and abrasive micro scale wear tests were performed. The tests were realized using a ball cratering device, developed by Rui Vilar et al. Figure 4.43 presents a schematic diagram of the ball cratering device.

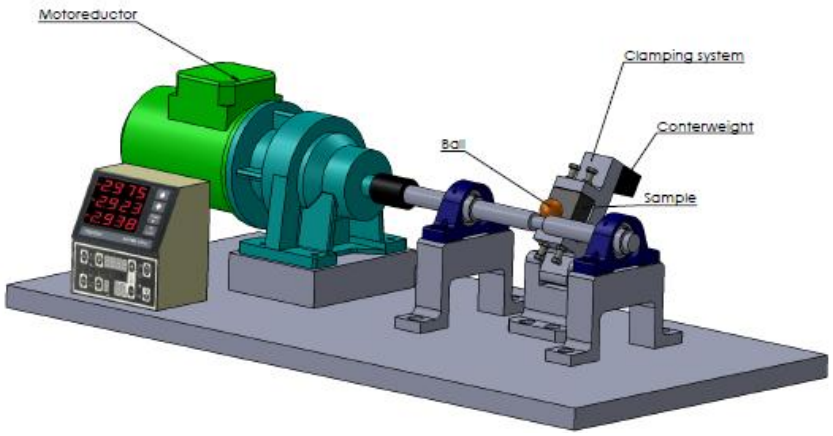

Figure 4.43: Schematic diagram of ball cratering device

As it can be observed from Figure 4.43, the ball is clamped between coaxial shafts and driven by an electric motor and rotates against the surface of the sample to be tested. The normal load is generated from the weight of the ball. The total sliding distance is calculated by recording the number of rotations through a measuring device which is connected to the shaft. The ball is kept in permanent contact with the samples surface.

In this work, the counter body was a tungsten carbide (WC-Co) sphere, with a diameter of 19 mm and a hardness of 1200 HV. The rotation speed of the ball was 200 rpm, which corresponds to a linear slide of 190 mm/s. A constant sliding distance of 500 m (sliding dry), 150 m (abrasive) and a normal of 0.4 N were used. For the abrasive wear test, the abrasive slurry consisted of commercial-grade silicon carbide grit (size designation F1200) in distilled water, with a concentration of 350 g/L. This concentration was selected to ensure good feed of the abrasive particles in the contact zone between the two materials, avoiding the formation of non spherical wear craters [146]. The mean abrasive particle size was 4.25 μm. The shape of the particles was highly irregular and angular, as presented in Figure 4.44. The craters diameter was measured by optical microscopy.

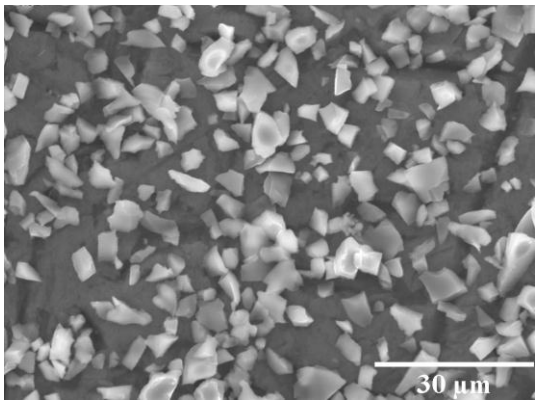

Figure 4.44: SEM micrograph of F1200 SiC abrasive particles

4.7.1.1 Mathematical analyze of the worn surface

The model that allows the wear coefficient calculation based on the removed material volume was initially established by Kassman et al. [148]. Later, it was generalized by Rutherford and Hutchings [149] for non planar samples and for the simultaneous calculation of wear coefficients of coating and substrate.

The rotation of a spherical counter body on a flat sample generates a spherical calotte (crater), with curvature radius R and height h, Figure 4.45 [150].

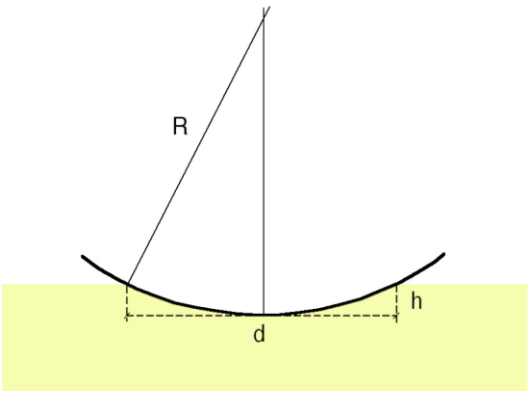

Figure 4.45: Schematic representation of the spherical calotte formed during wear test [150]

The volume of the calotte is given by:

$$V = \frac{\pi}{3} h^2 (3R - h) \quad (4.16),$$

From Figure 4.45:

$$R^2 = \left(\frac{d}{2}\right)^2 + (R - h)^2 \quad (4.17),$$

Where d is the diameter of the spherical calotte generated by the rotation of the sphere on the sample surface.

From equation 4.13 results:

$$\frac{d^2}{4R} - 2h + \frac{h^2}{R} = 0 \quad (4.18),$$

Assuming that R>>h, results:

$$h \cong \frac{d^2}{8R} \quad (4.19),$$

By replacing the value of h in equation 4.12, the volume of the calotte becomes:

$$V \cong \frac{\pi}{3} \frac{d^4}{64R^2} (3R - h) \quad (4.20),$$

For R>>h, the volume of the removed material becomes:

$$V \cong \frac{\pi d^4}{64R} \quad (4.21),$$

This relationship assumes that the shape of the crater is conformal to the shape of the ball and allows the following relationships between the diameters of the spherical calotte (d), wear rate (Q) and wear coefficient (K). Therefore, the wear rate can be calculated using the following equation [149]:

$$Q = \frac{V}{L} = \frac{\pi d^4}{64RL} \quad (4.22)$$

Where:

- Q, wear rate;
- V, volume of the removed material;
- R, radius of the sphere;
- d, crater diameter;
- L, sliding distance.

The wear coefficient can be calculated as follows [149]:

$$K = \frac{Q}{F_N} = \frac{\pi d^4}{64RLF_N} \quad (4.23)$$

Where:

- K, wear coefficient;
- Q, wear rate;
- F_N, normal load;
- d, crater diameter;
- L, sliding distance.

4.7.1.2 Dry sliding wear

Dry sliding wear was performed on Duplex and non-Duplex samples by means of ball cratering method. The investigations were performed on cylindrical samples, with a diameter of 12 mm and length of 4 mm. In order to achieve a high reliability of the results, all tests were performed at least two times for each structural state.

The average values of the wear coefficient, determined according to equation 4.23, are shown in Figure 4.46.

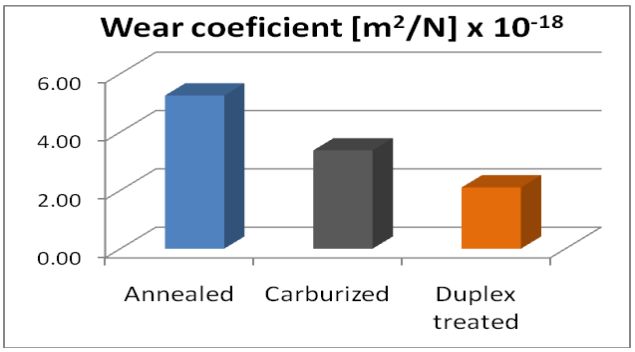

Figure 4.46: Wear coefficient variation

It can be observed a decrease of the wear coefficient for Duplex treated state (2.10 x$10^{-18}$$m^2N^{-1}$), compared to annealed state (5.25 x $10^{-18}$$m^2$ N^{-1}) and carburized state (3.37 x $10^{-18}$$m^2$ N^{-1}). The wear rates were calculated according to equation 4.22. The wear rate decreased from 2.09 ×10^{-18} m^2 (annealed state) to 8.38×10^{-19} m^2 (Duplex treated state), as it can be observed from Figure 4.47.

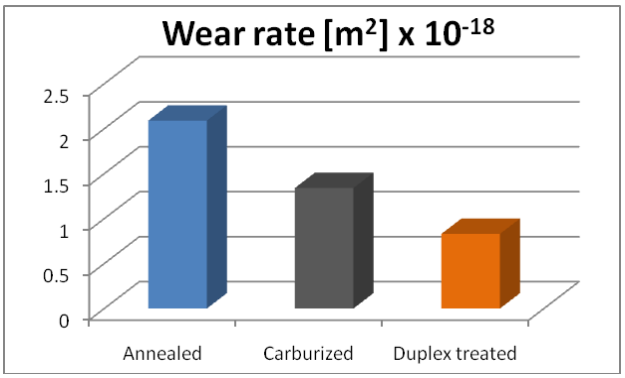

Figure 4.47: Wear rates

In order to investigate the wear mechanisms involved, the worn surfaces were observed by scanning electron microscopy. The SEM micrographs of the worn surfaces for annealed state are presented in Figure 4.48.

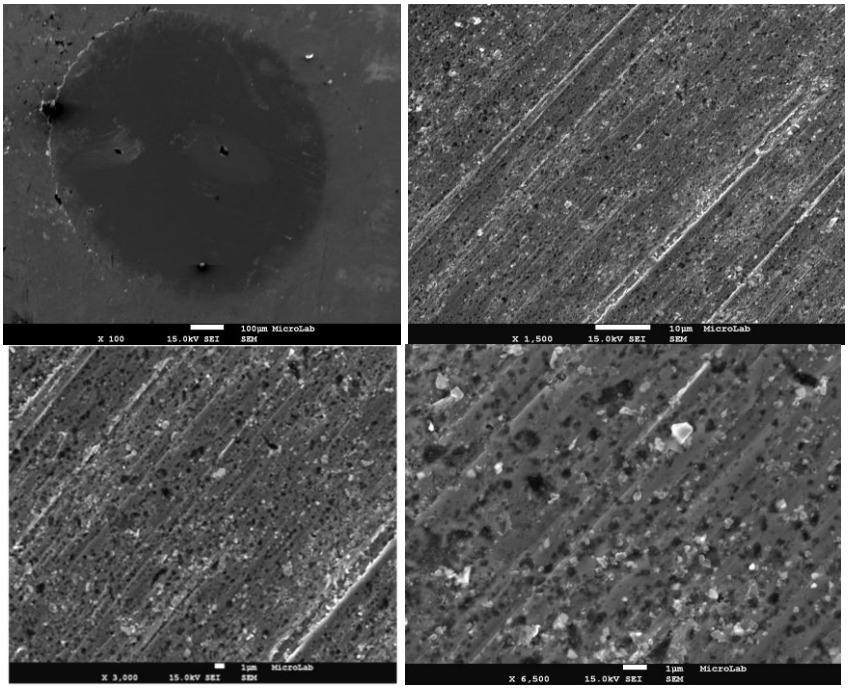

Figure 4.48: SEM micrographs of annealed worn surface

Various mechanisms seem to be occurring simultaneously in the sliding wear behaviour of annealed samples against WC-Co counter body at room temperature. The worn surface presents parallel grooves formed by scratching the surface with hard particles (typical of abrasive wear), flat zones showing plastic deformation caused by the action of the counter body and rough cavities, suggesting that the material was removed and probably transferred to the counter body. Also it can be observed the presence of wear debris. EDX analyze of the worn surface is presented in Figure 4.49.

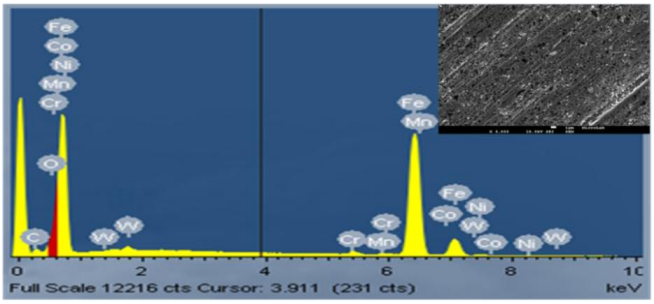

Figure 4.49: EDX analyze of the worn surface

EDX investigation shows the presence of W and Co, demonstrating that was adherence and transfer of material between the sample and counter body. It reveales also the presence of Fe, C Mn, Cr, Ni, due to the chemical composition of EN 16MnCr5. The surface contains O, which indicates the formation of some oxides during wear tests. The elements distribution is presented in Figure 4.50.

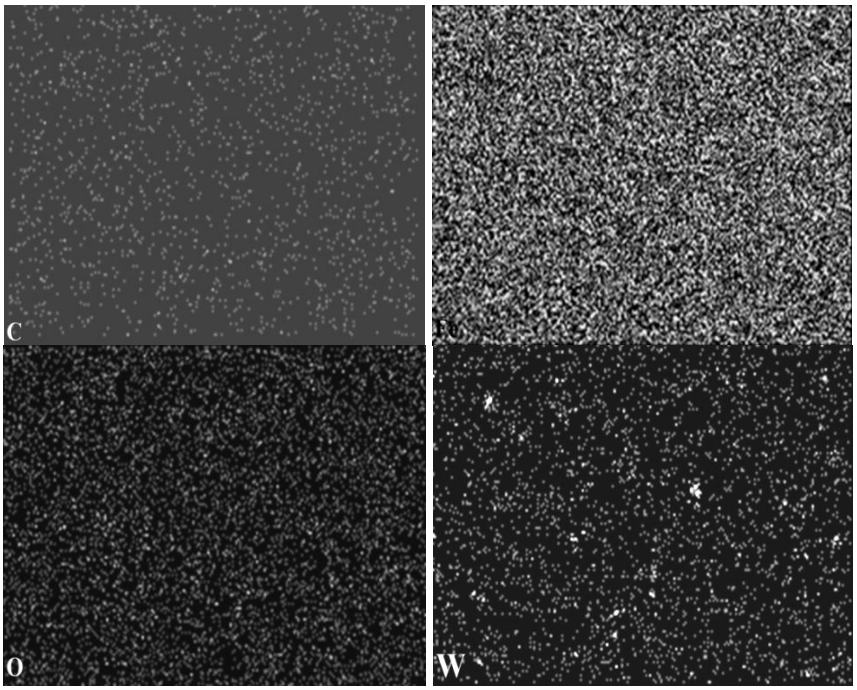

Figure 4.50: EDX mapping of annealed worn surface

From Figure 4.49 it can be observed that W is distributed throughout most of the worn surface. The SEM micrographs of the worn surfaces for carburized state are presented in Figure 4.51.

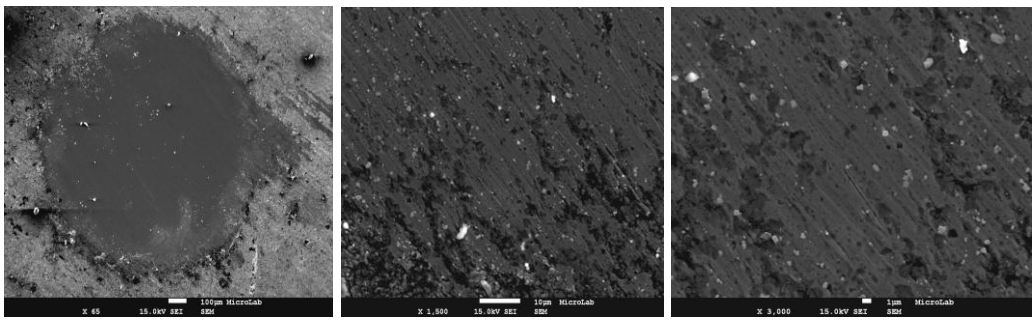

Figure 4.51: SEM micrographs of carburized worn surface

Similar to annealed state, the worn surface presents parallel grooves formed by scratching the surface with hard particles, some areas with plastic deformation caused by the action of the counter body and regions in which the material was removed and probably transferred to the counter body. In this case also it can be noticed the presence of wear debris. EDX analyze of the worn surface is presented in Figure 4.52.

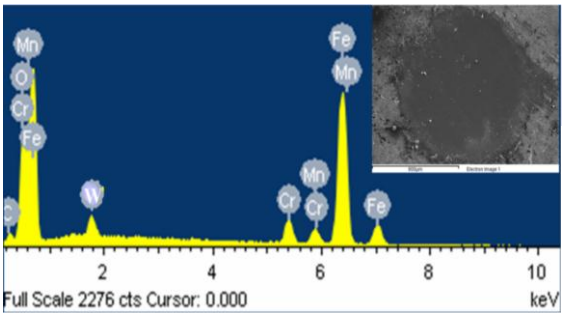

Element	App Conc.	Intensity Corrn.	Weight%	Weight% Sigma	Atomic%
W K	0.15	0.5810	3.84	0.47	12.61
O K	1.32	1.7660	10.90	0.68	26.85
Cr K	0.46	1.1365	5.89	0.23	4.46
Mn K	0.32	0.9427	4.95	0.28	3.55
Fe K	4.86	0.9538	74.42	0.75	52.52
Totals			100.00		

Figure 4.52: EDX analyze of carburized worn surface

EDX investigation shows the presence of W, demonstrating that was adherence and transfer of material between the sample and counter body. It reveales also the presence of Fe, C Mn, Cr, due to the chemical composition of EN 16MnCr5. The surface contains O in significan amount, which indicates the formation of some oxides during wear tests. The elements distribution is presented in Figure 4.53.

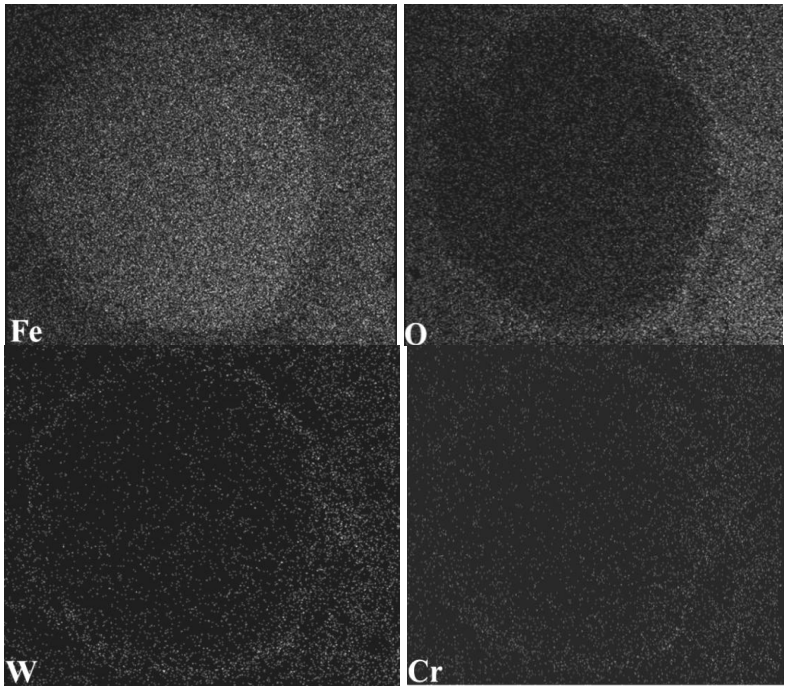

Figure 4.53: EDX mapping of carburized worn surface

From Figure 4.52 it can be observed that W is distributed throughout most of the worn surface. The SEM micrographs of the worn surfaces for Duplex treated state are presented in Figure 4.54.

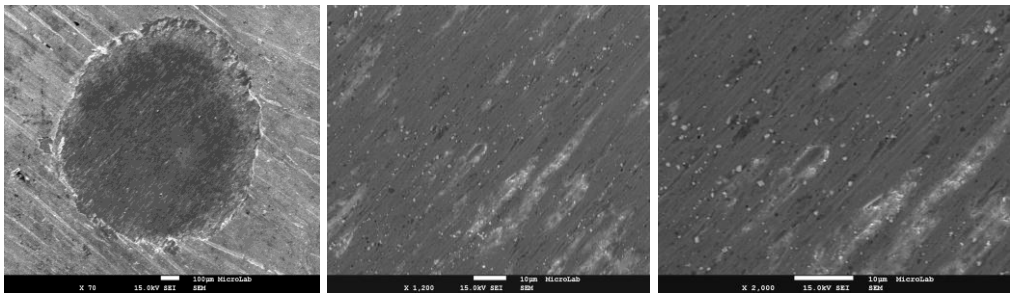

Figure 4.54: SEM micrographs of Duplex treated worn surface

For Duplex treated state also, the worn surface show parallel grooves and some plastic deformation surface caused by the action of the counter body. It can be observed also small zones in which the material has been removed. EDX analyze of the worn surface is presented in Figure 4.55.

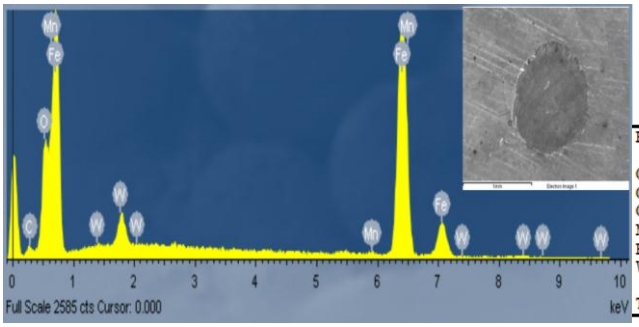

Element	App Conc.	Intensity Corrn.	Weight%	Weight% Sigma	Atomic%
C K	0.22	0.5522	2.36	0.37	9.26
O K	1.41	1.7001	4.89	0.58	14.41
Cr K	0.10	1.1912	0.50	0.13	0.45
Mn K	0.14	0.9660	0.88	0.18	0.76
Fe K	14.70	0.9851	87.99	0.72	74.26
W M	0.35	0.6142	3.38	0.28	0.87
Totals			100.00		

Figure 4.55: EDX analyze of Duplex treated worn surface

EDX investigation shows the presence of W, demonstrating that was adherence and transfer of material between the sample and counter body. It reveales also the presence of Fe, C Mn, Cr, due to the chemical composition of EN 16MnCr5. The surface contains O in significant amount, which indicates the formation of some oxides during wear tests. The elements distribution is presented in Figure 4.56.

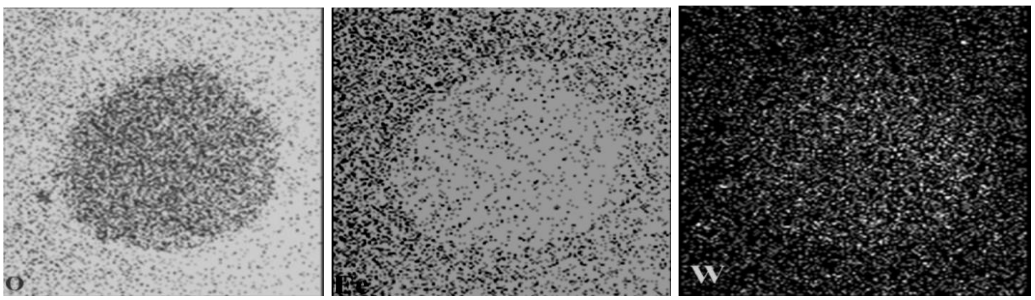

Figure 4.56: EDX mapping

4.7.1.3 Abrasive wear

In order to achieve a high reliability of the results, all tests were performed at least two times for each structural state. They were conducted without interruption, and the abrasive slurry was continuously agitated and fed between the ball and specimen with the help of a peristaltic pump.

The wear coefficient of Duplex and non-Duplex samples was calculated according to equation 4.23. The average value of wear coefficient for annealed state is $1.57x10^{-17}m^2N^{-1}$, $1.40x10^{-18}m^2N^{-1}$ for carburized state and $1.10x10^{-18}m^2N^{-1}$ for Duplex treated state. It can be observed a decrease of the wear coefficient for Duplex treated state compared to annealed state, Figure 4.57.

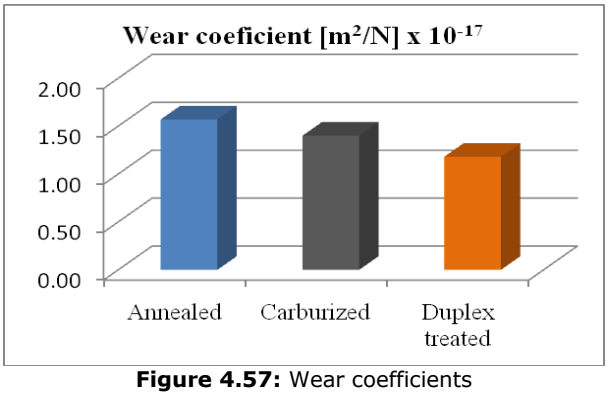

Figure 4.57: Wear coefficients

The wear rates were calculated according to equation 4.22. The wear rate decreased from 6.27 $\times 10^{-18}$ m^2 (annealed state) to 4.73$\times 10^{-18}$ m^2 (Duplex treated state) due to a higher hardness of Duplex treated samples, as it can be observed from Figure 4.58

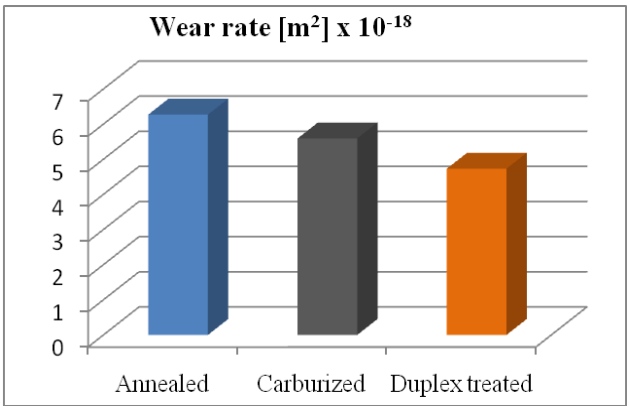

Figure 4.58: Wear rates

The SEM micrographs of the worn surfaces for annealed state are presented in Figure 4.59.

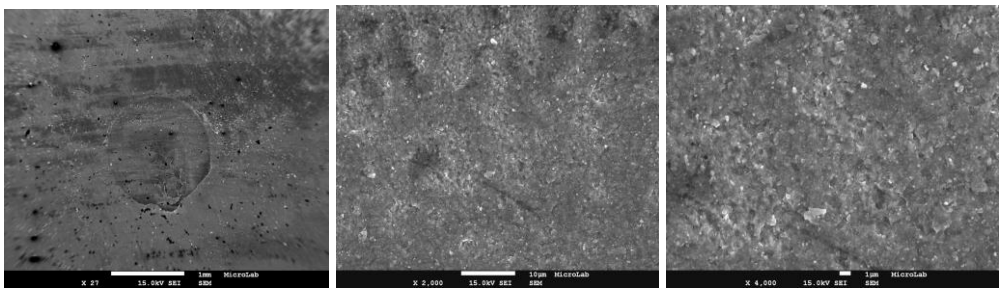

Figure 4.59: SEM micrographs of worn surface

From Figure 4.58 it can be observed that the worn surface corresponds to three-body abrasive wear. SiC particles indent and roll over the surface during the tests instead of sliding, wearing material uniformly. Also, the worn surface presents multiples indentations. The worn surface was investigated by EDX analyze, Figure 4.60.

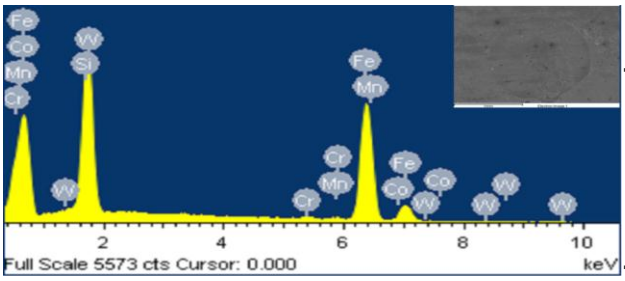

Element	App Conc.	Intensity Corrn.	Weight%	Weight% Sigma	Atomic%
C K	0.84	0.3010	16.06	2.14	38.69
Si K	7.23	1.0258	40.67	1.12	41.91
Cr K	0.09	0.9429	0.58	0.12	0.32
Fe K	5.16	0.8933	33.31	0.95	17.26
Co K	0.15	0.8758	1.01	0.29	0.49
W M	1.08	0.7454	8.37	0.77	1.32
Totals			100.00		

Figure 4.60: EDX analyze of annealed sample worn surface

EDX investigation reveals a significant amount of Si. It reveales also the presence of Fe, C Mn, Cr, due to the chemical composition of EN 16MnCr5. The element distribution in the worn surface is presented in Figure 4.61.

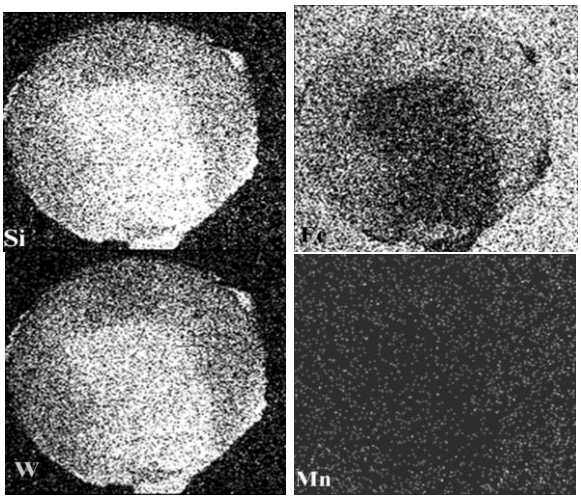

Figure 4.61: EDX mapping

The SEM micrographs of the worn surface for carburized state are presented in Figure 4.62.

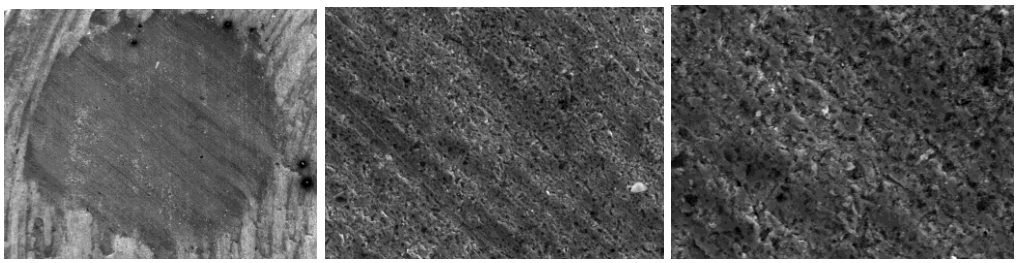

Figure 4.62: SEM micrographs of carburized worn surface

From Figure 4.61 it can be observed that the worn surface corresponds to three-body abrasive wear. SiC particles roll over the surface instead of sliding, wearing material uniformly. Also, the worn surface presents multiples indentations. The worn surface was investigated by EDX analyze, Figure 4.63.

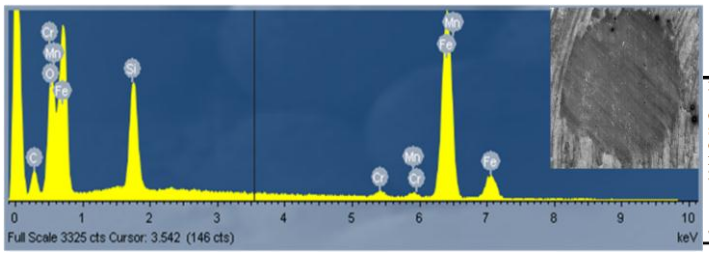

Element	App Conc.	Intensity Corrn.	Weight%	Weight% Sigma	Atomic%
O K	0.84	0.3010	16.06	2.14	38.69
Si K	7.23	1.0258	40.67	1.12	41.91
Cr K	0.09	0.9429	4.58	0.12	0.32
Fe K	5.16	0.8933	33.31	0.95	17.26
Mn K	0.15	0.8758	3.01	0.29	0.49
C K	0.11	0.1234	2.21	0.23	0.35
Totals			100.00		

Figure 4.63: EDX analyze of carburized worn surface

EDX investigation reveals a significant amount of Si. It reveales also the presence of Fe, C Mn, Cr, due to the chemical composition of EN 16MnCr5. The element distribution in the worn surface is presented in Figure 4.64.

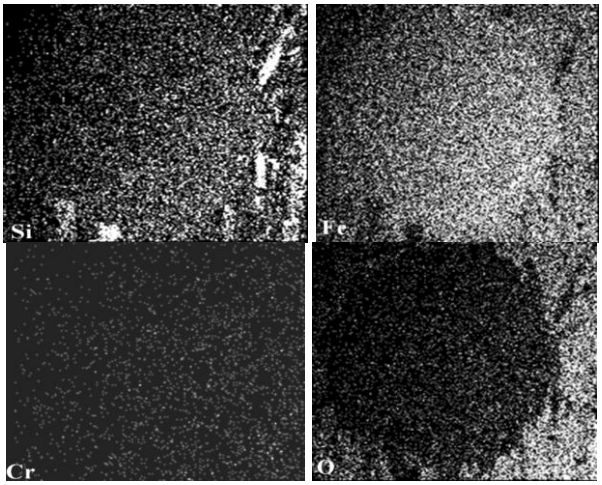

Figure 4.64: EDX mapping of carburized sample worn surface

The SEM micrographs of the worn surface for Duplex treated state are presented in Figure 4.65.

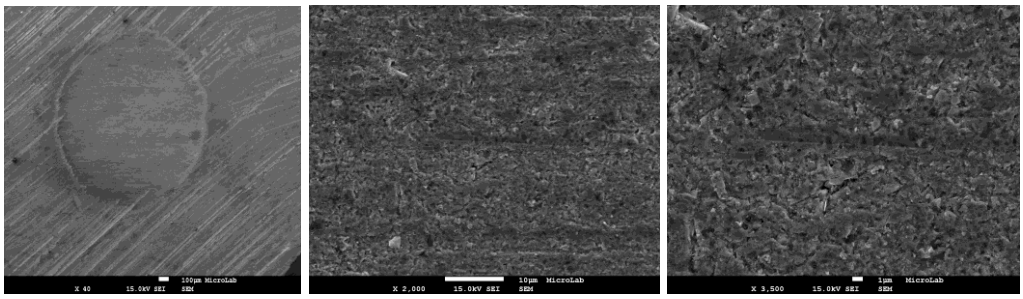

Figure 4.65: SEM micrographs of Duplex samples worn surface

From Figure 4.65 it can be observed that the worn surface corresponds to three-body abrasive wear. The SiC particles roll over the surface instead of sliding, wearing material uniformly. Also, the worn surface has multiples indentations. The worn surface was investigated by EDX analyze, Figure 4.66.

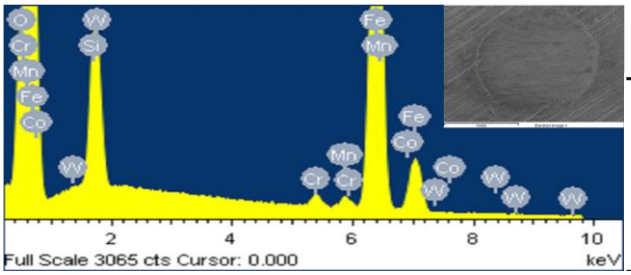

Element	App Conc.	Intensity Corrn.	Weight%	Weight% Sigma	Atomic%
C K	0.84	0.3010	16.06	2.14	38.69
Si K	7.23	1.0258	40.67	1.12	41.91
Cr K	0.09	0.9429	0.58	0.12	0.32
Fe K	5.16	0.8933	33.31	0.95	17.26
Co K	0.15	0.8758	1.01	0.29	0.49
W M	1.08	0.7454	8.37	0.77	1.32
Mn K	0.15	0.8758	3.01	0.29	0.49
Totals			100.00		

Figure 4.66: EDX analyze of Duplex worn surface

EDX investigation reveals a significant amount of Si. It reveales also the presence of Fe, C Mn, Cr, due to the chemical composition of EN 16MnCr5. The element distribution in the worn surface is presented in Figure 4.67

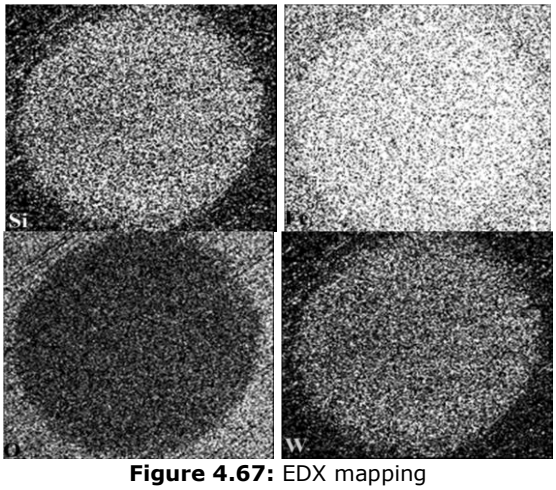

Figure 4.67: EDX mapping

4.7.2 Pin-on-disk

The sliding wear rate and coefficient of friction of the investigated samples were determined using a CSM pin-on-disc tribometer presented in Chapter 3, Figure 3.11. The unit consists of an arm to which the pin is attached, a sample holder which allows the mounting of square or disc shaped samples, an electronic force sensor for measuring the friction force, and software for displaying the parameters and storing data for analysis. The sliding distance was 500 m, with a 10 m/s velocity under a 5 N load against a WC-Co ball of 6 mm diameter. The relative humidity was 65%.

The friction coefficients were recorded by measuring the deflection of the tribometers elastic arm. The signal for the coefficient of friction is displayed in real time during the test on a PC screen, by measuring the deflection of the elastic arm, Figure 4.68 [151].

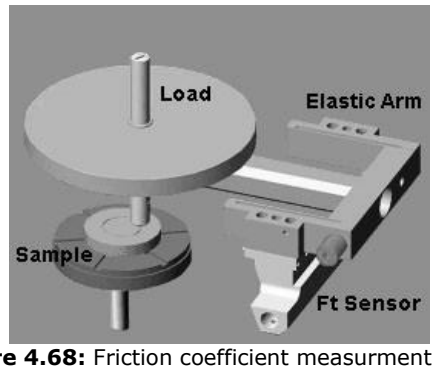

Figure 4.68: Friction coefficient measurment [151]

The wear rate is quantified by measuring the wear groove and determining the amount of removed material of both sample and ball. The wear rate K is calculated with the equation presented in Chapter 1, by adapting it to the shape of the wear groove.

The friction coefficients for each structural state are presented in Figure 4.69.

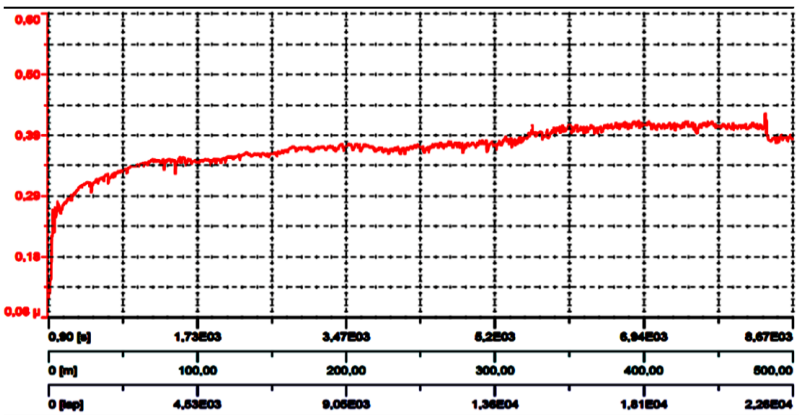

a- annealed state;

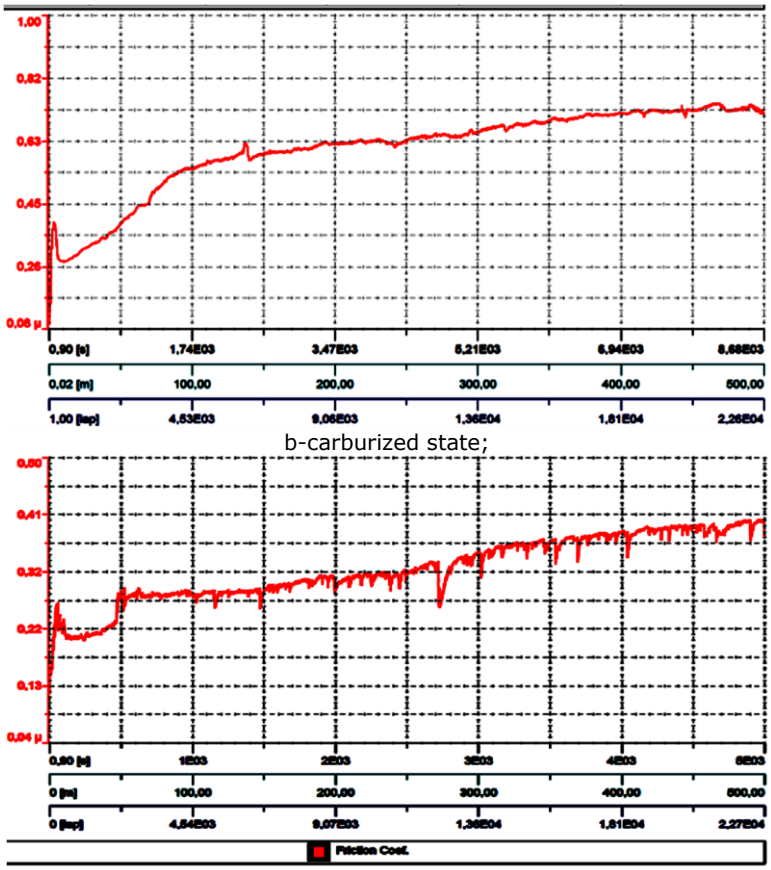

b-carburized state;

c- Duplex treated;

Figure 4.69: Friction coefficient: a - annealed state; b – carburized state; c – Duplex treated state [91]

The minimum, medium and maximum values of friction coeficient corresponding to each structural state are presented in the Table 4.14.

Table 4.14: Friction coefficient of the samples

Structural state	μ_{min}	μ_{max}	μ_{mediu}
Annealed state	0.421	0.743	0.632
Carburized state	0.275	0.475	0.375
Duplex treated state	0.119	0.321	0.225

The lowest friction coefficient was obtained for Duplex treated state (0.321), but it is more rugged compared to untreated state. This low value can be attributed to the finer microstructure of Duplex treated samples.

The wear track measurements of the samples were performed using a digital microscope and are ilustrated in Figure 4.70.

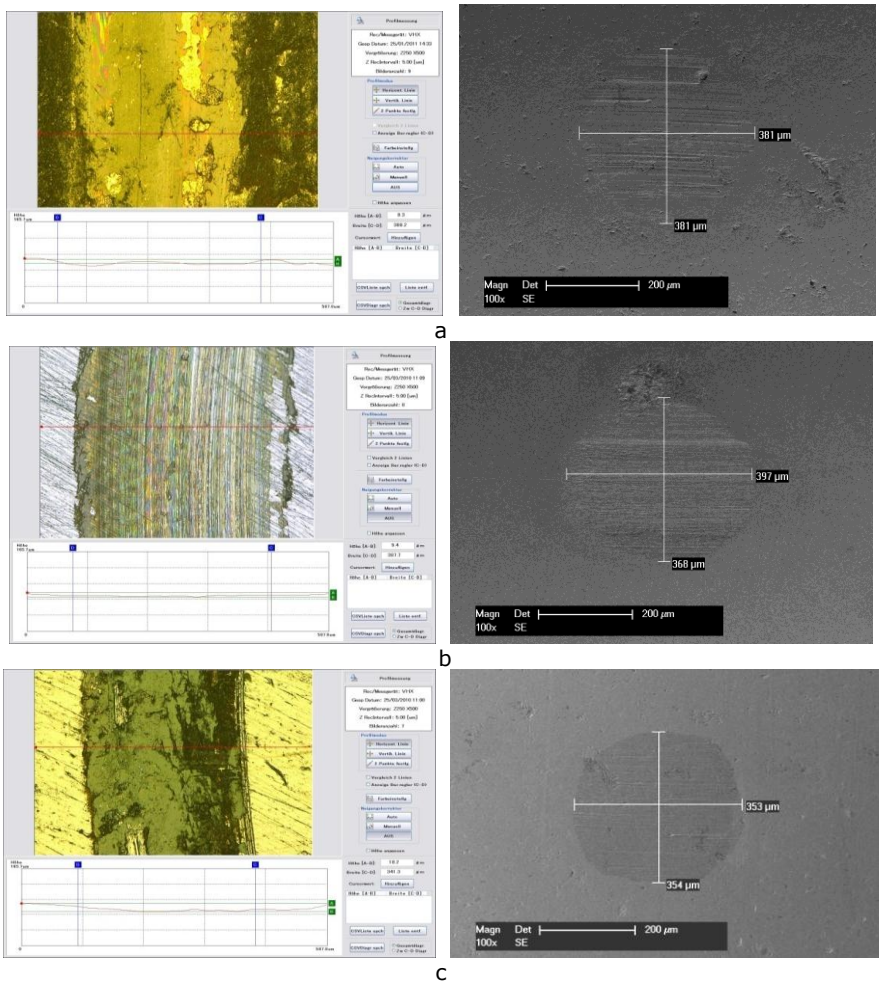

Figure 4.70: Wear track and ball wear of the samples: a - tempered sample; b – carburized sample; c – Duplex treated sample

The sliding wear rates were determined with the TRIBOX software, by introducing the measured area of the wear tracks and the diagonals of the testing balls worn cape. The results are presented in Table 4.15.

Table 4.15: Wear measurements of the samples

Structural state	**h [µm]**	**s [µm]**	**A [µm²]**	**Ball wear diagonals [µm]**	**Wear rate [10^{-5} mm²]**
Tempered state	18.2	341.	4149.8	381x381	3.66
Carburized state	9.4	387.	2430.6	368x397	2.14
Duplex treated	8.3	388.	2148.7	353x354	1.89

The histogram of the wear rates for each structural state is presented in Figure 4.71.

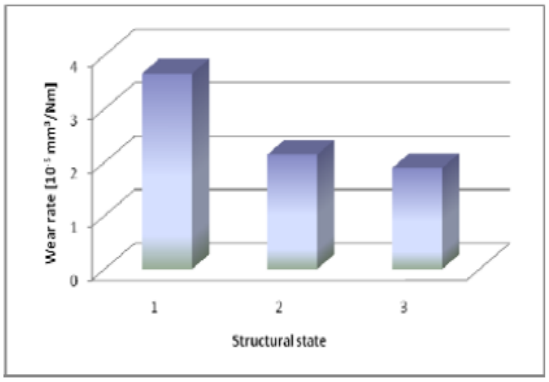

Figure 4.71: Wear rate: 1- tempered sample; 2 – carburized sample; 3 – Duplex treated sample

As it can be observed from the histogram, the Duplex surface treatment consisting in carburizing followed by high frequency surface induction and low tempering reduce the wear rate by 51% compared with the annealed state and by 12% compared with the carburize state. This reduction of the wear rate can be attributed to the presence of martensite in the structure of Duplex treated samples, which provides a higher hardness of the surface layer.

4.8 Fatigue behaviour

As mentioned in Chapter 1, fatigue is the progressive and localized structural damage that occurs when a material is subjected to cyclic loading. Fatigue occurs when a material is subjected to repeated loading and unloading. If the loads are above a certain threshold, microscopic cracks will begin to form at the surface. Eventually a crack will reach a critical size, and the structure will suddenly fracture. The shape of the structure will significantly affect the fatigue life [58].

Duplex and non-Duplex specimens were submitted to rotating bending in order to study the effect of the surface modification on the fatigue resistance.

4.8.1 Rotating bending fatigue

The rotating bending fatigue test consists in the application of a known constant bending stress (due to a bending moment), combined with the rotation of the sample around the bending stress axis until its failure [59]. The design of the machine is presented in Figure 4.72.

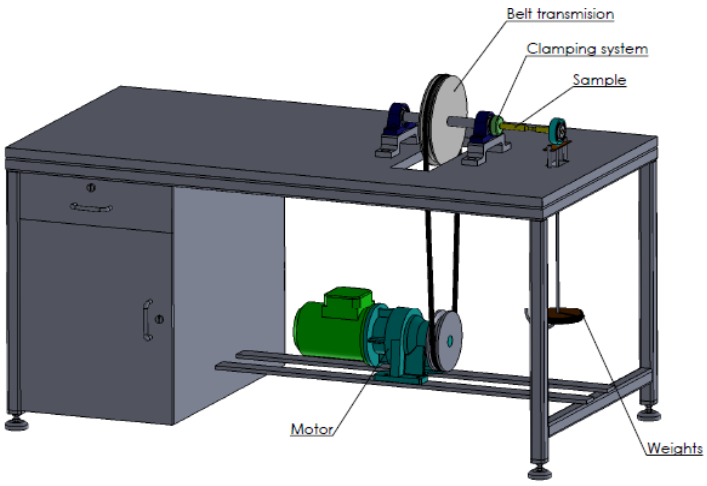

Figure 4.72: Rotating bending fatigue machine

The main parts of the machine are:

- the electric motor, which gives the rotation;
- three main bearings which create the support;
- one load bearing, where the load is applied;
- a counter, which records the number of cycles to failure of the specimens.

The rotation and simultaneous bending on which the fatigue machine operates ensures that the bending stresses which leads to stretch the upper layers of the specimen and compress the bottom layers as is applicable in stationary beams; is evenly distributed around the entire circumference of the specimen.

The bending fatigue tests were performed on Duplex and non-Duplex specimens. Typical fatigue specimen configuration is presented in Figure 4.73.

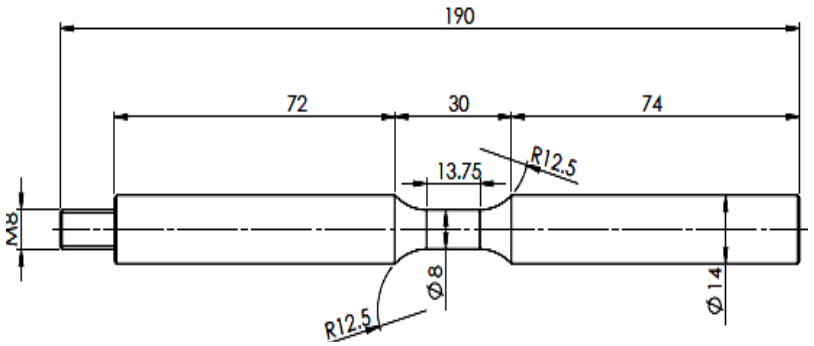

Figure 4.73: Rotating bending fatigue specimens

In order to determine the fatigue limit of Duplex and non-Duplex is necessary to test multiple identical samples. Therefore, 10 specimens of Duplex treated and 10 specimens untreated were tested. The first specimen was loaded so that the maximum tension is slightly lower than the material's mechanical resistance (R_m). The specimen fractured at N1 number of cycles. The second specimen was loaded so that the maximum tension is lower than the tension obtained in the previous load.

The number of cycles to failure in this case will be N2>N1. The same applies to the remaining samples [56, 57]. For the other specimens, the tests were realized similar. The results obtained for Duplex and non-Duplex samples are presented in Figure 4.74.

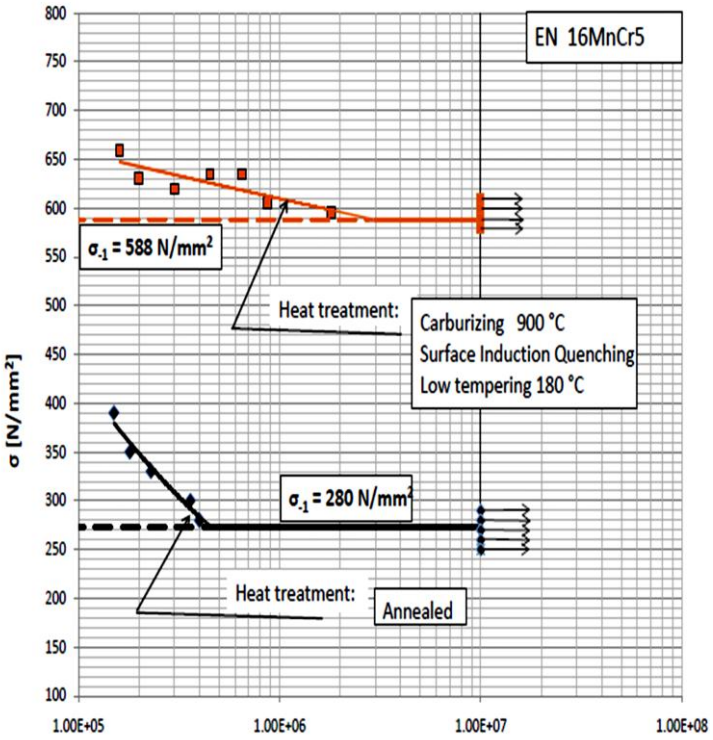

Figure 4.74: Fatigue limit of treated and untreated samples

As it can be observed from Figure 4.73, the fatigue limit increased from 280 N/mm^2 (untreated state) to 588 N/mm^2 (Duplex treated state), due to high compressive stresses induced by the thermal treatment of surface induction quenching.

4.9. Conclusions

The Duplex treatment selected for this study consists in the combination of gas carburizing and surface induction quenching on EN16MnCr5 carburizing steel.

The first step in realizing the Duplex treatment consists in a gas carburizing treatment. Gas carburizing was done in an endothermic atmosphere produced by mixing endogas and enriching hydrocarbon gas, at 900 °C, and maintained 6 hours and 40 minutes. The second step in realizing the Duplex treatment consisted in high frequency surface induction quenching, resulting a quenched layer thickness of 0.8 mm. To reduce the internal stresses was realized a low tempering treatment, at 180 °C for 30 minutes.

The structural characterization was realized by means of optical microscopy, scanning electron microscopy, X-ray diffraction and glancing incidence X-ray analysis. Optical microscopy revealed that in annealed state, the structure is composed of ferrite (Feα) and perlite (P). After carburizing, the superficial layer is formed of perlite grains surrounded by a fine network of secondary cementite (Ce_{II}). In Duplex treated state, the structure is formed of tempered martensite and residual austenite.

The result of X-ray analysis showed only the presence of iron phases (Feα) on the annealed samples. For the carburized samples, X-ray diffraction analysis reveals the presence of iron phases (Feα) and iron carbides (Fe_3C and Fe_2C). As expected, martensite phases ($C_{0.14}Fe_{1.86}$) were determined on the Duplex treated samples. In addition to the martensite phase, austenite phase (retained austenite, Fe_γ), iron phases and iron carbide phases were determined on Duplex treated specimens.

The microhardness tests showed that the hardness values of Duplex treated samples decreases from the surface to the core depending on the carbon profile. At the surface, the hardness values ranged from 806 HV0.2 to 370 HV0.2, while in the core, the values are constant, ranging from 310 to 320 HV0.2. The maximum value of 806 $HV_{0.2}$ was obtained at a distance of 0.2 mm from surface, due to the presence of a higher proportion of residual austenite at surface, as illustrated by glancing incidence X-ray diffraction. Regarding the carburized state, the hardness also decreases from surface to core, obtaining in the surface a maximum value of 750 HV0.2. In the core, the values are constant, ranging from 310 to 320 HV0.2. The hardness values obtained for the annealed state are constant, ranging from 310 to 320 HV0.2.

Duplex and non-Duplex specimens were subjected to instrumented indentation tests in order to determine the mechanical properties. The values of bulk modulus increased from 135 GPa (annealed state) to 245 GPa (Duplex state), which represents an increase of about 80%. The average values of Martens hardness corresponding to annealed state is 1.98 GPa, 2.63 GPa for carburized state and 6.06 GPa for Duplex treated state. It can be observed that the value of Martens hardness for Duplex state increased 5 times compared to annealed state and 2 times compared to carburized state respectively.

The corrosion behavior of Duplex and non - Duplex samples was electrochemical investigated in different environments by means of linear polarization. In 3% NaCl it was obtained a corrosion rate of 0.53 mm $year^{-1}$ for annealed state, 0.30 mm $year^{-1}$ for carburized state, and 0.26 mm $year^{-1}$ for Duplex treated state. It can be observed a decrease of the corrosion rate of about 50 % for the Duplex treated sample compared to annealed state. In 0.5 M H_2SO_4, the corrosion rate decreased from 4.79 mm $year^{-1}$(untreated state) to 2.28 mm $year^{-1}$ (Duplex treated), which corresponds to a decrease of about 52%. In 0.1 M H_2SO_4, the corrosion rate decreased from 3.78 mm $year^{-1}$ (untreated state) to 1.36 mm $year^{-1}$ (Duplex treated), which corresponds to a decrease of about 75%. The corrosion products were identified by means of glancing incidence X-ray diffractions. The analysis revealed, in each solution used, the presence of hematite (iron oxide) phases for each structural state. The surface of the corroded samples was analyzed by image acquisition and by energy dispersive X-ray spectrometry (EDX). The tendency towards pitting corrosion can be observed for all structural states. EDX analyses showed that the corroded surface of all the samples contains nearly all the constituent elements of EN 16 MnCr5 (Mn, Cr, Si, etc) and additionally O in a significant amount.

In order to determine the wear behaviour of Duplex and non-Duplex samples, dry sliding, abrasive micro scale and pin-on-disk wear tests were performed.

For dry sliding, it can be observed a decrease of the wear coefficient for Duplex treated state (2.10 $x10^{-18}m^2N^{-1}$), compared to annealed (5.25 x $10^{-18}m^2$ N^{-1}) and carburized state (3.37 x $10^{-18}m^2$ N^{-1}). The wear rate decreased from 2.09 $\times 10^{-18}$ m^2 (annealed state) to 8.38$\times 10^{-19}$ m^2 (Duplex treated state). The wear mechanisms involved was determined by scanning electron microscopy. The worn surfaces present parallel grooves formed by scratching the surface with hard particles, flat zones showing plastic deformation and rough cavities, suggesting that the material was removed and transferred to the counter body. EDX investigation shows the presence of W distributed throughout most of the worn surface, which demonstrates that was adherence and transfer of material between the sample and counter body.

For abrasive wear, the wear coefficient decreased from 1.57 x 10^{-17} (untreated samples) to 1.10 x 10^{-18} (Duplex treated samples). The wear rate decreased from 6.27 x 10^{-18} m^2 (untreated samples) to 4.37 x 10^{-18} m^2 (Duplex treated state) SEM analysis reveals the wear mechanism corresponds to three-body abrasive wear. SiC particles roll over the surface instead of sliding, wearing material uniformly.

Regarding the pin-on-disk tests, the wear rate decreased from 3.66 x 10^{-5} mm^3N^{-1} m^{-1} (annealed state) to 1.89 mm^3 N^{-1} m^{-1} (Duplex treated).

Duplex and non-Duplex specimens were submitted to rotating bending in order to study the effect of the surface modification on the fatigue resistance. The fatigue limit increased from 280 N/mm^2 (untreated state) to 588 N/mm^2 (Duplex treated state), due to high compressive stresses induced by surface induction quenching.

5. INVESTIGATIONS OF DUPLEX TREATMENT CONSISTING IN NITRIDING FOLLOWED BY WORK HARDENING THROUGH SHOT PEENING

5.1 Introduction

The Duplex treatment selected for this study is represented by the combination of plasma nitriding and work hardening through shot peening. As a rule, these treatments are applied separately. In recent years, a growing interest is observed in literature regarding the combination of these treatments [97, 98].

The nitriding process, first developed in the early 1900's, continues to play an important role in many industrial applications. It is often used in the manufacture of aircraft, bearings and automotive components, textile machinery, and turbine systems. Nitriding is a ferritic thermo-chemical treatment, in which nitrogen is diffused into a specimen surface, at a temperature within the range 480-570°C. This diffusion process is based on the solubility of nitrogen in iron. After nitriding, a thin compound layer, and a relative thick diffusion layer are produced on the specimen surface. The compound layer, also known as the white layer, consists predominantly of ε ($Fe_{2-3}N$) and/or γ' (Fe_4N) phases [131, 132]. Figure 5.1 presents a schematic representation of typical nitrided surface [177].

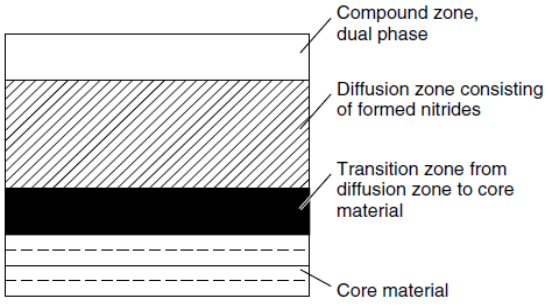

Figure 5.1: Schematic representation of typical nitrided surface [152].

The properties produced by nitriding can be summarized as follows:

- High surface hardness and wear resistance, together with reduced risk of scuffing and galling;
- High fatigue strength and due to the residual compressive stress induced;
- Improved corrosion resistance [132];

A significant advantage of nitriding is less distortion compared with carburizing due to the relatively low process temperature. A disadvantage is, however, the long treatment time caused by the slow diffusion process at a low temperature. The main methods for nitriding are gas nitriding, plasma nitriding and salt-bath nitriding [131].

Shot peening is a cold working process in which small spheres, also known as shots, bombard the surface of a part. The process is schematically presented in Figure 5.2 [153].

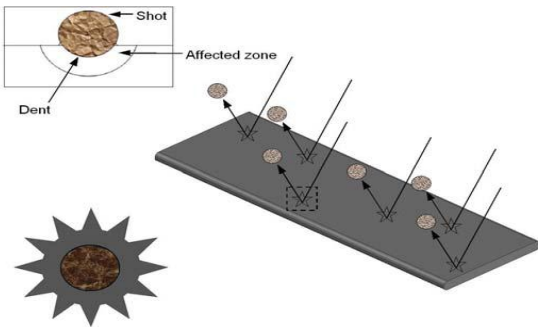

Figure 5.2: Schematic representation of shot peening process [153]

During the process, each shot that strikes the material, acts as a tiny peening hammer, creating on the surface small dimples. These dimples create a uniform layer of compressive stress at the metal surfaces. Compressive stresses are beneficial in increasing the resistance to fatigue failures, corrosion fatigue, stress corrosion cracking, fretting, galling and erosion caused by cavitations.

Shots play the key role in the peening process. They are spherical in shape and manufactured in different sizes from different materials, such as cast steel, carbon steel, ceramics, glass etc [179]. The selection of the shot is based on the peened material, its hardness, intensity, allowable contamination and permissible surface roughness [180]. The shot size depends on the smallest feature size that needs to be peened. According to Gillespie, the shots must be at least as hard as the peened material. The key peening parameters that affect the compressive stresses are the shot size, shot velocity, angle of impact, the part material and hardness, and friction [153].

5.2 Duplex treatment technology

The material used in realizing the Duplex treatment was EN 34CrNiMo6 steel, with the chemical presented in Chapter 3, Table 3.2. The material was supplied in annealed state, in bar form, with a length of 3 m and a diameter of 20 mm. The Duplex treatment was performed on cylindrical samples, with a diameter of 10 mm and length of 30 mm. The samples were cut using a STREAM LINE SLV OEM 30 machine, from endowment of National R&D Institute for Welding and Material Testing of Timisoara.

The first step in realizing the Duplex treatment consisted in gas nitriding. Gas nitriding is based on a heterogeneous reaction between an ammonia gas atmosphere and a steel surface at temperatures between 500 and 580°C. Ammonia content, furnace temperature and time control of determines the hard layer morphology. Usually the hard layer can be divided into a "white layer" and a compound layer consisting of metal nitrides of thickness 20 um or less, and a diffusion layer below, containing nitride precipitation at grain boundaries and dissolved atomic nitrogen in the ȁ-iron lattice of some mm thickness [131]. The transfer mechanism of the nitrogen in gas nitriding is presented in Figure 5.3.

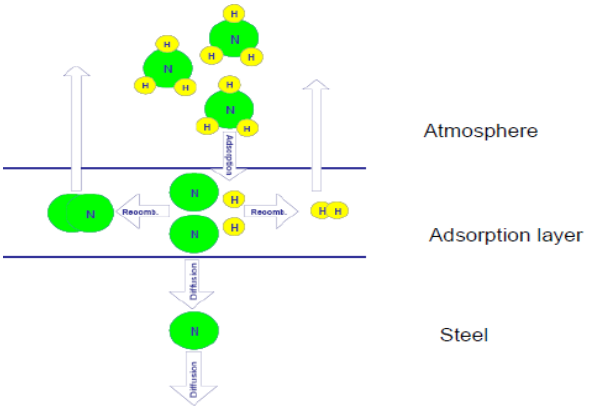

Figure 5.3: Schematic of the nitrogen transfer mechanism in gas nitriding [154]

The performance of this process depends on the material, surface shape and condition, and on the pretreatment of the work-piece, as well as the nitriding process parameters. The first step in realizing the Duplex treatment consisted in gas nitriding.

Prior to gas nitriding process, the samples were subjected to heat treatment, consisting of quenching followed by tempering, thus ensuring high strength and toughness of the core and good support for the nitrided layer. The parameters of this treatment are presented in Table 5.1.

Table 5.1: Parameters of quenching and high tempering treatments

Treatments	Heating temperature [°C]	Maintenance time [min]	Cooling environment
Quenching	850	60	Oil
High tempering	600	30	Air

Tempering temperature was chosen to exceed the nitriding temperature, in order to maintain the mechanical properties obtained after nitriding, except superficial hardness. The treatment was realized using a SIRIO oven from endowment of Manufacturing and Materials Department of Politehnica University of Timisoara, Figure 5.4.

Figure 5.4: Heating equipment

For the gas nitriding treatment, discs of 10 mm diameter and length of 4 mm were cut from the thermal treated samples. Prior to gas nitriding the samples were chemically cleaned following a series of distinct steps:

- rinsing in deionised water;
- Degreasing in two successive baths of methanol ultrasonic agitated, each with duration of 5 minutes.

After cleaning, the samples were placed in the nitriding furnace at Duroterm facility from Bucharest. The furnace was flushed with nitrogen and the reaction temperature was established. Furnace residence time started when ammonia was introduced into the system. The temperature of the process was 540°C with a maintenance time of 20h and the dissociation rate ranged from 25% to 40%. The thickness of the obtained nitrided layer was 0.4 mm. The third stage of the Duplex treatment consisted in a mechanical treatment of work hardening through shot peening. The treatment parameters are presented in Table 5.2

Table 5.2: Shot peening parameters

Particles dimensions [mm]	0.8-2
Pression [bar]	5
Distance of shots [mm]	50-60

5.3 Structural characterization

5.3.1 Optical microscopy

Duplex and non-Duplex samples were examined by optical microscopy following a series of distinct steps as presented in Chapter 4. The resulting micrographs of Duplex and non-Duplex samples are presented in Figure 5.5 [155].

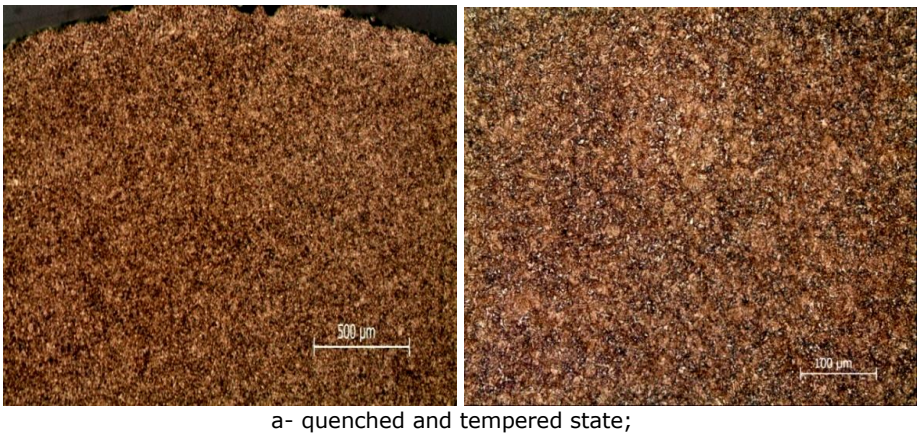

a- quenched and tempered state;

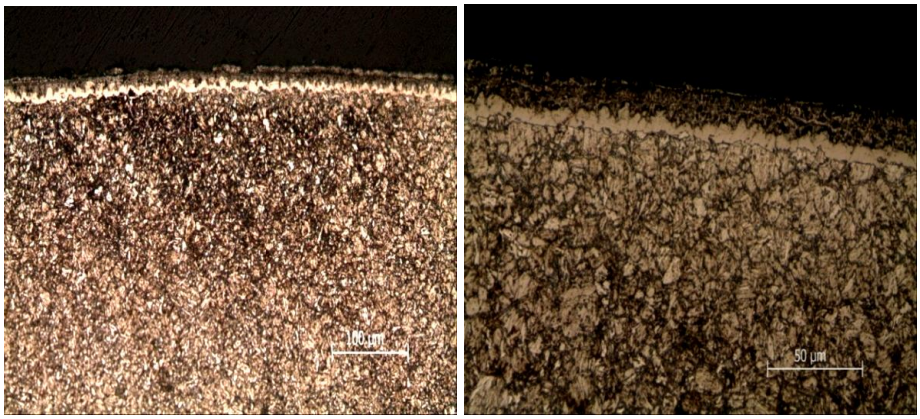

b - nitrided state;

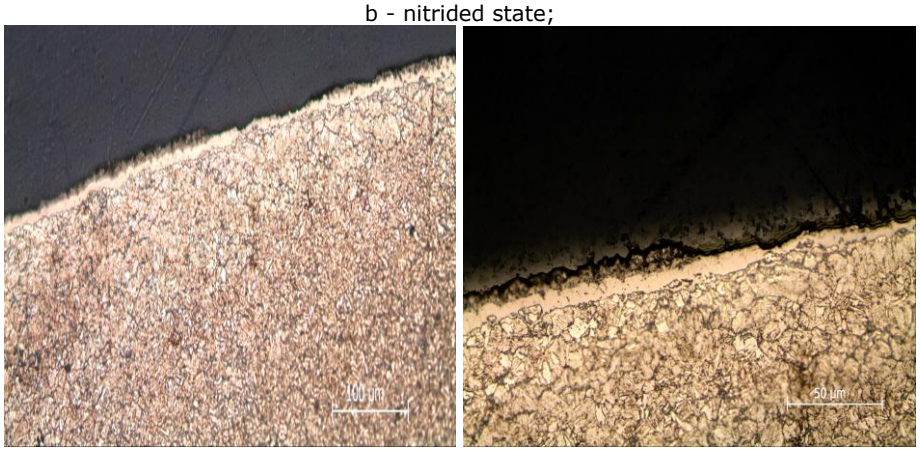

c - Duplex treated state;

Figure 5.5: Micrographs: a – quenched and tempered state; b – nitrided state; c – Duplex treated state.

In quenched and tempered state, Figure 5.5 a, the structure is composed of a ferito-cementitic mechanical mixture, namely sorbite. In Figure 5.5 b can be seen the presence of the compound layer consisting of iron nitrides (Fe_3N and Fe_4N). It can be also observed the white layer, which is uniform and very thin, with a thickness of about 15 µm. Under the white layer it can be observed the diffusion layer, which has a thickness of 280 µm. The diffusion layer consists of interstitial solid solutions of nitrogen in alpha iron, in which can be found nitrides precipitates at the grain boundaries, Figure 5.5 b. The total thickness of the nitrided layer is 0.4 mm. After shot peening the structure remains the same, Figure 5.5 c.

5.3.2 Scanning electron microscopy (SEM)

Duplex and non – Duplex samples were investigated by scanning electron microscopy. The results are presented in Figure 5.6.

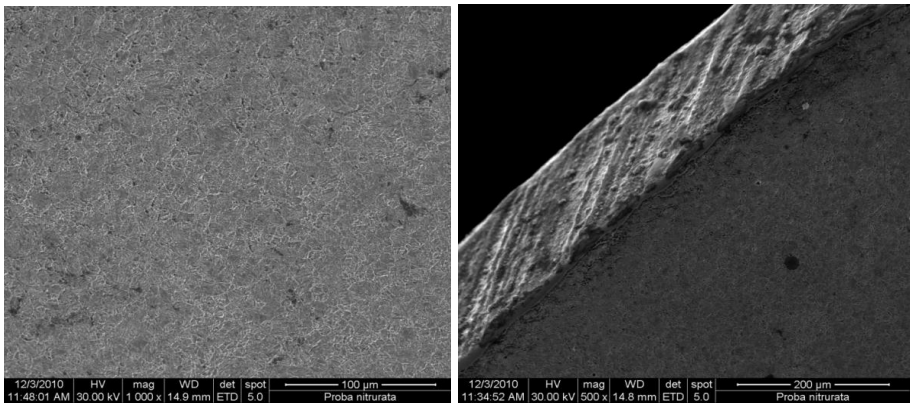

a b

Figure 5.6: Scanning electron microscopy micrographs:
a- quenched and tempered state;b- nitrided state;

5.3.3 X-ray diffractions

In order to identify the constituent phases, X-ray analyze was performed on Duplex and non-Duplex samples. X-ray diffraction was Cu Kα monochromatic radiation of wavelength 1.541840 Å. The parameters are presented in Table 5.3.

Table 5.3: XRD parameters

Intensity [mA]	Tension [KV]	Step size	Time per step [s]	Scan speed [s]	Scan angle [°]
30	40	0.04	0.5	0.08	20-90

Figure 5.7 a, b, c shows the X-ray diffraction patterns for untreated, nitrided and Duplex treated samples.

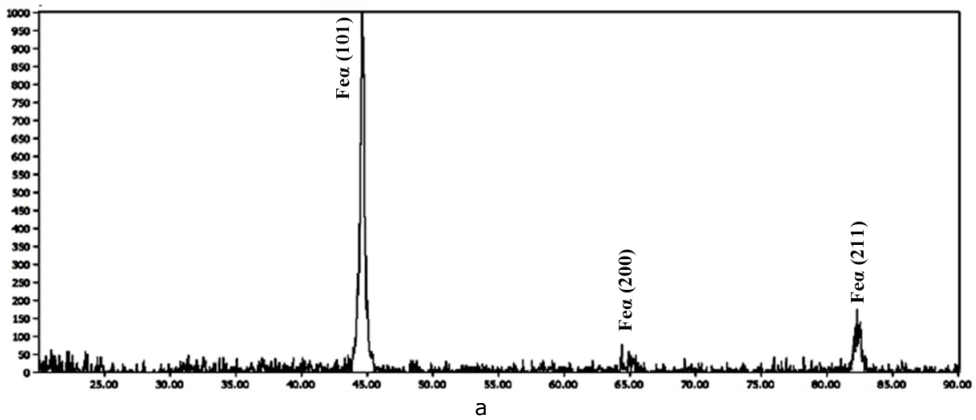

a

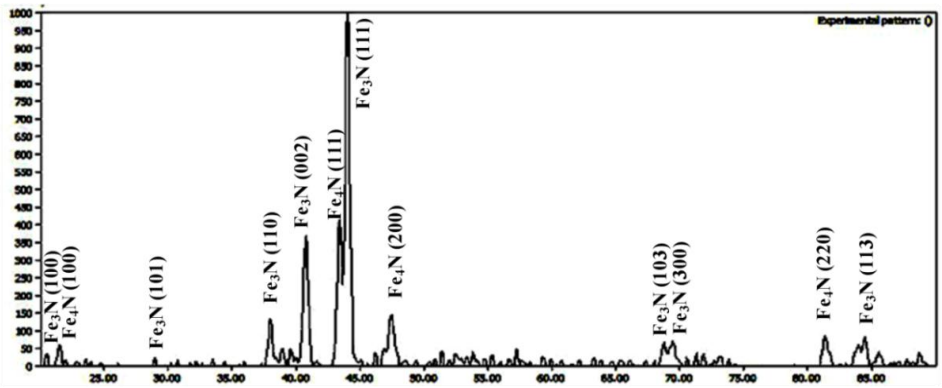

b

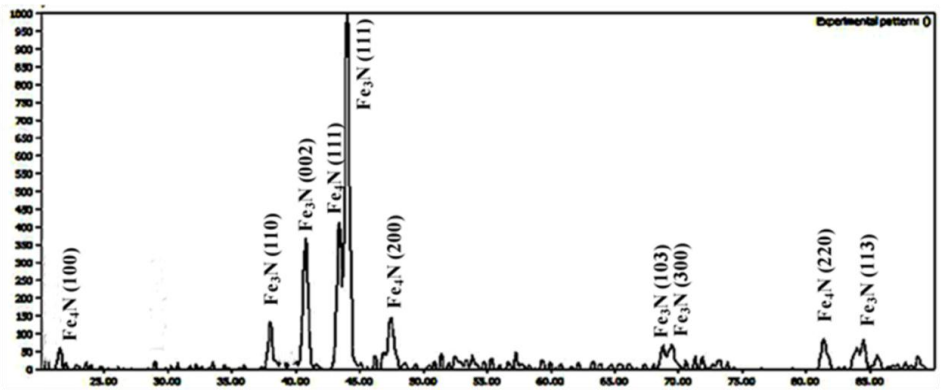

c

Figure 5.7: X-ray diffraction patterns: a – quenched and tempered state; b – nitrided state; c – Duplex treated state

The result of X-ray analysis showed only the presence of iron phases on the untreated samples. The reflections from the cubic iron phases produce 3 peaks, that can be indexed as (101), (200) and (211), which occur at 2θ values of approximately 44.674º, 65.023° and 82.335 respectively (Figure 5.7 a).

For the nitrided samples, X-ray diffraction analyzes reveals only the presence of iron nitrides. Reflections of hexagonal ε-Fe_3N phase produce 8 peaks, that can be indexed as (100), (101), (110), (002) and (111), (103), (300) and (113), which occur at 2θ values of approximately 21.850°, 29.898°, 38.326°, 41.256°, 43.742°, 68.293°, 69.301° and 61.262°. Cubic iron nitride γ'-Fe_4N reflection produce 4 peaks, that can be indexed as (100), (111), (200) and (220), which occur at 2θ values of approximately 22.042°, 43.685°, 48.104° and 57.955° (Figure 5.7 b). Determination of iron nitride phases proved that the nitriding process was effectively carried out.

Iron nitride phases (Fe_3N and Fe_4N) were determined on the Duplex treated samples, as expected. Reflections of hexagonal ε-Fe_3N phase produce 6 peaks, that can be indexed as (110), (002) and (111), (103), (300) and (113), which occur at 2θ values of approximately 38.326°, 41.256°, 43.742°, 68.293°, 69.301° and 61.262°. Cubic iron nitride γ'-Fe_4N reflection produce 4 peaks, that can be indexed as (100), (111), (200) and (220), which occur at 2θ values of approximately 22.042°, 43.685°, 48.104° and 57.955°, Figure 5.7 c.

5.3.4 Glancing incidence X-ray diffraction

Glancing incidence analyze was performed on Duplex and non - Duplex samples using a Siemens D5000 diffractometer. The test parameters are presented in Table 5.4.

Table 5.4: Glancing incidence X-ray diffraction parameters

Intensity [mA]	Tension [KV]	Step size	Increment	Scan speed [°/min]	Scan angle [°]	Div.slit	
						Actual	Requested
30	40	0.04	0.04	5	20-90	0.100	0.100

The glancing incidence patterns are presented in Figure 5.8.

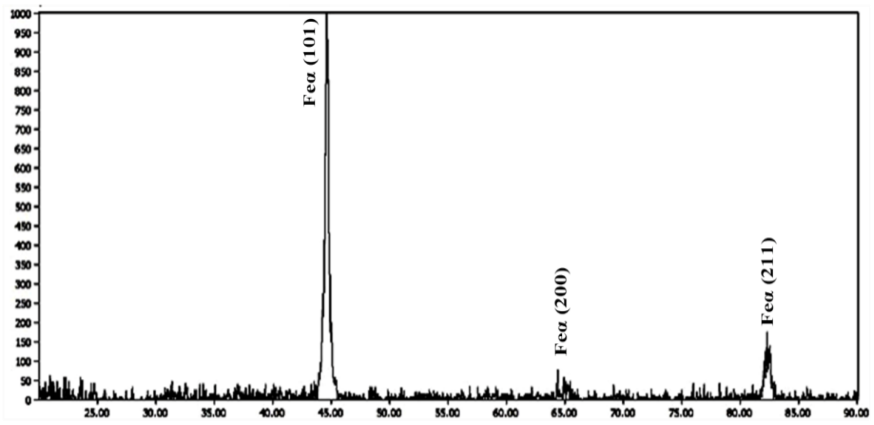

a – quenched and tempered;

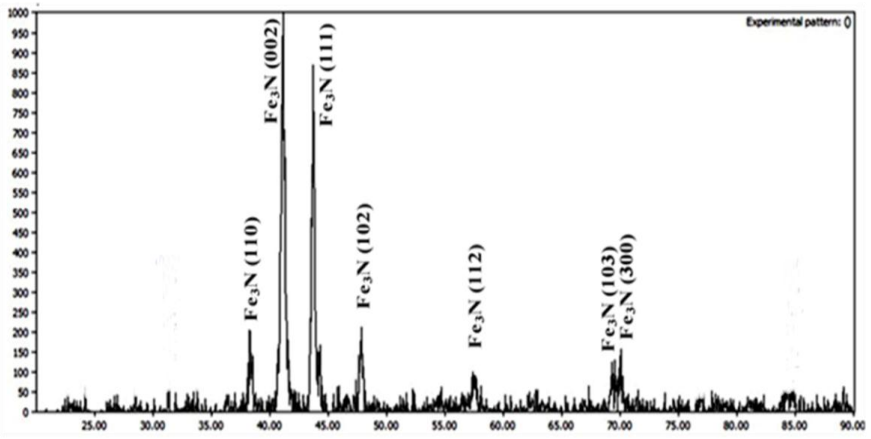

b - nitrided;

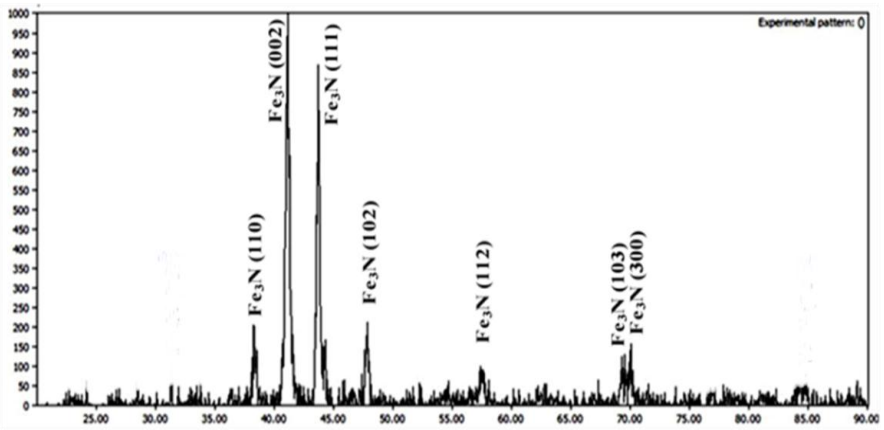

c – Duplex treated;

Figure 5.8: Glancing incidence X-ray diffraction patterns: a – quenched and tempered state; b – nitrided state; c – Duplex treated state

As it can be observed from figure 5.8 a, only iron phases (Fe-α) are presented in the untreated samples structure. The reflection of Fe-α produce 3 peaks indexed as (101), (111) and (201), at 2θ values of approximately 44.674º, 65.023° and 82.335°.

Figure 5.8 b reveals only the presence of iron nitride Fe_3N phase in the structure of nitride samples. Reflections of hexagonal Fe_3N phase produce 7 peaks, that can be indexed as (110), (002), (111), (102), (112), (103), and (300), which occur at 2θ values of approximately 38.326°, 41.256°, 43.742°, 47.151°, 57.561°, and 69.301°. As mentioned before, glancing incidence reveals information about top layers of small thickness. Therefore, at the marginal layer, the structure of the carburized samples is formed only of Fe_3N.

From Figure 5.8 c it can be observed only the presence of Fe_3N phase on the Duplex treated samples. Reflections of hexagonal ε-Fe_3N phase produce 7 peaks, that can be indexed as (110), (002), (111), (102), (112), (103), and (300), which occur at 2θ values of approximately 38.326°, 41.256°, 43.742°, 47.151°, 57.561°, and 69.301°.

5.4 Micro-hardness tests

The Vickers hardness test was used in testing the cross-section micro hardness. The samples were cut, polished with 800 grit paper and then a 200gf load and 15 s loading time was used in Volpert Micro-Vickers Hardness Tester Digital. The hardness was measured from the surface down to the substrate and plotted in Figure 5.9.

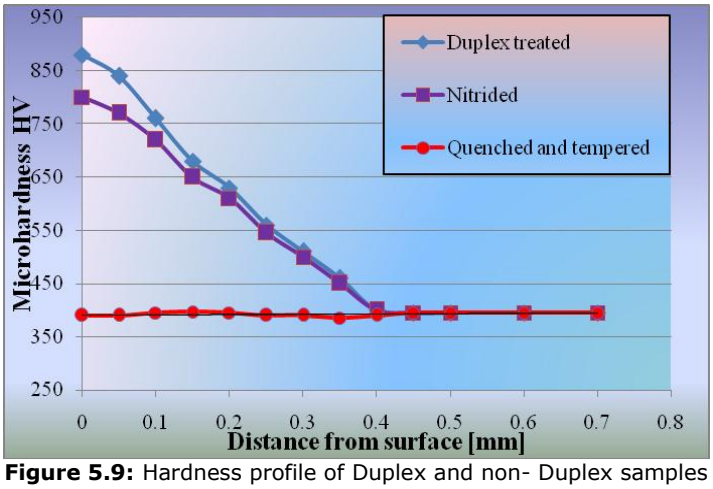

Figure 5.9: Hardness profile of Duplex and non- Duplex samples

The maximum value of hardness of 880 HV0.2 was obtained in the Duplex treated state. At distances over 0.4 mm from the surface, the hardness remains constant, with values in range of 390-395 HV0.2. In nitrided state was obtained a maximum value of 800 HV0.2, near the white layer. In the diffusion layer, the hardness decreases with the distance from the surface. In the quenched and tempered state, the hardness is constant, ranging between 390-395 HV0.2. It can be noted that, compared with the untreated state, the hardness increased about 2.38 times for the Duplex treated sample.

5.5 Instrumented indentation tests

5.5.1 Bulk modulus determination

In this study, bulk modulus of Duplex and non – Duplex samples was determined from the analysis of the load-depth curves [156], using a Dynamic Ultra Micro Hardness (DUH) tester equipped with a diamond Berkovich indenter type. The indentation prints are presented in Figure 5.10.

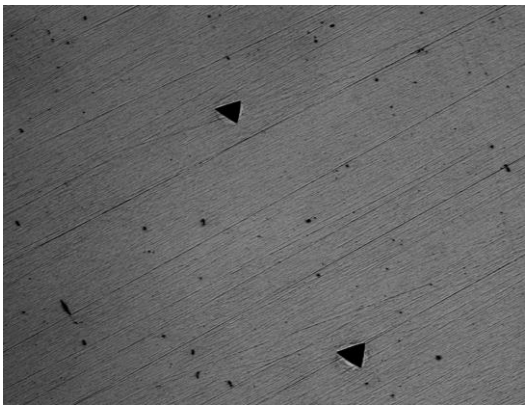

Figure 5.10: Indentation print

Each specimen was subjected to load-unload cycle under the same amount of maximum load and the loads vs. penetration depth curves were plotted, Figure 5.11. The holding time at loading was 15 s. To get more accurate values twelve measurements, with the applied load ranging from 100 to 1000 mN, were performed. The results obtained are presented in Table 5.5.

Tabelul 5.5: Values obtained by means of micro-indentation test

Measurements	Quenched and tempered state			Nitrided state			Duplex treated state		
	F [mN]	h_{max} [µm]	h_r [µm]	F [mN]	h_{max} [µm]	h_r [µm]	F [mN]	h_{max} [µm]	h_r [µm]
1	102.19	1.2276	1.1388	101.95	1.1023	0.984	101.32	0.8426	0.7085
2	101.87	1.4164	1.3386	101.94	1.1165	1.0571	101.22	0.8922	0.7637
3	207.47	1.9455	1.8056	207.69	1.6513	1.4597	207.73	1.0811	0.8554
4	207.87	2.0398	1.8996	207.69	1.7509	1.5725	209.99	1.1457	0.9273
5	407.31	3.1578	2.9536	406.95	2.4518	2.1557	410.07	1.8932	1.5916
6	407.95	3.1431	2.9403	406.73	2.6158	2.3318	406.37	1.8131	1.4914
7	609.86	3.9095	3.630	609.7	3.2166	2.8235	609.78	1.9897	1.543
8	611.52	3.8177	3.5161	609.49	3.3330	2.9445	609.77	2.2263	1.8106
9	809.14	4.3551	3.9967	808.14	3.9898	3.5017	809.06	2.4532	1.9224
10	810.41	3.8826	3.4646	808.15	3.8159	3.3122	808.65	2.4824	1.9637
11	1010.9	4.6774	4.2464	1008.45	4.4121	3.793	1007.33	2.6597	2.0278
12	1008.4	5.0388	4.6148	1007.39	4.7802	3.7934	1007.53	2.6562	1.9564

Before micro indentation testing can be performed, it is necessary to create a high-quality surface in order to ensure both accuracy and repeatability of the tests. Therefore, the samples have been metallographically mounted, grinded and polished.

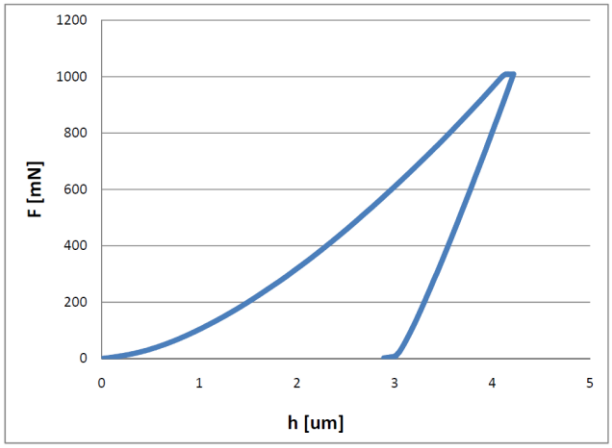

a – Quenched and tempered;

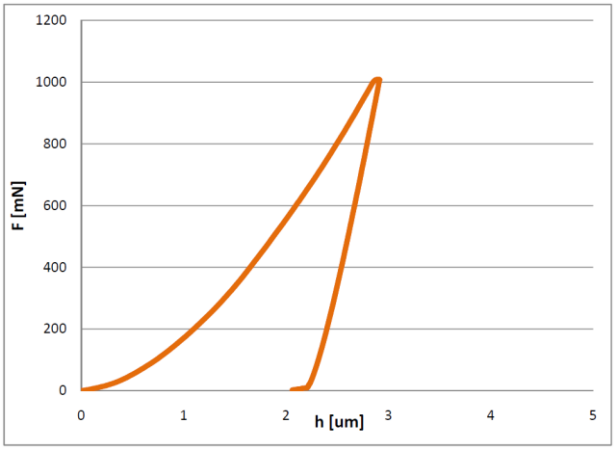

b – Nitrided state;

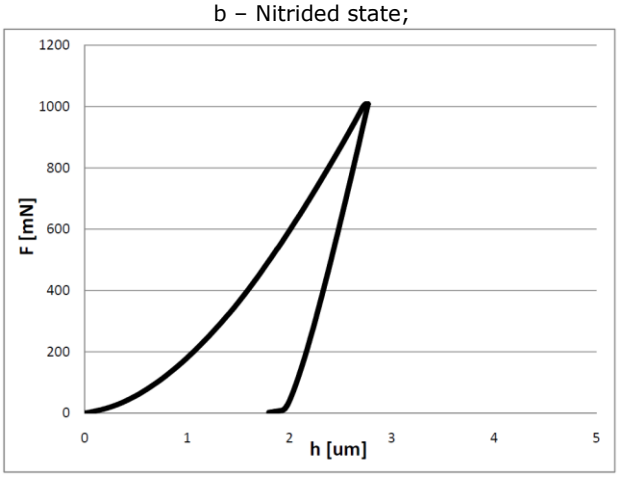

c - Duplex treated;

Figure 5.11: Load – penetration depth curve: a – quenched and tempered state; b – nitrided state; c – Duplex treated state.

As it can be observed from Figure 5.11 and Table 5.5, the penetration depths of Duplex treated samples are much lower compared with the penetration depths of quenched and tempered state. The bulk modulus can be calculated from the total compliance of the sample and of the instrument, according to equation 4.9.

The instrument compliance C_f for Duplex and non - Duplex samples was determined by plotting the inverse of the contact stiffness (1/S) as function of the inverse contact depth $1/h_c$, figure 5.12. The representation is linear, so the slope is directly linked to the bulk modulus of the material.

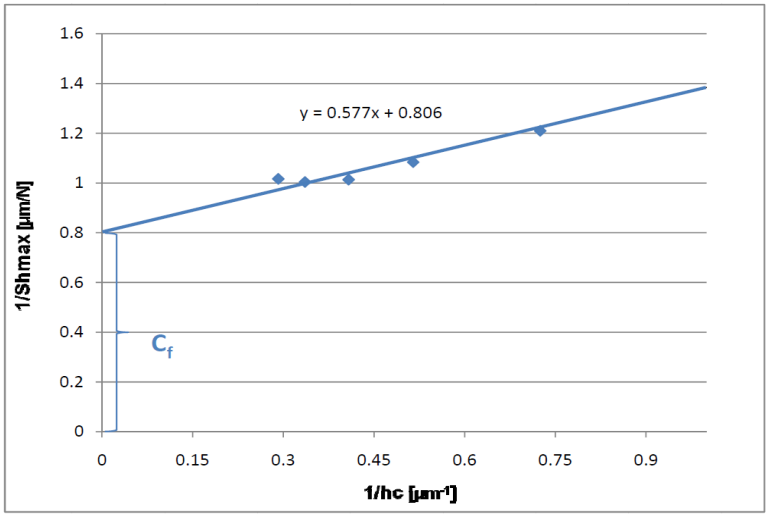

a – quenched and tempered;

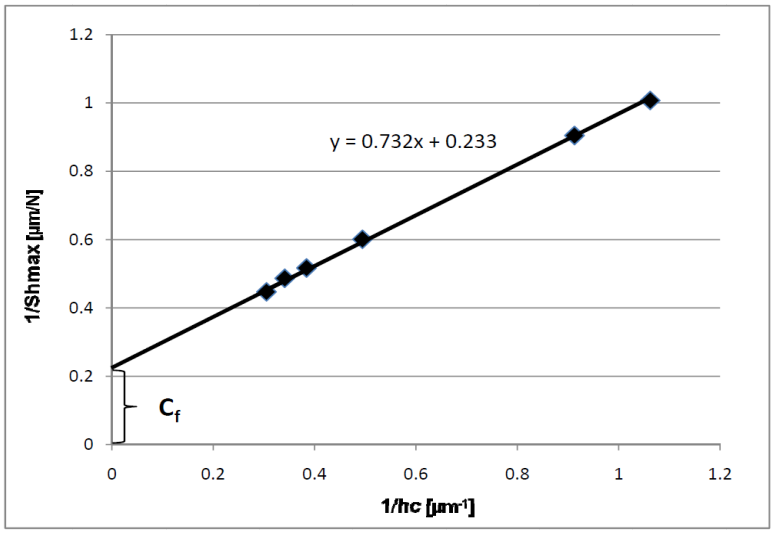

b – Nitrided;

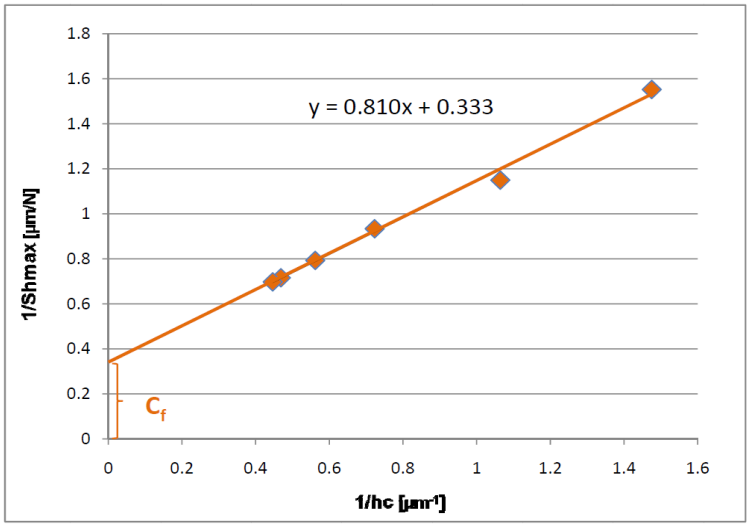

c - Duplex treated;

Figure 5.12: 1/S as a function of 1/hc performed on: a - annealed state; b - carburized state; c - Duplex treated state;

The bulk modulus of each sample was determined according to equation 4.9. Taking into consideration the elastic properties of the indenter, 1140 GPa for the bulk modulus and 0.07 for the Poisson's ratio and by taking 0.3 for the Poisson's ratio of the material, we obtain the values for the reduced and bulk modulus presented in Table 5.6.

Table 5.6: Values of bulk and reduced modulus

Structural state	Reduced modulus, E_R [GPa]	Bulk modulus, E_m [GPa]
Quenched and tempered	147	165
Nitrided	210	237
Duplex treated	240	265

It can be observed that bulk modulus increased from 165 GPa (annealed state) to 265 GPa (Duplex treated state).

5.5.2 Hardness determination

The values of Martens hardness for Duplex and non Duplex samples are presented in Table 5.7.

Table 5.7: Martens hardness values for Duplex and non – Duplex samples

No.	Annealed				Carburized				Duplex			
	F [mN]	h_{max} [mm]	HM [GPa]	HM ave	F [mN]	h_{max} [mm]	HM [GPa]	HM ave	F [mN]	h_{max} [mm]	HM [GPa]	HM ave
1	102.19	1.22	**2.65**	**3.86**	101.95	1.10	**3.29**	**4.19**	101.32	0.84	**5.56**	**7.85**
2	101.87	1.41	**1.98**		101.94	1.11	**3.21**		101.22	0.89	**4.95**	
3	207.47	1.94	**2.21**		207.69	1.65	**3.10**		207.73	1.08	**7.32**	
4	207.87	2.03	**2.01**		207.69	1.75	**2.75**		209.99	1.14	**6.57**	
5	407.31	3.15	**1.69**		406.95	2.45	**2.87**		410.07	1.89	**4.86**	
6	407.95	3.14	**1.70**		406.73	2.61	**2.50**		406.37	1.81	**5.28**	
7	609.86	3.90	**1.69**		609.7	3.2166	**2.55**		609.78	1.98	**6.96**	
8	611.52	3.81	**1.78**		609.49	3.3330	**2.37**		609.77	2.22	**5.45**	
9	809.14	4.35	**1.85**		808.14	3.9898	**2.23**		809.06	2.45	**6.19**	
10	810.41	3.88	**2.38**		808.15	3.8159	**2.45**		808.65	2.48	**6.03**	
11	1010.9	4.67	**2.06**		1008.45	4.4121	**2.33**		1007.33	2.65	**6.79**	
12	1008.4	5.03	**1.75**		1007.39	4.7802	**1.95**		1007.53	2.65	**6.81**	

As it can observed from Table 5.7, the average values of Martens hardness corresponding to quenched and tempered state is 3.86 GPa, 4.19 GPa corresponding to the nitrided state and 7.85 GPa for Duplex treated state. Martens hardness for Duplex state (Figure 5.13) increased 2 times compared to quenched and tempered and 1.5 times compared to nitrided state, respectively.

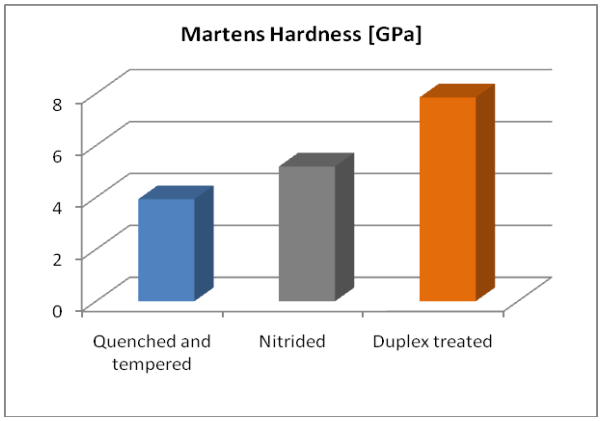

Figure 5.13: Martens hardness

5.5.3 Internal stresses

After obtaining the characteristic indentation curves under different applied loads, the residual stresses were calculated as presented in Chapter 4. In this case, the internal stresses induced by work hardening through shot peening were determined by comparing the load-unload curves of quenched and tempered samples, which were considered the virgin material, with the load-unload curves of Duplex treated samples, considered the stressed material. The residual stress values are presented in Table 5.8 and illustrated in Figure 5.14.

Table 5.8: Values of the residual stress

Fm [mN]	hc [µm]	Fm [mN]	hc [µm]	A_0 [mm^2]	A_C [mm^2]	ρ_{ave} [N/mm^2]	Residual stress [MPa] By Suresh et al	Residual stress [MPa] by Atar et al
102.19	1.16	101.32	0.74	3.56E-05	1.46E-05	2868.45	**-1352**	**-393**
207.47	1.84	207.73	0.91	8.95E-05	2.20E-05	2317.13	**-1815**	**-475**
407.31	3.00	406.37	1.57	2.39E-04	6.53E-05	1707.03	**-1410**	**-397**
609.86	3.70	609.78	1.65	3.62E-04	7.24E-05	1685.62	**-1186**	**-344**
809.14	4.09	809.06	2.06	4.41E-04	1.12E-04	1833.44	**-1148**	**-327**
1010.90	4.35	1007.53	2.13	5.01E-04	1.20E-04	2017.46	**-1732**	**-435**

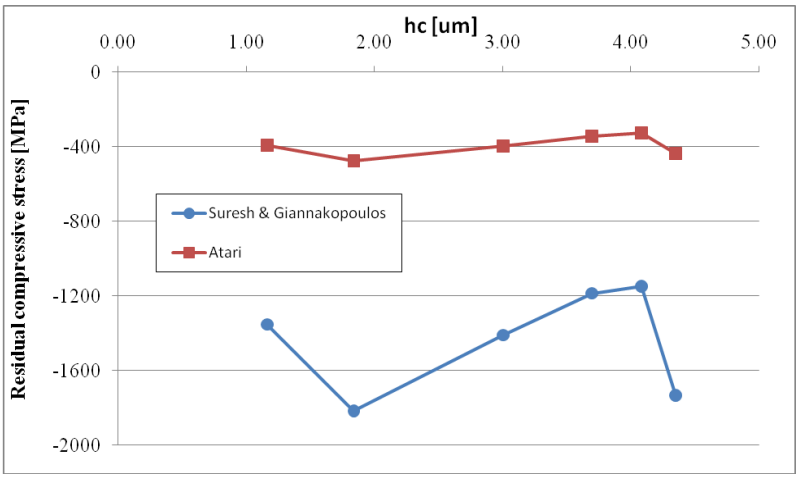

Figure 5.14: Residual Compressive Stress variations function indentation depths

The stress measurement revealed high compressive stresses ranging between -393 MPa and -435 MPa (Atari method) and -1352 MPa to -1732 MPa (Suresh method), as it can observed from Figure 5.14.

5.6 Corrosion behaviour

The corrosion behavior of Duplex and non - Duplex samples was electrochemical investigated in different environments by means of linear polarization. For the tests, the samples were prepared as presented in Chapter 4.

The electrochemical experiments were carried out at room temperature, by a three electrode cell assembly, as presented in the previous chapter. The parameters related to the corrosion resistance, specifically, the polarization resistance (R_p), the corrosion current density (i_{corr}) and the potential of corrosion (E(I=0)), were obtained using the software Corrview.

5.6.1 Corrosion behaviour in 3 % NaCl

The linear polarization curves obtained for Duplex and non- Duplex samples are shown in Figure 5.15. The curves were obtained by plotting the current density change depending on the applied potential in time.

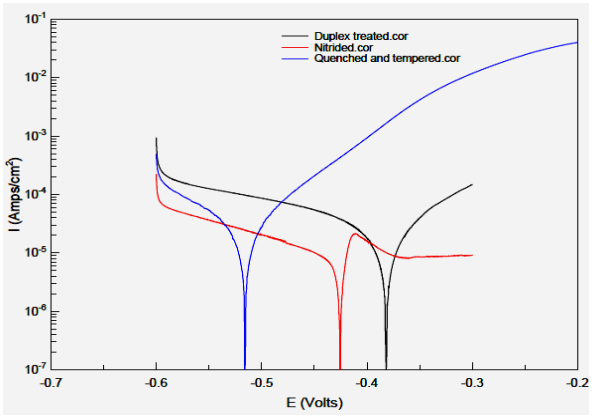

Figure 5.15: Polarization curves of Duplex and non- Duplex samples tested

As it can be observed from Figure 5.15, the corrosion potential of Duplex treated sample is swept to more positive values compared to the corrosion potential of nitrided and untreated samples, which indicates that the Duplex treated samples are nobler. But, it can be also observed that the nitrided sample pasivated. The kinetic parameters of corrosion process are presented in Table 5.9 [155].

Table 5.9: Parameter values of corrosion test in 3% NaCl

Structural state	Annodic slope, ba [mV]	Cathodic slope, bc [mV]	Corrosion potential, - E_{corr} [V]	Polarization resistance, R_p [Ohm/cm^2]	Current density i_{corr} [A/cm^2]
Quenched and tempered	104.27	333.19	0,516	12.35	$6.28*10^{-5}$
Nitrided	175.41	194.82	0,428	136.66	passivated
Duplex state	123.3	301.19	0,388	141.48	$3.737*10^{-5}$

From Table 5.9 it can be observed that the current density decreases from $6.28*10^{-5}$A/cm^2 (quenched and tempered state) to $3.737*10^{-5}$ A/cm^2 (Duplex treated state). The shift of current density from higher to smaller values indicates improved corrosion behaviour. Hence, the Duplex treated sample has a higher corrosion resistance. Also, the polarization resistance increased from`12.35 Ohm/cm^2 (annealed state) to 141.48 Ohm/cm^2 (Duplex state), which indicates a better corrosion behaviour of Duplex treated samples. According to equation 4.15, it was obtained a corrosion rate of 0.73 mm year^{-1} for untreated state, <1 μm year^{-1} for nitrided state, and 0.43 mm year^{-1} for Duplex treated state. Figure 5.16 presents the corrosion rate for the three structural states. It can be observed an increase of Duplex treated sample corrosion rate of about 45%, compared to untreated sample.

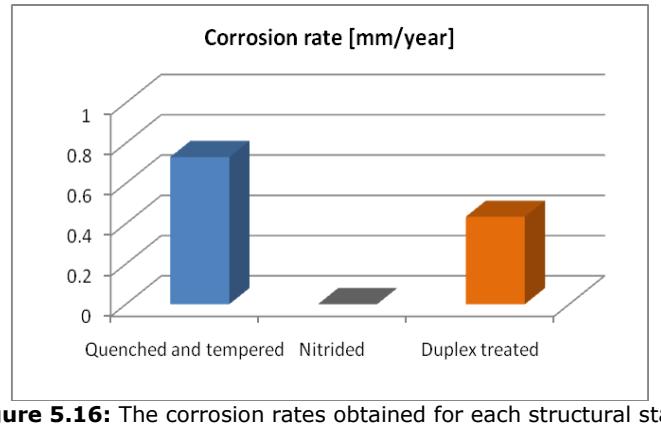

Figure 5.16: The corrosion rates obtained for each structural state

In order to identify the corrosion products, glancing incidence X-ray diffractions tests were performed. The test parameters are presented in Table 5.10.

Table 5.10: Glancing incidence X-ray diffraction parameters

Intensity [mA]	Tension [KV]	Step size	Increment	Scan speed [°/min]	Scan angle [°]	Div.slit	
						Actual	Requested
30	40	0.04	0.04	5	20-90	0.100	0.100

The patterns for each structural state are presented in Figure 5.17.

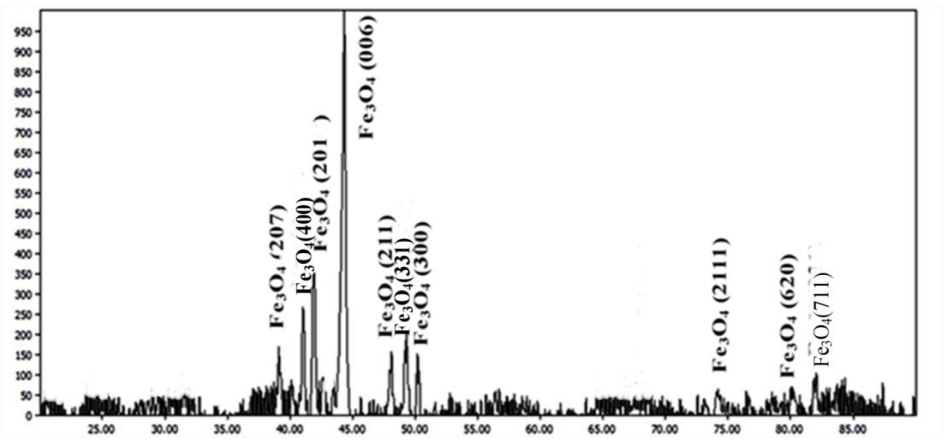

a- quenched and tempered;

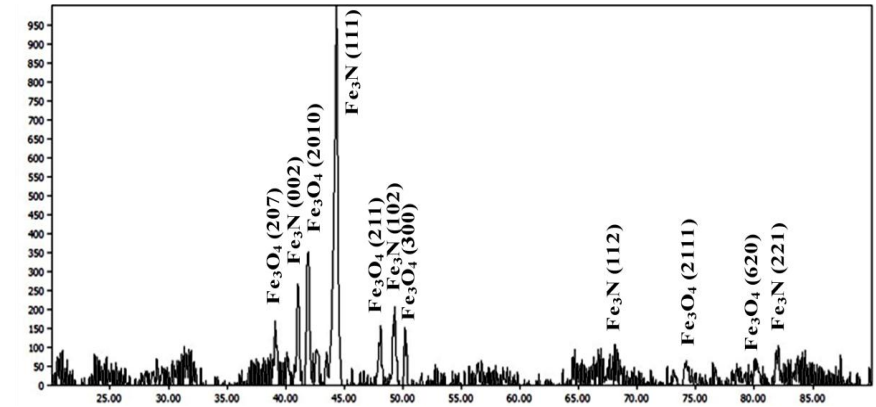

b- nitrided;

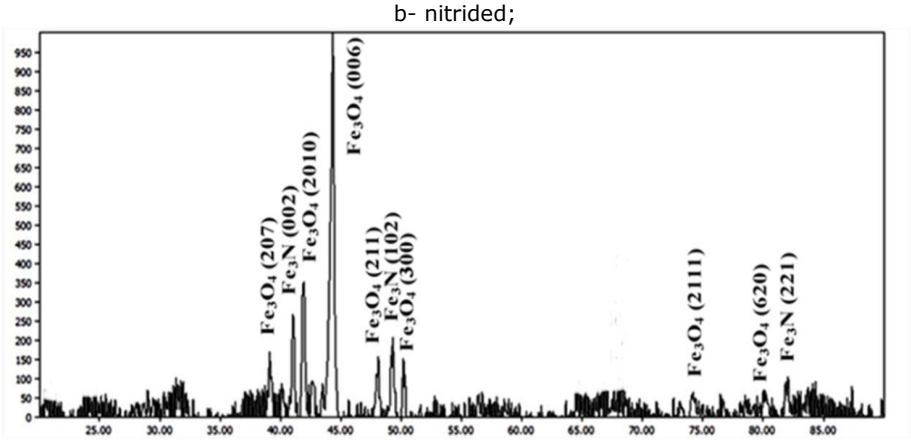

c- Duplex treated;

Figure 5.17: Glancing incidence X-ray diffractions patterns: a – quenched and tempered state; b – nitrided state; c - Duplex treated state;

For the untreated sample, the phase analysis reveals only onecrystallographic phase Fe_3O_4(magnetite). Magnetite reflection produce 10 peaks, that can be indexed as (207), (400), (2010), (006), (211), (331), (300), (2111), (620) and (711) and occur at 2θ values of approximately 39.852°, 41.031°, 42.141°, 44.127°, 48.125, 49.065, 50.116, 74.125, 79.451, and 82.611 ° (Figure 5.17 a).

For the nitrided samples, glancing incidence X-ray diffraction analyzes reveals the presence of iron nitride phases and magnetite. Reflections of hexagonal Fe_3N phase produce 4 peaks that can be indexed as (002), (102), (112), (221) and occurs at 2θ values of approximately 41.252°, 47.151°, 57.561°, 85.641°. Magnetite reflection produce 5 peaks, that can be indexed as (207), (2010), (300), (2 111), (620) and occur at 2θ values of approximately 39.852°, 42.141°, 50.116, 74.125, and 79.451°.(Figure 5.17 b).

Glancing incidence analyze showed the presence of Fe_3N and Fe_3O_4 phases in Duplex treated samples. Reflection of Fe_3N produce 3 peaks, that can be indexed as (002), (102), (221) and occurs at 2θ values of approximately 41.252°, 47.151°, 85.641°. Magnetite reflection produce 7 peaks, that can be indexed as as (207), (2010), (006), (211), (331), (300), (2111), (620) and (711) and occur at 2θ values of approximately 39.852°, 42.141°, 44.127°, 48.125°, 49.065°, 50.116°, and 74.125°, Figure 5.17 c.

The surfaces of the corroded samples were analyzed by image acquisition and by energy dispersive X-ray spectrometry (EDX). Figure 5.18 presents SEM images of corroded surfaces of Duplex and non- Duplex samples.

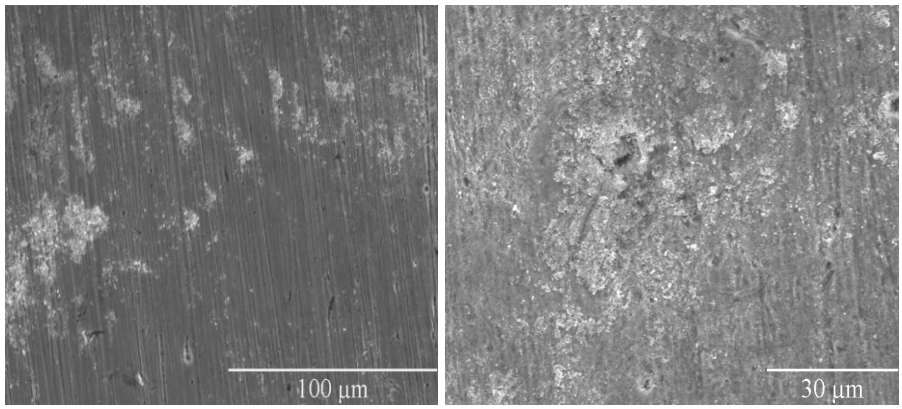

a- quenched and tempered;

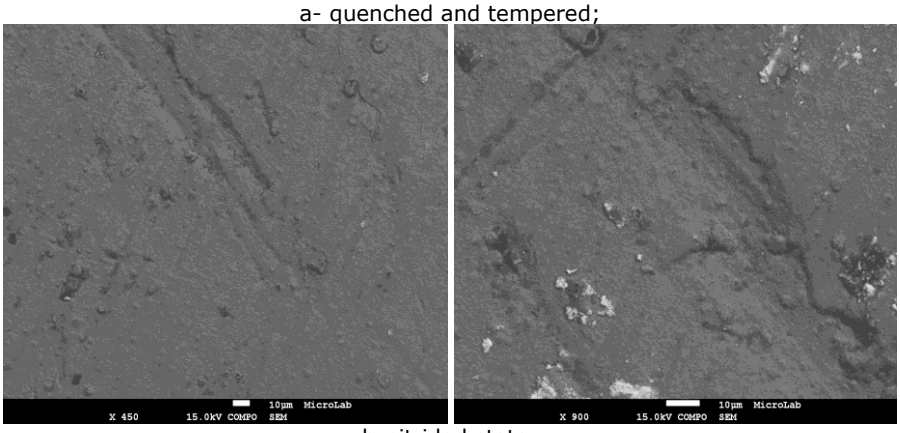

b-nitrided state;

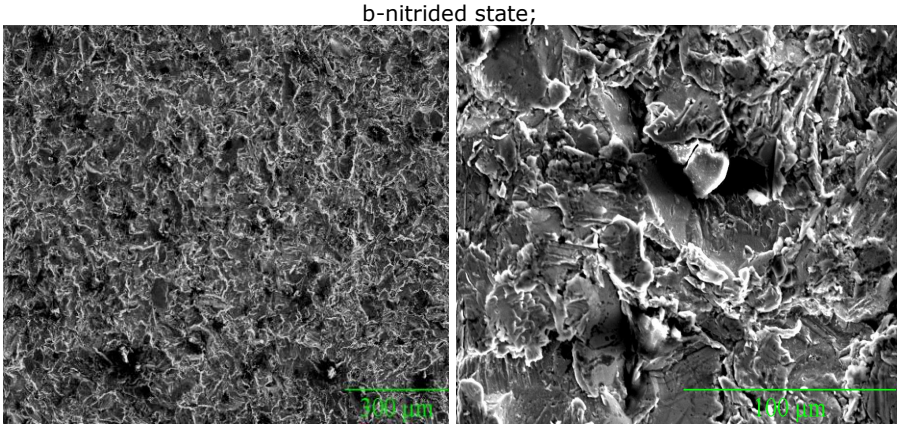

c- Duplex state;

Figure 5.18: SEM imagines of corroded surfaces: a – annealed state; b - carburized state; c- Duplex treated state

From Figure 5.18 it can be observed the tendency towards pitting corrosion for untreated and Duplex treated state. The nitride sample does not presents pits on

the surface, due to the formation of a protective layer (passivation). In order to determine the elemental composition of the corroded samples, EDX investigations were carried out, Figure 5.19

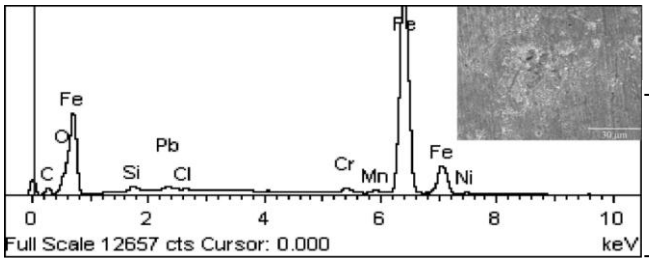

Element	App Conc.	Intensity Corrn.	Weight%	Weight% Sigma	Atomic%
C K	3.08	0.4320	6.46	0.39	22.81
O K	4.14	1.2362	3.03	0.31	8.04
Na K	0.14	0.3751	0.33	0.08	0.61
Si K	0.49	0.6428	0.69	0.04	1.05
Cl K	0.15	0.7983	0.17	0.04	0.20
Cr K	1.34	1.2058	1.00	0.05	0.82
Mn K	0.63	0.9528	0.60	0.06	0.46
Fe K	91.95	0.9731	85.44	0.49	64.92
Ni K	1.16	0.8717	1.21	0.09	0.87
Pb M	0.92	0.7781	1.07	0.13	0.22
Totals			100.00		

a - quenched and tempered;

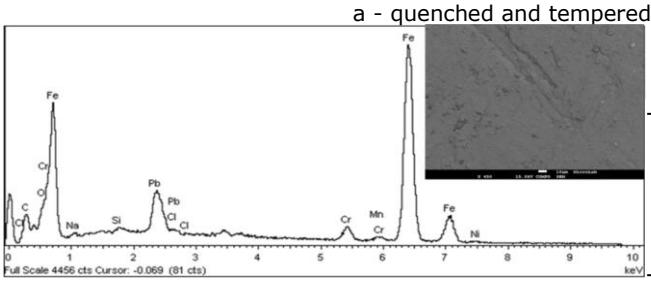

Element	App Conc.	Intensity Corrn.	Weight%	Weight% Sigma	Atomic%
C K	3.08	0.4320	6.46	0.39	22.81
O K	4.14	1.2362	3.03	0.31	8.04
Na K	0.14	0.3751	0.33	0.08	0.61
Si K	0.49	0.6428	0.69	0.04	1.05
Cl K	0.15	0.7983	0.17	0.04	0.20
Cr K	1.34	1.2058	1.00	0.05	0.82
Mn K	0.63	0.9528	0.60	0.06	0.46
Fe K	91.95	0.9731	85.44	0.49	64.92
Ni K	1.16	0.8717	1.21	0.09	0.87
Pb M	0.92	0.7781	1.07	0.13	0.22
Totals			100.00		

b - nitrided;

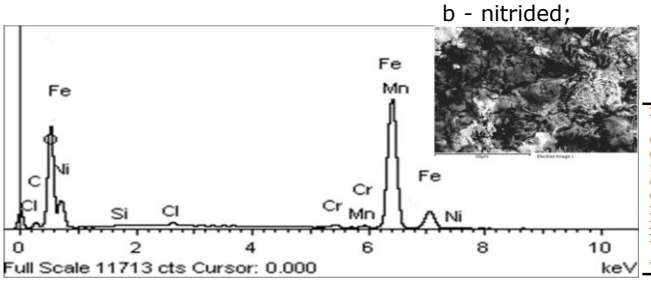

Element	App Conc.	Intensity Corrn.	Weight%	Weight% Sigma	Atomic%
C K	0.96	0.4623	2.71	0.54	7.15
O K	30.66	1.5123	26.36	0.39	52.28
Si K	0.09	0.6652	0.17	0.04	0.19
Cl K	0.35	0.8053	0.57	0.05	0.51
Cr K	0.61	1.1502	0.69	0.05	0.42
Mn K	0.48	0.9173	0.68	0.07	0.39
Fe K	48.47	0.9328	69.55	0.52	38.37
Ni K	0.44	0.8552	0.66	0.10	0.36
Totals			100.00		

c- Duplex treated;

Figure 5.19: EDX spectrums: a - quenched and tempered; b - nitrided; c - Duplex treated;

As it can be observed from Figure 5.19, the corroded surface of all the samples contains nearly all the elements of EN 34CrNiMo6 (Mn, Cr, Si, etc) and additionally O indicating that nearly all the elements participate in the corrosion layer formation. Very clearly, the corroded surface is much richer in Fe while poorer in every metallic element. Another obvious aspect is that the surface contains O in a significant amount. Furthermore, clorium, which is present in the solution (NaCl), is also present in the corroded surface. Due to the paint used to protect the surface which was not tested, Pb is another element present in EDX spectrum. The elements distribution for each sample is presented in Figure 5.20.

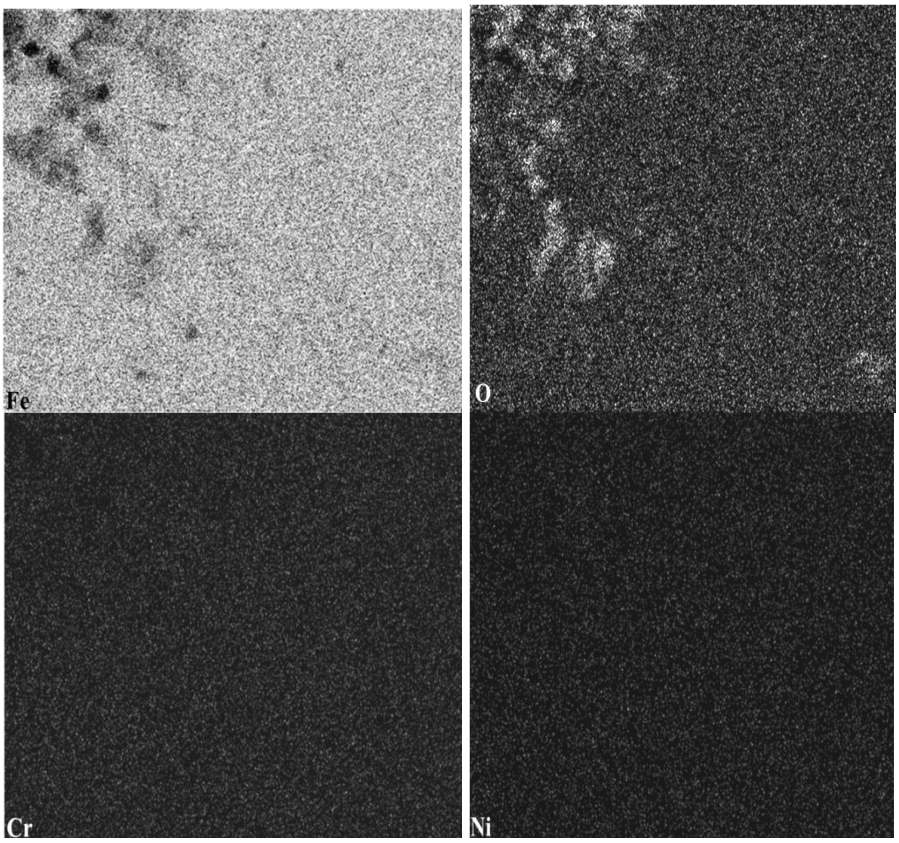

a – quenched and tempered state;

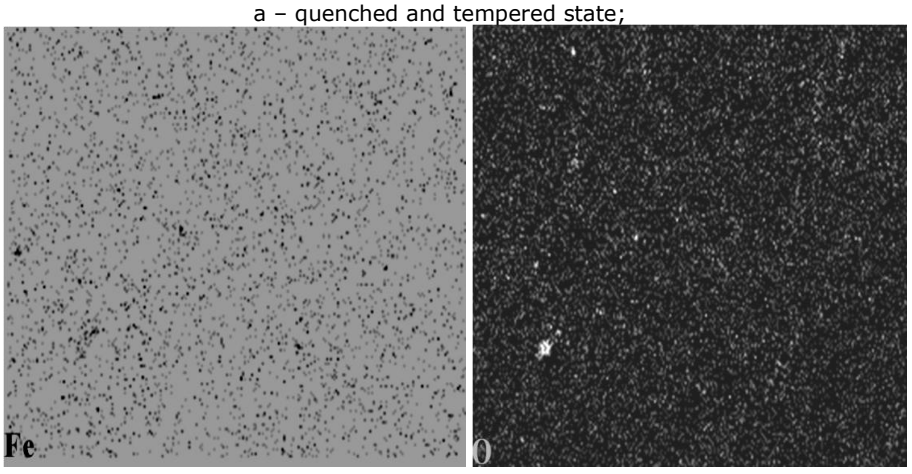

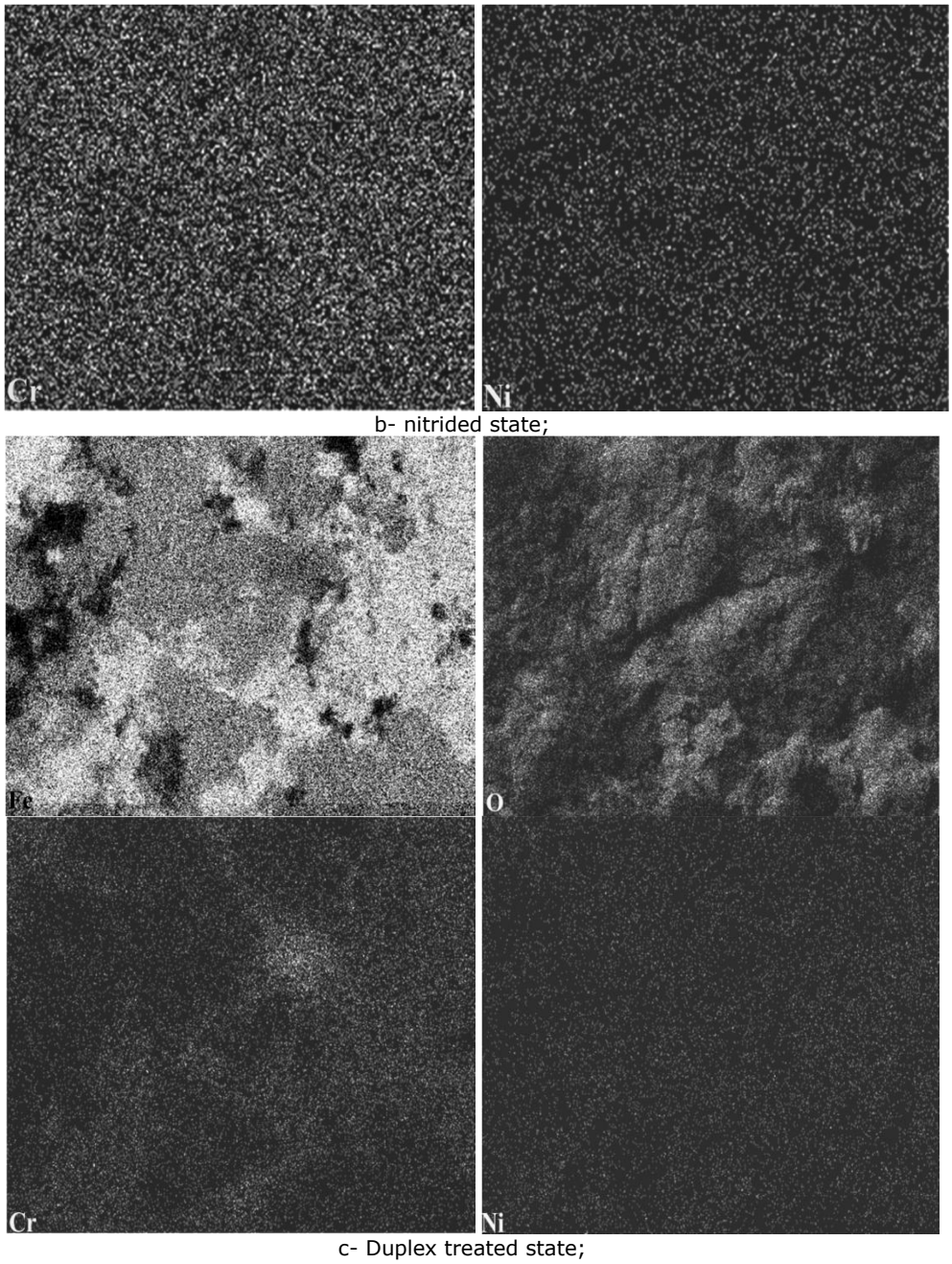

b- nitrided state;

c- Duplex treated state;

Figure 5.20: EDX element distribution: a – quenched and tempered state; b – nitrided state; c - Duplex treated state.

5.6.2 Corrosion behaviour in 0.5 M H_2SO_4

The linear polarization curves obtained for Duplex and non- Duplex samples are presented in Figure 5.21.

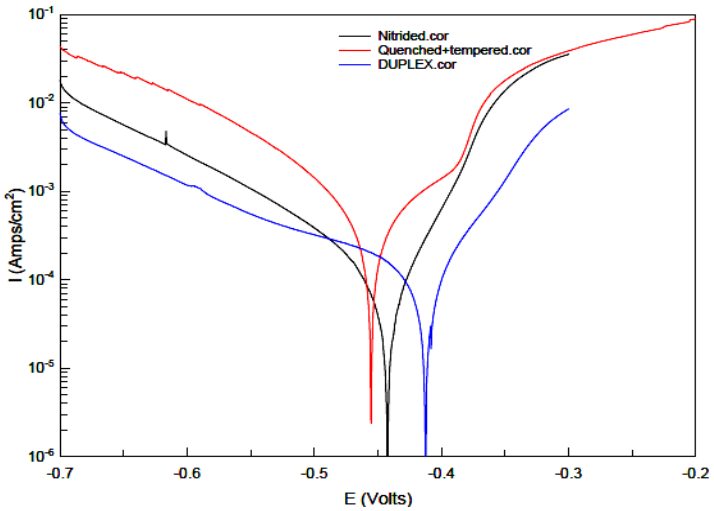

Figure 5.21: Liniar polarization curves of Duplex and non-Duplex samples

As it can be observed from figure 5.21, the corrosion potential of Duplex treated sample is swept to more positive values compared to the corrosion potential of nitrided and untreated samples, which indicates that the Duplex treated samples are nobler. The kinetic parameters of corrosion process are presented in Table 5.11.

Tabelul 5.11: Parameter values of corrosion test in 0.5 M H_2SO_4

Structural state	Annodic slope, ba [mV]	Cathodic slope, bc [mV]	Corrosion potential, $-E_{corr}$ [V]	Polarization resistance, R_p [Ohm/cm^2]	Current density, i_{corr} [A/cm^2]
Quenched and tempered	113.3	133.7	0,455	49.23	$7.49*10^{-4}$
Nitrided	25.57	31.81	0.433	111.75	$2.84*10^{-4}$
Duplex state	82.38	82.47	0.391	144.91	$4.23*10^{-4}$

From Table 5.11 it can be observed that the current density decreases from $7.49*10^{-4}$A/cm^2 (quenched and tempered state) to $4.23*10^{-4}$A/cm^2 (Duplex treated state). The shift of current density from higher to smaller values indicates improved corrosion behaviour. Hence, the Duplex treated sample has a higher corrosion resistance. Also, the polarization resistance increased from 49.23 Ohm/cm^2 (quenched and tempered state) to 144.91 Ohm/cm^2 (Duplex state), which indicates a better corrosion behaviour of Duplex treated samples.

According to equation 4.15, it was obtained o corrosion rate of 8.71 mm year^{-1} for untreated state), 3.30 mm year^{-1} for nitrided state, and 4.23 mm year^{-1} for Duplex treated state. Figure 5.22 presents the corrosion rate of the three structural states. It can be observed a decrease of the corrosion rate of about 54 % for the Duplex treated sample compared to untreated state.

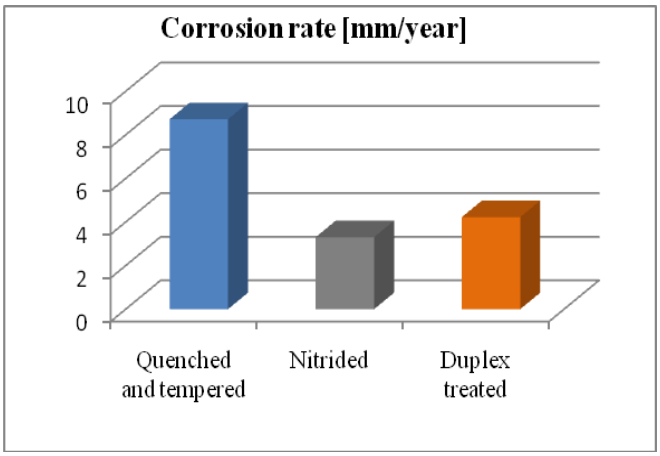

Figure 5.22: The corrosion rates obtained for each structural state

In order to identify the corrosion products, glancing incidence X-ray diffractions tests were performed. The test parameters are presented in Table 5.12.

Table 5.12: Glancing incidence X-ray diffraction parameters

Intensity [mA]	Tension [KV]	Step size	Increment	Scan speed [°/min]	Scan angle [°]	Div.slit	
						Actual	Requested
30	40	0.04	0.04	5	20-90	0.100	0.100

The patterns for each structural state are presented in Figure 5.23

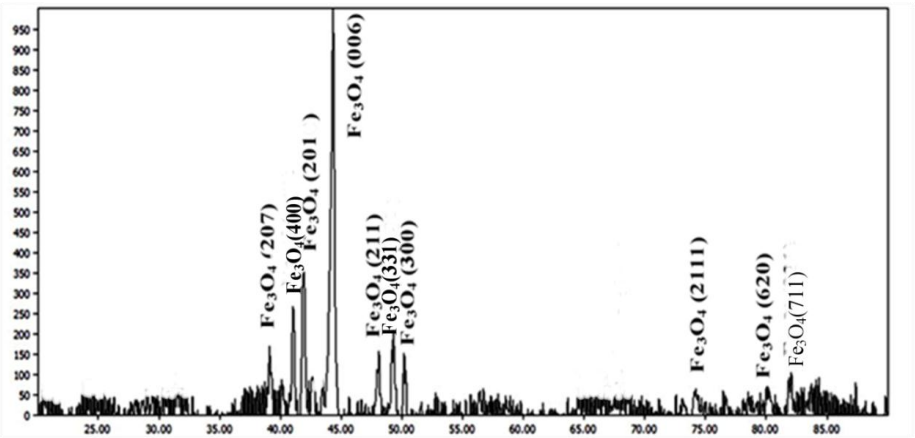

a- quenched and tempered;

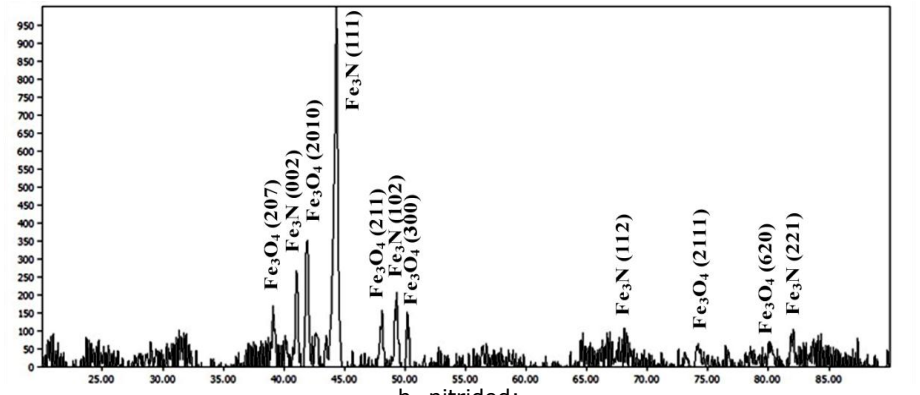

b- nitrided;

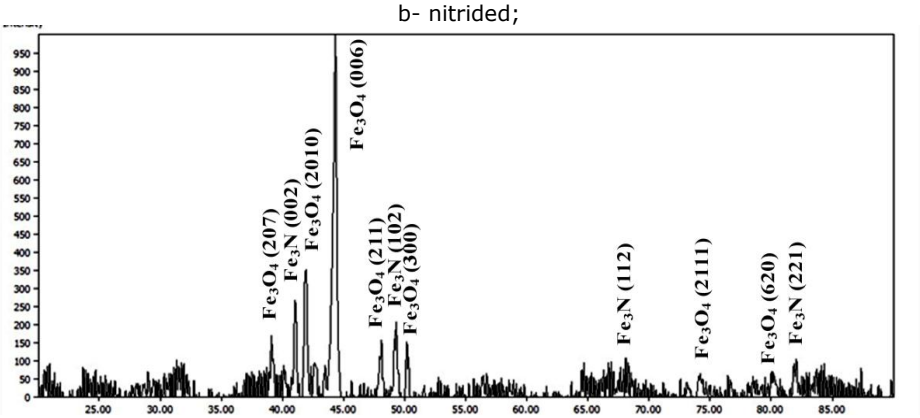

c- Duplex treated;

Figure 5.23: Glancing incidence X-ray diffractions patterns: a – quenched and tempered state; b – nitrided state; c - Duplex treated state;

For untreated state, the phase analysis reveals only one crystallographic Fe_3O_4 (magnetite). Reflection of this phase produce 10 peaks, that can be indexed as (207), (400), (2010), (006), (211), (331), (300), (2111), (620) and (711) and occur at 2θ values of approximately 39.852°, 41.031°, 42.131°, 44.127°, 48.125, 49.065°, 50.116°, 74.125°, 79.451°, and 82.611° (Figure 5.23 a).

For the nitrided samples, glancing incidence X-ray diffraction analyzes reveals the presence of iron nitride and magnetite phases. Magnetite reflection produce 6 peaks, that can be indexed as (207), (2010), (211), (300), (2111), (620), which occur at 2θ values of approximately 39.852°, 42.131°, 48.125°, 50.116°, 49.065°, 74.125° and 79.451°. Reflections of hexagonal Fe_3N phase produce 5 peaks that can be indexed as (002), (111), (102), (112), (221) and occurs at 2θ values of approximately 41.252°, 43.7409, 47.151°, 57.561°, 85.641° (Figure 5.23 b).

Glancing incidence analyze showed the presence of Fe_3N and Fe_3O_4 phases in Duplex treated samples. Reflection of Fe_3N produce 4 peaks, that can be indexed as (002), (102), (112) (221) and occurs at 2θ values of approximately 41.252°, 47.151°, 57.561° and 85.641°. Magnetite reflection produce 7 peaks, that can be indexed as (207), (2010), (006), (211), (331), (300), (2111), (620) and (711) and occur at 2θ values of approximately 39.852°, 42.141°, 44.127°, 48.125°, 49.065°, 50.116°, and 74.125°, Figure 5.23 c.

The surfaces of the corroded samples were analyzed by SEM and by energy dispersive X-ray spectrometry (EDX). Figure 5.24 presents SEM images of corroded surfaces of Duplex and non- Duplex samples.

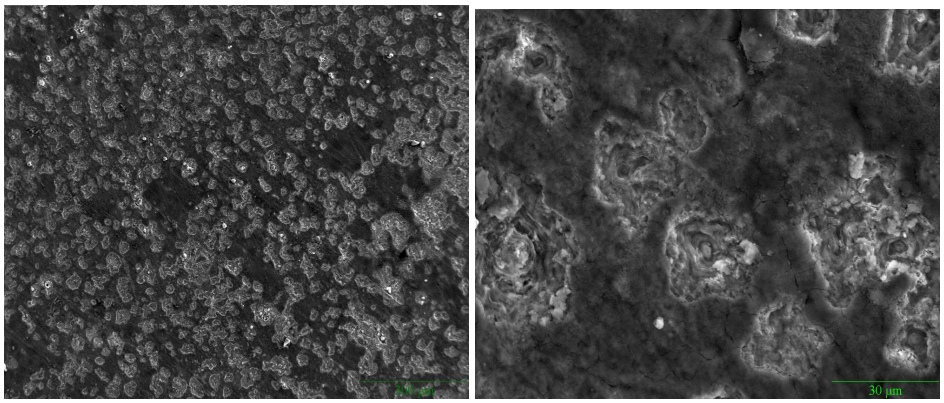

a- quenched and tempered state;

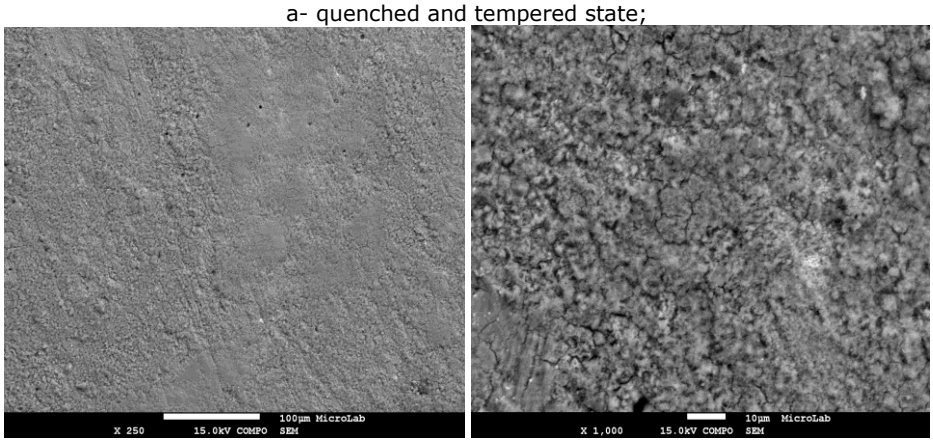

b - nitrided state;

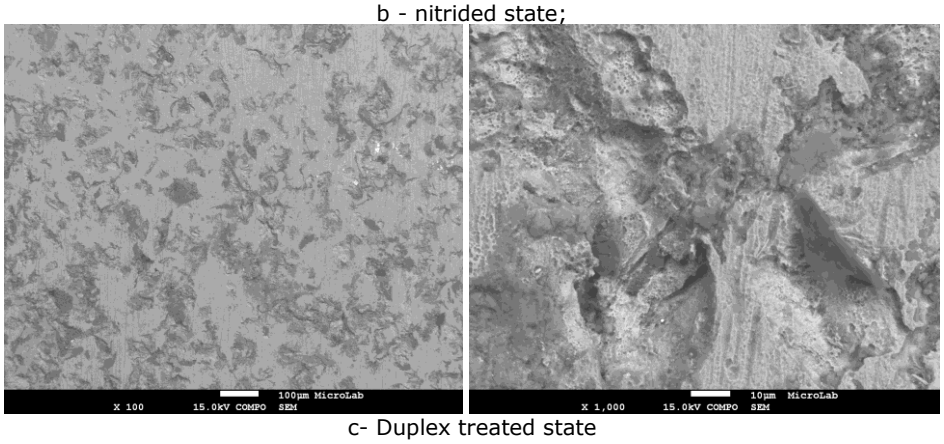

c- Duplex treated state

Figure 5.24: SEM imagines of corroded surfaces: a – quenched and tempered state; b - nitrided state; c- Duplex treated state.

From Figure 5.24 it can be observed the tendency towards pitting corrosion for each structural state. Small pits and micro-cracks can be observed on the

corroded surfaces. Also, it can be noticed that the surface of quenched and tempered state is severely damaged. Pits are present in a significant amount and very deep also.

In order to determine the elemental composition of the corroded samples EDX investigations were carried out, Figure 5.25.

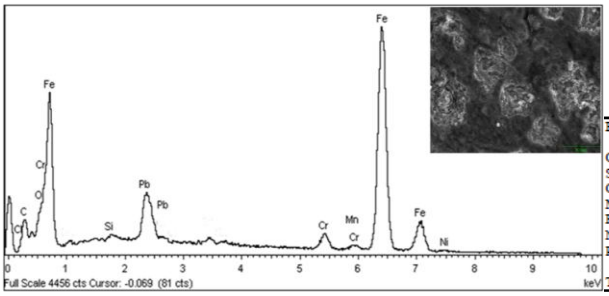

Element	App Conc.	Intensity Corrn.	Weight%	Weight% Sigma	Atomic%
O K	10.83	1.9057	23.69	0.56	56.55
S K	0.50	0.9775	2.48	0.12	2.53
Cr K	0.48	1.0977	2.11	0.15	1.33
Mn K	0.12	0.9088	0.66	0.18	0.39
Fe K	12.48	0.9233	67.85	0.59	38.53
Ni K	0.22	0.8824	1.20	0.29	0.67
PbM	1.97	0.7901	3.79	0.26	1.52
Totals			100.00		

a- quenched and tempered state;

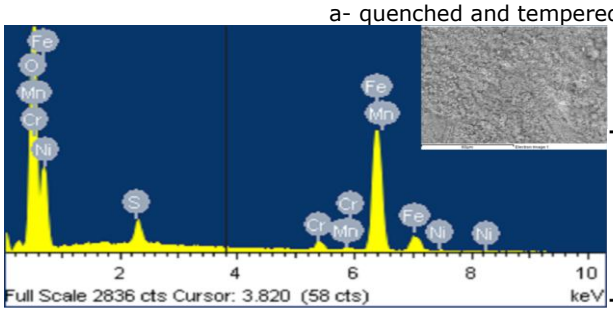

Element	App Conc.	Intensity Corrn.	Weight%	Weight% Sigma	Atomic%
O K	10.83	1.9057	27.69	0.56	56.55
S K	0.50	0.9775	2.48	0.12	2.53
Cr K	0.48	1.0977	2.11	0.15	1.33
Mn K	0.12	0.9088	0.66	0.18	0.39
Fe K	12.48	0.9233	65.85	0.59	38.53
Ni K	0.22	0.8824	1.20	0.29	0.67
Totals			100.00		

b - nitrided state;

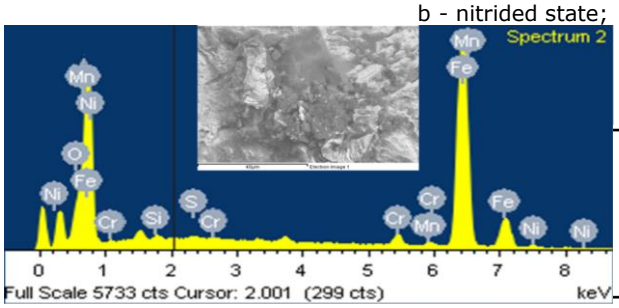

Element	App Conc.	Intensity Corrn.	Weight%	Weight% Sigma	Atomic%
O K	1.16	1.7973	6.11	0.32	6.91
Si K	0.11	0.8097	0.44	0.06	0.81
S K	0.07	0.9832	0.22	0.06	0.36
Cr K	0.84	1.2109	2.27	0.10	2.28
Mn K	0.28	0.9733	0.95	0.13	0.91
Fe K	27.72	0.9906	88.69	0.41	85.80
Ni K	0.45	0.9283	1.57	0.20	1.40
Totals			100.00		

c - Duplex treated state;

Figure 5.25: EDX spectrums: a - quenched and tempered; b - nitrided; c - Duplex treated;

As it can be observed from Figure 5.25, the corroded surface of all the samples contains elements of EN 34CrNiMo6 (Mn, Cr, Si, etc) and additionally O, which indicates the formation of oxides on the surfaces. The corroded surface is richer in Fe while poorer in other element. Another obvious aspect is that the surface contains O in a significant amount, especially for the annealed samples. Due to the chemical composition of the paint used to protect the surface which was not tested, Pb is another element present in EDX spectrum (Figure 5.25 a). The elements distribution for each sample is presented in Figure 5.26.

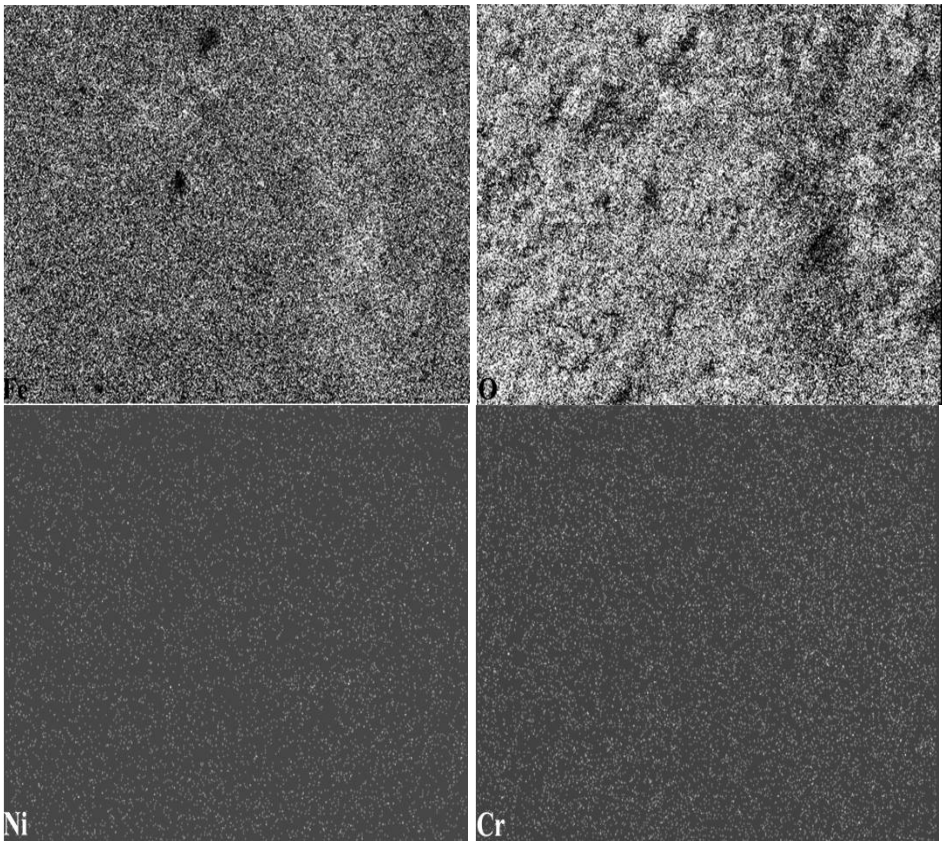

a- quenched and tempered state;

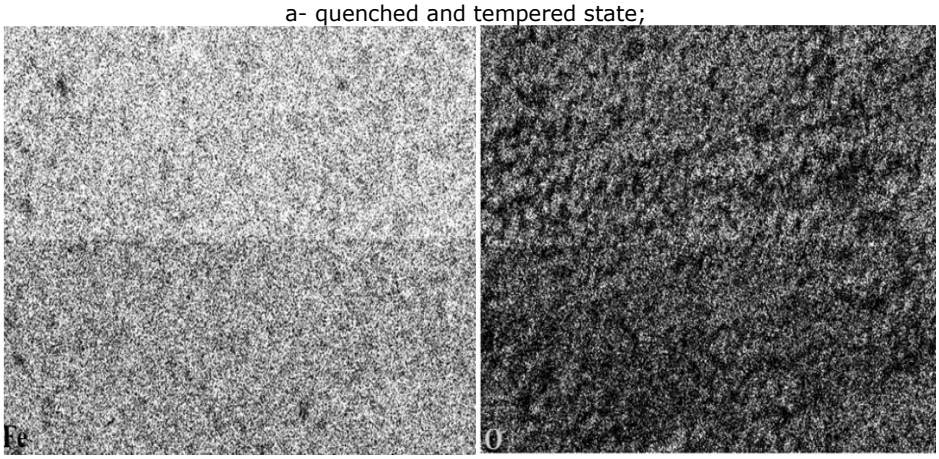

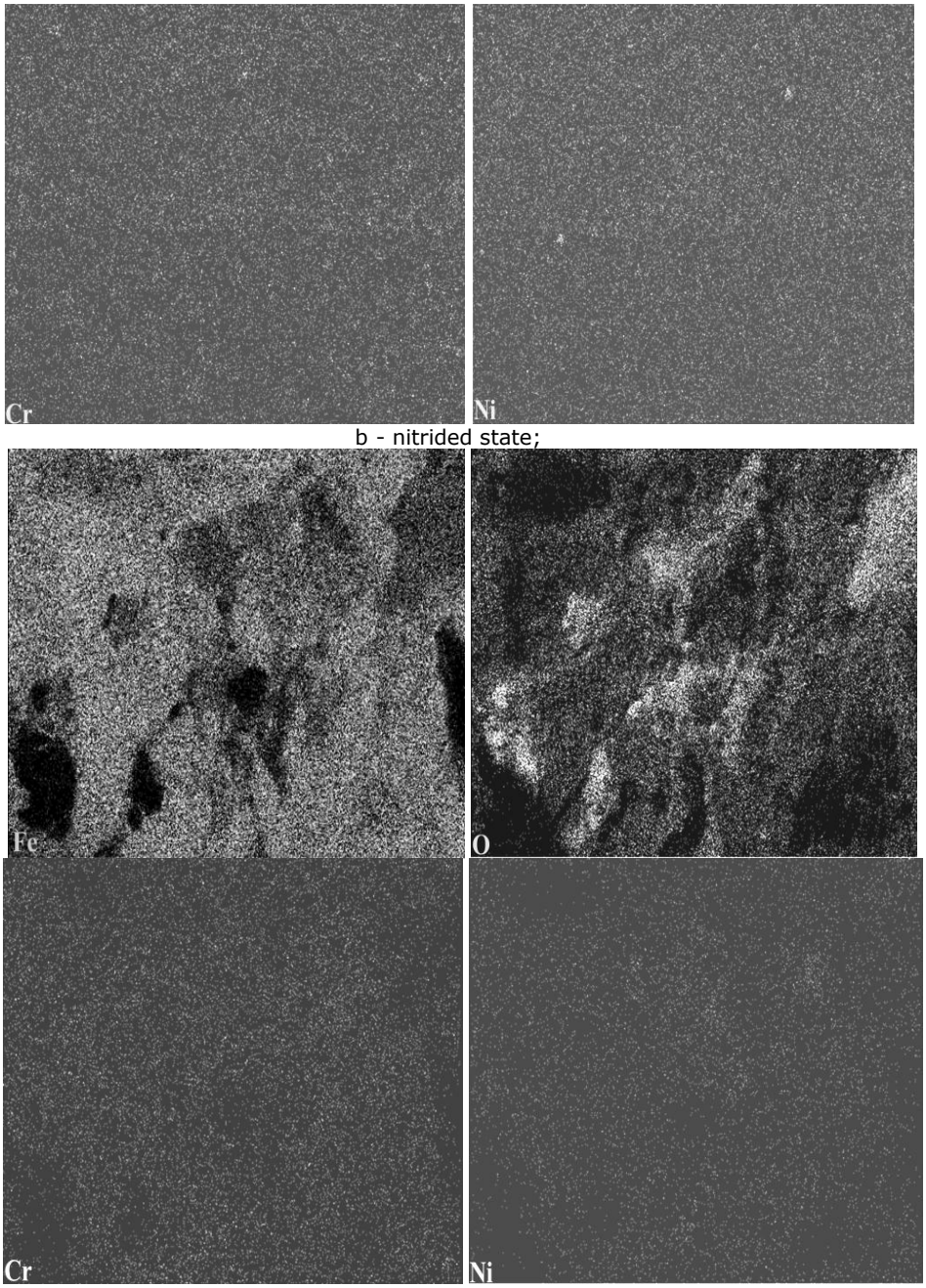

b - nitrided state;

c- Duplex treated state;

Figure 5.26: EDX element distribution: a – quenched and tempered state; b – nitrided state; c - Duplex treated state.

5.6.3 Corrosion behaviour in 0.1 M H_2SO_4

The linear polarization curves obtained for Duplex and non- Duplex samples are presented in Figure 5.27.

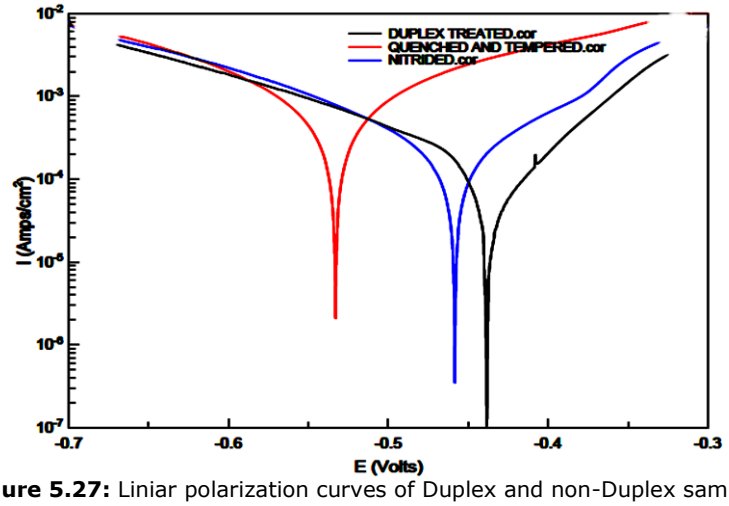

Figure 5.27: Liniar polarization curves of Duplex and non-Duplex samples

As it can be observed from Figure 5.27, the corrosion potential of Duplex treated sample is swept to more positive values compared to the corrosion potential of nitrided and quenched and tempered samples, which indicates that the Duplex treated samples are nobler. The kinetic parameters of corrosion process are presented in Table 5.13.

Tabelul 5.13: Parameter values of corrosion test in 0.1 M H_2SO_4

Structural state	Annodic slope, ba [mV]	Cathodic slope, bc [mV]	Corrosion potential, $-E_{corr}$ [V]	Polarization resistance, R_p [Ohm/cm^2]	Current density, i_{corr} [A/cm^2]
Quenched and tempered	174.23	129.10	0.533	38.29	$6.81*10^{-4}$
Nitrided	177.78	189.62	0.458	97.47	$1.64*10^{-4}$
Duplex state	128.64	110.53	0.435	120.94	$3.89*10^{-4}$

From Table 5.14 it can be observed that the current density decreases from $6.81*10^{-4}$A/cm^2 (quenched and tempered state) to $3.89*10^{-4}$A/cm^2 (Duplex treated state). The shift of current density from higher to smaller values indicates improved corrosion behaviour. Hence, the Duplex treated sample has a higher corrosion resistance. Also, the polarization resistance increased from 38.29 Ohm/cm^2 (annealed state) to 120.94 Ohm/cm^2 (Duplex state), which also indicates a better corrosion behaviour of Duplex treated samples.

According to equation 4.15, it was obtained a corrosion rate of 7.92 mm year^{-1} for untreated samples), 1.90 mm year^{-1} for nitrided state, and 2.89 mm year^{-1} for Duplex treated state. Figure 5.28 presents the corrosion rate of the three structural states. It can be observed a decrease of the corrosion rate of about 60 % for the Duplex treated sample compared to quenched and tempered state.

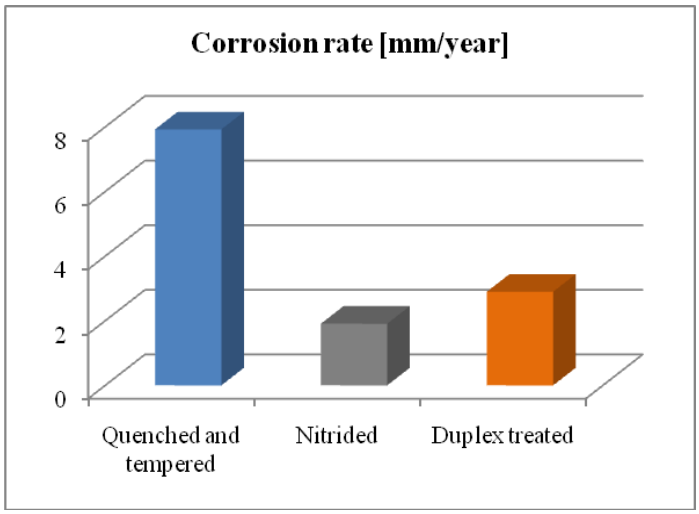

Figure 5.28: The corrosion rates obtained for each structural state

In order to identify the corrosion products, glancing incidence X-ray diffractions tests were performed. The patterns for each structural state are presented in Figure 5.29.

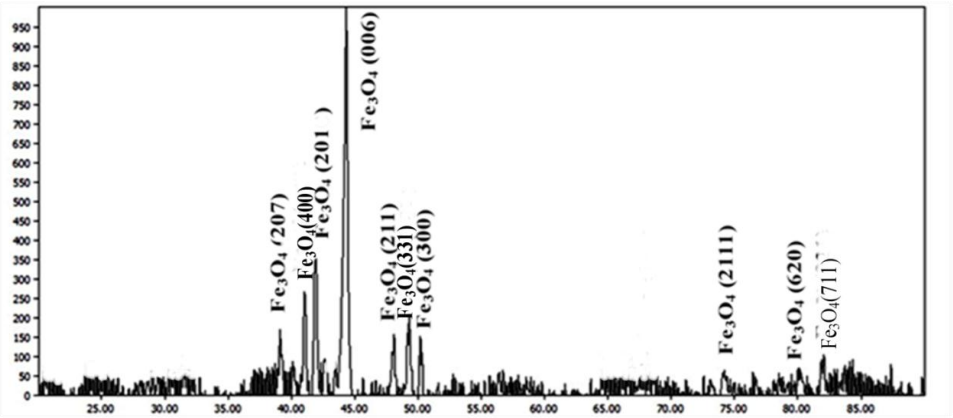

a- quenched and tempered;

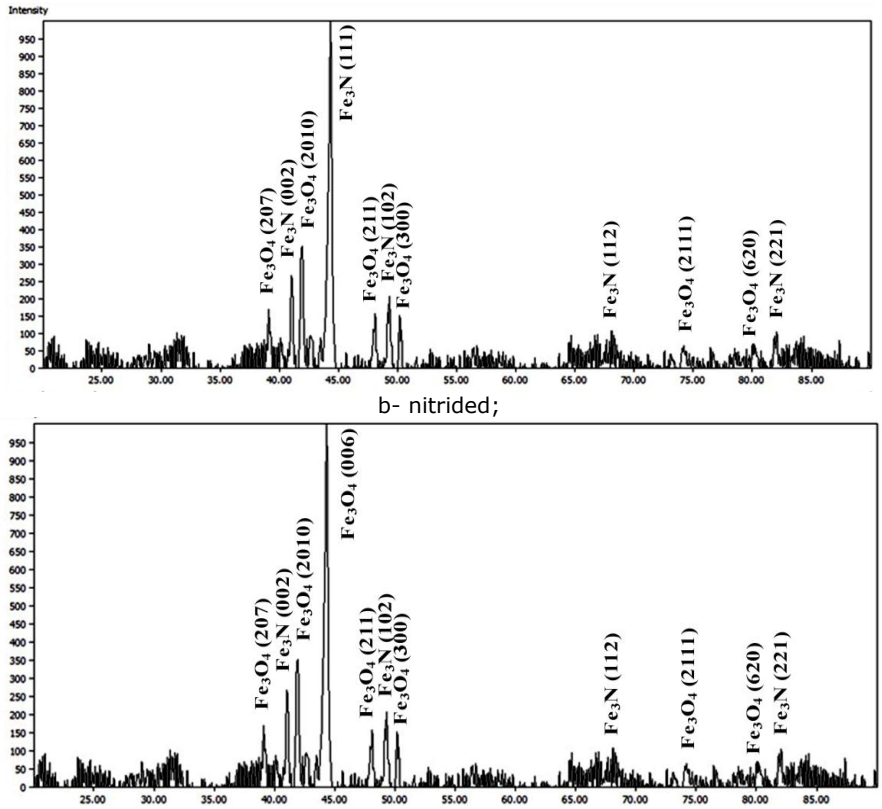

Figure 5.29: Glancing incidence patterns: a – quenched and tempered state; b – nitrided state; c - Duplex treated state;

For untreated state, the phase analysis reveals only one crystallographic Fe_3O_4 (magnetite). Reflection of this phase produce 10 peaks, that can be indexed as (207), (400), (2010), (006), (211), (331), (300), (2111), (620) and (711) and occur at 2θ values of approximately 39.852°, 41.031°, 42.131°, 44.127°, 48.125, 49.065°, 50.116°, 74.125°, 79.451°, and 82.611° (Figure 5.29 a). For the nitrided samples, glancing incidence X-ray diffraction analyzes reveals the presence of iron nitride and magnetite phases. Magnetite reflection produce 6 peaks, that can be indexed as (207), (2010), (211), (300), (2111), (620), which occur at 2θ values of approximately 39.852°, 42.131°, 48.125°, 50.116°, 49.065°, 74.125° and 79.451°. Reflections of hexagonal Fe_3N phase produce 5 peaks that can be indexed as (002), (111), (102), (112), (221) and occurs at 2θ values of approximately 41.252°, 43.7409, 47.151°, 57.561°, 85.641° (Figure 5.29 b).

Glancing incidence analyze showed the presence of Fe_3N and Fe_3O_4 phases in Duplex treated samples. Reflection of Fe_3N produce 4 peaks, that can be indexed as (002), (102), (112) (221) and occurs at 2θ values of approximately 41.252°, 47.151°, 57.561° and 85.641°. Magnetite reflection produce 7 peaks, that can be indexed as (207), (2010), (006), (211), (331), (300), (2111), (620) and (711) and occur at 2θ values of approximately 39.852°, 42.141°, 44.127°, 48.125°, 49.065°, 50.116°, and 74.125°, Figure 5.29 c.

The surfaces of the corroded samples were analyzed by SEM and by energy dispersive X-ray spectrometry (EDX). Figure 5.30 presents SEM images of corroded surfaces of Duplex and non- Duplex samples.

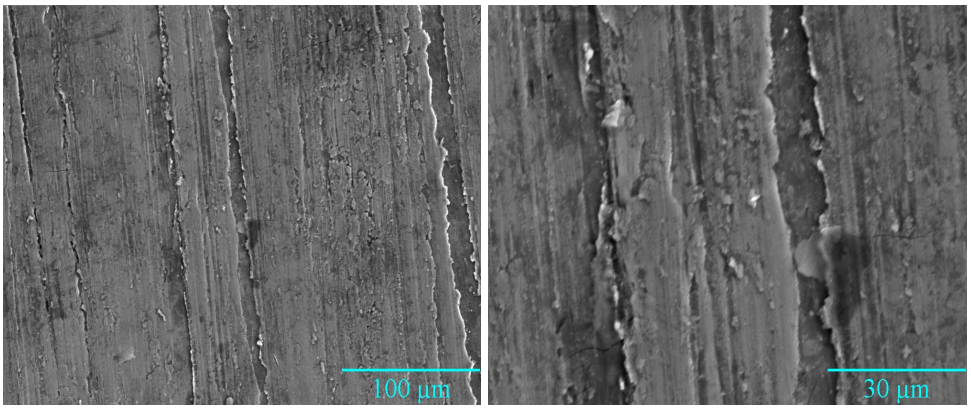

a- quenched and tempered state;

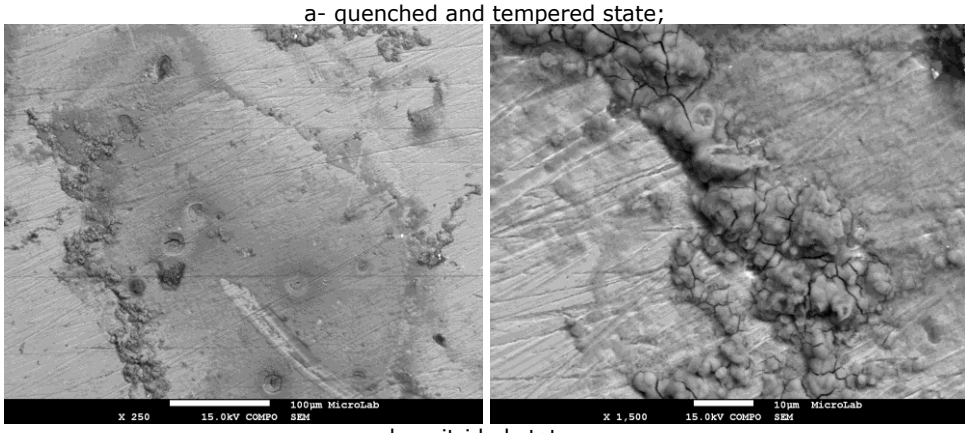

b - nitrided state;

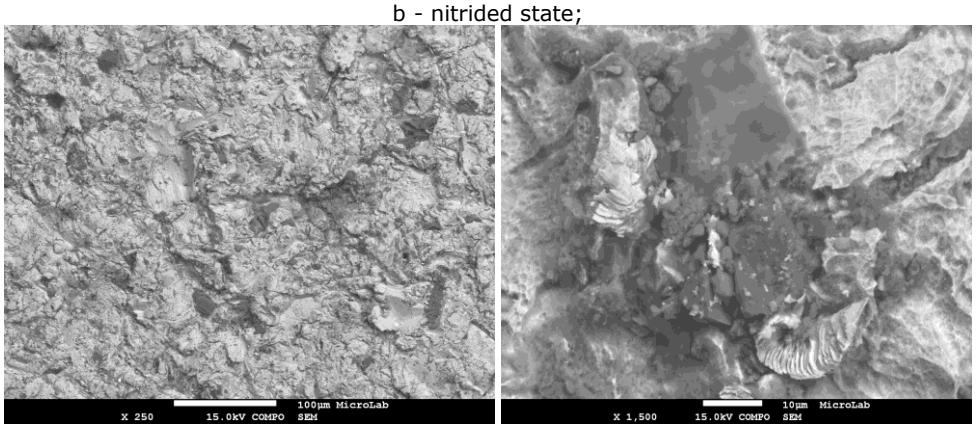

c- Duplex treated state

Figure 5.30: SEM imagines of corroded surfaces: a – quenched and tempered state; b - nitrided state; c- Duplex treated state.

From Figure 5.30 it can be observed the tendency towards pitting corrosion for each structural state. Small pits and micro-cracks can be observed on the corroded surfaces.

In order to determine the elemental composition of the corroded samples, EDX investigations were carried out, Figure 5.31.

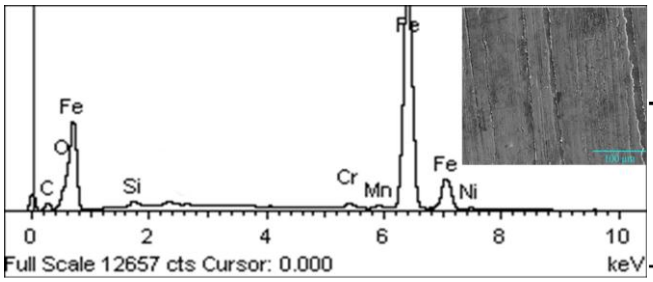

Element	App Conc.	Intensity Corrn.	Weight%	Weight% Sigma	Atomic%
O K	7.82	1.8380	14.59	0.21	41.09
Si K	0.09	0.8195	0.38	0.03	0.61
S K	0.06	0.9781	0.23	0.03	0.32
Cr K	0.29	1.1698	0.85	0.04	0.73
Mn K	0.16	0.9422	0.58	0.06	0.47
Fe K	23.69	0.9596	84.66	0.73	68.33
Ni K	0.32	0.9061	1.21	0.09	0.93
Totals			100.00		

a- quenched and tempered state;

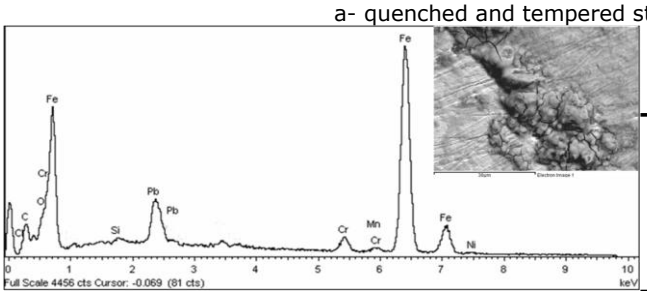

Element	App Conc.	Intensity Corrn.	Weight%	Weight% Sigma	Atomic%
C K	3.08	0.4320	2.46	0.39	22.81
O K	4.14	1.2362	13.03	0.31	8.04
Si K	0.49	0.6428	0.69	0.04	1.05
Cr K	1.34	1.2058	1.00	0.05	0.82
Mn K	0.63	0.9528	0.60	0.06	0.46
Fe K	91.95	0.9731	83.42	0.49	64.92
Ni K	1.16	0.8717	0.70	0.09	0.87
Totals			100.00		

b- nitrided state;

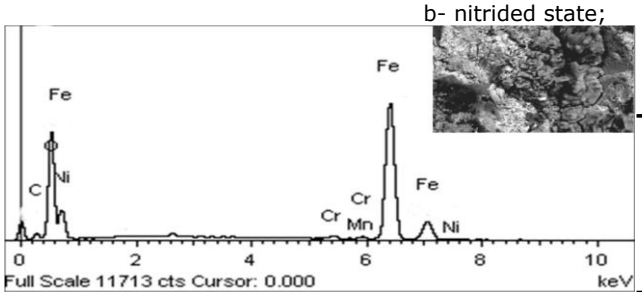

Element	App Conc.	Intensity Corrn.	Weight%	Weight% Sigma	Atomic%
C K	3.08	0.4320	2.46	0.39	22.81
O K	4.14	1.2362	13.03	0.31	8.04
Si K	0.49	0.6428	0.69	0.04	1.05
Cr K	1.34	1.2058	1.00	0.05	0.82
Mn K	0.63	0.9528	0.60	0.06	0.46
Fe K	91.95	0.9731	83.42	0.49	64.92
Ni K	1.16	0.8717	0.70	0.09	0.87
Totals			100.00		

c - Duplex treated state;

Figure 5.31: EDX spectrums: a - quenched and tempered; b - nitrided; c - Duplex treated;

As it can be observed from Figure 5.31, the corroded surface of all the samples contains nearly all the elements of EN 34CrNiMo6 (Mn, Cr, Si, etc) and additionally O indicating that nearly all constituents participate in the formation of corrosion layer. Very clearly, the corroded surface is much richer in Fe while poorer in every metallic element. Another obvious aspect is that the surface contains O in a significant amount, especially for the annealed samples. Due to the chemical composition of the paint used to protect the surface which was not tested, Pb is another element present in EDX spectrum (Figure 5.31b). The elements distribution for each sample is presented in Figure 5.32.

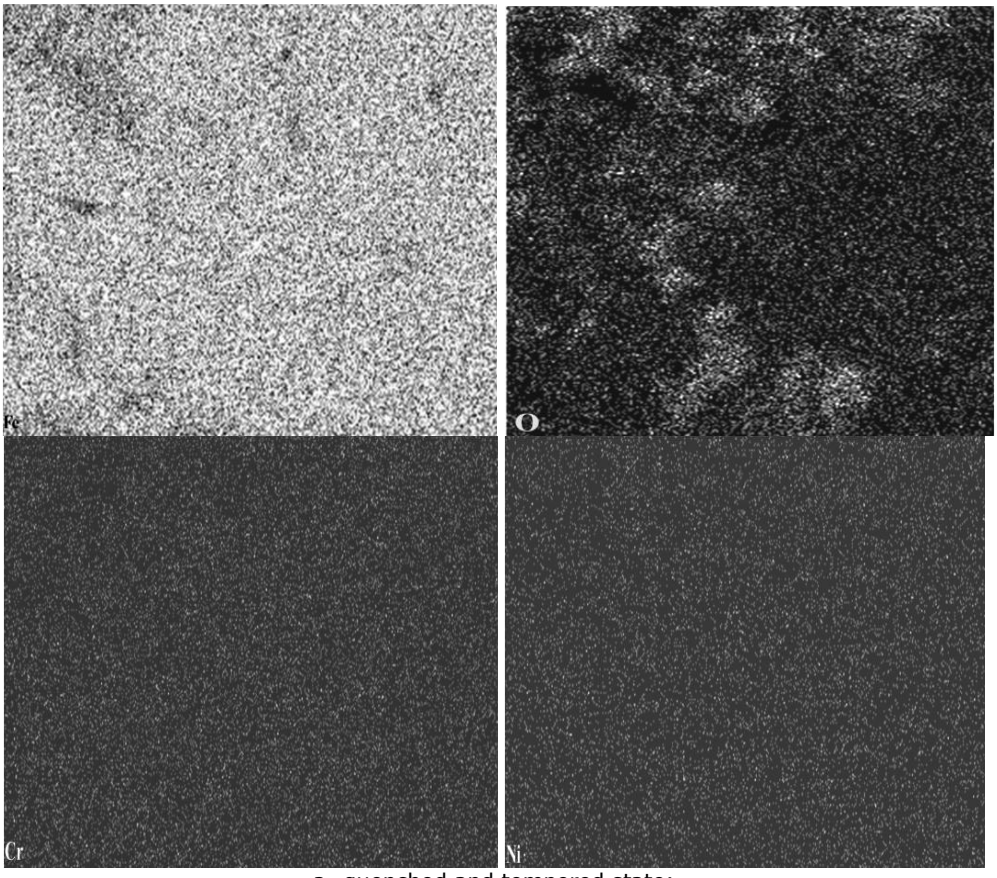

a- quenched and tempered state;

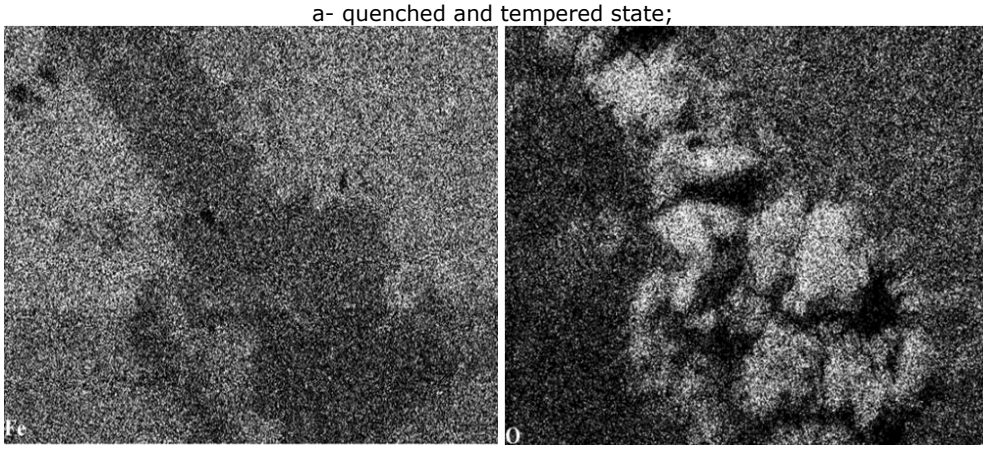

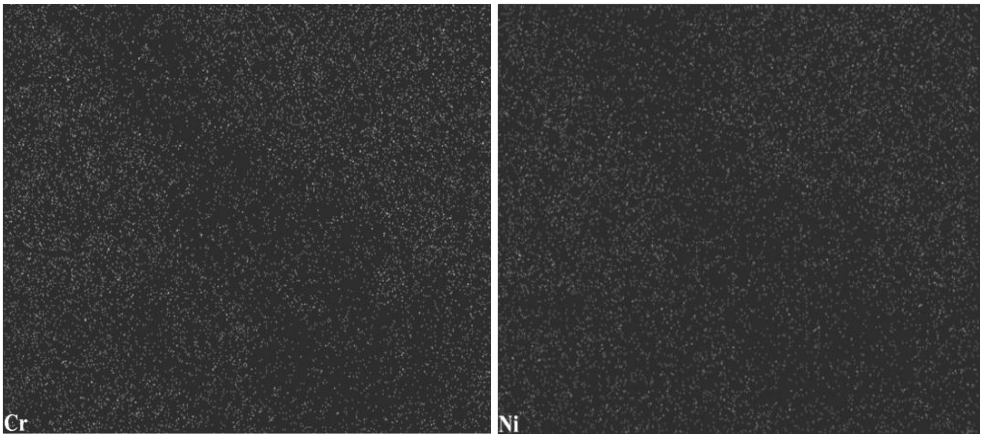

b- nitrided state;

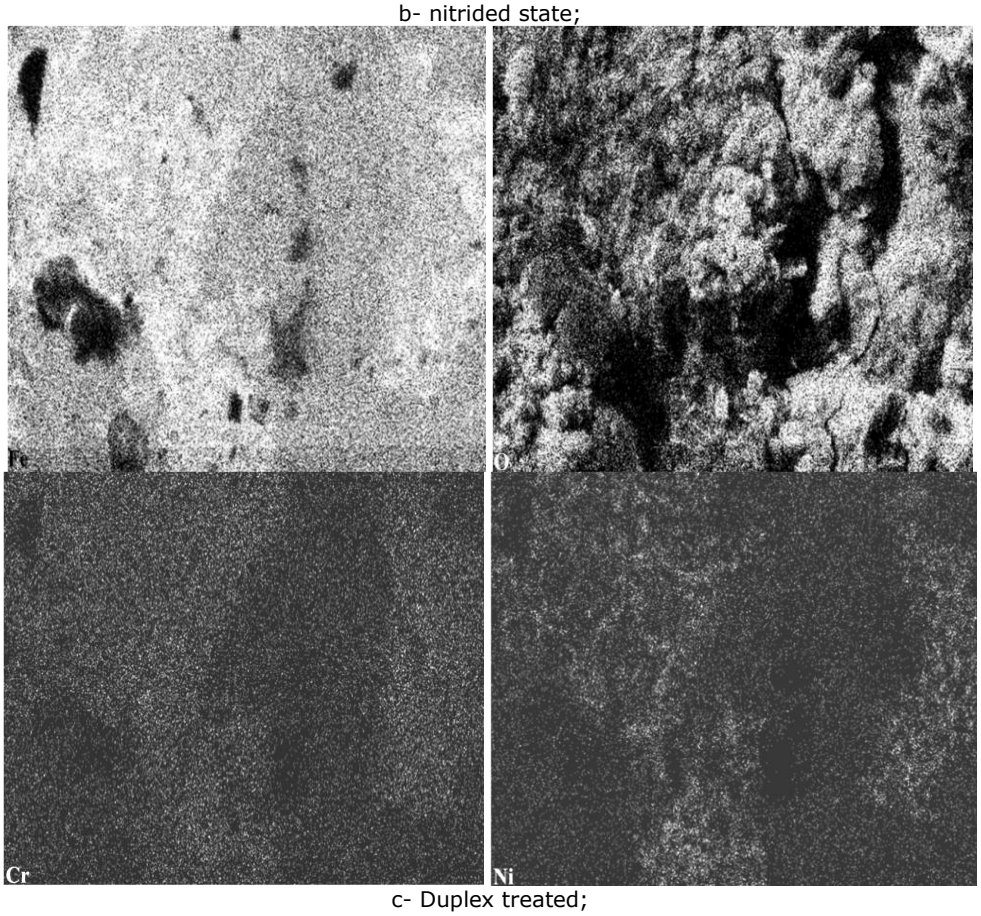

c- Duplex treated;

Figure 5.32: EDX element distribution: a – quenched and tempered state; b – nitrided state; c - Duplex treated state;

5.7 Wear behaviour

In order to determine the wear behaviour of Duplex and non-Duplex samples, dry sliding and abrasive micro scale wear tests were performed. The tests were realized using a ball cratering device, as presented in the previous chapter.

5.7.1 Dry sliding wear behavior

The investigations were performed on cylindrical samples, with a diameter of 12 mm and length of 4 mm. In order to achieve a high reliability of the results, all tests were performed at least two times for each structural state.

In this work, the counter body was a tungsten carbide (WC-Co) sphere, with a diameter of 19 mm and a hardness of 1200 HV. The rotation speed of the ball was 200 rpm, which corresponds to a linear slide of 190 mm/s. A constant sliding distance of 500 m and a normal of 0.4 N were used. The average values of the wear coefficient, determined according to equation 4.23, are shown in Figure 5.33.

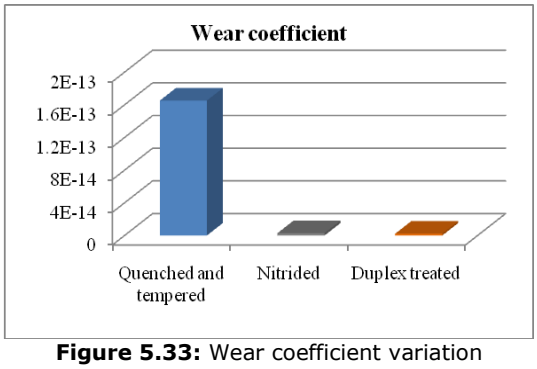

Figure 5.33: Wear coefficient variation

It can be observed a significant decrease of the wear coefficient for Duplex treated state ($1.65x10^{-13}m^2N^{-1}$), compared to quenched and tempered ($2.21 \times 10^{-15}m^2\ N^{-1}$). The wear rates were calculated according to equation 4.22. The wear rate decreased from $6.60 \times 10^{-14}\ m^2$ (quenched and tempered state) to $8.84 \times 10^{-16}\ m^2$ (Duplex treated state), as it can be observed from Figure 5.34.

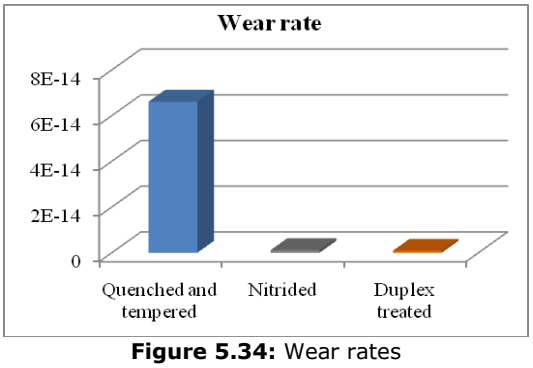

Figure 5.34: Wear rates

In order to investigate the wear mechanisms involved, the worn surfaces were observed by scanning electron microscopy. The SEM micrographs of the worn surfaces for quenched and tempered state are presented in Figure 5.35.

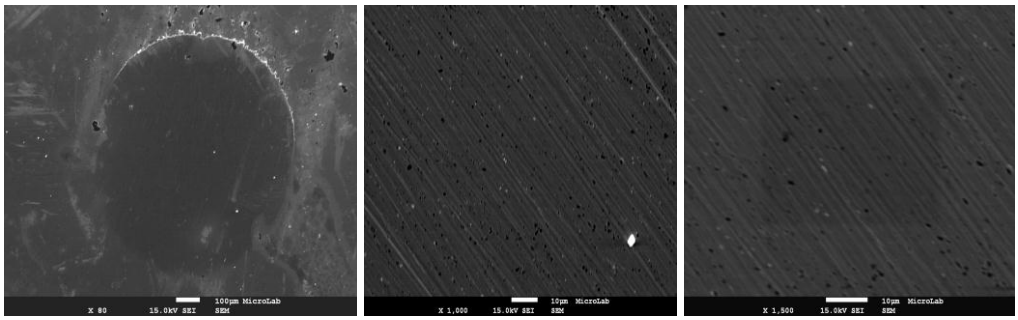

Figure 5.35: SEM micrographs of quenched and tempered worn surface

Various mechanisms seem to be occurring simultaneously. The worn surface presents parallel grooves formed by scratching the surface with hard particles, flat zones showing plastic deformation caused by the action of the counter body and rough cavities, suggesting that the material was removed and probably transferred to the counter body. EDX analyze of the worn surface is presented in Figure 5.36.

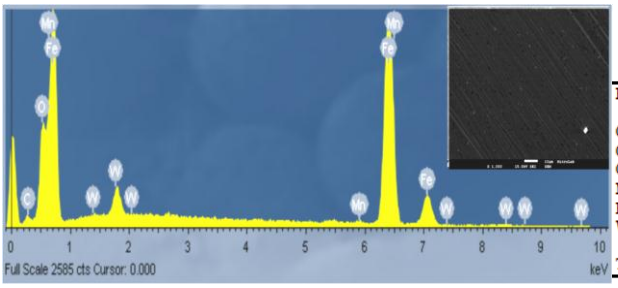

Element	App Conc.	Intensity Corrn.	Weight%	Weight% Sigma	Atomic%
C K	0.22	0.5522	2.36	0.37	9.26
O K	1.41	1.7001	4.89	0.58	14.41
Cr K	0.10	1.1912	0.50	0.13	0.45
Mn K	0.14	0.9660	0.88	0.18	0.76
Fe K	14.70	0.9851	87.99	0.72	74.26
W M	0.35	0.6142	3.38	0.28	0.87
Totals			100.00		

Figure 5.36: EDX analyze of quenched and tempered sample

EDX investigation shows the presence of W, demonstrating that was adherence and transfer of material between the sample and counter body. It reveales also the presence of Fe, C Mn, Cr, due to the chemical composition of EN 34CrNiMo6. The surface contains also O, which indicates the formation of some oxides during wear tests. The elements distribution is presented in Figure 5.37.

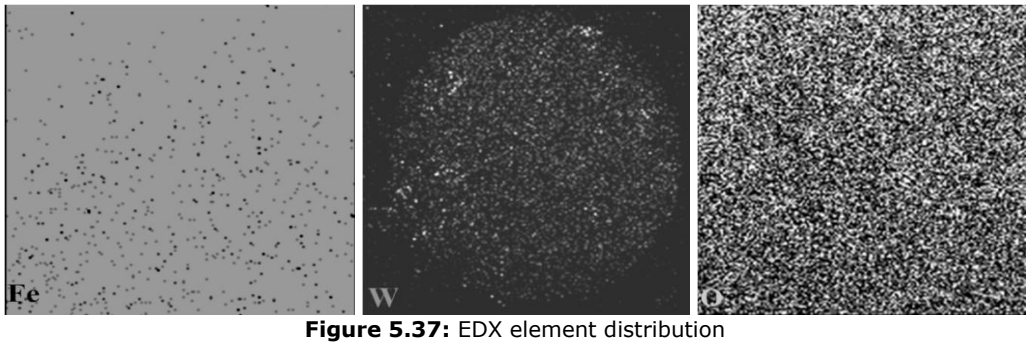

Figure 5.37: EDX element distribution

The SEM micrographs of the worn surfaces for nitrided state are presented in Figure 5.38.

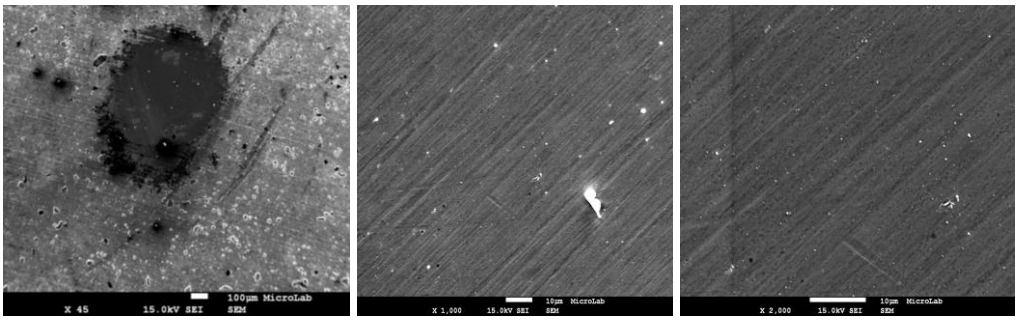

Figure 5.38: SEM micrographs of nitrided worn surface

The worn surface presents parallel grooves formed by scratching the surface with hard particles, flat zones showing plastic deformation caused by the action of the counter body. EDX analyze of the worn surface is presented in Figure 5.39.

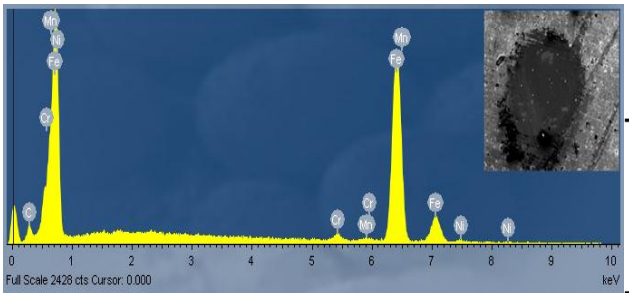

Element	App Conc.	Intensity Corrn.	Weight%	Weight% Sigma	Atomic%
C K	0.86	0.5454	5.03	0.48	19.76
Cr K	0.56	1.2124	1.48	0.15	1.34
Mn K	0.21	0.9654	0.71	0.20	0.61
Fe K	28.06	0.9833	91.08	0.59	76.93
Ni K	0.49	0.9214	1.70	0.32	1.37
Totals			100.00		

Figure 5.39: EDX analyze of nitrided worn surface

EDX investigation shows the presence of W, demonstrating that was adherence and transfer of material between the sample and counter body. It reveales also the presence of Fe, C Mn, Cr, Ni, due to the chemical composition of EN 34CrNiMo6. The surface contains also O, which indicates the formation of some oxides during wear tests. The elements distribution is presented in Figure 5.40.

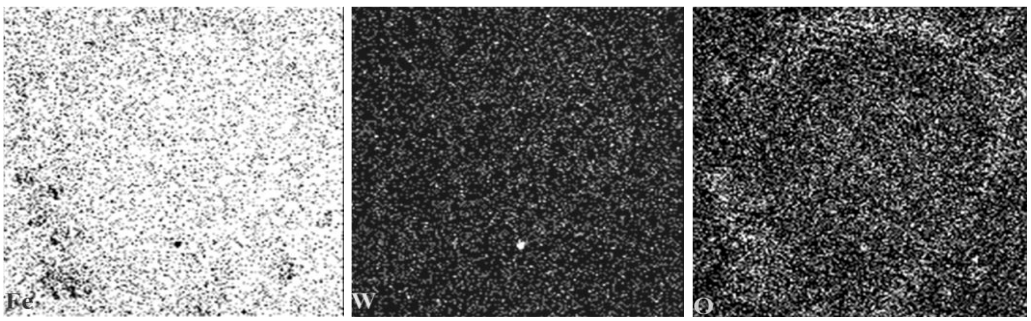

Figure 5.40: EDX map

The SEM micrographs of the worn surfaces for Duplex treated state are presented in Figure 5.41.

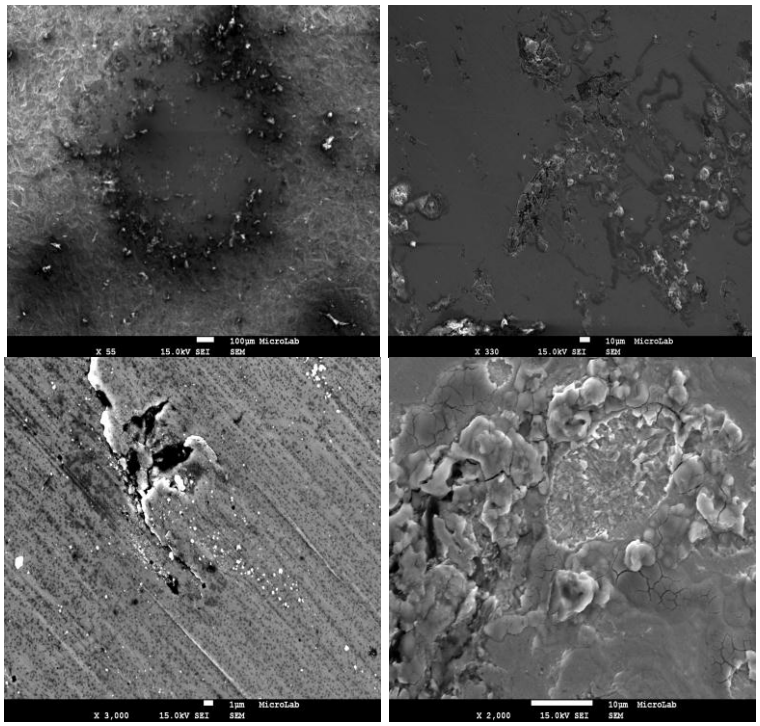

Figure 5.41: SEM micrographs of Duplex treated worn surface

Various mechanisms seem to be occurring simultaneously. The worn surface presents parallel grooves formed by scratching the surface with hard particles (abrasive wear), flat zones showing plastic deformation caused by the action of the counter body and rough cavities, suggesting that the material was removed and transferred to the counter body. It can be observed the presence of the micro-cracks. EDX analyze of the worn surface is presented in Figure 5.42.

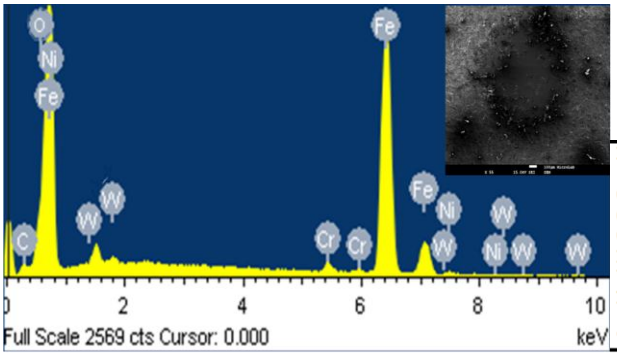

Element	App Conc.	Intensity Corrn.	Weight%	Weight% Sigma	Atomic%
C K	0.91	0.5966	5.42	0.34	14.57
O K	10.37	1.7415	16.09	0.41	42.55
Cr K	0.43	1.1236	1.37	0.11	0.85
Fe K	18.21	0.9269	69.56	0.52	40.21
W K	0.18	0.9053	5.71	0.28	0.39
Ni K	0.29	0.8832	1.18	0.22	0.65
Totals			100.00		

Figure 5.42: EDX analyze of Duplex treated worn surface

EDX investigation shows the presence of W, demonstrating that was adherence and transfer of material between the sample and counter body. It reveales also the presence of Fe, C Mn, Cr, Ni, due to the chemical composition of EN 34CrNiMo6. The surface contains also O, indicating the formation of some oxides during wear tests. The elements distribution is presented in Figure 5.43.

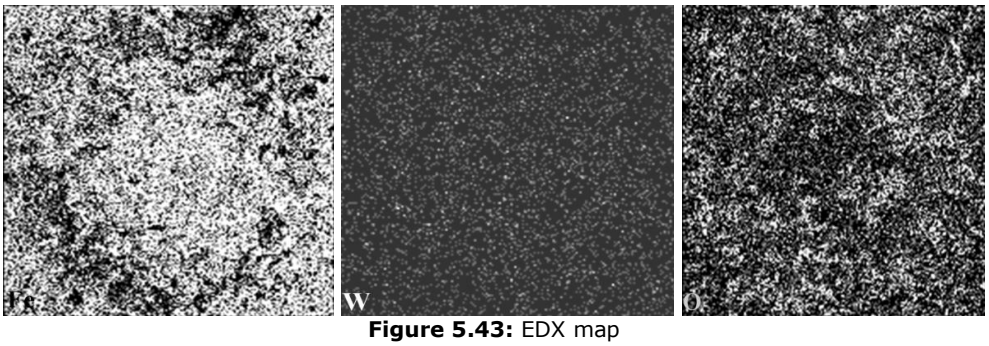

Figure 5.43: EDX map

5.7.2 Abrasive wear

The investigations were performed on cylindrical samples, with a diameter of 12 mm and length of 4 mm. In order to achieve a high reliability of the results, all tests were performed at least two times for each structural state. The investigations were performed similar to the ones presented in Chapter 4.

The average values of the wear coefficient, determined according to equation 4.23, are shown in Figure 5.44.

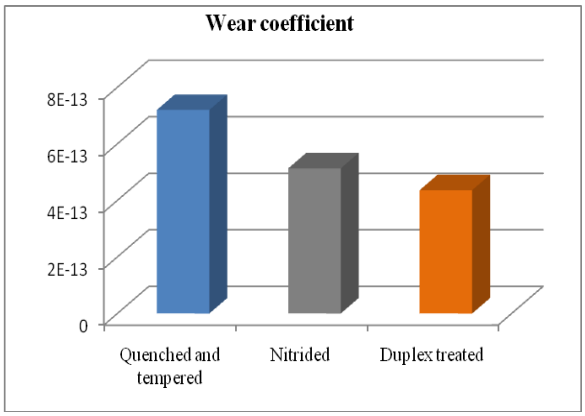

Figure 5.44: Wear coefficient variation

It can be observed a decrease of the wear coefficient for Duplex treated state (4.36 x$10^{-13}$$m^2N^{-1}$), compared to untreated sample (7.2 x $10^{-13}$$m^2$ N^{-1}) and nitrided state (5.13 x $10^{-13}$$m^2$ N^{-1}). The wear rates were calculated according to equation 4.18. The wear rate decreased from 2.88×10^{-13} m^2 (untreated state) to 1.74×10^{-13} m^2 (Duplex treated state), as it can be observed from Figure 5.45.

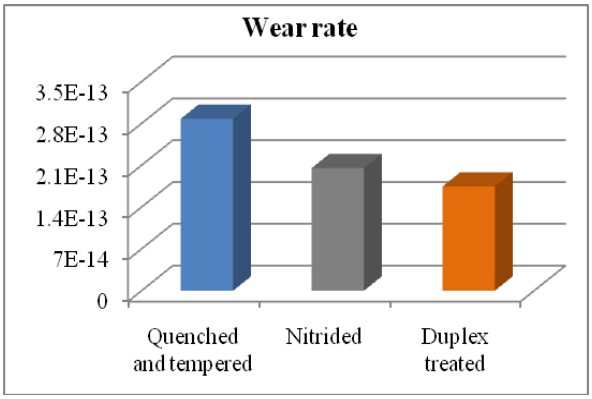

Figure 5.45: Wear rates of Duplex and non-Duplex samples

In order to investigate the wear mechanisms involved, the worn surfaces were observed by scanning electron microscopy. The SEM micrographs of the worn surfaces for quenched and tempered state are presented in Figure 5.46.

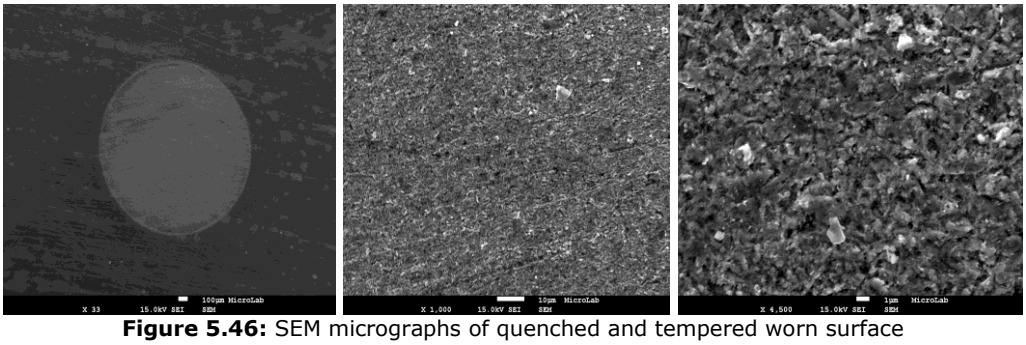

Figure 5.46: SEM micrographs of quenched and tempered worn surface

From Figure 5.46 it can be observed that the worn surface corresponds to three-body abrasive wear. SiC particles indent and roll over the surface during the tests instead of sliding, wearing material uniformly. The worn surface was investigated by EDX analyze, Figure 5.47.

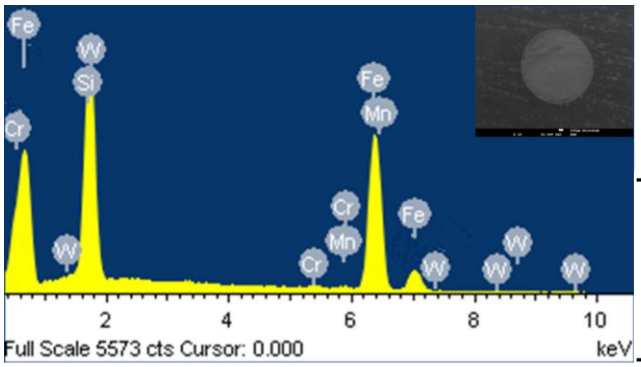

Element	App Conc.	Intensity Corrn.	Weight%	Weight% Sigma	Atomic%
MnK	0.84	0.3010	16.06	2.14	38.69
Si K	7.23	1.0258	40.67	1.12	41.91
Cr K	0.09	0.9429	0.58	0.12	0.32
Fe K	5.16	0.8933	33.31	0.95	17.26
W M	1.08	0.7454	9.37	0.77	1.32
Totals			100.00		

Figure 5.47: EDX analyze of quenched and tempered worn surface

EDX investigation reveals a significant amount of Si. It reveales also the presence of Fe, C Mn, Cr, due to the chemical composition of EN 34CrNiMo6. The element distribution in the worn surface is presented in Figure 5.48.

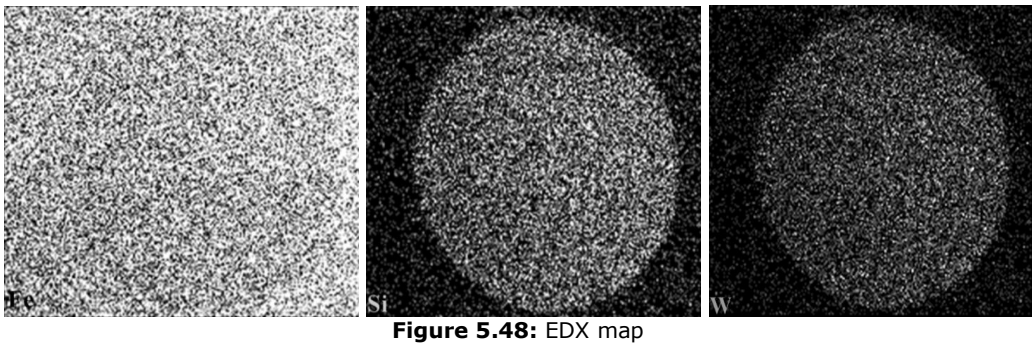

Figure 5.48: EDX map

The SEM micrographs of the worn surfaces corresponding to nitrided state are presented in Figure 5.49.

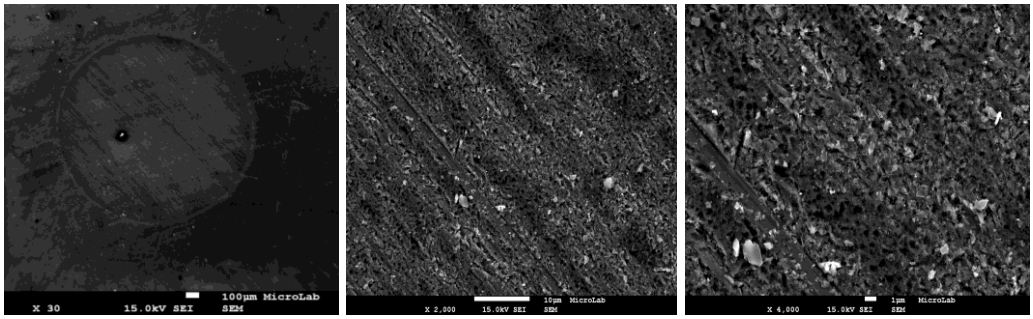

Figure 5.49: SEM micrographs of nitrided worn surface

The worn surface presence the same characteristics as the worn surface of untreated sample. The EDX analysis is presented in Figure 5.50.

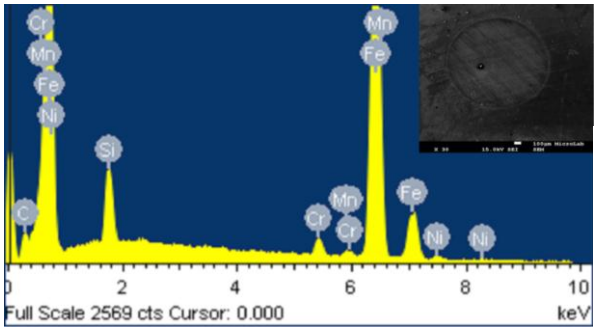

Element	App Conc.	Intensity Corrn.	Weight%	Weight% Sigma	Atomic%
C K	0.03	0.2816	12.76	3.21	31.79
CrK	0.01	0.8556	1.97	0.41	2.19
Si K	0.25	0.9327	38.42	1.83	40.93
Fe K	0.30	0.9203	46.84	2.23	25.09
NiK	0.29	0.8832	1.18	0.22	0.65
MnK	0.21	0.9654	0.71	0.20	0.61
Totals			100.00		

Figure 5.50: EDX mapping of Duplex worn surface

EDX investigation reveals a significant amount of Si. It reveales also the presence of Fe, C Mn, Cr, Ni due to the chemical composition of EN 34 CrNiMo6. The element distribution in the worn surface is presented in Figure 5.51.

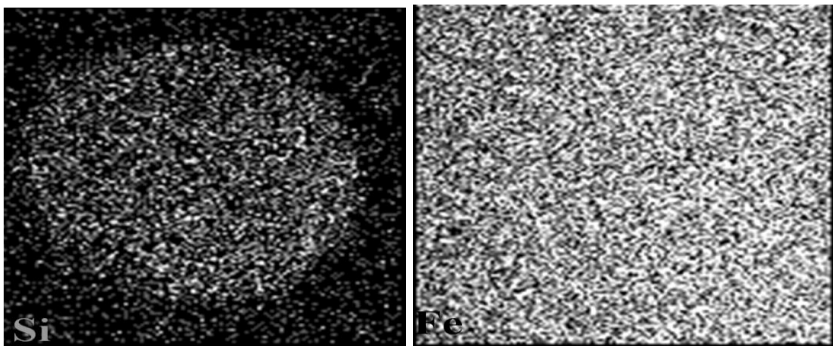

Figure 5.51: EDX mapping of Duplex worn surface

The SEM micrographs of the worn surfaces for Duplex treated state are presented in Figure 5.52.

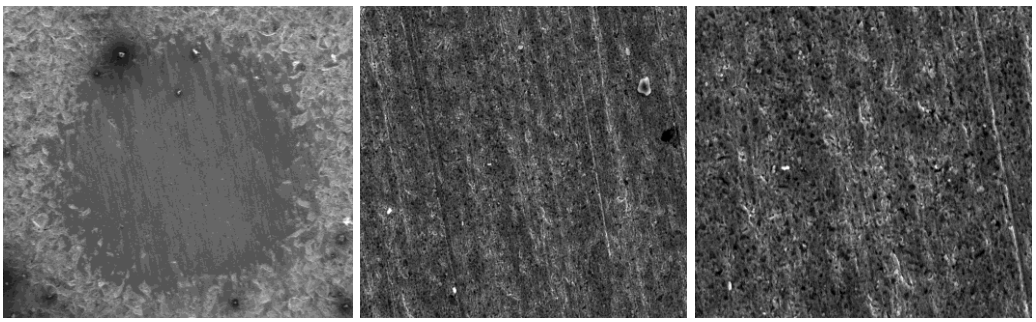

Figure 5.52: SEM micrographs of nitrided worn surface

From Figure 5.52 it can be observed that the worn surface corresponds to three-body abrasive wear. SiC particles indent and roll over the surface during the tests instead of sliding, wearing material uniformly. It can be also observed regions of plastic deformation. The worn surface was investigated by EDX analyze, Figure 5.53.

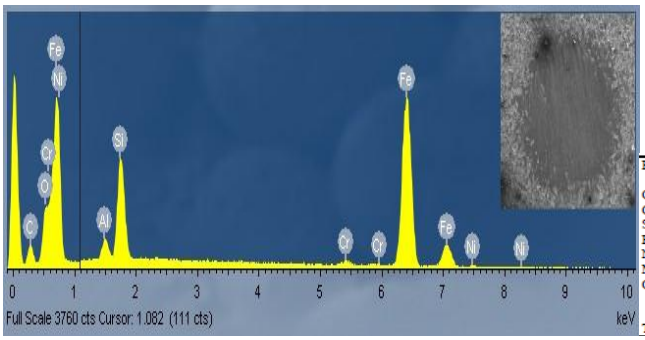

Element	App Conc.	Intensity Corrn.	Weight%	Weight% Sigma	Atomic%
C K	0.03	0.2816	12.76	3.21	31.79
CrK	0.01	0.8556	1.97	0.41	2.19
Si K	0.25	0.9327	38.42	1.83	40.93
Fe K	0.30	0.9203	46.84	2.23	25.09
NiK	0.29	0.8832	1.18	0.22	0.65
MnK	0.21	0.9654	0.71	0.20	0.61
OK	0.22	0.8453	6.76	0.45	0.52
Totals			100.00		

Figure 5.53: EDX mapping of Duplex worn surface

EDX investigation reveals a significant amount of Si. It reveales also the presence of Fe, C Mn, Cr,Ni due to the chemical composition of EN 34 CrNiMo6. The element distribution in the worn surface is presented in Figure 5.54.

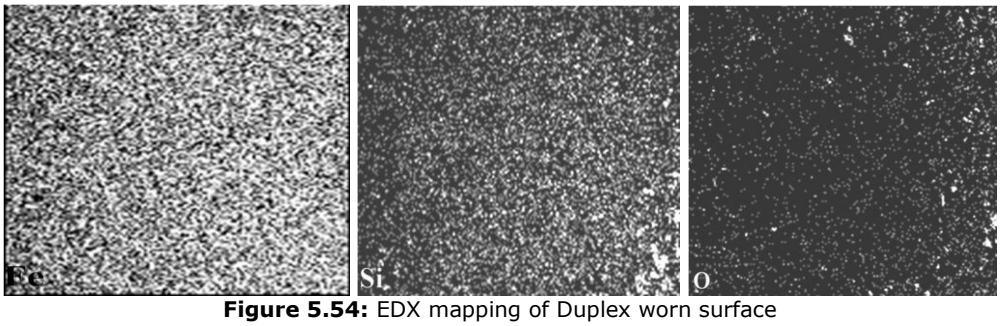

Figure 5.54: EDX mapping of Duplex worn surface

5.8 Fatigue behaviour

Duplex and non-Duplex specimens were submitted to rotating bending in order to study the effect of the surface modification on the fatigue resistance. The investigations were realized similar as presented in Chapter 4. The results obtained for Duplex and non-Duplex samples are presented in Figure 5.55.

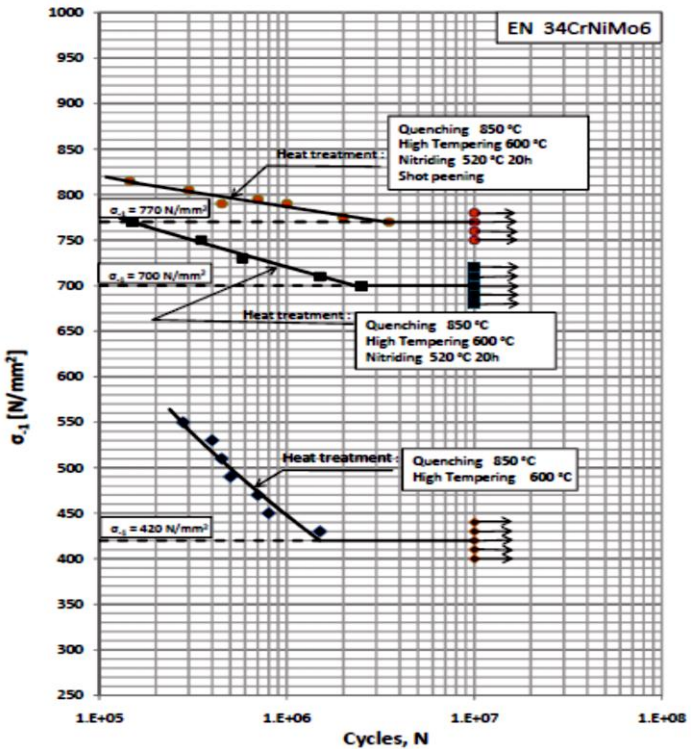

Figure 5.55: Fatigue limit

As it can be observed from Figure 5.55, the fatigue limit increased from 420 N/mm^2 (untreated state) to 770 N/mm^2 (Duplex treated state), due to high compressive stresses induced by the mechanical treatment of work hardening through shot peening.

5.9 Conclusions

The Duplex treatment selected for this study consists in the combination of gas nitriding and shot peening on EN 34 CrNiMo6 low alloyed steel.

The first stage in realizing the Duplex treatment consisted in a hardening treatment, at a temperature of 850 °C, maintained for a period of 60 minutes, and oil cooled. After that, a high tempering treatment was realized at a temperature of 600 °C, maintenance for 30 minutes and air cooled. The second stage of the Duplex treatment consisted in a gas nitriding treatment, at 540 °C, maintained for about 20 hours and air cooled. The thickness of the nitride layer is 0.4 mm. The third stage of the Duplex treatment consisted in a mechanical treatment of shot peening.

The structural characterization was realized by means of optical microscopy, scanning electron microscopy, X-ray diffraction and glancing incidence X-ray analysis. In quenched and tempered state, the structure is composed of sorbite. For the nitrided samples, the analysis reveals the presence of typical nitride layers. The compound layer consists of iron nitrides (Fe_3N and Fe_4N). Under the compound layer it can be observed the white layer, and the diffusion layer, which has a thickness of 280 μm. After shot peening the structure remains the same.

The result of X-ray analysis showed only the presence of iron phases (Fe-α) on the untreated samples. For the nitrided samples, X-ray diffraction analyzes reveals only the presence of iron nitrides (Fe_3N and Fe_4N). Determination of iron nitride phases proved that the nitriding process was effectively carried out. Iron nitride phases (Fe_3N and Fe_4N) were determined on the Duplex treated samples, as expected. Glancing incidence analysis confirmed the results obtained by X-Ray diffractions.

The microhardness tests showed that the hardness values of Duplex treated specimen's decreases from the surface to the core. The maximum value of hardness of 880 HV0.2 was obtained in the Duplex treated state. At distances over 0.4 mm from the surface, the hardness remains constant, with values in range of 390-395 HV0.2. In nitrided state was obtained a maximum value of 800 HV0.2, near the white layer. In the diffusion layer, the hardness decreases with the distance from the surface. In the quenched and tempered state, the hardness is constant, ranging between 390-395 HV0.2. It can be noted that, compared with the untreated state, the hardness increased about 2.38 times for the Duplex treated sample.

Duplex and non-Duplex specimens were subjected to instrumented indentation tests in order to determine the mechanical properties. The values of bulk modulus increased from 165 GPa (untreated state) to 265 GPa (Duplex state), which represents an increase of about 80%. The average values of Martens hardness corresponding to quenched and tempered state is 3.86 GPa, 4.19 GPa for nitrided state and 7.89 GPa for Duplex treated state. It can be observed that the value of Martens hardness for Duplex state increased 2 times compared to untreated state and 1.5 times compared to nitrided state, respectively.

The stress measurement by means of instrumented indentation revealed high compressive stresses induced by the Duplex treatment, ranging between -393 MPa and -435 MPa (Atari method) and -1352 MPa to -1732 MPa (Suresh method)..

The corrosion behavior of Duplex and non - Duplex samples was electrochemical investigated in different environments by means of linear polarization. The corrosion rate was calculated using Faraday equation according to ASTM G 59 and G 102. In 3% NaCl, it was obtained o corrosion rate of 0.73 mm $year^{-1}$ for untreated state, and 0.43 mm $year^{-1}$ for Duplex treated state. It can be observed a decrease of the corrosion rate of about 40 % for the Duplex treated sample compared to untreated state. In 0.5 M H_2SO_4, the corrosion rate decreased from 8.71 mm $year^{-1}$(untreated state) to 4.22 mm $year^{-1}$ (Duplex treated), which corresponds to a decrease of about 50%. In 0.1 M H_2SO_4, the corrosion rate decreased from 7.92 mm $year^{-1}$ (untreated state) to 2.89 mm $year^{-1}$ (Duplex treated), which corresponds to a decrease of about 70%. The corrosion products were identified by means of glancing incidence X-ray diffractions. The analysis revealed, in each solution used, the presence of iron nitrides and magnetite (iron oxide) phases for each structural state. The surface of the corroded samples was analyzed by image acquisition and by energy dispersive X-ray spectrometry (EDX). The tendency towards pitting corrosion can be observed for all structural states. EDX analyses showed that the corroded surface of all the samples contains nearly all the constituent elements of EN 34CrNiMo6 (Mn, Cr, Si, etc) and additionally O in a significant amount.

In order to determine the wear behaviour of Duplex and non-Duplex samples, dry sliding and abrasive micro scale wear tests were performed.

For dry sliding, it can be observed an increase of the wear coefficient for Duplex treated state ($2.21 \times 10^{-15} m^2 N^{-1}$), compared to untreated ($1.65 \times 10^{-13} m^2\ N^{-1}$) and nitrided state ($2.93 \times 10^{-15} m^2\ N^{-1}$). The wear rate decreased from 6.60×10^{-14} m^2 (untreated samples) to 8.84×10^{-16} m^2 (Duplex treated state). In order to investigate the wear mechanisms involved, the worn surfaces were observed by scanning electron microscopy. Various mechanisms seem to be occurring simultaneously in the sliding wear behaviour of the samples. The worn surfaces present parallel grooves formed by scratching the surface with hard particles (abrasive wear), flat zones showing plastic deformation caused by the action of the counter body and rough cavities, suggesting that the material was removed and probably transferred to the counter body. For abrasive wear, the wear coefficient decreased from 7.2×10^{-13} (untreated samples) to 4.36×10^{-13} (Duplex treated samples). It can be observed a decrease of about 42%. The wear rate decreased from 2.88×10^{-13} m^2 (untreated samples) to 1.74×10^{-13} m^2 (Duplex treated state), which corresponds to a decrease of about 45%. SEM and EDX analysis reveals the wear mechanism corresponds to three-body abrasive wear. SiC particles roll over the surface instead of sliding, wearing material uniformly.

Duplex and non-Duplex specimens were submitted to rotating bending in order to study the effect of the surface modification on the fatigue resistance. The fatigue limit increased from 420 N/mm^2 (untreated state) to 770 N/mm^2 (Duplex treated state), due to high compressive stresses induced by the mechanical treatment of shot peening. Taking into consideration the results obtained, it can be affirmed that the combination of gas nitriding and work hardening through shot peening improved the resistance to wear and fatigue of the treated samples.

6. FINITE ELEMENT ANALYSIS OF ROTATING BENDING FATIGUE TEST

6.1 Introduction in Finite Element Analysis

Finite Element Analysis (FEA), also known as Finite Element Method (FEM) is based on the premise that an approximate solution to any complex engineering problem can be reached by subdividing the problem into smaller, more manageable (finite) elements. Using finite elements, complex partial differential equations that describe the behavior of structures can be reduced to a set of linear equations that can easily be solved using the techniques of matrix algebra. The finite element method is used virtually in many engineering areas, namely aerospace, automotive, biomedical, chemical, electronics and plastics industries. In addition, it has been used extensively for accident reconstruction and forensic investigations [157, 158].

Like any other numerical approximation method, the solutions that are produced by finite element analysis contain also some errors. The magnitude of the errors is dependent on the type, size, and fineness of the used model. That is the reason why not all finite element models are created equal. Indeed, the industrial experience is the most critical factor in obtaining accurate results [159]. Processes that use FEM involve carrying out a sequence of steps in some way. Those sequences take two configurations, depending on (i) the environment in which FEM is used and (ii) the main objective: model-based simulation of physical systems, or numerical approximation to mathematical problems [160]. A common use of FEM is represented by the simulation of physical systems, which requires the models of such systems. Consequently, the methodology is often called model-based simulation. The process is illustrated in Figure 6.1 [158]. The centerpiece is the physical system to be modeled. Accordingly, this configuration is called the Physical FEM.

The processes of idealization and discretization are carried out to produce the discrete model. The solution step is handled by an equation solver often customized to FEM, which delivers a discrete solution (or solutions).

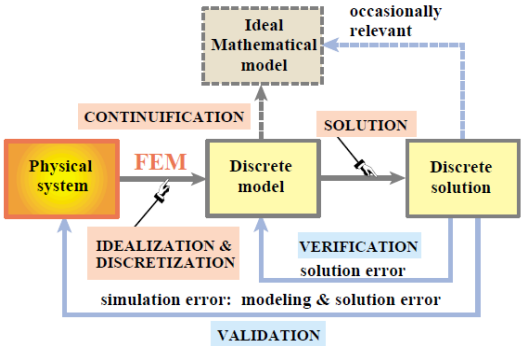

Figure 6.1: The Physical FEM [158]

Figure 6.1 also presents an ideal mathematical model. It may be presented as a continuum limit or "continuification" of the discrete model.

The concept of error arises in the Physical FEM in two ways. These are known as verification and validation, respectively. Verification is realized by replacing the discrete solution into the discrete model to obtain the solution error.

Substitution in the ideal mathematical model in principle provides the discretization error. This step is rarely useful in complex engineering systems. Validation tries to compare the discrete solution against observation by computing the simulation error, which combines modeling and solution errors. As the latter is typically unimportant, the simulation error in practice can be identified with the modeling error.

The errors are determined by comparing the discrete solution against experiments, as illustrated in Figure 6.2 [158]. The minimization conditions are generally nonlinear (even if the model is linear).

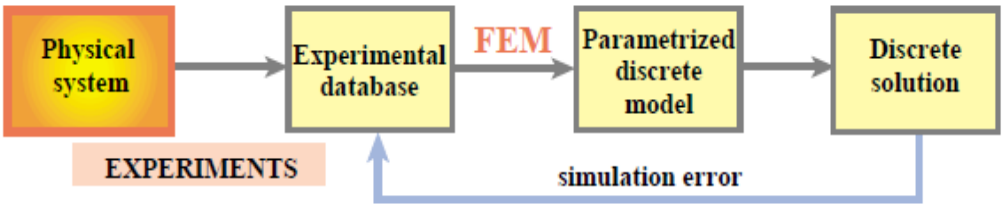

Figure 6.2: Model updating process in the Physical FEM [158]

Physical testing is clearly impractical for every design. In most applications, fatigue-safe life design requires prediction of component fatigue life that accounts for predicted service loads and materials. Computer-aided engineering (CAE) programs use three major methods to determine the total fatigue life. These are [160]:

Stress life (SN)

This is based on stress levels only, and uses the Wöhler method only. Although unsuitable for components with areas of plasticity, and providing poor accuracy for low cycle fatigue, it is the easiest to implement, has ample supporting data, and offers a good representation of high cycle fatigue.

Strain life (EN)

This approach provides more detailed analysis of plastic deformation in localized regions, and it is used for low cycle fatigue applications. However, some uncertainties in the results exist.

Linear Elastic Fracture Mechanics (LEFM)

This method assumes that a crack is already present and detected, and predicts crack growth with respect to stress intensity. This can be practical when applied to large structures in conjunction with computer codes and periodic inspection. Because of its ease of implementation and the large amounts of material data available, the most commonly used method is SN.

The finite element analysis obtains values of the temperatures, stresses, flows, or other desired unknown parameters by minimizing a functional energy.

Based on the law of conservation of energy, the finite element energy must be equal to zero. The finite element method obtains the correct solution for any finite element model by minimizing the energy functional. The minimum of the functional is found by setting the derivative of the functional with respect to the unknown grid point potential for zero.

Thus, the basic equation [158] for finite element analysis is

$$\frac{\partial F}{\partial p} = 0 \tag{6.1}$$

where F is the energy functional and p is the unknown grid point potential (In mechanics, the potential is displacement) to be calculated. This is based on the principle of virtual work, which states that if a particle is under equilibrium, under a set of a system of forces, then for any displacement, the virtual work is zero. Each finite element will have its own unique energy functional.

As an example, in stress analysis, the governing equations for a continuous rigid body can be obtained by minimizing the total potential energy of the system. In the finite element displacement method, the displacement is assumed to have unknown values only at the nodal points, so that the variation within the element is described in terms of the nodal values by means of interpolation functions [160].

6.2 Simulation of rotating bending fatigue test on Duplex treated consisting in gas carburizing and surface induction quenching specimens using FEA

The finite element analysis was performed on EN 16MnCr5 untreated and Duplex treated steels specimens using CosmosWorks FEA software. The finite element analysis was used to determine the stress concentration factors for the critical dimension, and determine the nominal stress applied for the purpose of life prediction. The analysis started from the 3D geometrical model of the specimen used in rotating bending fatigue test (Figure 6.3).

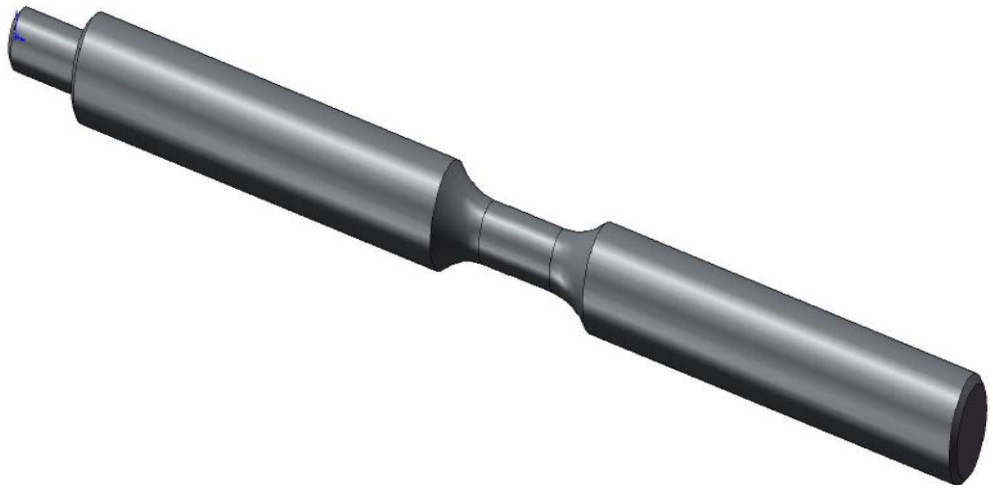

Figure 6.3: 3D model of the specimen used in rotating bending fatigue test

Model Meshing

The mathematical equations generated by the differential equation that defines the stress state, written for each point of the system will be solved by the computer. For this, the 3D model must be meshed.

Finite element method (FEM) is a method of approximation, and therefore lots of inevitable errors occurs, that can lead to inadequate results. The appearance of these errors are caused by the computer equipment which has limited number of digits available to describe any number, which sometimes can prove to be too reduced for these kinds of problems. To minimize the accumulation of calculation errors, the meshing domain must consider the following issues:

- a coarse mesh allows shortening calculation process, but this can lead to instability and obtaining inconclusive results;
- a fine mesh will lead to more stable and adequate results, but taking a lot of time during mathematical calculations [158].

Considering the above issues, a much finer mesh was selected in areas where the stress evolution is faster and of higher interest (in the calibrated area). In Figure 6.4 is shown the mesh structure of the 3D model of the specimen used in rotating bending fatigue test. The mesh consists in 96334 elements and 141780 nodes.

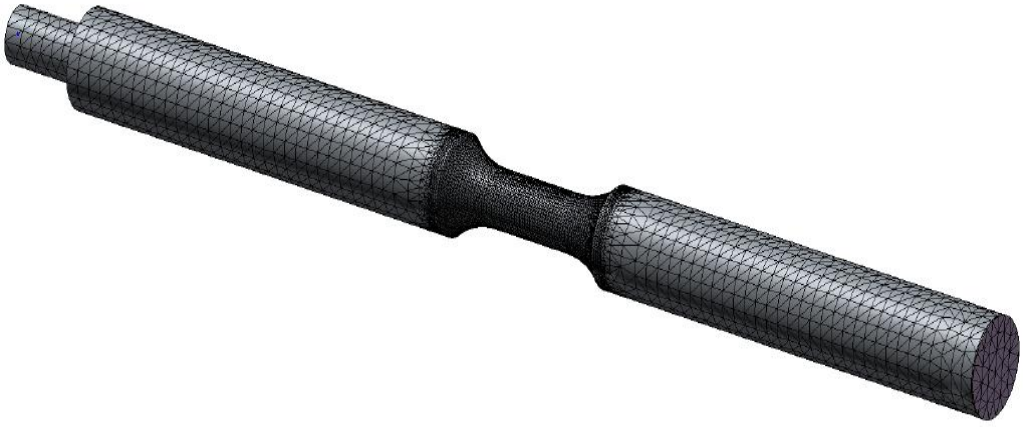

Figure 6.4: Meshing model used in rotating bending fatigue test

Loads and restraints are necessary to define the service environment of the model. The results of analysis depend directly on the specified loads and restraints. Loads and restraints are applied to geometric entities as features that are fully associative to geometry and automatically adjust to geometric changes. The model was constrained at one end and loaded with a constant force at the other end, see Figure 6.5.

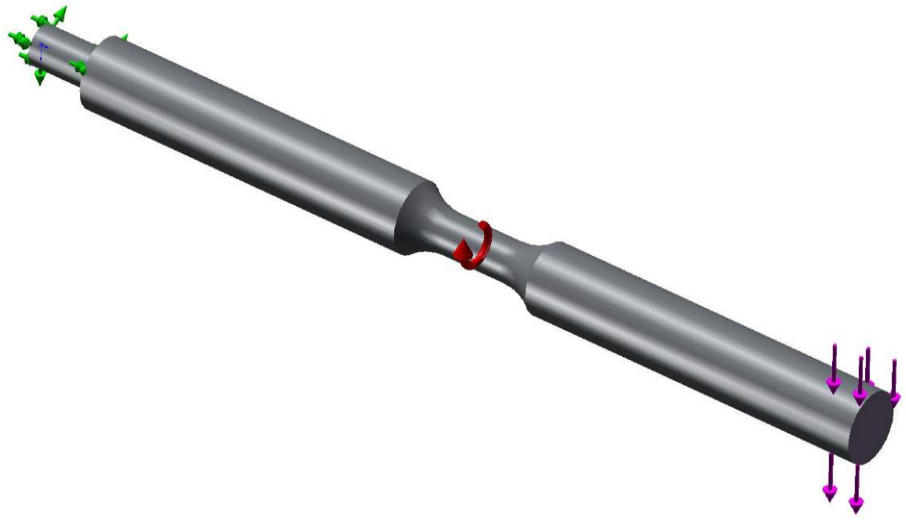

Figure 6.5: Defining the loads and restraints

The stress distribution in the central area is roughly symmetrical, with a region characterized by maximum stress of σ_{max} = 480 MPa and regions with minimum stresses of σ_{min} = 146 MPa (Figure 6.6).

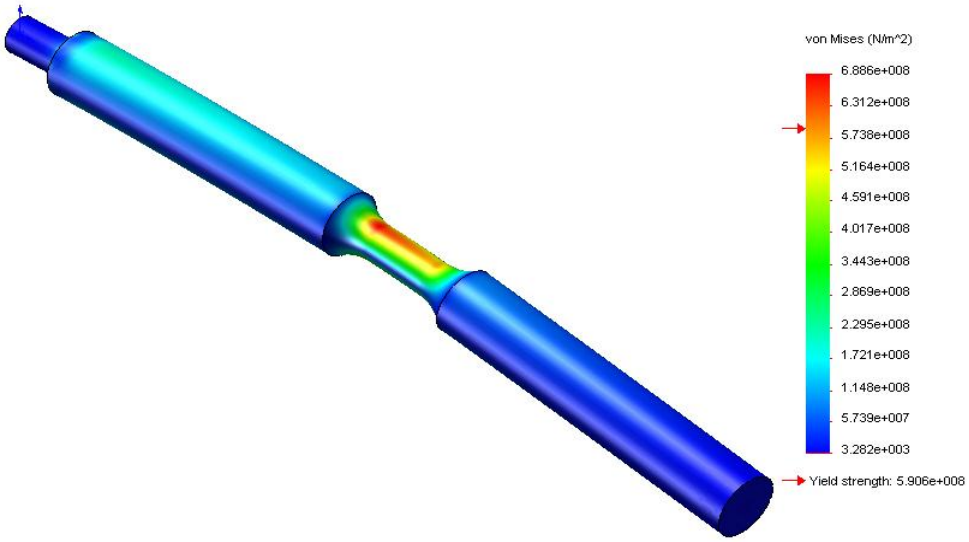

Figure 6.6: Von Mises stress distribution plot for annealed state

The resultant displacements plot and the equivalent strain plot for annealed state are presented in Figure 6.7 and Figure 6.8 respectively.

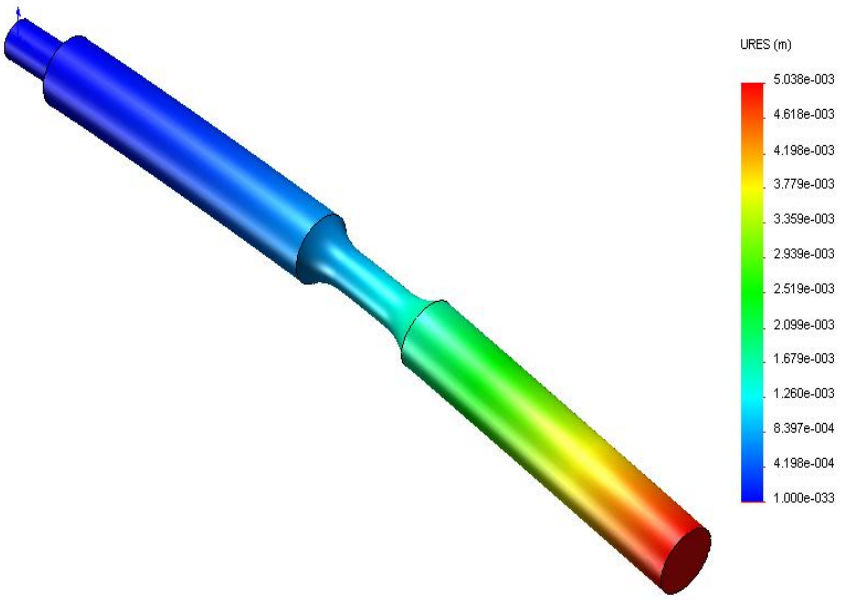

Figure 6.7: Resultant Displacements Plot for annealed state

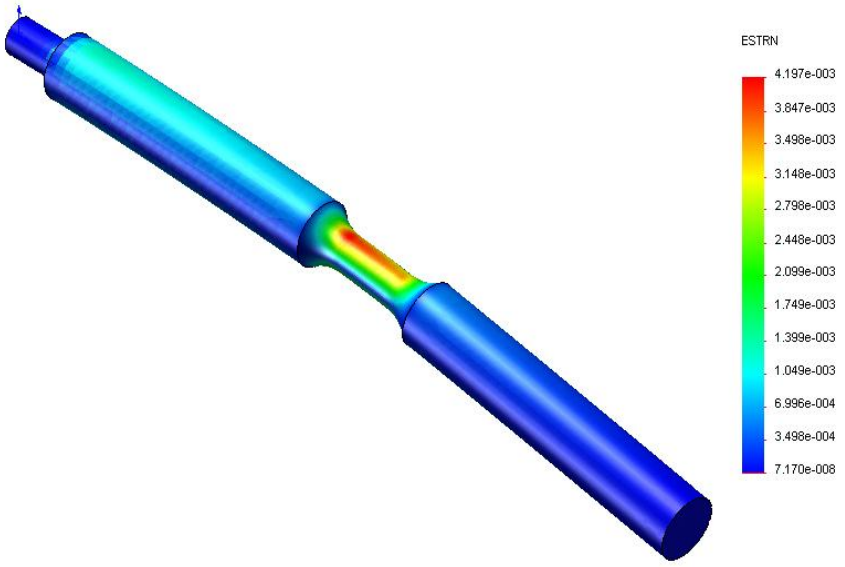

Figure 6.8: Equivalent Strain Plot for annealed state

The total life plot for the annealed state displayed in Figure 6.9 shows that failure due to fatigue is likely to occur in the calibrated region after approximately 25000 cycles.

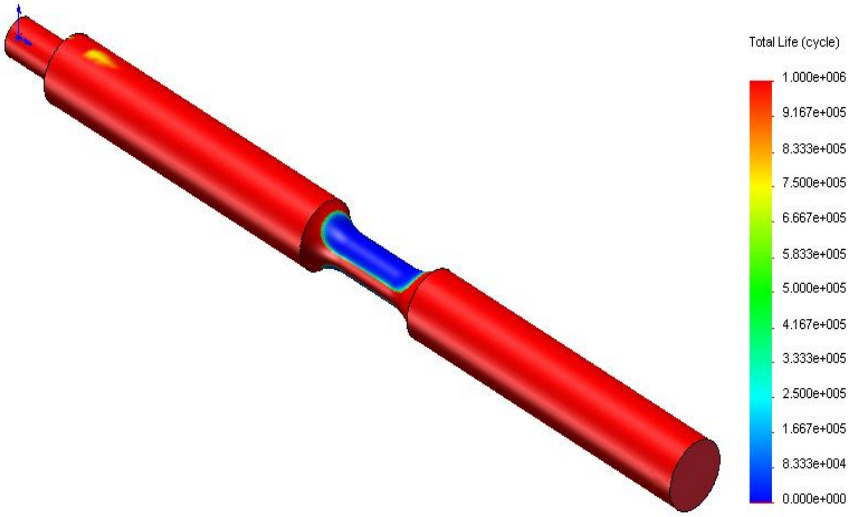

Figure 6.9: Life Plot

The stress distribution in the central area of the Duplex treated specimen is presented in Figure 6.10.

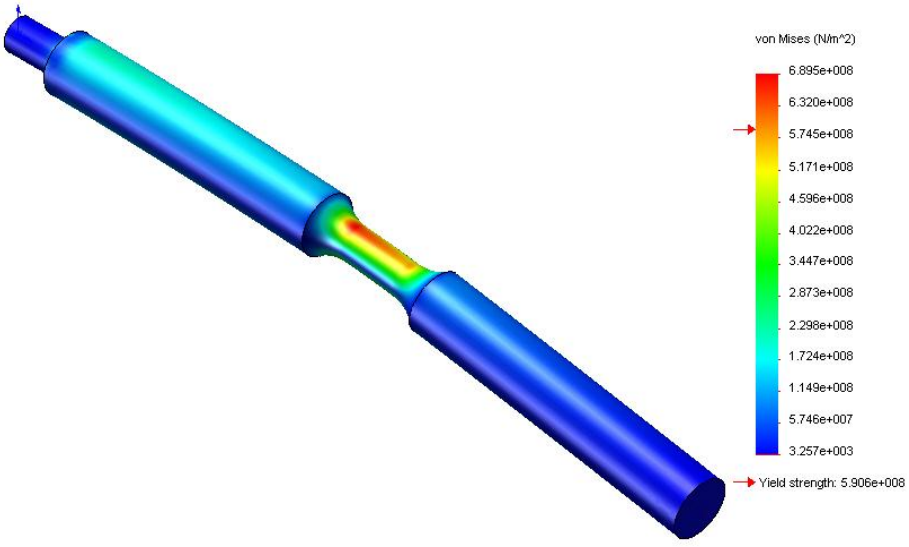

Figure 6.10: Von Mises stress distribution plot for Duplex treated state

The resultant displacements plot for Duplex treated state and the equivalent strain plot are presented in Figure 6.11 and Figure 6.12 respectively.

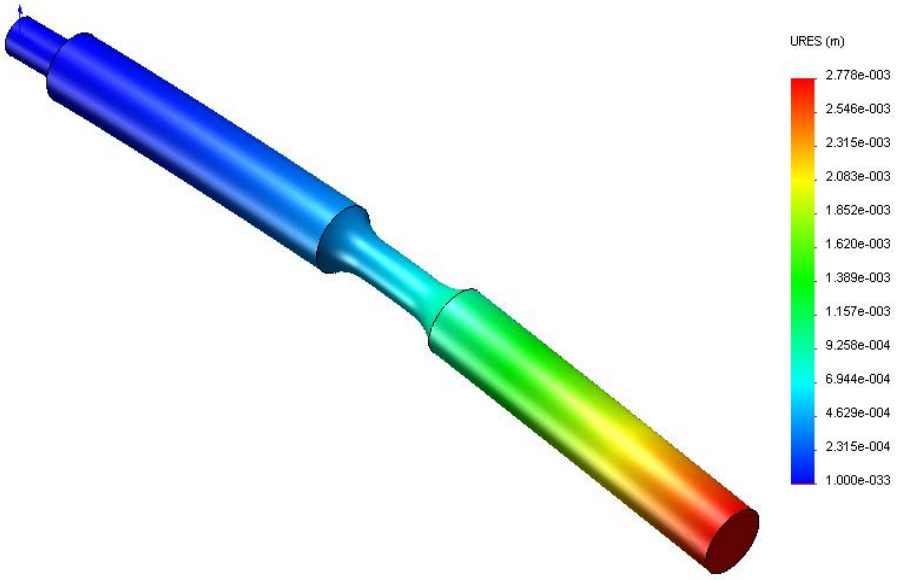

Figure 6.11: Resultant Displacements Plot for Duplex treated state

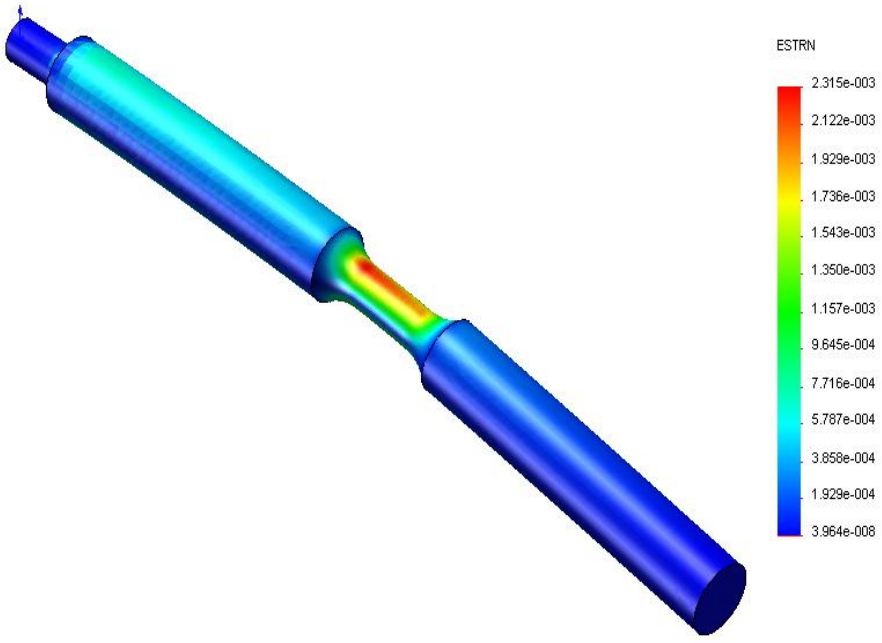

Figure 6.12: Equivalent Strain Plot for Duplex treated state

The total life plot displayed in Figure 6.13 shows that failure due to fatigue is likely to occur in the calibrated region after approximately 41670 cycles.

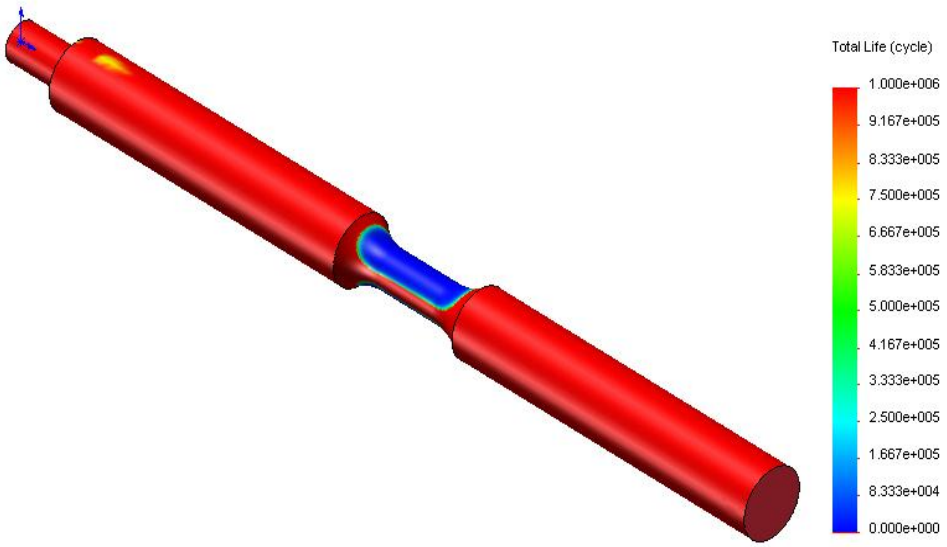

Figure 6.13: Life Plot

The purpose of the experimental tests was to validate the proposed theoretical model. For each loading mass, the specimens were tested until the crack appears. The results obtained are presented in Table 6.1.

Table 6.1. Von Mises Stress and Life cycles values

Structural state	Von Mises Stress [MPa]	Life cycles
Annealed	468	25000
Duplex treated	689	41670

6.3 Simulation of rotating bending fatigue test on Duplex treated consisting in nitriding followed by work hardening through shot peening using FEA

The simulation was made similar to the first Duplex treatment, using the same mesh, loadings and restraints. The stress distribution in the central area of the quenched and tempered state is roughly symmetrical, with a region characterized by maximum stress of σ_{max} = 689 MPa and regions with minimum stresses of σ_{min} = 327 MPa (Figure 6.14).

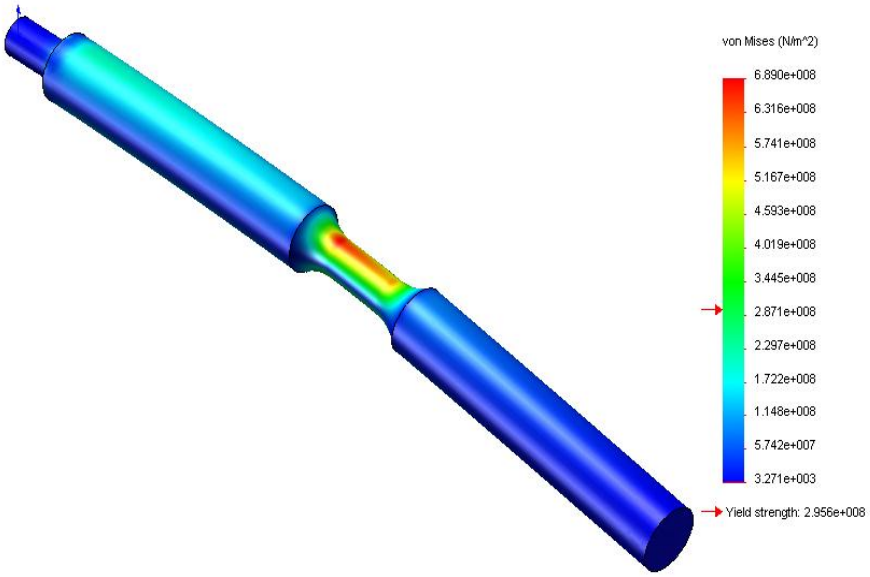

Figure 6.14: Von Mises stress distribution plot for quenched and tempered state

The resultant displacements plot and the equivalent strain plot for quenched and tempered state are presented in Figure 6.15 and Figure 6.16.

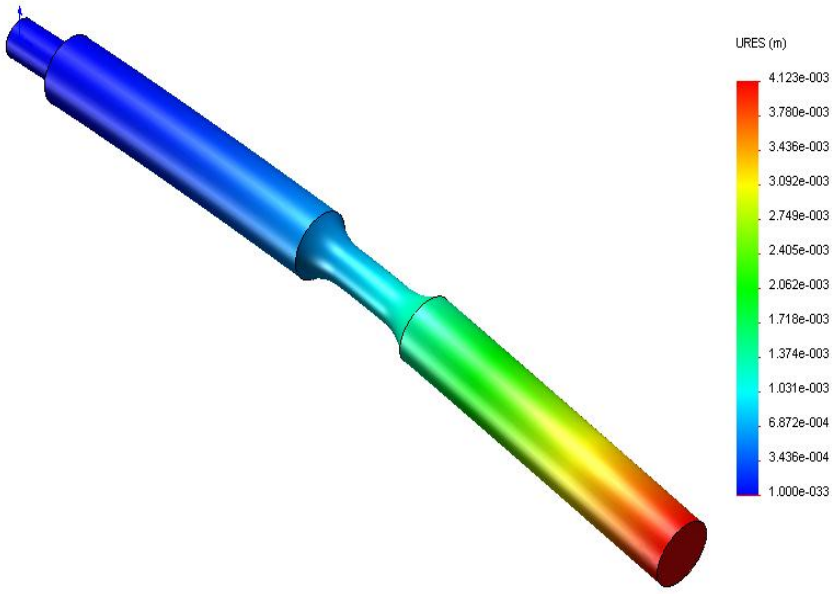

Figure 6.15: Resultant Displacements Plot

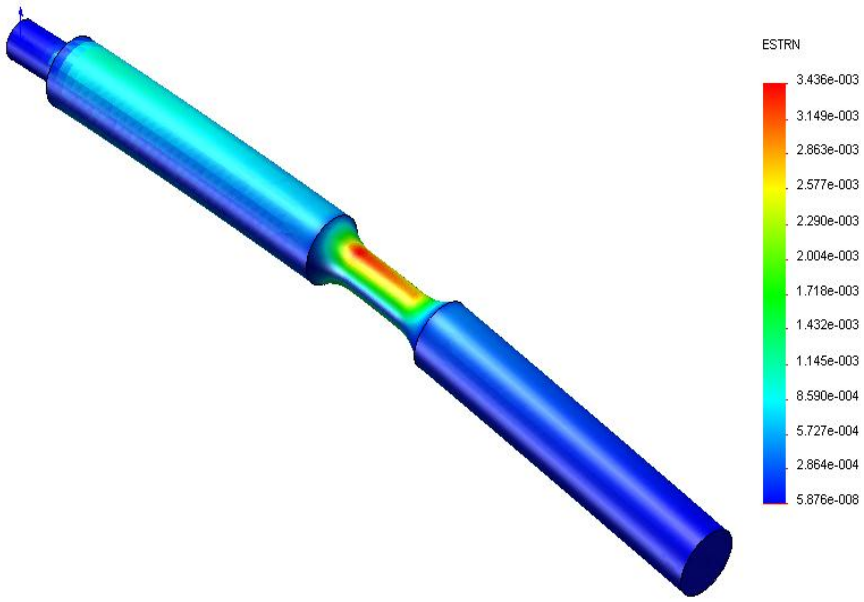

Figure 6.16: Equivalent Strain Plot

The total life plot is displayed in Figure 6.17 and shows that failure due to fatigue is likely to occur in the calibrated region after approximately 24895 cycles.

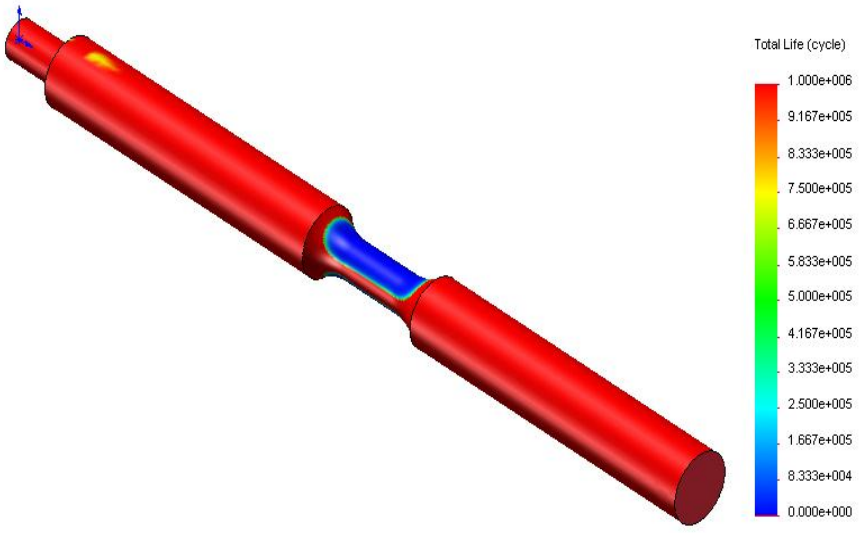

Figure 6.17: Life Plot

The stress distribution in the central area of the nitrided state is presented in Figure 6.18.

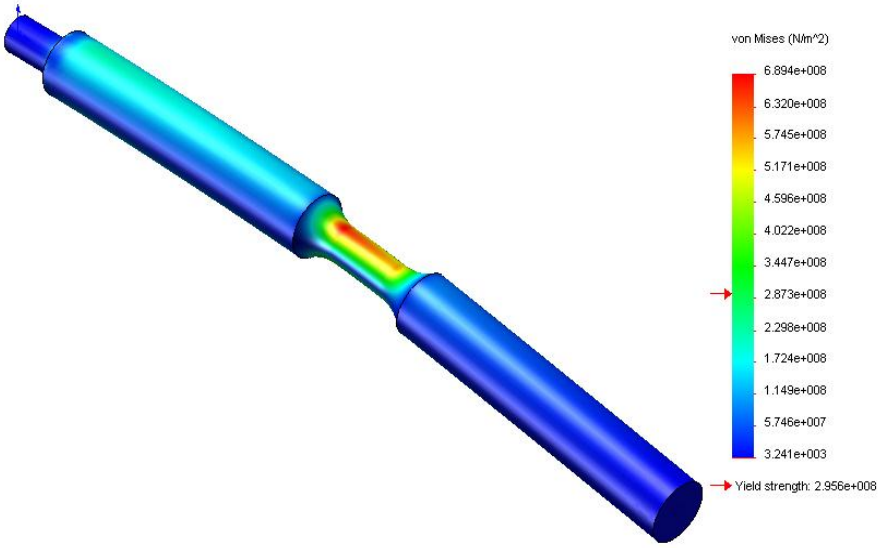

Figure 6.18: Von Mises stress distribution plot for nitrided state

The resultant displacements plot and the equivalent strain plot for nitrided state are presented in Figure 6.19 and Figure 6.20.

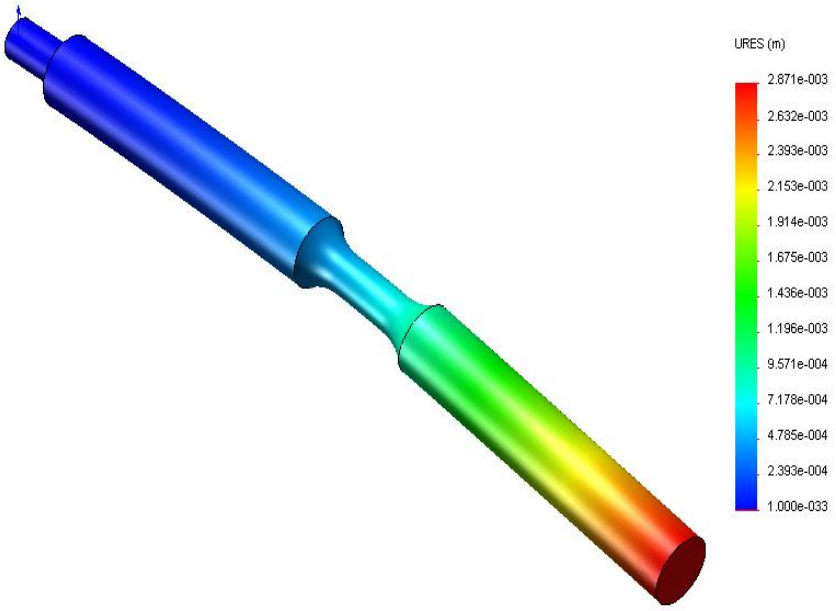

Figure 6.19: Resultant Displacements Plot for nitrided state

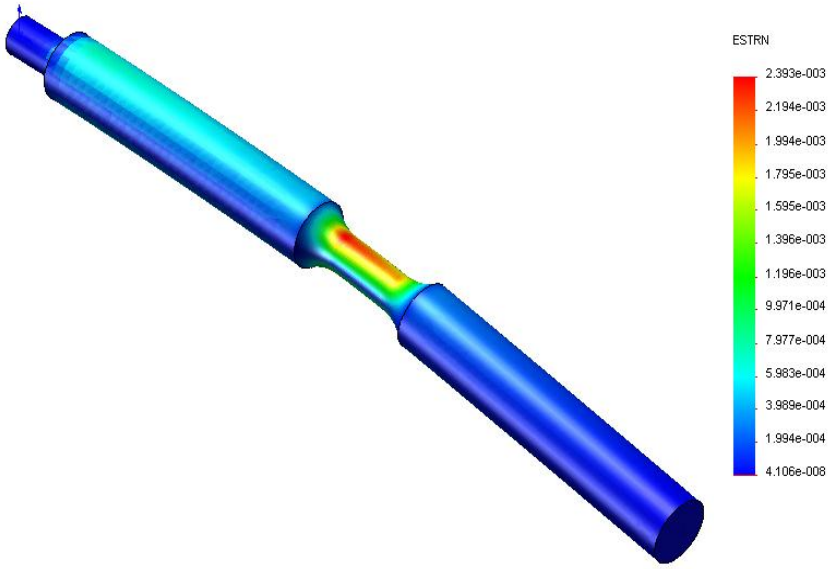

Figure 6.20: Equivalent Strain Plot for nitrided state

The total life plot is displayed in Figure 6.21 and shows that failure due to fatigue is likely to occur in the calibrated region after approximately 31672 cycles.

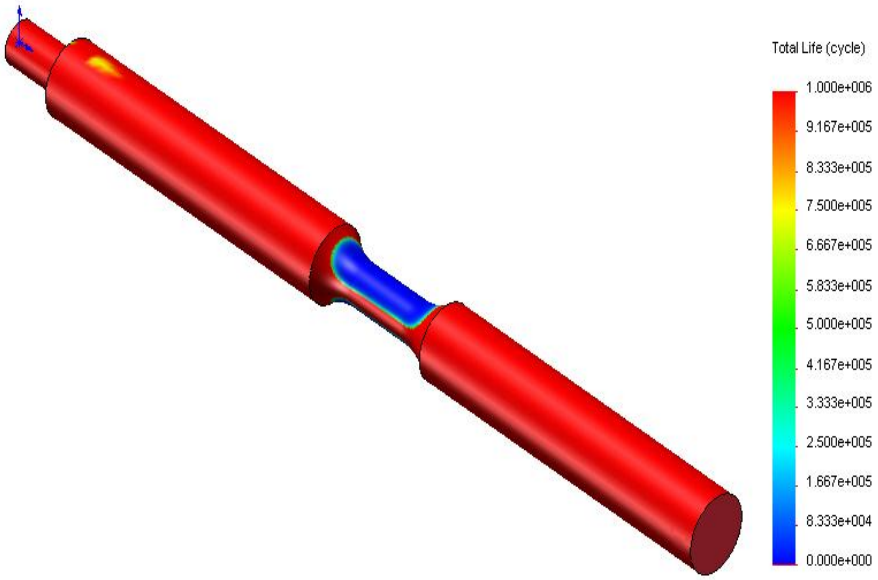

Figure 6.21: Life Plot for nitrided state

The stress distribution in the central area of the Duplex treated state is presented in Figure 6.22.

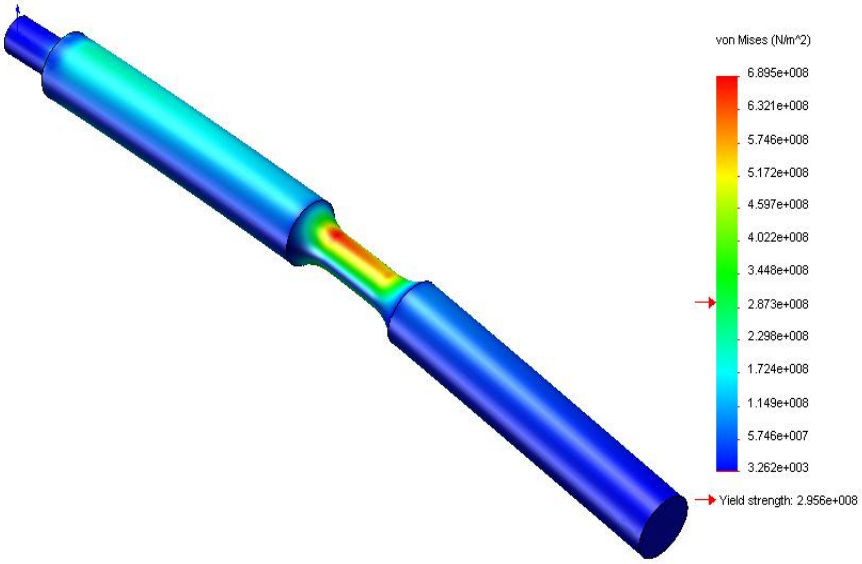

Figure 6.22: Von Mises stress distribution plot for Duplex treated state

The resultant displacements plot and the equivalent strain plot for Duplex treated state are presented in Figure 6.23 and Figure 6.24.

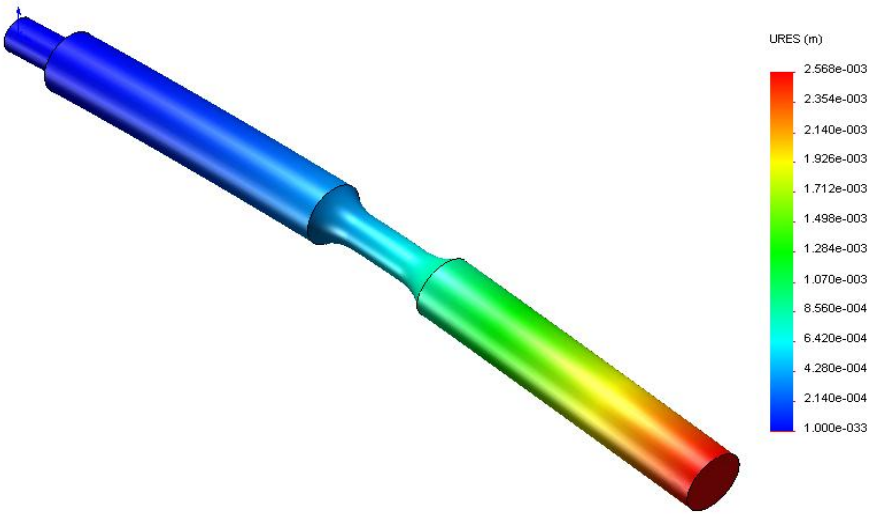

Figure 6.23: Resultant Displacements Plot for Duplex treated state

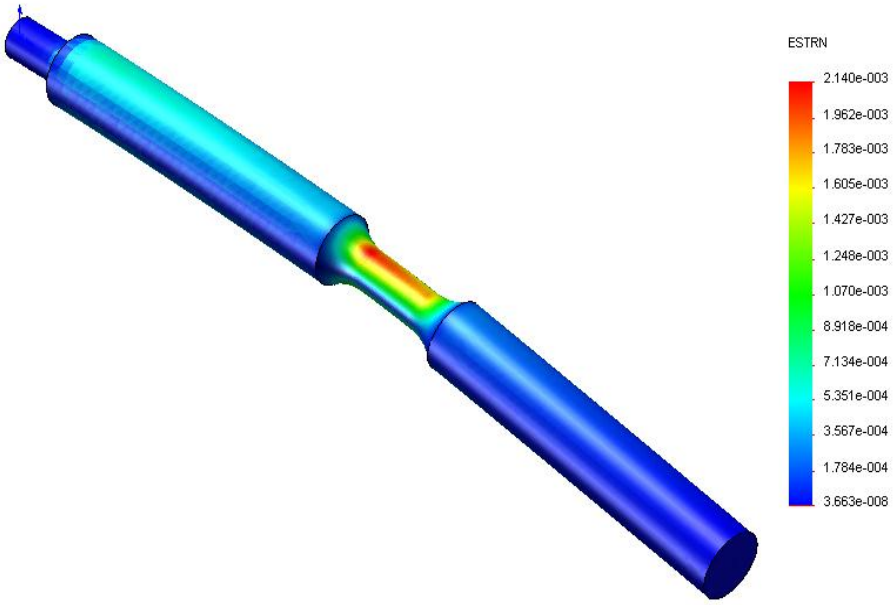

Figure 6.24: Equivalent Strain Plot for Duplex treated state

The total life plot is displayed in Figure 6.25 and shows that failure due to fatigue is likely to occur in the calibrated region after approximately 52462 cycles.

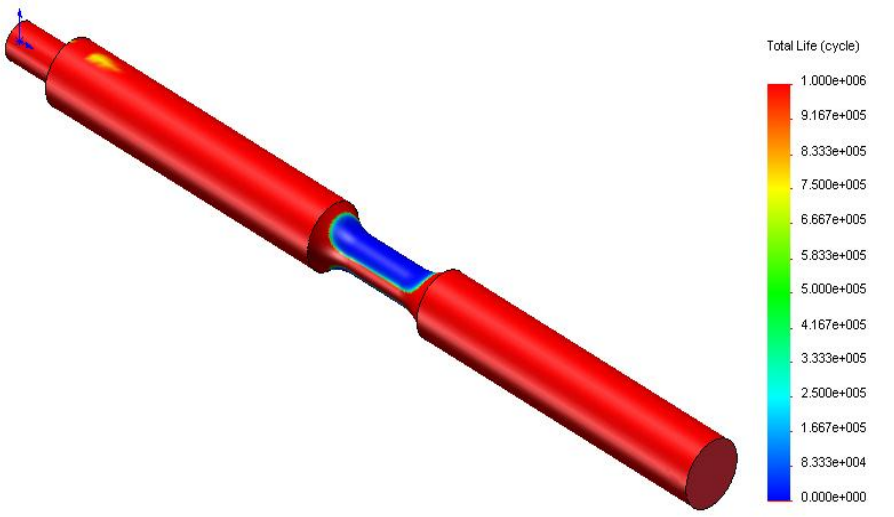

Figure 6.25: Life Plot for Duplex treated state

The results obtained by simulation are presented in Table 6.2.

Table 6.2. Von Mises Stress and Life cycles values

Structural state	Von Mises Stress	Life cycles
Quenched and temperated	400	24895
Nitrided	580	31762
Duplex treated	690	52462

6.4 Conclusions

The finite element analysis was performed on EN 16MnCr5 and EN 34CrNiMo6 untreated and Duplex treated steels specimens using CosmosWorks FEA software. The method was used in order to evaluate the life time of untreated and treated materials.

After performing the simulation, it can be concluded that the results obtained through Finite Element Analysis for the Duplex treated state are better compared to untreated states.

7. CONCLUSIONS, PERSONAL CONTRIBUTIONS AND FUTURE WORK

7.1 Conclusions

The Duplex treatments selected for this study consisted of gas carburizing followed by surface induction quenching and gas nitriding followed by shot peening, respectively.

Regarding the first treatment, the experiments performed lead to the following conclusions:

- The structure of Duplex treated samples consisted of tempering martensite and residual austenite, pearlite and secondary cementite in the case of carburized samples and only ferrite for the untreated samples. The structure was confirmed by X-ray and glancing incidence X-ray diffractions analysis;
- The micro-hardness of Duplex treated samples increased up to a value of 806 $HV_{0.2}$ due to the presence of martensite phases in their structure. The maximum value was reached at a distance of 0.2 mm from surface, due to the presence of a higher proportion of residual austenite at surface, as illustrated by glancing incidence X-ray diffraction analysis. Compared with the micro-hardness values of untreated samples, it can be observed an increase of about 2.6 times for the values of Duplex treated samples micro-hardness;
- The values of bulk modulus determined by means of instrumented indentation tests increased from 135 GPa (annealed state) to 245 GPa (Duplex state), which represents an increase of about 80%. The Martens hardness also increased from 1.98 GPa (untreated) to 6.06 GPa (Duplex treated state).
- The stress measurement performed by micro-indentation revealed high compressive stresses, ranging between -990 MPa and -1527 MPa (Suresh method) and -415 MPa to -640 MPa (Atari method);
- Corrosion tests performed in different solutions showed that the corrosion rate decreased significantly for Duplex treated samples compared to untreated samples. Glancing incidence analysis showed the presence of iron oxides (hematite) on the corroded samples. The corroded surfaces were investigated by scanning electron microscopy, which revealed the tendency towards pitting corrosion for all structural states.
- Duplex treated samples posses superior wear resistance, both in sliding and abrasive tests, compared to untreated samples, due to a higher hardness. The worn surfaces were investigated by scanning electron microscopy, which revealed various wear mechanism. In sliding wear tests, the worn surface presents parallel grooves formed by scratching the surface with hard particles, flat zones showing plastic deformation caused by the action of the counter body and rough cavities, suggesting that the material was removed and probably transferred to the counter body. In abrasive wear tests, SEM analysis revealed three-body wear mechanism.

- The fatigue limit determined by rotating bending fatigue tests increased from 280 N/mm^2 (untreated state) to 588 N/mm^2 (Duplex treated state), due to high compressive stresses induced by surface induction treatment.

Regarding the Duplex treatment consisting in gas nitriding and shot peening, the experiments performed lead to the following conclusions:

- The structure of Duplex treated samples consisted of the two typical nitriding layers (white and diffusion layer), and tempered sorbite for the untreated samples. The structure was confirmed by X-ray and glancing incidence X-ray diffractions analysis;
- The micro-hardness of Duplex treated samples increased up to a value of 880 $HV_{0.2}$ Compared with the micro-hardness values of untreated samples, it can be observed an increase of about 2.3times for the values of Duplex treated samples micro-hardness;
- The values of bulk modulus determined by means of instrumented indentation tests increased from 165 GPa (untreated) to 265 GPa (Duplex state), which represents an increase of about 80%. The Martens hardness also increased from 3.93 GPa (untreated) to 7.85 GPa (Duplex treated state).
- The stress measurement revealed high compressive stresses ranging between -393 MPa and -435 MPa (Atari method) and -1352 MPa to -1732 MPa (Suresh method);
- Corrosion tests performed in different solutions showed that the corrosion rate decreased significantly for Duplex treated samples compared to untreated samples. Glancing incidence analysis showed the presence of iron oxides (magnetite) on the corroded samples. The corroded surfaces were investigated by scanning electron microscopy, which revealed the tendency towards pitting corrosion for all structural states.
- Duplex treated samples posses superior wear resistance, both in sliding and abrasive tests, compared to untreated samples, due to a higher hardness. The worn surfaces were investigated by scanning electron microscopy, which revealed the same wear mechanisms as the previous treatment.
- The fatigue limit determined by rotating bending fatigue tests increased from 420N/m^2 (untreated state) to 770N/m^2 (Duplex treated state), due to high compressive stresses induced by the shot peening treatment.

7.2 Personal contributions

Taking into consideration the objectives, as well as the results of theoretical and experimental investigations obtained during this thesis, the main personal contributions can be summarized as follows:

- The selection of Duplex surface treatments by analyzing the advantages and disadvantages of possible combinations.;
- The materials selection considering their application and cost;
- The optimization of the treatments parameters so that the properties obtained from the first treatment are not damaged by the application of the second one;

- The role of internal stresses determined by means of micro instrumented indentation tests in the increase of fatigue resistance;

7.3 Future work

The theoretical and experimental studies conducted in the present thesis emphases the current trends in Surface Engineering, as well as the vastness of this domain. In this regard, some further research directions can be outlined:

- The combination of other surface treatments, which can provide high resistance to wear, corrosion and fatigue;
- Modeling of mass transfer in Duplex treatments;

REFERENCES

[1] Kenneth H., Matthews A., *Coatings Tribolgy Properties, Mechanisms, Techniques and Applications in Surface Engineering*, Tribology and Interface Engineering Series, No. 56, Oxford, ISBN 978-0-444-52750-9, 2009;
[2] http://www.machinerylubrication.com/Read/389/machines-wear-out;
[3] Rabinowicz E., *Friction and Wear of Materials,* 2nd edition, Wiley, New York, 1995;
[4] Blau P., Tribology web page:
https://www.ms.ornl.gov/researchgroups/SPM/methods, 2008;
[5] Bach Fr.-W, Laarmann A, Wenz T., *Modern Surface Technologies,* ISBN: 3-527-31532-2, 2006;
[6] Bell, T., *Surface Engineering: a rapidly developing discipline*, European Journal of Engineering Education, Vol. 12(1), pp. 27–32, 1987;
[7] Bell, T., *Wealth creation through surface engineering*, Surface Engineering News, LINK Surface Engineering Programme Secretariat, 1994;
[8] Bell T., Dong H., Sun Y., *Realizing the potential of duplex surface engineering*, Tribology International, Vol. 31, No. 1–3, pp. 127–137, 1998;
[9] Haefer, R., *Surface and thin film technology*, Ed. Springer Verlag, 1987;
[10] Blau P. J., *Friction and wear transitions of materials – Break-in, Run-in, Wear-in*, Ed. Noyes Publications, 1989;
[11] Bhushan, B., *Principles and Applications in Tribology*, Ed. John Wiley Sons, New York, 1999;
[12] Abel P. B., Ferrante J., *Surface physics in tribology*, Modern Tribology Handbook, Vol. 1, CRC Press, New York, pp. 5–47, 2001;
[13] Buckley D., *Properties of surfaces*, CRC Handbook of Lubrication – Theory and Practice of Tribology, Volume II Theory and Design, Ed. CRC Press Inc., Boca Raton, Florida, pp.17–30, 1984;
[14] Suh N. P., *Tribophysics*, Ed. Prentice-Hall, Englewood Cliffs, New Jersey, USA, pp. 489, 1986;
[15] Pasaribu H. R., *Friction and wear of zirconia and alumina ceramics doped with CuO,* Ph. D. Thesis, University of Twente, Netherlands, ISBN 90-365-2143-2, 2005;
[16] http://en.wikipedia.org/wiki/Friction;
[17] Nosonovsky M., Bhushan B., *Scale effect in dry friction during multiple-asperity contact*, Trans. ASME, Journal of Tribology, Vol.127, pp. 37–46, 2005;
[18] Ruina, A., Rudra P., *Introduction to Statics and Dynamics*, Oxford University Press., pp. 713, 2002;
[19] Hibbeler R. C., *Engineering Mechanics,* Ed. Prentice Hall, pp. 393, ISBN 0-13-127146-6, 2007;
[20] Beer F. P., Johnston E. R., *Vector Mechanics for Engineers,* McGraw-Hill, ISBN 0-07-297688-8, pp. 397, 1996;
[21] Meriam, J. L., Kraige L. G., *Engineering Mechanics,* Ed. John Wiley & Sons, ISBN 0-471-60293-0, pp. 328, 2002;
[22] Dowson D., *History of Tribology*, Ed. Professional Engineering Publishing, London, pp.768, 1998;

[23] Bowden F. P., Tabor D., *Friction and lubrication of solids*, Ed. Clarendon Press, Oxford, 1950;
[24] http://www.stle.org/resources/lubelearn/friction/default.aspx;
[25] Tangena A. G., *Tribology of thin film systems*, Doctoral thesis, Eindhoven Technical University, pp. 130, 1987;
[26] Rabinowicz E., *Friction coefficients of noble metals over a range of loads*, Wear, Vol. 159 pp. 89–94, 1992;
[27] Tabor D., *Adhesion and friction*, The Properties of Diamond. Field, J.E., Ed. Academic Press, pp. 325–350, 1979;
[28] Ashby M. F., Jones D. R. H., *Engineering Materials 1*, Second Edition, Ed. Elsevier Science, pp. 322, 1996;
[29] http://www.engin.brown.edu/courses/en3/Notes/Statics/friction/friction.htm;
[30] Rabinowicz E., *The wear coefficient – magnitude, scatter and uses*. International Lubrication Conference, San Francisco, USA, pp. 6, 1980;
[31] Buciumean M., Miranda A. S., Silva F. S., *Wear behaviour of the Al7175 alloy under different bulk stress states*, 10th Conference on Tribology, Bucharest, 2007;
[32] Halling J**.,** *Principles of Tribology*, MacMillan Education Ltd, Hampshire-London, 1987;
[33] Archard J. F., Hirst W, *The wear of metals under unlubricated conditions*, Proceedings of the royal society of London, Series A (236), pp. 397–410, 1956;
[34] Hutchings I.M., *Tribology: Friction and Wear of Engineering Materials*, Ed. Edward Arnold, London, pp. 273, 1992;
[35] Rabinowicz E., *Variation of friction and wear of solid lubricant films with film thickness*, ASLE Trans.10, pp. 1-9, 1967;
[36] Kato K., Adachi K., *Metals and ceramic,* Modern Tribology Handbook, Vol. 2, CRC Press, New York, pp. 771–785, 2001;
[37] Kato K., Adachi K., *Wear mechanisms,* In: Modern Tribology Handbook, Vol. 1. CRC Press, New York, pp. 273–300, 2001;
[38] Bayer R.G., *Mechanical Wear Prediction and Prevention*, New York, pp. 657, 1994;
[39] Ding Y., Jones R., Khunell B. T., *Elastic–plastic finite element analysis of spall formation in gears*, Wear, Vol. 197 pp. 197–205, 1996;
[40] Ioannides E., Bergling G., Gabelli A., An *analytical formulation for the life of rolling bearings*, Acta Polytechnica Scandinavica, Mechanical Engineering Series, The Finnish Academy of Technology, No.137, pp. 80 1999;
[41] Jiang J., Stack M. M., *Modelling sliding wear: from dry to wet environments*, Wear, Vol. 261, pp. 954–965, 2006;
[42] Celis J.P., Ponthiaux P., Wenger F., *Tribo-corrosion of materials: interplay between chemical, electrochemical, and mechanical reactivity of surfaces*, Wear, Vol. 261, pp. 939–946, 2006;
[43] Lim S. C., *Recent developments in wear mechanism maps,* Tribology International, Vol. 31, pp. 87–97, 1998;
[44] http://www.gordonengland.co.uk/wear.htm;
[45] http://www.machinerylubrication.com/Read/389/machines-wear-out;
[46]http://www.pall.com/main/industrial-manufacturing/why-is-filtration-important-3779.page;
[47] Hokkirigawa K., Kato K., *An experimental and theoretical investigation of ploughing, cutting and wedge formation during abrasive wear*, Tribology International, Vol. 21, pp. 51-58, 1988;
[48] Archard J., *Contact and rubbing of flat surfaces,* Journal of Applied Physics, Vol. 24, pp. 981-988;

[49] Bogaerts W., *Materials Engineering for the Chemical Process Industries*, 2008;
[50] http://gekengineering.com/Downloads/Free_Downloads/Corrosion_Introduction.pdf;
[51] http://www2.tech.purdue.edu/at/courses/at308/Technical_Links/Ac43-13-1B/CH6_2.pdf;
[52] Chaturvedi T. P., *Corrosion behaviour of orthodontic alloys - a review,* India, 2005;
[53] Suresh S., *Fatigue of Materials*, Cambridge University Press, 1998;
[54] Sachs N.W., *Understanding the Surface Features of Fatigue Fractures: How They Describe the Failure Cause and the Failure History*, Journal of Failure Analysis and Prevention, Vol. 5, 2005;
[55] http://www.asminternational.org/content/ASM/StoreFiles/05224G_Chapter14.pdf;
[56] Tripa P., Hluşcu M., *Rezistenţa Materialelor*, Ed. Mirton, Timişoara, 2007;
[57] Dumitru I., Faur N., *Elemente de calcul şi aplicaţii în rezistenţa materialelor*, Timisoara, 1997;
[58] Schijve J., *Fatigue of Structures and Materials*, Ed. Kluwer Academic Publishers, 2001;
[59] Kato H., *Sliding wear of nitride steels*, PhD Thesis, 1993;
[60] Eyre T. S., *The mechanism of wear*, Tribology International, Vol. 11, pp. 91-96, 1987;
[61] Kato K., Diao D.F., Tsutsumi M., T*he wear mechanism of ceramic coating film in repeated sliding friction*, International Conference on Wear of Materials, Orlando, USA, 1991;
[62] James H., Smart R. G., Reynolds J. A., *Surface treatments in engine component technology*, Wear, Vol.34, pp. 373-382, 1975;
[63] Bell T., Surface Engineering: past, present and future, Surface Engineering, Vol. 6, pp. 31-40, 1990;
[64] Eckstein, H.J, *Technology of Heat Treatment of Steel*, Leipzig, 1977;
[65] Vollertsen F., Vogler S., *Material properties and microstructure*, Munich, 1989;
[66] Rickerby D.S., Matthews A., *Advanced Surface Coatings: A Handbook of Surface Engineering*, Glasgow, pp. 364, 1991;
[67] Melford D. A., *Future of Surface Engineering in the UK*, London, 1991;
[68] Holleck H., Lahres M., Woll P., *Multilayer coatings – influence of fabrication parameters on constitution and properties*, Surface and Coatings Technology, Vol. 41, pp.179-190, 1990;
[69] Bell T., Dong H., Sun, Y, *Realising the potential of duplex surface engineering*, Tribology International, pp. 127-137, 1998;
[70] Bell, T., *Realising the potential of surface engineering in the 21st century*, *Executive Engineer*, Vol. **5**(1), 1997;
[71] Sun Y., Bell T., *Combined plasma nitriding and PVD treatments*, Transactions of the Institute of Metal Finishing, Vol. **70** (1), pp. 38-44, 1992;
[72] Kessler O.H., Hoffmann F.T., Mayr P., *Combinations of coating and heat treating processes: establishing a system for combined processes and examples*, Surface and Coatings Technology, Vol. 108-109, pp. 211-216, 1998;
[73] Dingremont N., Dergmann E., Collignon P., *Application of duplex coatings for metal injection moulding*, Proceedings of 9th International Congress on Heat Treatment and SurfaceEngineering, France, pp. 131–137, 1996;
[74] Staines A. M., *Trends in plasma-assisted surface engineering processes*, Heat Treatment of Metals, No. 4, 1991;

[75] Staines A. M., Bell T., *Multiple surface treatments for low alloy steels*, Paper presented at the conference 'Engineering the Surface', The Institute of Metals, 1986;
[76] Spies H.-J., Larisch B., Hoeck, K., Optimisation of TiN hard coatings on prenitrided low alloy steels, Surface Engineering, Vol.11, pp. 319-323, 1995;
[77] Leyland A., Fancey K.S., Matthews A., *Plasma nitriding in a low pressure triode discharge to provide improvements in adhesion and load support for wear resistant coatings*, Surface Engineering, Vol.7, pp. 207–215, 1991;
[78] Dong H., Sun Y., Bell T., Enhanced corrosion resistance of duplex coatings, Surface and Coatings Technology, Vol. 90, pp. 91-101, 1997;
[79] Rie K.T., Recent advances in plasma diffusion processes, Surface and Coatings Technology, Vol.112, 1999;
[80] Rie K.T., Broszeit E., Plasma diffusion treatment and duplex treatment recent development and new applications, Surface and Coatings Technology, Vol.76/77, 1995;
[81] Menthe E., Rie K.T., Plasma nitriding and plasma nitrocarburising of electroplated hard chromium to increase the wear and the corrosion properties, Surface and Coatings Technology, Vol. 112, 1999;
[82] Klimek K.S., Ahn H., Seebach I., Wang M., Rie K.T., Duplex process applied for die-casting and forging tools, Surface and Coatings Technology, Vol. 174/175, 2003;
[83] Klimek K.S., Gebauer-Teichmann A., Kaestner P., Rie K.T., Duplex-PACVD coating of surfaces for die casting tools, Surface and Coatings Technology, Vol. 201, 2007;
[84] Pfohl C., Rie K.T., Plasma duplex treatment of satellite, Surface Coatings Technology, Vol. 142/144, 2001;
[85] Batista J. C. A., Godoy C., Matthews A., Impact testing of duplex and non-duplex (Ti,Al)N and Cr–N PVD coatings, Surface and Coatings Technology, Vol. 163–164, 2003;
[86] Crummenauer J., Vetter J., Thermochemical treatment with added corrosion and wear protection, Proceedings of the 22 Heat Treating Society and 2nd International Surface Engineering Congress, 15-17 September, Indianapolis, USA;
[87] Michler T., Grische M., Bewilogua K., Hleke A., Continuously deposited duplex coatings consisting of plasma nitriding and a-C:H:Si deposition,. Surface and Coatings Technology, Vol.111, 1999;
[88] Alsaran A., Celik M., Study on compound layer formed during plasma nitro-carburizing of AISI 5140 steel, Journal of Materials Science, Vol. 11, pp.1759-1761, 2003;
[89] Keßler O., Hoffmann F., Mayr P., Proceedings of the 2nd International Conference on Quenching and the Control of Distortion, 4–7 November 1996, pp. 171–178, Cleveland, Ohio;
[90] Qiang Y.H., Ge S. R., Microstructure and tribological behaviour of nitro-carburizing quenching duplex treated steel, Tribology International, Vol.32, pp. 131-136, 1999;
[91] **Dobra R.M**., Mitelea I., Locovei C., Improvement of wear resistance of mechanical parts using Duplex treatments, ModTech International Conference - New face of TMCR Modern Technologies, Quality and Innovation - New face of TMCR, 25-27 May 2011, Vadul lui Voda-Chisinau, Republic of Moldova, pp. 329-333;
[92] Halabi J., Improvement of mechanical properties combining ferritic nitrocarburizing and induction quenching, Proceedings of the ASM 1st International Automotive Heat Treating Conference, pp. 201-208, 1998;
[93] Marsh K.J., Shot Peening: Techiques and Applications, London, 1993;

[94] Almen J. O., Black, P.H., Residual stresses and fatigue in metals, McGraw-Hill Book
Company, 1963;
[95] Guagliano M., Guidetti M., Riva, E., Contact fatigue failure analysis of shot peened gears, Engineering Failure Analysis, Vol.9, pp.147-158, 2002;
[96] Ohsawa M., Honda R., *Improvement of hardened surface by shot peening,* Proceedings of the II International Conference on Shot Peening, Chicago (USA), pp. 147-158, 1984;
[97] Kobayashi M., Hasegawa K., *Effect of shot peening on the pitting fatigue strength of carburized gears*, 1988;
[98] Guagliano M., Vergani L., *Fatigue crack growth behavior of nitrided and shot peened specimens*, Engineering Failure Analysis, Vol.9, pp.147-158, 2002;
[99] Guanhua D., Jawen H., Naisai H., *The effect of shot peening on the residual stress and fatigue property of nitrured layer of 42CrMo steel*, 5th Annual Conference of CMES HTI, Tianjin, 1991;
[100] Jingpu Z., *Effect of shot peening on contact fatigue behavior of 40Cr steel after compound heat treatment*, Proceedings of the II International Conference on Shot Peening (ICSP2), Chicago (USA), pp. 215-224, 1984;
[101] Pariente I., Guagliano M., Influence of shoot peening on the fatigue behavior of a gas-nitrided low alloy steel, Atti del Congresso IGF19, Milano, 2-4 July, 2007;
[102] Nakonieczny A., Pokorska I., *Possibilities of strengthening of diffusion nitrided layers by shot-peening,* 2nd International Conference on the Heat Treatment and Surface Engineering of Tools and Dies, 25–28 May 2008, Slovenia, 2008;
[103] Celis J.P., Drees D., Huq M.Z., Wu P.Q., De Bonte M., *Hybrid Processes - A versatile technique to match process requirements and coating needs*, Surface and Coatings Technology, Vol. 113, No. 1-2, pp. 165-181,1999;
[104] Kessler O.H., Hoffmann F.T., Mayr P., *Combinations of coating and heat treating processes: establishing a system for combined processes and examples*, Surface and Coating Technology, Vol. 108 - 109, No. 1-3, pp. 211-216,1998;
[105] Aya H., Flórez J., *A review of producing hard coatings by means of duplex treatments using an electroplated coating-thermochemical treatment combination*, Ing. Investig., Vol 31, No. 3, 2011;
[106] Menthe E., Rie, K.-T., *Plasma nitriding and plasma nitrocarburizing of electroplated hard chromium to increase the wear and the corrosion properties*, Surface and Coatings Technology, Vol. 112, No. 1-3, pp. 217-220, 1999;
[107] Wang L., Nam, K.,S., Kwon, S.,C., *Transmission electron microscopy study of plasma nitriding of electroplated chromium coating*, Applied Surface Science, Vol. 207, No. 1-4, pp. 372-377, 2003;
[108] Wang L., Nam, K.,S., Kwon, S.,C., *Effect of plasma nitriding of electroplated chromium coatings on the corrosion protection C45 mild steel*., Surface and Coatings Technology, Vol. 202, No. 2, 2007;
[109] Nam K.-S., Lee K.-H., Kwon S.-C., Lee D.Y., Song Y.-O., *Improved wear and corrosion resistance of chromium (III) plating by oxynitrocarburising and steam oxidation*, Materials Letters, Vol. 58, No. 27-28, 2004;
[110] Arkharov V.I., Yar-Mukhamedov Sh.Kh., Pavlik L.G., *The effect of gas carburizing on the structure and properties of electrolytic chromium deposits*., Materials Science, Vol. 8, No. 6, 1974, pp. 664-665;
[111] http://www.ibw-irretier.de/media/5830c56dfa9debc3ffff804bfffffff2.pdf;
[112] Mahboubi F., Duplex treatment of plasma nitriding and plasma oxidation of plain carbon steel, Surface Engineering, Surface Instrumentation and Vacuum Technology, Vol.79, 2005;

[113] Marušić K., Otmačić H., Landek D., CajneF. r, E. Stupnišek-Lisac, *Modification of carbon steel surface by the Tenifer process of nitrocarburizing and post-oxidation,* Surface & Coatings Technology, Vol. 201, 2006;
[114] Zhang J. W., Shiozawa K., Zhou W.N., Zhan W.H., *Effect of nitrocarburizing and post-oxidation on fatigue behavior of 35CrMo alloy steel in very high cycle fatigue regime*, International Journal of Fatigue, Vo. 33, Issue 7, July 2011;
[115] **R. M. Dobra**, I. Mitelea, "The corrosion resistance of steels treated by duplex treatments", Scientific Bulletin of "Politehnica" University of Timişoara, Transactions on Mechanics, ISSN: 1224-6077, Ed. Politehnica Timişoara, Roumania, Vol. 56 (70), Special ISSUE 1, Nov. 2011, pp. 61-65.
[116] Vermesan G., Vermesan E., Jichisan-Matiesan D., Cretu A., Negrea G., Vermesan H., M. Vlad.: *Introducere in Ingineria Suprafetelor*, Editura Dacia, ISBN 973-35-0922-1, Cluj Napoca, 1999;
[117] http://www.dipity.com/jalkhouri16/History-of-technology/;
[118] http://www.freshpepper.net/
[119] Mao, K., Sun, Y., Bell, T., *An initial approach to the link of multi-layer coatings contact stresses and the surface engineered gears*, Surface and Coatings Technology, Vol.201, 2007;
[120] Seidel, R., Luig H., *Friction and wear processes in hot die forging*, Proceedings of the International European Conference on Tooling Materials, September 7-9, pp. 467-480, 1992;
[121] Klimek K.S.; Gebauer A., Kaestner P., Rie K.-T., *Duplex-PACVD coating of surfaces for die casting tools*, Surface and Coatings Technology, 2006;
[122] Stoiber M.., *Low-friction TiN coatings deposited by PACVD*, Surface & Coatings Techhnology, Vol.163-164, 2003;
[123] Leskovšek V., *PACVD Duplex Coating for Hot Forging of High Strength Steels for Automotive Applications,* Strojarstvo, Vol.**53** (1), pp.39-44, 2011;
[124]
http://www.saarstahl.com/fileadmin/english/7131_7139_16MnCr5_16MnCrS5.pdf
[125]
www.ims.it/cmscontent.nsf/DocumentsByIDWeb/5RQMFR/16MnCr5_UNI_10084.pdf
[126]http://www.acerosdelperu.pe/en/pdf-productos-aceros-del-peru/34CrNiMo6.pdf
[127] Bousfield B, *Surface preparation and microscopy of materials,* John Wiley & Sons Hoboken, New Jersey, 1992;
[128] Goodhew F. J., Humphreys P. J. *Electron microscopy and analysis,* Taylor & Francis London, 1998;
[129] B. D. Cullity ,S. R. Stock, *Elements of X-ray diffraction,* Prentice Hall Englewood Cliffs, New Jersey, 1999;
[130] A. van Brussel, *Glancing angle X-ray diffraction: a different approach*, Applied Physics Letter, 1993;
[131] Mitelea I., Tillman W., *Stiinta Materialelor în Construţia de maşini*, Ed. Sudura, 1998;
[132] Serban V.A., *Stiinta Materialelor*, Ed. Politehnica;
[133] George E. Totten, Maurice A.H. Howes, *Steel Heat Treatment Handbook,* New York, 1997;
[134] Sundelöf E., *Modelling of Reactive Gas Transport*, Licentiate Thesis**,** Stockholm 2003;
[135] Udrescu L., Duma S., *Aplicaţii ale transferului termic şi masic la solide*, Ed. Politehnica, 2001;

[136] Oliver W. C., Phar G. M., *Measurement of hardness and elastic modulus by instrumented indentation: Advances in understanding and refinements to methodology*, Journal of Materials Research, 2003;
[137] S. Suresh, A. Giannakopoulos, *A new method for estimating residual stresses by instrumented sharp indentation*, Acta mater, Vol. 46, No. 16, 1998;
[138] D. Chicot, A. Tricoteaux, *Mechanical Properties of Ceramics by Indentation: Principle and Applications*, Ceramic Materials, ISBN 978-953-307-145-9, 2010;
[139] S. Suresh, A. Giannakopoulos, *Determination of elastoplastic properties by instrumented sharp indentation,* Scripta Materialia, Vol. 40, No. 10, pp. 1191–1198, 1999;
[140] **R. M. Dobra,** I. Mitelea, Evaluation of mechanical properties by instrumented indentation of Duplex treated steels, 7th Conference on Advanced Materials, Brasov, 2012;
[141] Atar E., Sarıoğlu C, *Residual stress estimation of ceramic thin films by X-ray diffraction and indentation techniques, Scripta Materialia* 48, 1331-1336, 2003;
[142] S. Millard, L. Sadowski, *Novel method for linear polarisation resistance corrosion measurement*, NDTCE'09 Non-Destructive Testing in Civil Engineering Nantes, France, June, 2009;
[143] **R. M. Dobra,** I. Mitelea, M. Bobină, *Corrosion behaviour of duplex treatment based on gas carburizing and surface induction quenching*, Metalurgia International;
[144] E. Santner, D. Klaffke, G. Meier zu Kocker, *Comprehensive tribological characterisation of thin TiN based coatings*, Wear 190,1995;
[145] H. Ronkainen, K. Holmberg et. al, Surface and Coatings Technology, Vol. 43–44, 1990;
[146] H. Vetters et al., *Development and validation of test methods for thin hard coatings* (FASTE), Final Report, EU Contract, MAT1-CT 940045;
[147] M.G. Gee et.al., *Progress towards standardisation of ball cratering*, Wear 255, 2003;
[148] A. Kassman, S. Jacobson, L. Erickson, P. Hedenqvist, M. Olson, Surface Coatings Technology, Vol. 50, 1991;
[149] D.N. Allsopp, R.I. Trezona, I.M. Hutchings, *The effects of ball surface condition in the micro-scale abrasive wear test,* Tribology Letters, Vol.5, 1998;
[150] A. Almeida, F. Carvalho, P.A. Carvalho, R. Vilar, *Laser developed Al–Mo surface alloys: Microstructure, mechanical and wear behaviou*r, Surface & Coatings Technology, Vol. 200, 2006;
[151] http://www.csm-instruments.com/tribometer;
[152] Mei Yang, *Nitriding – fundamentals, modeling and process optimization,* Dissertation Submitted to the Faculty of the Worcester Polytechnic Institute, April 2012;
[153] Baskaran B., Sivakum M.S., Bob M., *Optimization of the fatigue strength of materials due to shot peening: A Survey,* International Journal Of Structural Changes In Solids – Mechanics and Applications, Vol. 2, No. 2, 2010;
[154] http://www.industrialheating.com/articles/89973-principles-of-gas-nitriding-part-2;
[155] **R. M. Dobra**, I. Mitelea, M. Bobină, "Corrosion performance of Duplex treatment based on gas nitriding and shot peening**"**, Metal 2012, 23 - 25 Mai, 2012, Brno, Czech Republic;
[156] **R. M. Dobra**, I. Mitelea, D. Buzdugan, Iancu Şerban, "Evaluation of mechanical properties by instrumented indentation of Duplex treatment consisting in gas nitriding and shot peening", Scientific Bulletin of "Politehnica" University of

Timişoara, Transactions on Mechanics, ISSN: 1224-6077, Vol. 56 (70), Special ISSUE 1, 2012;
[157] Radu, B., Codrean, C., *Finite element modeling of thermal field developed in induction brazing of stainless steels with quasi-amorphous brazing alloys*, M.T.P., IXth Edition Timişoara academic Days International Symposium, May 26-27, 2005;
[158] http://www.colorado.edu/engineering/cas/courses.d/IFEM.d/;
[159] http://www.sv.vt.edu/classes/MSE2094_NoteBook/97ClassProj/num/widas/history.html
[160] Wang L. et.al., *Fatigue life analysis of aluminum wheels by simulation of rotary fatigue test*, Journal of Mechanical Engineering, Vol. 57, 2009;